MULTI-SENSOR INSPECTION AND ROBOTIC SYSTEMS FOR DRY STORAGE CASKS

14-7356

Proactive Robotic Inspection of Nuclear Storage Enclosures

Project Team

Cliff Lissenden, Penn State
Arthur Motta, Penn State
Sean Brennan, Penn State
Karl Reichard, Penn State, Applied Research Laboratory
Igor Jovanovic, University of Michigan
John Popovics, University of Illinois
Travis Knight, University of South Carolina

Advisory Board

Dwight Clayton, Oak Ridge National Laboratory
John Scaglione, Oak Ridge National Laboratory
Ryan Meyer, Pacific Northwest National Laboratory
Harold Adkins, Pacific Northwest National Laboratory
Jeremy Renshaw, Electric Power Research Institute
Ravi Kota, Holtec International

DOE Technical Point of Contact

Steve Marschman, Idaho National Laboratory

Table of Contents

PART I. ABSTRACT

Once removed from service, fuel rod assemblies are cooled in a pool and then placed in dry storage until they can be transported to a repository for disposal. The extended duration that used nuclear fuel spends in dry storage makes it prudent to be able to nondestructively inspect the dry storage casks. The degradation mechanisms of most concern are chloride-induced stress corrosion cracking of the stainless steel canister that confines the spent fuel and distributed cracking of the concrete in the overpack structure. Multi-sensor inspection and robotic systems were researched, developed, built, and tested. One system operates completely outside the cask to inspect the concrete. The other system, known as the PRINSE system, for Proactive Robotic Inspection of Nuclear Storage Enclosures, enters the cask through an outlet vent and navigates around the outer surface of the stainless steel canister. The PRINSE system delivers sensors for: (i) real-time characterization of the canister surface in order to assess whether chlorides are present, (ii) detecting the presence of cracks using shear-horizontal ultrasonic guided waves, (iii) measuring the temperature of the canister surface, and (iv) a gamma radiation counter. The four sensing modalities are applicable to any cask containing a stainless steel canister, however the robotic delivery system is designed specifically for Holtec's HI-STORM family of casks.

Horizontal axis casks have exposed concrete surfaces. A fully contactless air-coupled scanning ultrasonic test platform and a frequency-wavenumber domain data analysis method are used for these concrete structures. Analysis, numerical simulation and experimental results demonstrate that distributed cracks in concrete can be detected and cracked regions localized within a scanned region of concrete. Vertical axis casks (like the HI-STORM family) have steel-clad concrete overpacks. In a separate effort, a semi-coupled test platform and a guided wave attenuation-based data analysis method are used for disbond detection. Analysis, numerical simulation and experimental results show that the bonding conditions of steel-concrete interfaces can be quantitatively characterized using the guided wave signal analysis scheme.

The PRINSE system is designed for vertical axis dry storage casks, specifically the HI-STORM family. The double pulse laser-induced breakdown spectroscopy (LIBS) system takes advantage of an optical fiber to deliver intense light to the canister surface that enables surface composition characterization in-situ in real time. Chlorine concentrations as low as 10 mg/m^2 were detected on stainless steel. Additionally, a simpler laser setup was created to detect sodium as a surrogate for chlorine, and sodium was detectable when the chlorine concentration was as low as 0.5 mg/m^2. The electromagnetic acoustic transducers (EMATs) enable detection of stress corrosion cracks. The EMATs generate shear-horizontal waves that propagate around the canister and are reflected by cracks enabling 100% of the canister weld lines to be inspected. The EMAT-based crack detection system was tested at the Pacific Northwest National Laboratory on a canister containing blind defects and was shown to detect the crack sizes it was designed to detect.

The PRINSE system is a novel marsupial robot. The command center and winch outside the cask control the delivery arm and train of cars that traverse the outside of the canister from the cask ventilation system. The sensors are housed in the cargo bays of three cars that comprise the train, which is lowered to the bottom of the canister by the winch. Encoders on the winch enable the sensors to be delivered to a prescribed location, e.g., for re-inspection of a problem area. The PRINSE system does not mar the canister surface, can be extracted manually in the case of a power failure, and is designed for an elevated temperature and gamma radiation environment, although not all components of the prototype are made from the final materials. The PRINSE system was tested on a full canister that was placed inside a HI-STORM cask at the Holtec Manufacturing Division. It was also demonstrated on a full-height mockup at Penn State to a live audience.

PART II. OBJECTIVES, EFFORT, AND ACCOMPLISHMENTS

1. FULL STATEMENT OF OBJECTIVES

1.1 As-Proposed Project Objective

Our research objective is to develop sensors, monitoring methodologies, and a delivery system to ensure safe dry storage of used nuclear fuel. Environmentally assisted cracking (EAC) and concrete deterioration are viewed as the most likely modes of degradation.

Four elements of the technical merit of our proposed research are especially noteworthy. (i) Laser induced breakdown spectroscopy (LIBS) and Raman spectroscopy (RS) delivered via an optical fiber will enable novel in-situ surface composition characterization of salts and reaction products. Delivery of intense laser pulses through a fiber makes this in-situ approach tractable because the laser and spectrometer do not need to be mounted on the robotic delivery device; i.e., only the lens head and fiber need to be delivered to the characterization site. (ii) Compact electromagnetic acoustic transducers (EMATs), which are noncontact sensors, will enable linear and nonlinear ultrasonic guided wave based methods to nondestructively inspect the canister. Because guided waves basically provide line scans, it is possible to inspect weld regions that are otherwise inaccessible. Nonlinear methods based on higher harmonic generation have strong potential to characterize defects associated with very early stages of degradation. Further, linear methods are available to detect corrosion pits in the canister. (iii) Degradation of bare concrete and steel-clad concrete will be assessed with ultrasonic methods. Near-interface propagating waves in layered structures will be used to characterize concrete in the vicinity of the cladding. Air-coupled transducers mounted on a scanner will assess bare external concrete surfaces, while interior surfaces will be accessed with the robotically guided wand introduced next. (iv) A hybrid robotically guided wand system will provide access to the harsh and hazardous environment within the confined spaces of the ventilation system of dry storage casks, as well as sensor positional awareness. The guided wand system comprises a motorized end effector with both electro-mechanical and air-articulated guidance, vacuum enabled fixtures to maintain positioning, universal adapters for mounting various types of sensing systems, and an external operator station for control and data acquisition/analysis/management. Systems will be designed to meet the unique needs of both horizontal and vertical storage casks.

The robotically guided wand system will have various other monitoring features: video and infrared cameras to monitor corrosion, bolts, seals, and water stains; thermocouples to measure temperature; a miniature Geiger-Mueller counter and novel fiber-based dosimeter for radiological surveying; hygrometer for relative humidity; and a vacuum system to collect dust samples for off-site compositional analysis. The research plan is divided into seven main tasks, where tasks 1-3 each entail sensor development in the laboratory. The tasks can be briefly summarized as: (1) surface composition measurement, (2) canister nondestructive inspection (NDI), (3) overpack NDI, (4) guided wand robotic system, (5) modeling and measurement of environment, (6) data, and (7) technology integration.

1.2 Adjustments to Project Objectives

The scientific community recognizes that successful research inevitably evolves as it progresses. Thus, adjustments are commonly made to the project objectives during the course of the project. In this project, we were steered by all involved parties to target chloride-induced stress corrosion cracking (SCC) as the specific form of environmentally assisted cracking, which we did. The LIBS research progressed so well for surface characterization that there was no incentive to also investigate Raman spectroscopy, as was planned originally. In as much as EMATs provide a robust way to inspect all weld lines for SCC in canisters having severe accessibility challenges, they were unable to actuate finite amplitude waves that generate measurable harmonics for nonlinear characterization of the extent of SCC, thus the development focused on reliable detection of SCC using linear ultrasonic guided wave methods. Additionally, the robotic delivery system was originally envisioned as a guided wand. However, once we gained more knowledge and experience with dry storage casks the design changed to a marsupial robotic system that is more suitable for the geometric constraints. Finally, to keep the focus on the primary LIBS and EMAT sensory systems, the supporting temperature and radiation measurements, and their robotic delivery, no attempt was made to include secondary hygrometer or vacuum systems. In the eyes of the project team these adjustments resulted in a superior product at the end of the project.

1.3 Technical Functions and Requirements

At the onset of the project the advisory board encouraged the project team to develop the technical functions and requirements for the inspection and robotic systems. The functions and requirements that we developed were presented to the advisory board, the DOE technical point of contact, and the dry storage community (EPRI Extended Storage Collaboration Program). Revisions were made based on the feedback and the document was finalized in the third quarter of the first year of the project. That document is reproduced in the remainder of this section.

1.3.1 Summary

Dry storage casks for used nuclear fuel were intended as an intermediate staging point of the fuel cycle, maintaining waste storage after wet storage and before transport to an underground repository for disposal. Now dry storage casks are needed to provide safe containment for a much longer duration. Inspection is necessary, but the casks were not designed with condition monitoring in mind. Potential degradation mechanisms that could threaten safe containment and future transport of used fuel must now be addressed through an inspection protocol that includes the mode of delivery, modern sensors, and ability to compare measurements over time. The goal of our integrated research project is to develop multi-sensor inspection and robotic systems for this purpose. Measurements inside the cask ventilation system will characterize the: temperature distribution, radiation field, salt concentration (if any), and cracking in the canister (if any). Measurements on the outer surface of the overpack will characterize the condition of the concrete.

This document identifies the technical functions and requirements of the systems to be developed. A subsequent document will enumerate the operational tests and measurements that will demonstrate the capabilities of the systems.

1.3.2 Definitions

Canister – sealed stainless steel cylinder backfilled with helium that contains the used fuel
Overpack – concrete structure designed to protect and shield the canister
Dry storage cask – entire storage system of canister and overpack
ALARA – as low as reasonably achievable
GW – guided wave
HAZ – heat affected zone
HI-STORM – overpack structure built by Holtec International
LIBS – laser induced breakdown spectroscopy
MPC – multi-purpose canister built by Holtec International
NDI – nondestructive inspection
RT – radiation/temperature
RTD – resistance temperature detector

1.3.3 Types of Canisters Considered

- The LIBS (laser induced breakdown spectroscopy), GW NDI (guided wave nondestructive inspection), and RT (radiation/temperature) sensing systems to be developed will be applicable to welded stainless steel canisters in either vertical or horizontal orientation.
- The robotic delivery system will be developed and demonstrated on the Holtec MPC/HI-STORM type of storage cask.
- The concrete NDI system will address both steel-clad concrete (HI-STORM) and exposed concrete (horizontal systems and some vertical systems), and will be deployed on the outer exposed surface of the overpack.

1.3.4 Access to the Canisters

- For robotic inspection, the HI-STORM ventilation system will provide access to the canister. Simulations and hardware tests will identify whether inlet and/or outlet vents will be used to provide access to the plenum space between the canister and the overpack. Gamma shields and bird screens on vents will be removed.
- The LIBS sensing system will require a single sensor delivery head, which will be optically interfaced (via optical fibers) to the externally located laser source and spectrometer.
- The GW NDI sensing system will require two or more sensor heads (one transmits while the others receive). In some cases these sensor heads need be located in different gaps between the HI-STORM guide channels, requiring two robots working in tandem. The canister domain that can be inspected with a single robot will be identified, as will the domain that requires tandem robots.
- The RT sensing system will require a single sensor delivery head and may be readily integrated with the LIBS system. It will be electrically interfaced (via electrical cabling) to the externally located power source and electronic measurement instrumentation.

1.3.5 Size Constraints

- Vent sizes vary, but the sensor and robotic systems will be designed for minimum inlet and outlet vent sizes of the HI-STORM 100S, which are approximately 10" high by 15" wide for the inlet, and 5.75" high by 25" wide for the outlet.
- The robotic system and accompanying sensors will be designed to navigate to and operate in the space between the guide channels of the overpack, which is roughly 2" in the radial direction by 8" in the circumferential direction. Note that not all HI-STORM models have full-length guide channels, but we are designing for the worst case.
- The maximum weight of the robot should not exceed approximately 10 lbs. This constraint is to ensure that a moderate pulling force will be sufficient to extract the robot if it loses power.
- In the event that sensor packaging exceeds the size and/or weight limits of the robot, the robot will be designed to be modular to swap sensor suites. Sensor data can be collected from multiple traversals.

1.3.6 Operational Implementation

- Operation of the multi-sensor robotic systems will be from outside the cask and will follow ALARA principles. If possible, operations will not block more than one inlet vent and one outlet vent at a time.
- The inspection period for one HI-STORM storage cask should not exceed 3 days (presuming 4 hours of inspection work per day).

1.3.7 Environmental Requirements

- The ventilation system of dry storage casks is a harsh environment. The temperature of the canister is elevated and there is radiation from the presence of the spent fuel inside the canister. The sensor and robotic systems that operate inside the overpack will be designed to operate with a maximum dose of 2.7×10^4 rad/hr (conservatively based upon peak dose predicted after 5-years, see report PNNL-22495). The development of sensing and robotic systems will progress in phases: {i} start with components that generally work up to 140-160°F (commercial off the shelf), {ii} seek modifications such as cooling and custom-built sensors/actuators/wiring for operations at 250°F (the temperature adopted by the Extended Storage Collaboration Project), and {iii} design further modifications for operations at temperatures up to 350°F (which corresponds to the maximum temperature in a vertical canister when the deliquescence threshold is first passed, signaling the potential initiation of the SCC process). Time and budget constraints may not permit fabrication and testing of systems for phase {iii}.
- With the exception of fiducial marks (high purity nuclear grade paint) for location tracking, the robotic system will be designed to leave no scratches or similar damage to the cask, and to leave nothing behind. If it ceases to operate, it will be retrievable with a tether.
- Filtered, cooled air may be injected into the cask environment to reduce the robot temperature.
- Modeling efforts will utilize the most updated codes for temperature and dose prediction specifically COBRA-SFS (Cycle 3) and MCNP6.1. Radiation fields will be computed over a

detailed energy spectrum. Material dose rates will be computed for robotic equipment and sensors and potential activation of components will be computed such as Cobalt-60. Models will incorporate detailed geometries including fuel assemblies and basket structure. Source strength will be based on specific burnup and cooling time for specific fuel assemblies at defined locations in the cask.

1.3.8 Material Compatibility Requirements

- Use of organic materials, such as plastics or rubbers, within the cask will be avoided, as will use of cobalt and Teflon.
- Recommended materials include aluminum, stainless steel, and possibly PEEK.
- The material hardness of external sensor and robotic components should not exceed that of grade 316L stainless steel to ensure that the canister will not be scratched.
- If organics are required (rubber hoses, etc.), they will be shielded with stainless steel tape or other radiation/temperature "resistant" materials. Furthermore, such organics will be air-cooled.

1.3.9 Localization and Replication of Results

- Mapping of the cask will be attempted with the goal to localize acquired data repeatedly to within 2 inches. If this goal is not obtained then defects found in a previous inspection will be re-located by a combination of localization and re-inspection within the domain of uncertainty.
- Tests will be done on mock-up systems to determine localization accuracy and quantify the statistics of positioning error.

1.3.10 Measurements to be Obtained, and Their Accuracy

- The LIBS sensor system will be designed to measure the chemical composition on the surface of the canister. Specifically, it will quantitatively measure the areal density of salt on the surface of the canister in the range of 0.05-10 g/m^2, which is based on the observation that a concentration of 0.1 g/m^2 resulted in SCC [see NUREG/CR-7170].
- The GW NDI sensor system will be developed to be sensitive to a semi-elliptical EDM notch 0.42" long and 0.21" deep inside the HAZ of a canister weld. These dimensions are based on being able to inspect for cracks twice before they grow through-wall and assumptions that the crack length-depth aspect ratio is 2:1, that inspections will occur in 5-year intervals, and that it takes 15 years for a crack to grow through-wall once it initiates. Based on finite element analysis of weld residual stress fields [Kusnick, Benson, and Lyons, December 2013, Technical Letter Report], the preferred orientation of stress corrosion cracks is transverse to the weld. An inspection protocol to inspect any location of the full penetration canister welds (i.e., circumferential, longitudinal, top, and bottom) will be created. The time to inspect 25, 50, 75, and 100% of all welds will be estimated.
- Surface temperatures of the canister will be measured with thermocouples or RTDs accurate up to a temperature of 400ºF.
- Radiation will be measured with a miniature Geiger-Mueller counter, capable to measure radiation fields of up to 10^5 rad/h.

- A noncontact ultrasonic NDI system will be mounted on a robotic scanning system to operate on the dry storage cask exterior in order to characterize the condition of overpack structures that have exposed concrete. To-be-developed data analysis schemes will enable automated damage evaluation once ultrasonic signals are obtained. Expected damage mechanisms will in most cases exhibit distributed micro-cracking, for example damage caused by freezing and thawing, alkali silica reactivity, sulfate attack and corrosion of internal embedded reinforcing steel. Concrete spalling and near-surface voiding will also be considered.
- A noncontact ultrasonic NDI system will be mounted on a robotic scanning system to operate on the dry storage cask exterior in order to characterize the condition of overpack structures that have steel cladding. To-be-developed data analysis schemes will enable automated damage evaluation once ultrasonic signals are obtained. In this case the expected damage takes the form of voids and major disbonds between concrete and steel cladding at the outside surface of the overpack.

1.3.11 Data Acquisition and Management
- A single electronic data collection system located external to the dry storage cask will acquire, process and fuse data from the different sensing systems.
- The data acquisition system shall collect data from the primary NDI inspection systems (LIBS, GW/NDI, and RT) as well as any additional environmental and robotic system guidance sensors.
- The data acquisition system shall store all data in a to-be-determined open format or formats to facilitate collaboration in the analysis of measurement results. The system will be designed to minimize loss of data in the event of a fault.

1.3.12 Validation Tests
- The robot will be tested in a radiation environment at the Radiation Science and Engineering Center at Penn State to determine the longevity of the individual components.
- Testing will be performed to ensure passive removal of the robot in the event of actuator failure.
- A mockup of a portion of the MPC/HI-STORM geometry will be constructed at Penn State to develop and demonstrate robotic delivery of LIBS and GW NDI sensors and to show that the sensors can detect surface salts and EDM (electrical discharge machining) notches at elevated temperature.
- The GW NDI sensor system probability of detecting EDM notches will be characterized, given robotic delivery inside a mockup of the Holtec MPC/HI-STORM cask.
- The ability of the GW NDI sensor system to detect and characterize stress corrosion cracks in stainless steel will be benchmarked with respect to conventional ultrasonic methods by laboratory testing.
- The robotic delivery of LIBS and GW NDI sensors will be demonstrated on a mockup of an MPC/HI-STORM cask provided by Holtec. The exterior scanning system that evaluates the

condition of the exterior of the overpack will also be demonstrated on both exposed concrete and steel-clad overpacks.

2. DESCRIPTION OF EFFORT PERFORMED

This introductory section is based substantially on a portion of a previously published article [1]. Also, we point out in advance that the units are not consistent throughout the body of this report.

The fuel cycle is an integral part of nuclear power generation. Once the nuclear fuel is spent the assemblies are removed from the reactor and placed in wet storage pools, which provide cooling. Eventually, the decay heat generation in the fuel assemblies is low enough that they can be taken out of wet storage and sealed in an inert environment inside dry storage casks before being transported to a repository for disposal.

In the absence of a final repository, the extended use of dry storage for spent nuclear fuel from U.S. nuclear power plants needs to be assessed to confirm the structural integrity of the storage casks. Structural integrity analysis entails (i) an intimate knowledge of potential failure modes, as well as the associated degradation processes, and (ii) nondestructive inspection. Because the canisters are encased in a concrete overpack the access is limited and/or costly.

When ready for dry storage, fuel assemblies in the cooling pool are loaded into the basket inside a welded cylindrical stainless steel canister that is roughly 2 m in diameter, 5 m long, and 15 mm thick. Once loaded, the lid is welded onto the canister and the canister is backfilled with helium. The canister is then transported to the Independent Spent Fuel Storage Installation (ISFSI) and placed inside an overpack for shielding, cooling, and protection. Overpacks vary considerably by vendor, but there are two basic types; vertical axis systems are thick-walled steel clad concrete cylinders concentric to the canister, and horizontal axis systems are cuboidal concrete boxes and have a steel frame to support the canister in a horizontal orientation. Both cask types have a well defined ventilation system to provide convective cooling of the canister; however, the gap between canister and overpack is on the order of 10 cm for vertical axis systems while the plenum is quite spacious in horizontal axis systems. The environment inside the overpack is too harsh for humans due to high temperature and radiation (primarily gamma). Besides, vertical axis systems are far too constrained for human access. Thus, any inspection of a canister inside an overpack needs to be done with the assistance of a robotic system. The alternative of removing the canister from the overpack for inspection is costly and cumbersome.

Degradation of the overpack would most likely be associated with concrete degradation due to freeze-thaw or alkali-silica reaction. A potential degradation mode for canisters, especially those located in marine environments, is chloride-induced stress corrosion cracking [2-4]. Stress corrosion cracking (SCC) is a complex phenomenon that causes crack growth at a stress intensity factor lower than the plane strain fracture toughness K_{IC} and that manifests itself differently depending on the material, the type and level of loading, and the environment [5,6]. Some stainless steel alloys can be sensitized by high temperature excursions that deplete chromium at the grain boundaries. For instance, welding can create a heat affected zone (HAZ) that becomes susceptible to SCC. Welding also creates thermal residual stresses, which in the case of canister welds are not stress relieved [4].

There are three conditions necessary for SCC to occur: the material is susceptible, existence of a tensile driving force, and the presence of a corrosive environment. The third, and critical, element is brought about in this case by the presence of chlorides in solution on the surface of the stainless steel. In a marine environment it is possible that airborne salts containing chlorides enter the cask through the inlet vents with the cooling air and get deposited on the surface of the stainless steel canister. Under the right combination of temperature and humidity the salt could deliquesce on the surface, thereby creating conditions whereby SCC could occur [6]. While crack initiation and growth is dependent upon all of the above factors, experience and expectations from modeling imply that cracks transverse to the weld or parallel to it are predisposed to occur in the HAZ. Experience also shows that stress corrosion cracks in austenitic stainless steel are primarily intergranular and therefore contain significant branching [7]. We want to emphasize that these are educated expectations and do not want to discount the possibility of other degradation processes. While the functions and requirements of the multi-sensor robotic inspection system for the canister are focused on SCC, it is expected to be flexible enough to detect cracks initiated through other mechanisms.

A robotic inspection system was developed to use LIBS for surface composition measurements on the stainless steel canister. To make this practical an optical fiber will be used to deliver the intense light from the laser to the surface and back to a spectrometer so that the laser and spectrometer can be located in a command center outside the cask. The robotic system will also deliver EMATs for crack detection using shear horizontal (SH) waves. One of the real advantages of using SH waves is that they do not require access to the entire surface of the canister. Some vertical axis overpack models have guide channels to maintain concentricity between the canister and overpack that effectively block access to roughly half the canister surface. In these cask models the robotic system is essentially constrained to move vertically between the guides. This is the design basis for our robotic inspection system. In addition to LIBS and EMAT measurements the robotic inspection system measures temperature with thermocouples and ionizing radiation with a miniature Geiger Muller tube.

References
[1] C.J. Lissenden, S. Choi, H. Cho, I. Jovanovic, A. Motta, K. Hartig, X. Xiao, S. Le Berre, S. Brennan, K. Reichard, R. Leary, B. McNelly, 2017, "Toward robotic inspection of dry storage casks for spent nuclear fuel," *ASME J. Pressure Vessel Technology*, Vol. 139, 031602.
[2] Tani, J., Mayazumi, M., Hara, N., 2008, Stress corrosion cracking of stainless-steel canister for concrete cask storage of spent fuel, *J. Nuc. Mat.* 379:42-47.
[3] He, X., Mintz, T.S., Pabalan, R., Miller, L., Oberson, G., 2014, Assessment of stress corrosion cracking susceptibility for austenitic stainless steels exposed to atmospheric chloride and non-chloride salts, *U.S. NRC NUREG/CR-7170*, Washington D.C.
[4] Chu, S., 2013, Failure modes and effects analysis (FMEA) of welded stainless steel canisters for dry cask storage systems, *Electric Power Research Institute Report 3002000815*, Palo Alto, CA.
[5] Hertzberg, R.W., 1996, *Deformation and Fracture Mechanics of Engineering Materials*, Wiley, New York.

[6] Enos, D.G., Bryan, C.R., Norman, K.M., 2013, Data report on corrosion testing of stainless steel SNF storage canisters, SAND2013-8314P, Sandia National Laboratories.

[7] Caseres, L., Mintz, T.S., Bayssie, M.M., 2010, Atmospheric stress corrosion cracking susceptibility of welded and unwelded 304, 304L, and 316L austenitic stainless steels commonly used for dry cask storage containers exposed to marine environments, U.S. NRC NUREG/CR-7030, Washington D.C.

2.1 Compositional Analysis

Chlorides on the surface of the dry storage canister (DSC) can be detected, and the concentration estimated, using LIBS. The setup involves a laser located outside the cask sending light pulses through an optical fiber to remote optics located in a robotic car. The collection optics, located in the same car, direct the light collected from the plasma through another optical fiber to a spectrometer, which is located outside the cask. Ultimately, the spectra are analyzed in real time to determine the chloride concentration.

2.1.1 Background and objectives

A typical Holtec cask system is comprised of a cylindrical stainless steel (SS) canister and a steel-clad concrete overpack with a passive ventilation design to draw the outside air into the overpack and remove the decay heat of the spent nuclear fuel. It is well known that in the presence of a corrosive environment, sensitized material, and tensile stress, cracks can propagate through the mechanism referred to as SCC. Chloride-induced SCC, primarily intergranular in nature, is deemed the most likely degradation mechanism of DSCs, especially those located in coastal areas, where airborne sea salt can easily enter through the cask venting system and deposit onto the outer surface of the DSC, including the HAZ of the weld lines, over a long service life. Other potential chloride sources such as road salt, cooling tower drift, and gaseous hydrogen chloride leaks could also lead to a corrosive environment. This work aimed at evaluating the corrosive environment provided by the presence of chlorine (Cl) that could threaten the integrity and safe operation of the DSCs. It is important to note that the mere presence of Cl does not represent a corrosive environment, unless the chlorides are in solution as can happen by deliquescence once the humidity increases and temperature decreases sufficiently.

2.1.2 Requirements for compositional analysis

Since an SCC-related lower limit of concern for Cl deposited on SS has not been identified, a goal was established to detect and quantify amounts ranging from 50 to 10000 mg/m^2 (see section 1.3.10). This range encompasses low amounts of chlorine, and in the event of signal saturation, the amount of Cl will most likely be in high enough concentration for chloride-induced SCC. Under ideal circumstances, this provides insight as to how much concern should be placed on preventive maintenance for the given cask.

Given the strict space constraints inherent with dry-cask storage, a chlorine detection device must be small enough to navigate through one of the cooling channels, while surviving the harsh environment imposed by heat and radioactivity of the spent fuel. Realization of a system compact and resilient enough to operate in the harsh and constrained environment of a cooling channel is not feasible with the currently available laser and spectroscopic instrumentation technology that reaches the requisite performance to measure low concentrations of chlorine. To overcome this challenge, a scheme of remote operation and detection is required that keeps high-cost, bulkier, and more environmentally sensitive equipment in a controlled area outside of the cask.

2.1.3 Technical approach

Laser-induced breakdown spectroscopy (LIBS), a type of atomic emission spectroscopy, has proven to be an effective approach for detection of Cl attached to stainless steel surfaces. Attributes such as no sample preparation, low sampling rate, high spatial resolution, and fast analytical response with a typical limit of detection of a few ppm, led to use of LIBS in many fields, including nuclear energy, security, environment, agriculture, and space, to name a few. However, the sensitivity of the Cl concentration measurement via LIBS is limited by the high ionization potential of Cl and by the difficulty in populating the relatively high upper level energy of neutral Cl for the transition of interest. This is especially the case when high-power laser pulses need to be delivered by flexible fiber optics through the duct of the air ventilation system of a cask. We devoted extensive efforts to the development of LIBS method and instrumentation that could be deployed in the Cl field measurement for inspection of the DSCs.

2.1.3.1 Principles and implementation of LIBS

LIBS involves focusing high-power laser pulses onto a sample surface to vaporize a small amount of material and generate a plasma that contains ionized and excited atoms and molecules soon after the laser ablation, as shown in Figure 2.1.1. A fraction of the optical emission from the plasma is collected and directed to a spectrometer, typically using an optical fiber. In the spectrometer the collected light is spectrally dispersed and usually recorded in a digital form by a pixelated detector. Proper electronic gating of detectors, such as intensified charge-coupled devices (ICCD), helps to better isolate the characteristic spectral lines originating from the bound-bound radiative transitions in ions, neutral atoms, and molecules from the continuum emission, primarily due to the free-free bremsstrahlung and free-bound recombination processes.
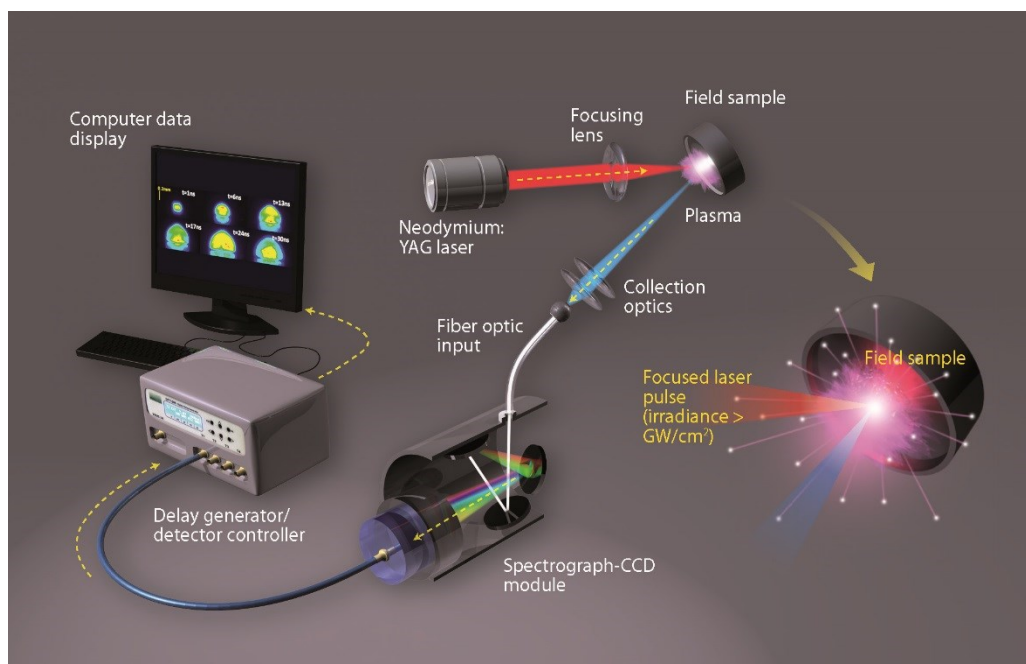
Figure 2.1.1. Principle and diagram of laser-induced breakdown spectroscopy (LIBS).

The ability to carry out remote measurements is one of the major advantages of LIBS, enabling its deployment in settings that are inaccessible or adverse to human health. Fiber-optics (FO) LIBS can significantly reduce the requirement on the instrument performance of the laser and optical system, especially over a long distance. It does not require delivery of the laser pulse via open line-of-sight and can therefore better shield personnel from laser hazards, which is very suitable for the application of DCSS inspection.

However, the relatively poor sensitivity compared to other optical emission spectroscopy prevented applications of LIBS in a broader range of problems, especially in the case of FOLIBS. In this situation when high-power laser pulses need to be delivered by flexible fiber optics through the duct of the air ventilation system of the cask, the maximum laser irradiance that can be achieved at the sample surface is limited by multiple factors related to the optical fiber, including its aperture, laser coupling efficiency, optical damage threshold, intermodal dispersion, and the focusing conditions that can be practically realized post fiber exit. A number of techniques have been introduced to improve the analytical performance of the LIBS technique by further optimizing various experimental parameters, such as ambient gas environment, sample surface morphology and temperature, material matrix, confining magnetic field, laser wavelength, pulse duration and shape, and the use of lasers in the burst mode. Double pulse (DP) excitation technique became one of the successful approaches, which was designed to separate the processes of laser ablation and plasma excitation and optimize them individually. In DP LIBS, the plasma emission could be significantly enhanced along with an increase of the signal-to-noise ratio due to greater mass ablated and higher temperatures achieved. The optimal inter-pulse delay in DP LIBS is on the order of a few microseconds. The collinear configuration (both of two successive pulses in a single burst propagate orthogonally to the sample surface) is considered to be the most relevant to this application.

2.1.3.2 Detection of Cl via LIBS

Efficient quantification of halogen elements is necessary in a wide variety of applications, but it is difficult mainly because of their energy level distribution, which is why they have been investigated to a lesser degree than metallic elements. Cl, for example, has the strongest emission lines in the vacuum ultraviolet (VUV) spectral region, which is not applicable for LIBS measurement in atmospheric environment due to the strong absorption by oxygen. Another problem is the transmission of silica-based optics and the lack of appropriate charge-coupled devices (CCD) with high sensitivity in this spectral region. Although measurements of Cl in air are possible in the near infrared (NIR) region, they are still difficult considering the weaker emission from excited-state transitions in NIR when compared to intense lines of the matrix (such as iron) that may interfere and have high laser irradiance required for excitation energies that exceed approximately 10 eV. Figure 2.1.2 depicts a simplified energy level diagram of the Cl atom with relevant NIR transitions between excited states of 4p $^4D^o$ and 4s ^4P. The 4p $^4D^o_{7/2}$ →4s $^4P_{5/2}$ transition at 837.6 nm is the most intense one that can be resolved from the spectral lines of the matrix. The free-bound transitions from the singly ionized state are also shown in the diagram, which contribute to the continuous background in the spectrum. The excitation energy of 10.4

eV of Cl is considerably higher than that of Na (2.1 eV). As a result, Cl has a relatively high plasma ignition threshold, which can be attained only through a much higher laser irradiance.
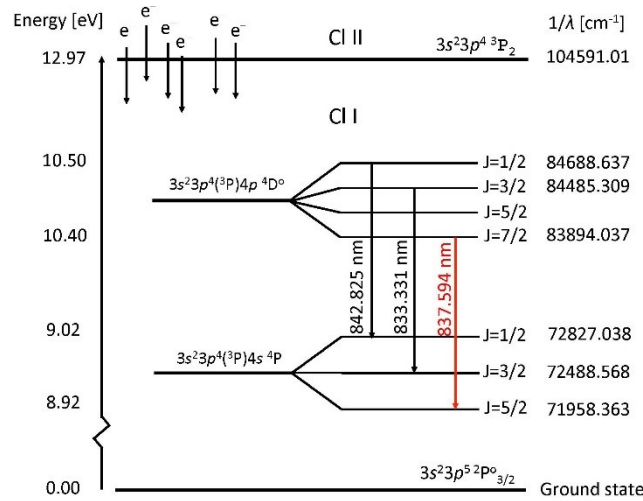
Figure 2.1.2. *Energy level diagram of Cl atom with relevant atomic transitions from*

4p ⁴Dᵒ →4s ⁴P used for detection of Cl in our experiments.

2.1.4 Sample preparation

Aiming at low-level chlorine measurement, we chose to adopt calibrated LIBS for quantitative analysis. Sufficient homogeneity of samples is critical for quantifying minor and trace elements with desired accuracy. We explored several methods to prepare homogeneous samples for testing.

2.1.4.1 Pipette-based process

The initial samples used were obtained by letting pure NaCl, in concentrations of 0.01 to 5 mol/L solution droplets dry on the surface of SS coupons (2.5 x 2.5 cm^2) at room temperature. 5 mol/L aqueous NaCl solution obtained from Alfa Aesar standards was used with appropriate dilution. Figure 2.1.3 shows scanning electron microscope (SEM) micrographs taken from a batch of samples obtained with this procedure. In every case, the pictures show that drying at room temperature provides poor salt homogeneity and little reproducibility. When drying, the droplets produce macroscopic crystals of salt with random repartition within the area of the droplets from one sample to the other, even if the same configuration is conserved from one sample to the other. Those samples were not suitable for the calibration of LIBS measurements.
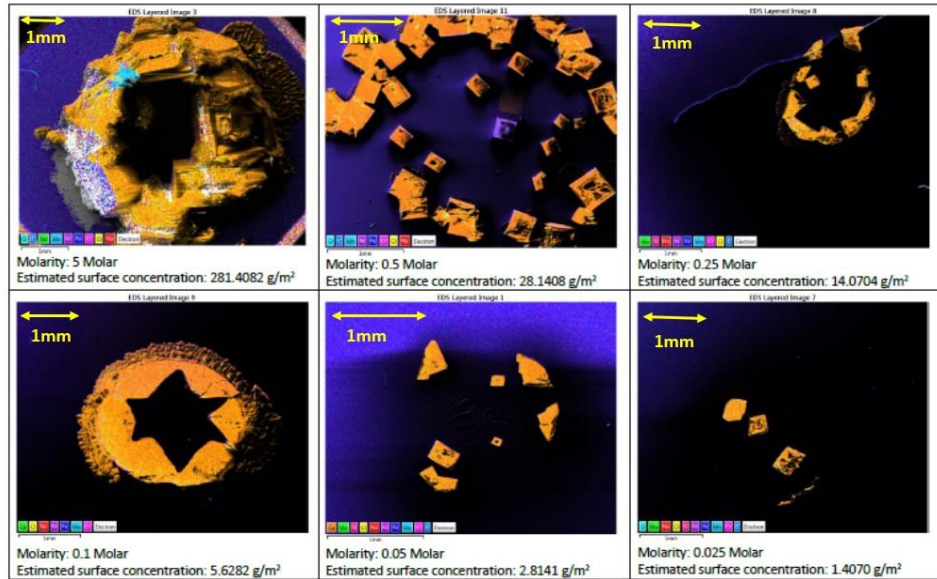
Figure 2.1.3. SEM/EDS images of pipette samples.

2.1.4.2 Vapor transportation process

A second method, vapor transport deposition, was tested to deposit salt at the surface of substrates. In this case, a layer of salt was deposited on the sample through a plasma of inert gas containing the salt. This method is used, for example, for fine coating of Zircaloys and the samples were realized by the laboratory of Dr. Wolfe at Penn State. These samples achieved high layer homogeneity, as shown in the SEM micrographs in Figure 2.1.4. However, it was time consuming to create a single sample and we were dependent of another laboratory to produce our samples, somewhat missing adaptability and convenience. Thus, we decided to investigate an independent procedure for standard sample fabrication.
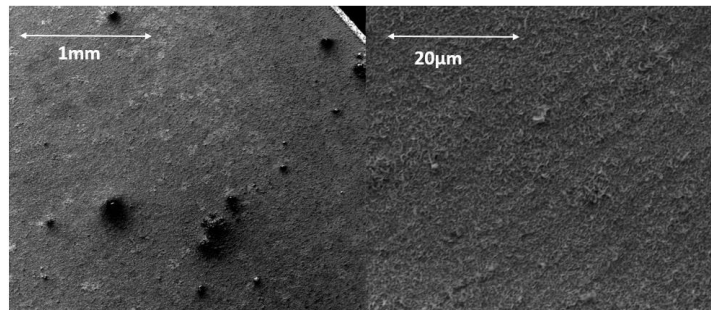
Figure 2.1.4. SEM image of vapor transportation samples.

2.1.4.3 Nebulizer-based process

The definitive procedure was achieved through the use of a Mira-Mist nebulizer, which allows creation of a fine-droplets mist, transported by inert gas (argon). Figure 2.1.5 illustrates the procedure. We used Alfa Aesar synthetic seawater diluted 100 or 1000 times (depending on the desired surface concentration). The solution was pumped at a regular rate of 0.25 mL/min into the nebulizer. From there it was transported by pressurized argon gas to the samples. Deposited

Cl surface concentrations were calculated using the well-known flow rate, the surface of deposition (16 cm^2) and the composition of the spray.
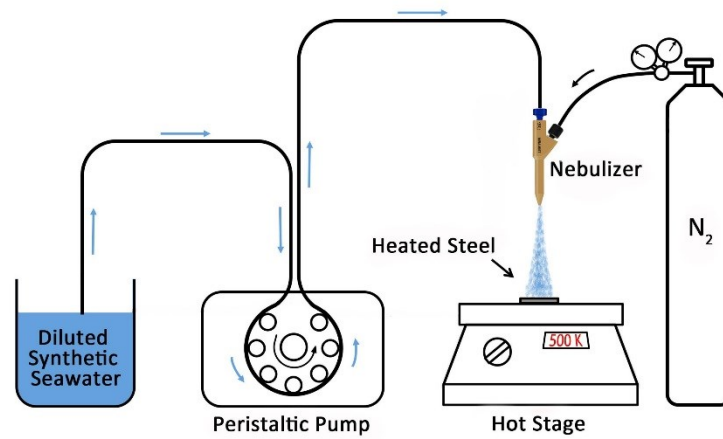
Figure 2.1.5. *Experimental setup of the nebulizer-based sample preparation process.*

Unsurprisingly, when dried at room temperature, the aggregation of aerosol particles on the surface of the SS substrates is severe, with the size of crystals much larger than that of the spraying aerosol. Although the salt distribution is sufficiently uniform when considering the diameter of a typical laser spot of several hundreds of μm in our LIBS implementation, the presence of crystallized salt particles may still cause diffraction or scattering of laser pulses and result in saturation of the emission intensity as the concentration increases. When deposited at a certain range of elevated temperatures, the crystallization of salt can disappear due to the instant vaporization of the water on contact with the surface. Therefore, high-temperature deposition is preferred, so that more homogeneous salt distribution on the SS substrates can be achieved. Figure 2.1.6 shows the surface topography of prepared samples by using SEM. At room temperature (Figure 2.1.6 (a)), salt crystals with an average diameter of 50 μm are spread over the surface of the SS substrate at the Cl concentration of 3 g/m^2, whereas continuous film of salt can be observed on the heated samples at comparable Cl concentrations, including the sample at the Cl concentration of 25 mg/m^2 as shown in Figure 2.1.6 (b). For lower concentration (2.5 mg/m^2 in Figure 2.1.6 (c)), the salt distribution shows regular features corresponding to the spraying pattern of the nebulizer. The samples prepared in this nebulizer-based process show sufficient homogeneity that could serve as standard sample for LIBS measurement.
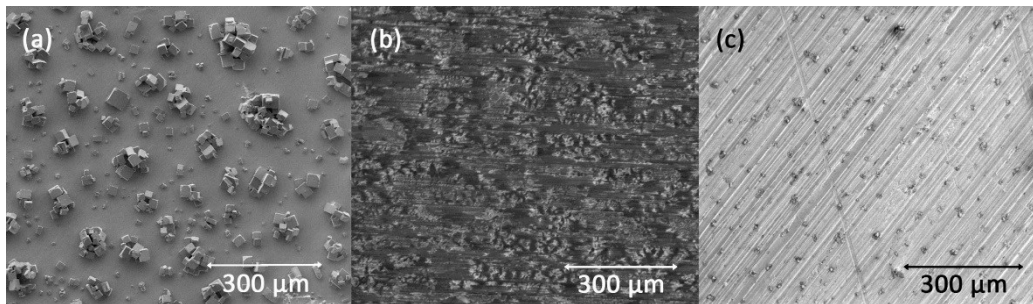
Figure 2.1.6. *SEM images of samples: (a) unheated 3000 mg/m^2; (b) heated 25 mg/m^2; (c) heated 2.5 mg/m^2.*

2.1.4.4 Benchmark methods

Quantitative EDS analyses were performed on an area of 300 x 300 μm^2. Figure 2.1.7 on the left shows the result of such an analysis performed on a batch of samples ranging between 2.5 and 25 mg/m^2 for Na and Cl signals. In this composition range, we observe a linear correlation between the calculated Na and Cl concentrations and signals, meaning that the expected concentration are consistent with one another (e.g. the signal corresponding to a calculated 25 mg/m^2 is indeed twice that from a calculated concentration 12.5 mg/m^2). Moreover the ratio of the slopes of Na and Cl curves with respect to Cl calculated concentration gives 0.76. This ratio was compared to the ratio of Na and Cl signals obtained for a very thick salt layer (>3 g/m^2), which could not have suffered speciation. The ratio of Na to Cl weight percent signals in this thick layer was 0.75, from which we conclude that negligible speciation occurred in our experimental setup.
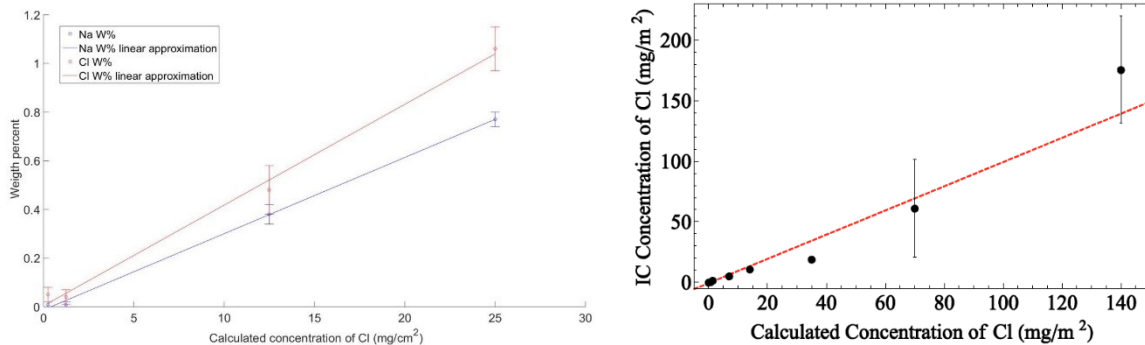
Figure 2.1.7. *EDS signal of Cl and Na (left), and IC measured Cl concentration (right) with respect to the calculated concentration.*

To obtain the absolute Cl concentrations of our samples, we used ion chromatography (IC). This liquid phase chromatography method allows a precise quantification of the considered anion in the solution of interest. This method can be regarded as absolute because of its very high reproducibility and because of the existence of precise tabulations. To use it, we created 2.5 x 2.5 cm^2 coupons with the desired calculated surface concentrations of Cl. We then immersed these samples in deionized water and diluted their salt layer with a micro-cleanser. The obtained solutions were then analyzed with anion chromatography to derive their concentration in Cl$^-$ verifying the calculated concentrations. Figure 2.1.7 on the right shows the results we obtained for samples with Cl concentrations in the range of 0.7–140 mg/m^2. The results agree relatively well between the calculated and the experimentally measured chlorine concentration. This result, coupled with the SEM-EDS proportionality assessment also showed that Na calculated concentrations were accurate, allowing the use of Na as a surrogate measurement for Cl. We could then conclude for the rest of our experiments that the calculated concentrations were effectively representative of the actual surface concentrations for Cl and Na. Thus, nebulizer samples have been chosen to serve as reference samples for LIBS measurements.

2.1.5 Surrogate detection of Cl

In addition to the limitations of LIBS measurements of Cl through FOLIBS discussed earlier, the interference of intense atomic emission lines of iron in the region of interest also contribute to the challenges, especially when quantitative concentration measurements are sought at low concentrations and when LIBS has to be delivered over an optical fiber. One possible alternative to this approach is to use the detection of alkali metals as a surrogate to infer the presence of salt (and thus, Cl), assuming that the concentration of these metals is proportional to that of Cl. The use of an alkali metal such as Na, K, Mg, as a surrogate to infer the presence of Cl in sea salt deposits has been proposed in the early stage of our study. To implement this idea, we assumed and verified that the Cl concentration scales proportionally with Na during the sample preparation process. Compared to Cl, the low excitation energy of the alkali metals results in a high sensitivity of LIBS measurement, where only a modest laser pulse energy is required. Typical limit of detection of a few ppm for metallic elements can be achieved in LIBS, and if alkali metals are detected at concentrations that suggest the presence of a significant concentration of Cl, more detailed direct measurements of Cl could be performed. This measurement approach appears to be a promising alternative to use LIBS on SS while avoiding the concerns of the interference from Fe, reduce limit of detection (LOD), reduce the laser pulse energy needed for the measurement, reduce the potential detrimental effect of laser ablation, enable measurements with simpler, single-pulse lasers rather than double-pulse lasers, and enable fiber-coupled LIBS for field deployment.

Figure 2.1.8 shows the experimental setup of open-beam LIBS. In our experiment, a frequency doubled Q-switched Nd:YAG laser (Spectra Physics Quanta-Ray PRO-250-10) with pulse duration of 10 ns and a repetition rate of 10 Hz was used. The second-harmonic pulses at a wavelength of 532 nm were attenuated to 40 mJ. Laser pulses were focused using a plano-convex lens with a focal length of 300 mm. The spot diameter on the sample surface, determined by the resulting laser ablation region shown in SEM results (Figure 2.1.8), was approximately 200 μm. A 3-axis travel translation stage was used to provide precise motion control of the sample to expose a "fresh" point on the surface of the sample when requested. Repeated measurements of different spots on the sample surfaces were performed for surface averaging.
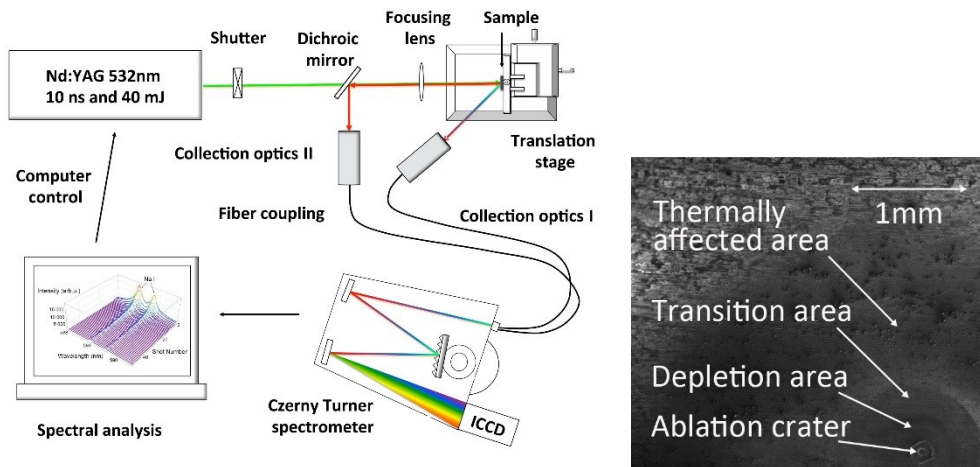
Figure 2.1.8. Experimental setup of LIBS measurement with open-beam delivery (left); SEM image of a typical laser shot on the standard sample (right).

The light emitted from the plasma was collected in standard atmospheric conditions by a 50-mm focal length lens positioned at 45° with respect to the incident beam for measurement of Na I (589 nm), Mg I (518 nm), and K I (766 nm) emission (collection optics I). The Na I (819 nm) and Cl I (837.6 nm) emission were collected in a coaxial configuration (collection optics II), in which a dichroic mirror passed the 532 nm light and reflected the light with wavelengths greater than 800 nm. A long pass filter with a cutoff near 600 nm was placed in front of the 50 mm collection lens to eliminate the second-order diffraction of the iron lines in the region near 400 nm. The light coupled into the 400-µm diameter quartz fiber was diverted into a Horiba Jobin Yvon iHR550 Czerny-Turner spectrometer with 1200 and 1800 grooves/ mm gratings and an Andor iStar 334T intensified charge-coupled device (ICCD). A LabVIEW-based data acquisition system was developed to provide proper timing between the mechanical shutter and the ICCD camera through a Stanford Research Systems DG645 delay generator, such that the shutter allowed the desired number of laser shots to pass through and the camera recorded the data with a set gate width and gate delay referenced to the laser pulse.

Figure 2.1.9 (a) shows the Na emission spectra in the spectral range of 587.0–591.5 nm at Na concentrations of 0.28–55 mg/m^2, corresponding to Cl concentration of 0.5–100 mg/m^2. Spectral emission of the hyperfine-split Na D lines at 589.0 nm (D_2) and 589.6 nm (D_1) has been measured with a gate delay and a gate width time of the ICCD camera of 1 µs and 0.1 µs, respectively, to avoid strong self-reversal effect and alleviate spectral line broadening of Na emissions. The doublet peaks increase and broaden with the increase of Na concentration, corresponding to increased electron density and temperature. No significant environmental background Na emission could be detected from the spectrum measured on a blank SS substrate. The emission spectra were averaged over 20 different locations of the sample with accumulation of two laser pulses on each spot. Multiple peak fitting with Lorentz distributions were used for spectral analysis. The Na D_2 line was used for quantification.

The dependence of the emission intensity of the Na D_2 line on calculated Na concentration is shown in Figure 2.1.9 (b). An exponential relationship is fitted between the calculated Na concentrations and the mean values of intensity of the D_2 line to account for self-absorption of Na I emission. The self-absorption effect is prominent for the Na D lines when the plasma is optically thick, which not only reduces the peak intensity, but also causes the observed line broadening. As a result, the linear dynamic range of this resonance line is limited to less than approximately 20 mg/m^2, but it still extends about two orders of magnitude down to 0.28 mg/m^2 with high sensitivity. A good correlation of the measured Na emission intensity with the calculated Na concentration is found with a R^2=0.94, suggesting that the measurement of Na can be a good surrogate for the measurement of salt concentration in laboratory environment, in which the Cl-to-Na ratio remains approximately constant during the deposition process in sample preparation.
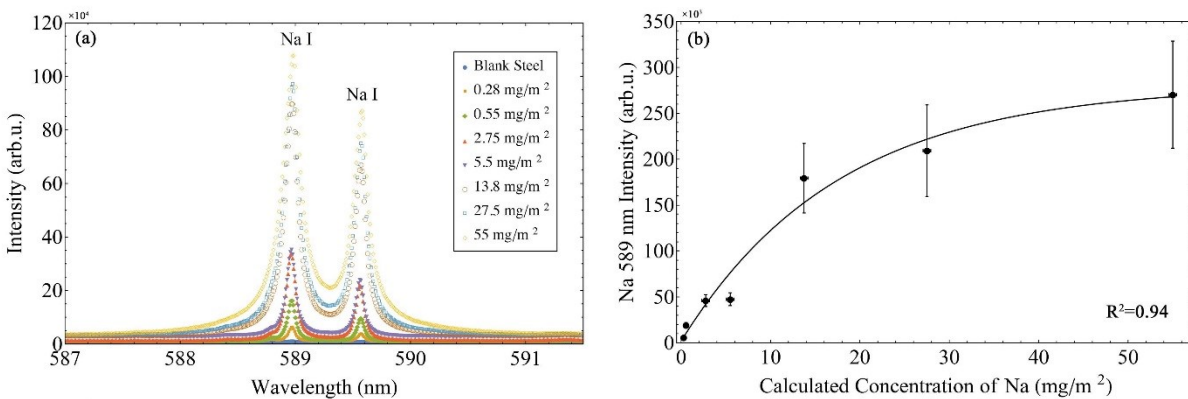
Figure 2.1.9. *Spectrum (a) and calibration curve (b) measured using the Na I doublet at 589 nm; the corresponding Cl concentration is in the range of 0.5-100 mg/m^2.*

The Na/Cl, Mg/Cl, and K/Cl mass ratios in artificial seawater are 0.55, 0.07, and 0.02, respectively, from which the concentrations of Na, Mg, and K are calculated. We assumed that these ratios were also constant during the short transport time in our laboratory environment. The emission spectra of Na I (819 nm), Mg I (518.4 nm), K I (766.4 nm) were averaged at five different locations. Another Na doublet at 818.3 nm have also been measured using a 2-µs gate delay and 10-µs gate width. The Na I line at 819.5 nm was quantified using a Lorentz fit. Figure 2.1.10 (a) shows the calibration curve for the intensity of Na I line at 819.5 nm. This calibration curve is linearly proportional to Na concentration within the range of 0.14–13.8 mg/m^2. The effect of self-absorption of this Na line is less significant due to the transition to an excited state and to the low Na concentration. Therefore, a linear model was used to fit the mean Na I emission intensity at 819.5 nm, obtaining a good correlation between the intensity and the concentration with a R^2=0.92. Mg and K were investigated as other potential surrogates for Cl measurement. The Mg I line at 518.4 nm was measured using a gate delay of 2 µs and gate width of 10 µs, while for the K I line at 766.4 nm, 0.5-µs delay and 5- s width were used. Since Mg and K are minor components in the sea salt solution and both emission lines overlap with intense Fe and/ or Ar lines, the sensitivity of LIBS based on these surrogate elements is limited. Figures 2.1.10 (b) and (c) show the dependence of Mg I and K I intensity on the calculated Mg and K concentrations in the ranges

of 1.4–13.8 mg/m^2 and 0.05–0.5 mg/m^2, respectively. Relatively poor correlation of the linear fits (R^2=0.68 for Mg and R^2=0.72 for K) have been obtained, indicating that the measurement of Mg and K are not the ideal surrogates for the measurement of Cl at such low concentrations in current experimental conditions.
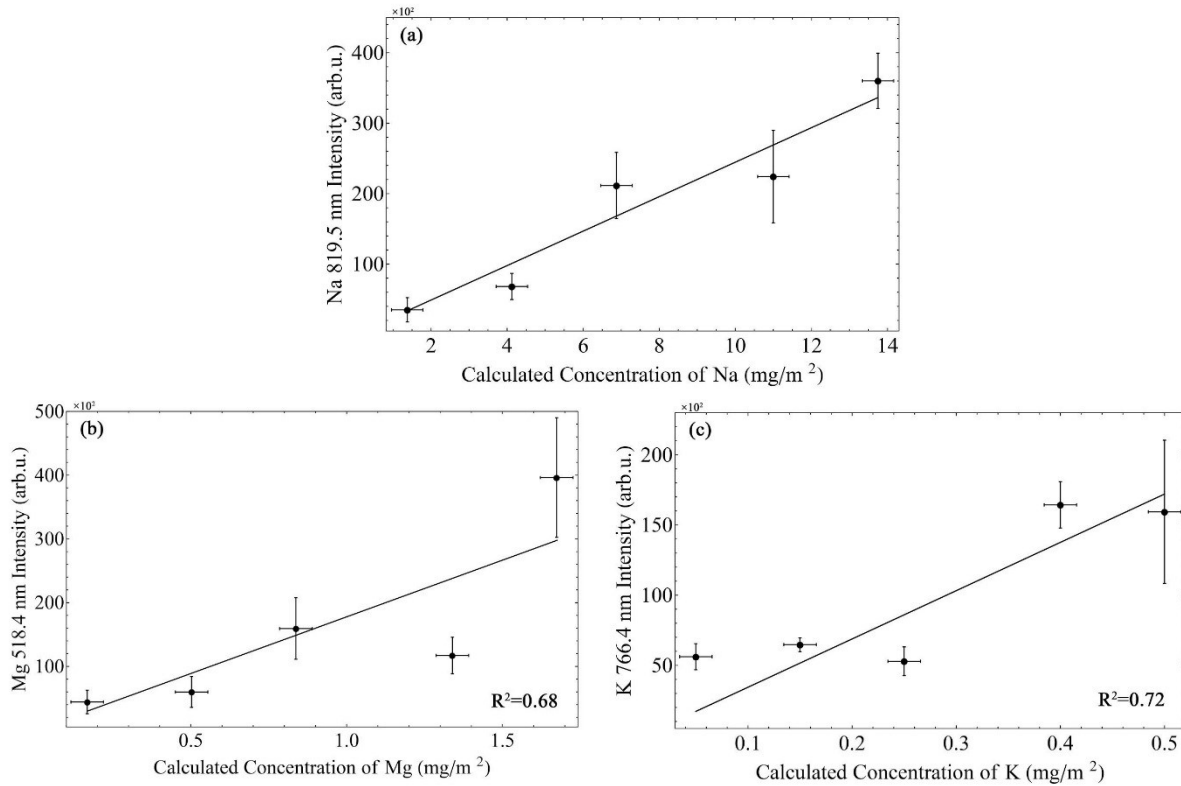
Figure 2.1.10. *Calibration curves developed using Na I at 819 nm (a), Mg I at 518 nm (b), and K I at 766 nm (c); the corresponding Cl concentration is in the range of 0.5-100 mg/m^2.*

Despite the advantages possessed, the surrogate measurement of Cl has limitations. Potential Cl depletion during the transport and deposition of sea salt aerosols in polluted coastal environments and in biogenic sulfuric acid atmosphere could occur as a consequence of pH-lowering reactions with atmospheric acids, leading to the volatilization of Cl as HCl. The potential change of Cl-to-Na ratio caused by this neutralization of sea salt aerosol particles would compromise the use of alkali elements as surrogates of Cl in LIBS measurements, unless this reaction process is well understood and characterized. In spite of this effect, the surrogate measurement by Na via LIBS technique can still be used to reduce the false negative rates in Cl detection, since it is a much more sensitive approach than the direct measurement of Cl on SS by LIBS. Due the significant reduction of the required laser intensity, surrogate LIBS measurement of Cl using Na is desirable for simple fiber delivery configurations and is a promising path for practical use in DCSF.

2.1.6 Direct detection of Cl

As we have discussed, surrogate measurement could be inaccurate due to the Cl speciation during transportation. Direct Cl measurement in FOLIBS is therefore motivated to a significant extent by the desire to overcome the limitations of the surrogate measurements. The following subsections present our efforts of approaching this goal.

2.1.6.1 Open-beam LIBS vs. fiber-optics (FO) LIBS

Figure 2.1.11 (a) shows the emission spectra obtained through open-beam delivery using the setup shown in Figure 2.1.8. Several Cl emission lines belonging to multiplet of 4p $^4D^o$→4s ^4P can be observed in the spectral range of 830.8–844 nm when a gate delay of 0.5 μs and gate width of 5 μs were used. In the spectra, the Cl I line at 837.6 nm has the highest intensity, and the neighboring intense emission of Fe I at 838.8 nm is also present. The other two Cl I lines at 833.3 nm and 842.8 nm from the Cl multiplet can be observed sitting on the intense Fe I group around 832–835 nm and the O I line at 842.8 nm. The intensity of this line increases linearly as the concentration of Cl increases from 2.5 mg/m^2 to 25 mg/m^2. It can also be seen in Figure 2.1.11 (a) that the intensity of the Fe I lines from the laser-ablated plasma of the matrix and the O I lines from the partial ionization of the air show no significant variation for different Cl concentrations due to plasma fluctuation originating from complex laser-material interaction. They could be considered as potential internal standards to reduce the experimental fluctuations of the emission intensity and the matrix effect typical for the LIBS technique. A good linear correlation of the calibration curve with respect to Cl concentration (R^2=0.94) has been obtained, as shown in Figure 2.1.11 (b).
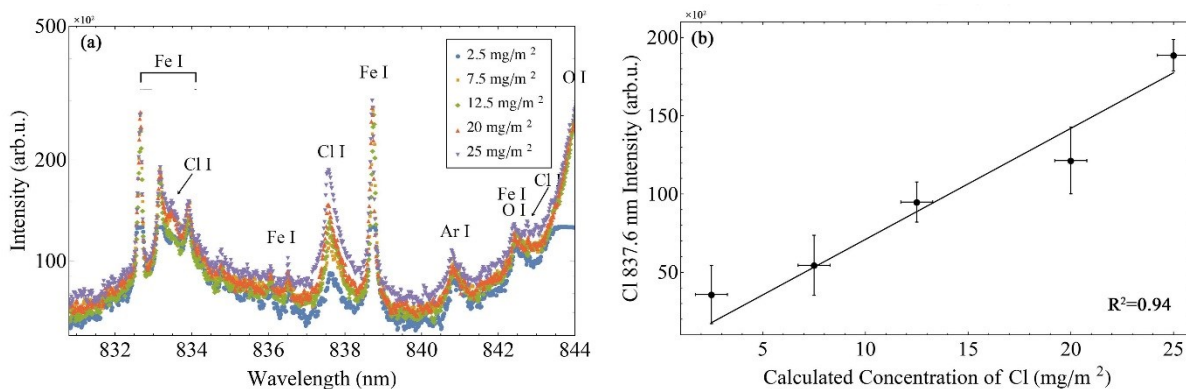
Figure 2.1.11. (a) Spectrum in the relevant spectral range and (b) calibration curve developed using the Cl I at 837.6 nm; the Cl concentration is in the range of 2.5-25 mg/m^2.

Although Cl can be directly detected in the open-beam LIBS measurement, it is difficult to be achieved in the field environment characteristics for ISFSIs, where fiber transport of a high-power laser pulse is needed as we have discussed. Figure 2.1.12 shows the initial setup of FOLIBS that was used to test direct detection of Cl. In this FOLIBS measurement, the Nd:YAG laser was attenuated to an energy range of 0-20 mJ. The laser was first coupled into a 10-m long Thorlabs step-index 1-mm core diameter multimode silica fiber (FT1000EMT), as shown in Figure 2.1.12 (a), and then focused onto the sample surface, as shown in Figure 2.1.12 (b). We found

experimentally that it is quite easy to quantify Cl deposited on the surface of stainless steel in the concentration range of 0.01-1 g/m^2 investigated by means of a surrogate Na measurement using a FOLIBS setup with laser pulse energy of ~8 mJ incident onto the sample surface. However, we were not able to detect Cl using this configuration. The laser irradiance threshold for ignition of Cl has to be verified to be within the limit of the transport fiber. Since it is well known that the laser ablation is a complex process that strongly depends on various factors, including the laser wavelength, the ignition threshold of Cl was evaluated at 532 nm and 1064 nm, available from our Nd:YAG laser.
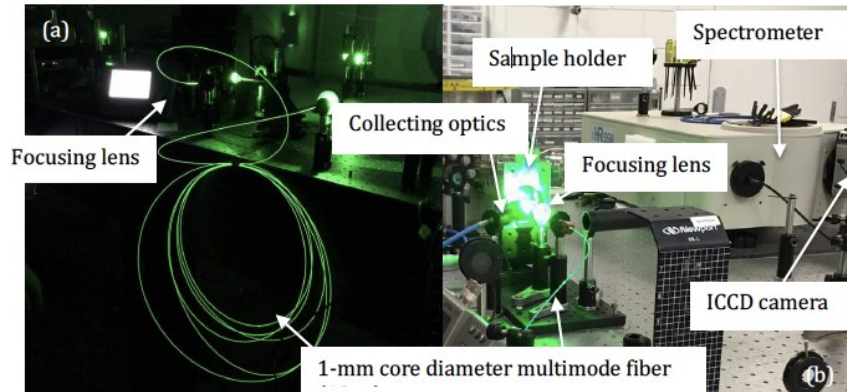
Figure 2.1.12. *Fiber delivery of 532 nm laser pulse in LIBS measurements: (a) fiber optic transport; (b) fiber coupling and LIBS analysis setup.*

Figure 2.1.13 shows the coupling efficiency of the Q-switched Nd:YAG laser that operated at fundamental (1064nm) and second (532nm) harmonic generation through the fiber. For both harmonics, a linear transmission rate is observed with an efficiency of roughly 60%. For the 532 nm laser, breakdown of the fiber begins to occur for an input energy of 20 mJ, allowing a maximum output of 12.8 mJ. For the 1064 nm laser, breakdown of the air is the limitation, with an energy input of 35 mJ and output of 20.5 mJ.
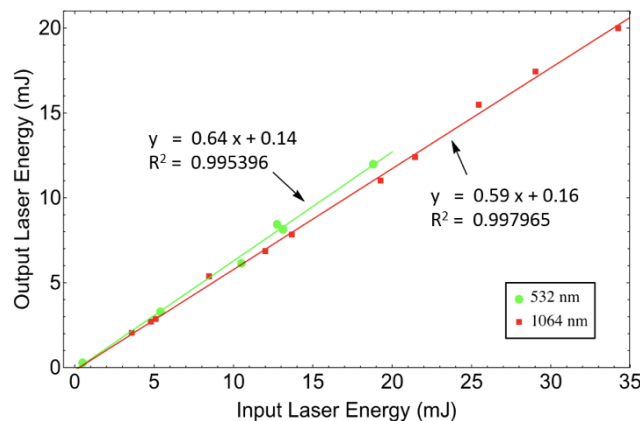
Figure 2.1.13. *Coupling efficiency for 532nm (green) and 1064nm (red) laser pulses into the Thorlabs step-index 1mm core diameter multimode fiber (FT1000EMT, 10m long).*

To evaluate the laser irradiance threshold, we voluntarily defocused the open beam delivery to obtain a comparable beam spot size so that we can transport it through the fiber (can be seen in Figure 2.1.15). Comparing the spectra in Figure 2.1.14 (a) and (b), the effect of laser wavelength is significant. The iron from the matrix is more likely to be excited at higher photon energies than the Cl from the salt deposition. The intensity ratio of Cl (837.6 nm) to iron line (838.8 nm) can increase to well over 1 when 1064-nm pulses are used. However, the intensity of this Cl line (837.6 nm) is always lower than the iron line (838.8 nm) when 532-nm pulses are used. This effect of wavelength led to a decision to use the fundamental wavelength of Nd:YAG laser for direct Cl measurements. Additionally, the lower energy threshold for igniting Cl by using 1064-nm pulses also has favorable consequences in FOLIBS, where a higher pulse energy can be transported over the optical fiber at 1064 nm. Through analyzing the spectra, the plasma ignition threshold of Cl is estimated to 0.31 GW/cm^2 (~13 mJ) for 1064-nm wavelength and 0.35 GW/cm^2 (~17 mJ) for 532-nm wavelength by extrapolating the linear fit to the experimental data. The energy needed to excite the Cl line using 532-nm pulses exceeds the maximum output laser energy of the fiber, while the energy delivery capacity at 1064 nm is sufficient for direct ignition of Cl. However, DP excitation may still be needed for detection of Cl at even lower concentrations.
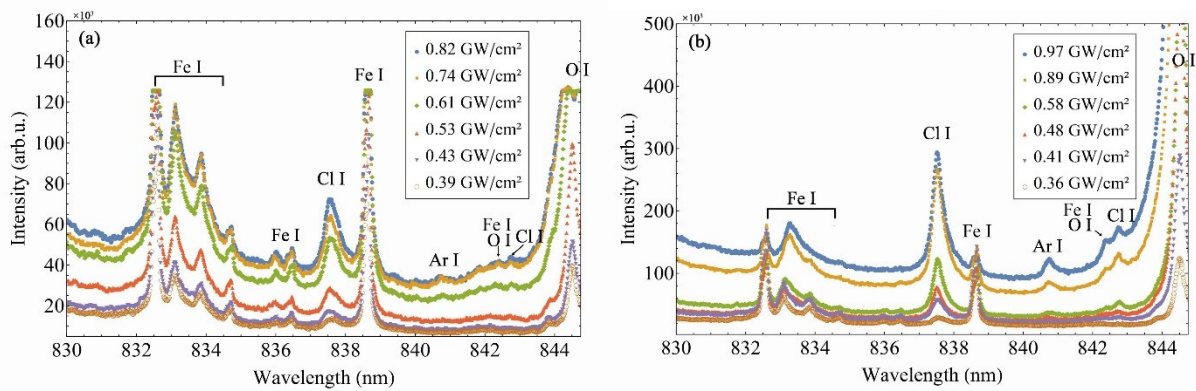
Figure 2.1.14. *Emission spectrum for various laser irradiance received on sample surface for (a) 532 nm and (b) 1064 nm wavelengths.*

2.1.6.2 Laboratory-based DP FOLIBS

The first DP FOLIBS setup is shown in Figure 2.1.15. The Q-switched Nd:YAG laser was operated at its fundamental wavelength of 1064 nm. The beam diameter was first reduced using a Galilean telescope, and then the pulse was split using a plate beamsplitter. With this configuration, the path of one of the resulting pulses was increased by 12 m with respect to the other path, resulting in an inter-pulse delay of 40 ns, when the pulses were recombined by means of two half-wave plates and a polarizing beamsplitter. The DP sequence was coupled into the 10-m long optical fiber using a plano-convex lens with a focal length of 300 mm. The minimum angular curvature during experiments was 35.4 rad/m. The input end face of the fiber was positioned slightly beyond the focus of the 300-mm lens to prevent fiber damage. Two tight-focusing plano-convex lenses (30 mm focal length) were used to collimate the highly divergent DP sequence from the fiber and focus the pulses onto the sample surfaces to form the plasma. The plasma emission was collected by a 50-mm plano-convex lens positioned at 45° with respect to the incident beam.

The spectral resolving system including the Czerny-Turner spectrometer (1200-grooves/mm) and the ICCD camera were the same as that used in the open-beam configuration.
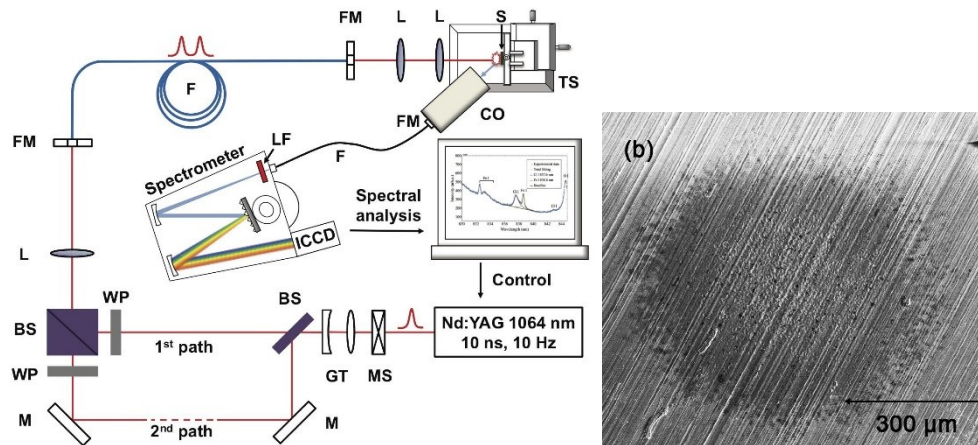
Figure 2.1.15. *Experimental setup of laboratory DP FOLIBS configuration (left); SEM image of the laser ablation spots (right).*

Figure 2.1.15 on the right shows the SEM image of the laser spots on the stainless steel substrates in the laboratory setup. A speckle pattern with a characteristic diameter of 600 μm can be observed due to the interference among the myriad guided modes in the fiber. It is known that when a DP approach is used, a greater into the preformed plasma rather than the underlying material. Consistent with this feature of the DP approach, we observe no surface structure, such as the large thermally affected area seen in earlier observations with open beam delivery, and which results from the high thermal gradient in the vicinity of the focal spot.

Plasma reheating by the second laser pulse in DP can increase the plasma temperature and facilitate the electron impact excitation reactions in the ablated material. Additionally, the DP technique can enhance the material removal, improve atomization, and increase the plasma volume. These mechanisms are reported to contribute to the enhancement of the characteristic emission from excited atoms. More importantly, by using the DP approach, twice the laser energy can be delivered through the optical fiber when compared to the SP, which is limited by optical damage to the fiber. The enhancement effect of DP excitation in FOLIBS can be clearly observed through direct comparison of SP and DP spectra of 100 mg/m^2 sample, obtained in the laboratory DP FOLIBS setup, as shown in Figure 2.1.16. Approximately a five-fold increase of the emission lines was achieved by use of DP technique relative to SP, which allows the detection of Cl at much lower concentrations. It should be noted that, in both SP and DP schemes, the FOLIBS systems operated approaching maximum power capacity.
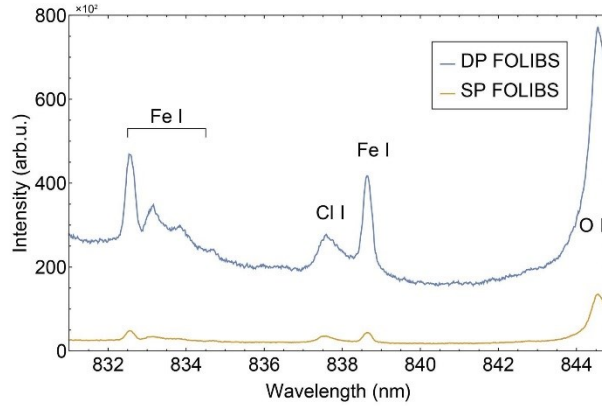
Figure 2.1.16. *Comparison of emission spectra of 100 mg/m² sample near the Cl I 837.6 nm line obtained using SP and DP excitation at 1064 nm in the laboratory FOLIBS setup.*

Figure 2.1.17 on the left shows the energy transmission efficiency of the multimode fiber used for laser pulse delivery. A maximum total input energy of 81 mJ was achieved for the DP sequence obtained in the laboratory setup. To confirm that proper alignment was achieved for both DP laser paths, we also recorded the output energy from a single-pulse (SP) input by blocking either of the DP laser paths. Linear regression of both SP and DP experiments show that the transmission efficiency was approximately 66%. A R-squared value of 0.99 obtained demonstrates both the absence of significant nonlinear effects and a high stability in coupling of laser pulses to the fiber, since each of the data points was collected in a different experiment over a period of time. As the length of the fiber is extended to 25 m in the fieldable setup, the broadening of the laser pulses when propagating through the fiber should be considered. A 1.1-ns broadening can be obtained for the input 15-ns laser pulse as seen in Figure 2.1.17 on the right. No significant effect due to this broadening was observed in our experiments.
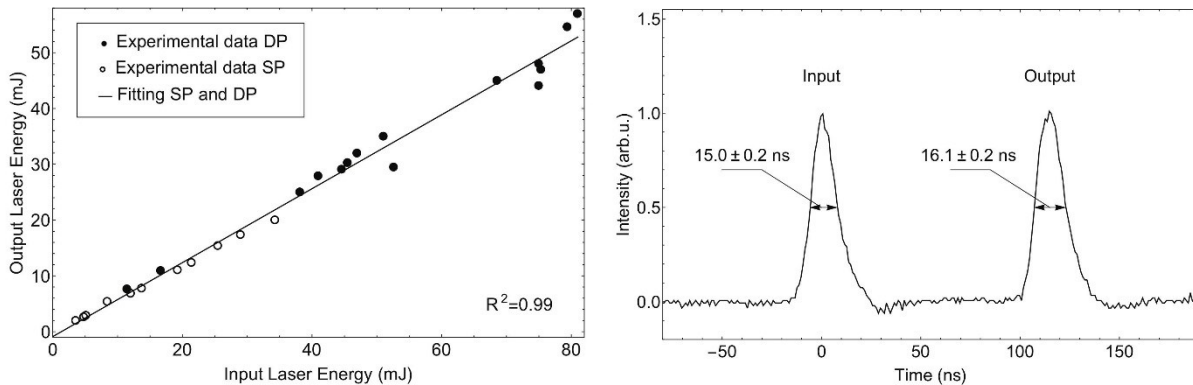
Figure 2.1.17. *Energy transmission efficiency of the 10-m step-index 1-mm core diameter multimode fiber (left); pulse duration measured before and after the 25-m long multimode fiber (right).*

To develop the calibration curve of the Cl I line at 837.6 nm in the laboratory DP FOLIBS setup, emission spectra in the spectral range of 830–844.8 nm were recorded and are shown in Figure

2.1.18 (a). The reported spectra represent an average of the emission measured at five different locations near the center of the standard sample, with a single DP sequence at each location. The input DP laser energy was 75 mJ. The ICCD gate delay, gate width and gain used are 0.1 μs, 15 μs, and 1000, respectively. Due to the long gate width used, the Cl line shows an asymmetric profile that is strongly influenced by the Stark effect. Multiple peak fitting with pseudo-Voigt distributions were used for spectral analysis to account for the spectral line intensity. An approach using a sigmoidally varied line width was adopted to analyze the asymmetric profile of the Cl peak. The peak area of the Cl I line and its neighboring Fe I line were used for quantification, where the Fe I line serves as an internal standard to account for the possible effect of plasma fluctuation.

Figure 2.1.18 (b) shows the dependence of relative peak area intensity of the Cl I line at 837.6 nm to the Fe I line at 838.8 nm on calculated Cl concentration in the range of 5–100 mg/m^2. The mean value of the relative peak area intensity was fitted using a linear model. The coefficient of determination of the linear fitting was found to be 0.91, which shows noticeable improvement from that of 0.87 determined by using the unnormalized signal, suggesting that the DP excitation technique with the use of Fe line as internal standard can improve the sensitivity of FOLIBS and allow direct Cl measurement on steel surfaces to as low as 10 mg/m^2. Another commonly used normalization method incorporating ratioing of the peak areas to the total plasma emission intensity do not show comparable performance as the internal standardization currently used in the work. It should be noted that the fixed inter-pulse delay of 40 ns in the laboratory setup precludes the maximization of the enhancement of the line intensity that the DP approach offers. The use of a DP laser with adjustable inter-pulse delay in the fieldable setup can improve the analytical performance of FOLIBS through optimized laser-plasma coupling.
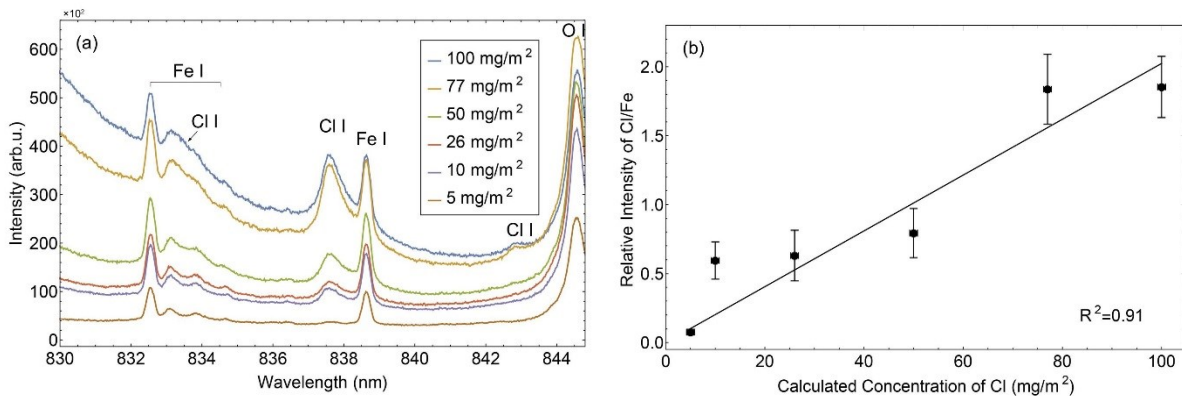
Figure 2.1.18. *Spectra and calibration curve of Cl obtained in the laboratory DP FOLIBS setup.*

2.1.7 Double pulse integration with PRINSE system and final demonstration

2.1.7.1 Fieldable DP FOLIBS

The fieldable DP FOLIBS setup has been designed to meet the space constraints of the PRINSE system and to allow rapid in-situ analysis. The separation of the DP FOLIBS system into two spatially separated assemblies connected via optical fibers satisfies the practical requirements of inspecting the DSC. One of the assemblies includes the DP laser, spectrometer, and ICCD camera,

and should be operated in a controlled environment with modest temperature changes and low humidity outside the DSC. A Q-switched Nd:YAG laser (Evergreen 70, Quantel) that houses two collinearly combined laser heads, allowing a continuously adjustable inter-pulse delay was used in this setup. The DP laser operated at 60 mJ per pulse with a pulse duration of 15 ns and a repetition rate of 10 Hz, considering the fact that the maximum total input energy of fiber optics was significantly increased due to much higher beam quality provided by the DP laser and the use of a longer laser pulse width (the transmission efficiency of the fiber started to degrade at approximately 120 mJ per DP sequence). The other assembly is comprised of remote optics for robotic delivery cars that are able to sustain harsh environment inside a cask. This assembly will be further discussed in the following subsections. In order to accommodate the requirements for field deployment, the lengths of the optical fibers used for laser delivery and spectral measurement were both extended to 25 m. A LabVIEW-based system provided timing control of both laser pulses and the ICCD gate through the ICCD's internal digital delay generator. For the purpose of characterizing the optics assembly in the lab environment, an automated 3-axis linear stage allowed for efficient and repeatable scanning of the stainless steel samples.

Enhancement effect is observed at different time scales depending on the characteristics of plasma formed by the laser ablation process. Parametric study of the optimum conditions for maximizing the Cl I emission intensity at 837.6 nm was conducted prior to the development of a calibration curve for direct Cl measurement in the fieldable FOLIBS setup. Automatic surface scanning with a raster step size of 1 mm was performed in fieldable DP FOLIBS setup. A total 25×25 sampling points were used over the sample surface. The peak area intensity of the Cl I line was analyzed using a custom LabVIEW program, developed specifically for real-time, batch processing analysis of spectra for onsite DSC inspection. A pseudo-Voigt peak shape with a polynomial baseline was used in the multiple peak fitting within the selected spectral range. In the parametric study, two parameters – the inter-pulse delay of the DP laser sequence and the time delay of the gate of the ICCD – were varied, while keeping the gate width and gain of the ICCD fixed.

Figure 2.1.19 shows the contour plot of the peak area intensity of the Cl I line at 837.6 nm obtained from a 50 mg/m^2 standard sample. The inter-pulse delay was varied between 800 ns and 1200 ns with a step size of 100 ns, whereas the gate delay was varied between 300 ns and 2700 ns with a step size of 300 ns. The gate width and the gain of the ICCD were 300 ns and 2500, respectively. The Cl I intensity for each set of parameters was averaged over fourteen randomized locations using the programmable sampling. Three DP acquisitions at each location were performed. The resulting contour map, which has been linearly interpolated, indicates the regions in which the LIBS signal is maximized at a Cl concentration of 50 mg/m^2, suggesting a 900-ns inter-pulse delay and a 600-ns gate delay exhibit the greatest enhancement of Cl emission. Therefore, we adopted an inter-pulse delay of 900 ns for developing the calibration curve in our fieldable FOLIBS setup through analyzing the spectra integrated from a gate delay of 300 ns to 2100 ns. To avoid severe Stark effect experienced in the laboratory setup, the gate width was reduced significantly. However, due to the limited field of view provided by the compact remote optics, a relatively long 1.9 μs gate width was kept, which results in a higher consistency of the

plasma emission, while still maintaining a good signal-to-background ratio by keeping the inter-pulse delay at 900 ns.
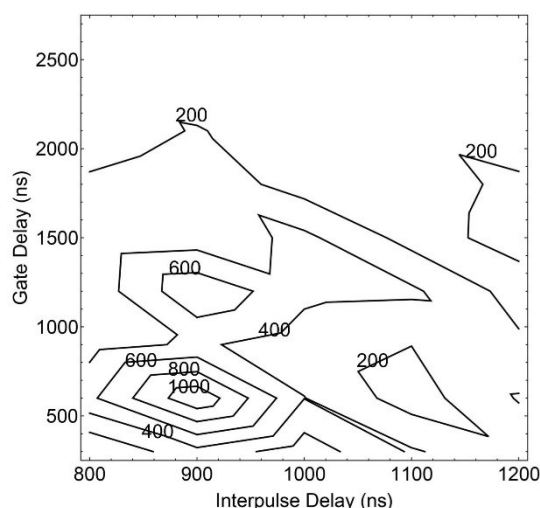
Figure 2.1.19. *Parametric contour map of the Cl I (837.6 nm) emission intensity versus the inter-pulse delay and the gate delay.*

The emission spectra in the spectral range of 831.5–842 nm are shown in Figure 2.1.20 (a), which represent an average of emissions from fourteen randomized locations on the sample surface with three DP samples taken at each location. The broadening of the Cl I line at 837.6 nm was less pronounced and the Cl to Fe intensity ratio was enhanced noticeably as compared to that obtained in the laboratory setup, which results in a better separation of the Cl I line from its neighboring Fe I line, and improves the accuracy of spectral analysis. Figure 2.1.20 (b) shows the dependence of the relative peak area intensity of the Cl I line to its neighboring Fe I line on the calculated Cl concentration in the range of 5–100 mg/m^2. The increased emission uncertainties shown in this calibration curve can be attributed to salt deposition profile that occurs due to the nature of sample preparation, in addition to plasma fluctuation. Figure 2.1.21 shows the lateral distribution of emission intensity of the Cl I line obtained from a 10 mg/m^2 sample by 25 × 25 automatic scanning over the entire sample surface. A well-defined deposition profile can be observed, which is consistent with the spraying pattern of the nebulizer. Although increasing the uncertainty, integrating over a surface area is more representative of the Cl surface concentrations that were calculated assuming a uniform distribution in comparison to making measurements only near the center of the area where salt was deposited. A linear relationship between the Cl to Fe intensity ratio and the calculated Cl concentration was found with good correlation (R^2=0.95), which indicates that direct Cl measurement in the fieldable FOLIBS system was achieved at the Cl concentration as low as 5 mg/m^2 with the assistance of DP excitation.
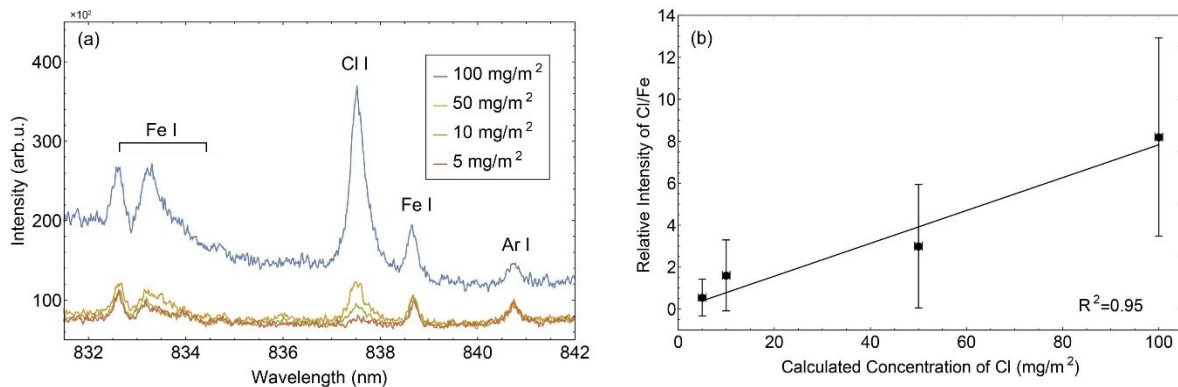
Figure 2.1.20. *Spectra (a) and calibration curve (b) of Cl obtained in the fieldable DP FOLIBS setup.*
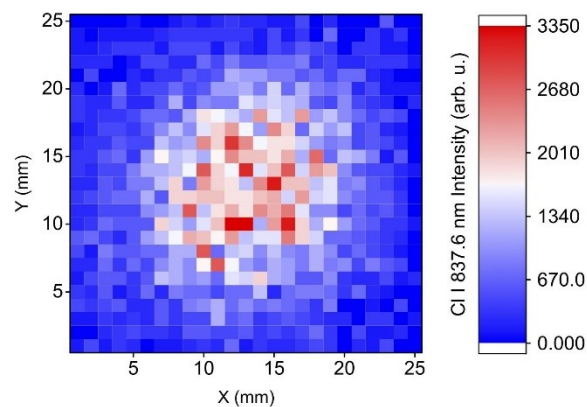
Figure 2.1.21. *Lateral distribution of the intensity of Cl I line at 837.6 nm obtained on a sample with Cl concentration of 10 mg/m².*

2.1.7.2 Integration with PRINSE system

The integration of the LIBS system into the PRINSE system encompassed three major tasks. First, it was necessary to develop an optical system that allows for the detection of chlorine, while not exceeding the allotted payload volume. Second, the final optical system had to be integrated with the robotic car. Third, the externally located components of the LIBS system (the laser source, fiber launch optics, spectrometer, and time-gated detector) needed to be packaged into a compact, mobile assembly that integrates with the PRINSE command and control network. Accomplishing the first task required multiple design iterations and experimentation, while the second task was highly dependent on the design of the PRINSE robotic system and the optical layout, both of which were concurrently developed. The third task could be carried out largely independently, but included important considerations, such as environmental conditions and laser safety.

Laser delivery and the collection of surface plasma emission are implemented as two separate optical systems and are interfaced to the external LIBS module via two optical fibers. Combining the two in a coaxial configuration employing a single optical fiber was considered, but not used due to challenges of efficiently coupling and collimating light of different wavelengths, with

different divergences, and with some differences in the source location *e.g.* the optimal location for plasma light collection is slightly above the sample surface). The two separate optical paths are arranged in a single holder designed to be 3D-printed. In order to maintain critical optical alignments, the collection optics are constrained in a single tube and adjusted as an assembly. This allows for a single point of adjustment for overlapping the focal spots of the two optical paths.

Two collinear and orthogonally polarized 1064-nm laser pulses are generated using a commercial double-pulse Q-switched Nd:YAG laser (Quantel Evergreen 70). Each sample location receives a sequence of three double pulses, and the sequences are conducted at the optimal laser repetition rate of 10 Hz. The beam is focused by a 200-mm plano-convex lens onto a cleaved fiber tip in order to couple the beam into the 1-mm core diameter fiber. This fiber is then added to the main PRINSE cable bundle (i.e., tether) and routed to car #2 in the robotic train. Inside the LIBS robotic delivery car, the fiber is terminated with an air-spaced double lens collimator, and the beam is then focused with a plane-convex lens and redirected with a 45º laser line mirror towards the target surface as shown in Figure 2.1.22. The lens and mirror coatings along the laser delivery optical path were chosen to maximize the transmission at the LIBS excitation laser wavelength (1064 nm). The use of three DP sequences ensures that all chlorine is removed from the surface at the target location.
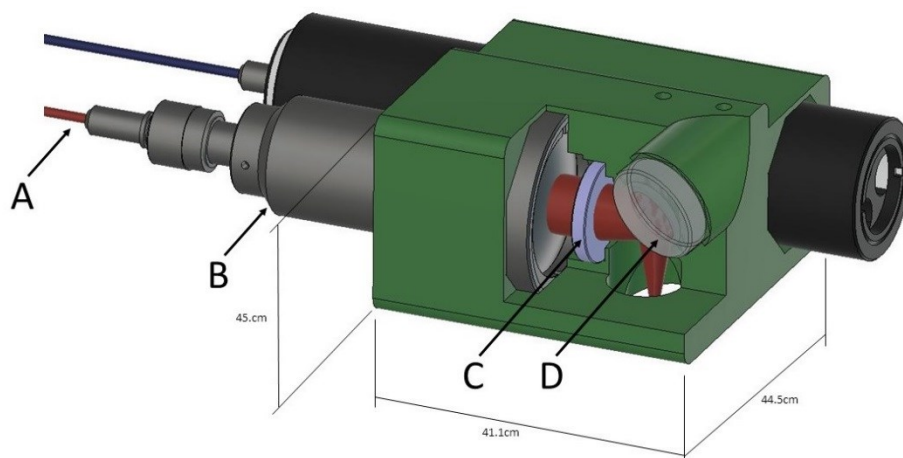
Figure 2.1.22*. Section view of the optics assembly showing LIBS laser delivery optics. The beam is delivered through the red fiber (A), collimated (B), focused (C) and reflected (D) towards the target surface. The laser beam is represented by a red path through the optics.*

The efficacy of excitation of chlorine emission is dependent on the laser intensity produced on the canister surface, which requires maximization of the delivered peak power for a given laser spot size. The peak power delivered to the canister surface is limited by several factors, including optical damage at the optical fiber input, coupling efficiency into the fiber, attenuation during propagation through the fiber and final LIBS optics, and temporal broadening of the laser pulse due to the multimodal dispersion in the fiber. The temporal broadening of the laser pulse after propagation through the 25-m long, 1-mm core diameter fiber was measured to be 7.3%, (from

15.0 ns to 16.1 ns). We experimentally determined that the maximum laser intensity produced on the canister surface when using this optical system was sufficient for excitation of the desired chlorine line. Optical damage at the fiber input was mitigated through fine adjustments of laser coupling and visual inspection of the quality of the cleaved fiber surface during tip preparation.

Due to the use of a class 4 laser, safety precautions were necessary. In order to improve safety while working in the field, the fiber coupling optics were enclosed in a light-tight box. This removes the requirement for eye protection for the operator and personnel in the area once the laser-fiber coupling procedures have been completed. Upon arrival to the operation site, the operator should verify the coupling efficiency and make adjustments as required. During this time, eye protection is required, since the enclosure has to be temporarily opened. The laser head includes two mechanical shutters that need to be opened by the operator. As a standard operating procedure, the shutters should only be opened either under controlled test conditions or once the PRINSE train has been inserted into the channel and measurements are to begin.

Once the plasma is formed, the plume expands away from the ablation site on the canister surface. A fraction of the light emitted by the plasma is collected and collimated by an off-axis parabolic mirror, focused with a 30-mm plano-convex lens, and passed through a high-pass filter, after which it is coupled into the second optical fiber as shown in Figure 2.1.23. All of the aforementioned optics are secured inside a standard lens tube with an access hole drilled orthogonally, allowing light from the plasma emission to reach the parabolic mirror. To help maintain proper distances between the optical components, aluminum sleeves are cut to the designed distances. Once coupled to the collection tube, the fiber is routed through the same tether back to the external LIBS module and terminated at the entrance to the spectrometer. The spectrometer is equipped with a set of three diffraction gratings (1200, 2400, and 3600 lines/mm). The plasma emission spectrum is digitized by an ICCD detector and processed using a real-time virtual instrument implemented in the LabView framework.
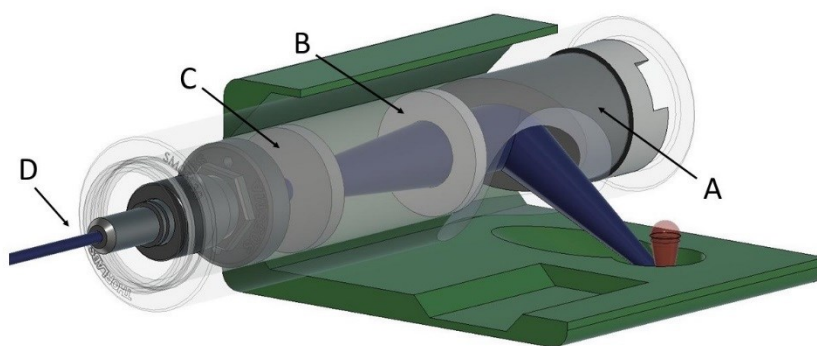
Figure 2.1.23. Section view of the assembly showing the LIBS collection optics. A portion of the plasma emission is collimated by a parabolic mirror (A), focused (B), filtered (C), and coupled into a 25-m long optical fiber (D) for transport to the LIBS external module. The path of the incident laser pulse is represented by the red cone, while the collected solid angle from plasma emission is represented by the blue beam path.

The spectral line chosen for detection is the neutral Cl I 837.6-nm line. We chose the 3600 lines/mm grating for our measurement. This grating provides a spectral window of 15.6 nm and a good spectral resolution that enables a clear observation of the two prominent iron (Fe I) lines (832.7 nm and 838.6 nm) in the vicinity of the selected Cl I line. The two intense characteristic peaks from iron are used to validate and optimize the system operation. They serve as a relative reference when measuring the chlorine concentration on the surface.

Antireflective coatings were chosen to minimize the attenuation of the 837.6-nm emission as it is transported through the optical system, from its origin in the plasma plume to the ICCD. Other species present in the plasma (such as iron) emit characteristic lines at wavelengths that may cause multi-order interference once diffracted by the spectrometer grating. In order to remove such interferences, a high-pass filter with a cutoff wavelength of 550 nm is used inside the optics holder.

Due to the spatial constraints, a parabolic mirror was chosen to efficiently collect and collimate plasma emission. The shortest focal length available in off-the-shelf components of 25.4 mm diameter was used, which results in a relatively small depth of focus (1 mm) and thus a limited field of view for the collection system. Due to the angle between the motion of the expanding plasma and the optical path, the image created by the optics sweeps across the fiber tip as the plasma expands. This, in turn, results in a limited time period over which the characteristic emission from the rapidly expanding plasma can be efficiently collected. An attempt to increase the light collected from this sweeping motion was made by introducing a cosine corrector diffuser, which homogenizes the light for more consistent coupling into fiber. However, this resulted in an unacceptably high loss of efficiency when coupling to the fiber. Because the collection optics are placed at an off-axis angle with respect to the principal direction of plume expansion, the combination of the angle at which the plasma is viewed, the ICCD detector delay, and integration time become interdependent and need to be carefully adjusted and calibrated.

The PRINSE positioning system provides an electronic signal, indicating that the motion of the car has exceeded the minimum distance of 1 mm. Once this signal has been received through the PRINSE control system, the LabView VI sends a command to the ICCD detector to commence data acquisition. The ICCD's built-in digital delay generator further sends a logic signal that triggers the generation of the laser pulse. The three DP sequences per location on the surface are accumulated within the ICCD data acquisition system and sent to the LabView VI. The data is logged locally in ASCII format, with each record consisting of a 1024-element array of data points representing the acquired spectrum. Real-time chlorine concentration analysis is also performed by use of previously measured calibration curves and the results are displayed to the operator. Once data collection is complete, a message is sent over the PRINSE network, which logs the event time and location along the DSC.

It is necessary for the LIBS final optics to establish the optimal distance to the surface and maintain it during operation to ensure consistency in laser focusing on the surface and in the collection of optical emission from the plasma. To meet this requirement, the optics holder was designed such that the base of the holder makes contact with the target surface of the DSC. The

remote optics holder is allowed to pivot inside the robotic car and is retracted from the target surface by a set of springs when not in operation. During sampling, a pneumatic actuator provides pressure for the holder to make a contact with the target. The choice of pneumatic actuation reduces the use of electronics inside the robotic car, increasing its robustness.

For ease of operation in the field, we designed an arrangement that allows for the external LIBS module to be placed on a single cart as shown in Figure 2.2.24. Ultimately, the contents of the cart would be part of the command center, which sits outside the cask on the ISFSI pad. However, due to the nature of the components used (laser, spectrometer, and ICCD), which are designed for operation in a controlled laboratory environment, environmental conditions must be considered. The use of air conditioning at near-room temperature and with low humidity and minimum temperature fluctuation is recommended for these components.
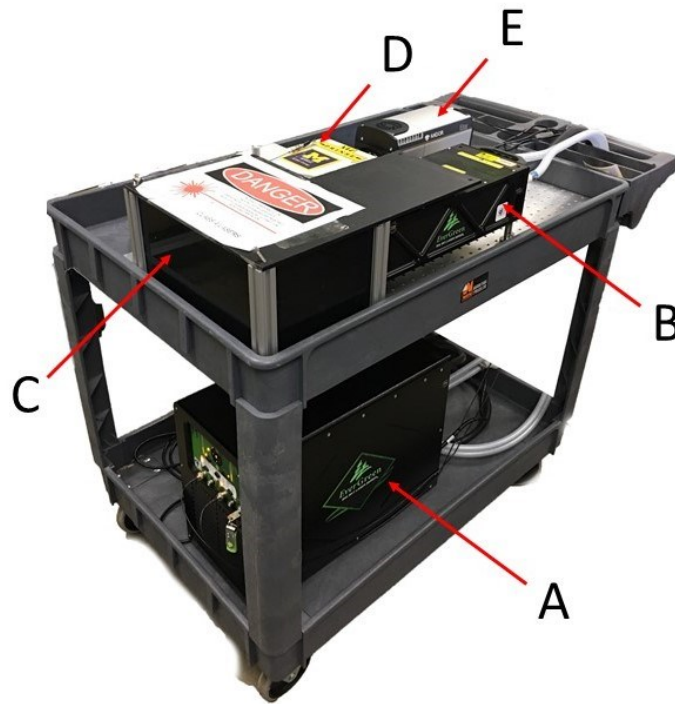
Figure 2.1.24. *The LIBS module is designed to fit onto a single cart, which contains the laser power supply (A), DP laser head (B), fiber launch enclosure (C), spectrometer (D), and ICCD detector (E).*

As shown in Figure 2.1.24, the cart holds the laser power supply, laser head, enclosed laser/fiber coupling optics, spectrometer, and ICCD. The cart further holds an uninterruptible power supply, with the entire system being powered by one 110-V power cord. A single USB cable interfaces the cart to the PRINSE system operator's computer. A Cat5-standard cable is used to transmit the PRINSE LIBS signal to the cart, and two optical fibers are routed from the cart to the robotic car.

As there are only three fine optical adjustments needed (two for laser/fiber coupling, and the collection tube), the PRINSE LIBS system can be rapidly deployed to make measurements in the field.

2.1.7.3 Final demonstration

At a technology demonstration held at Penn State, the LIBS subsystem was fully integrated into the PRINSE system and tests were conducted to ensure its complete functionality. The remote optics system integrated into the robotic train can be seen in Figure 2.1.25. While fully integrated, tests were conducted on a stainless steel sample with known concentrations of chlorine deposited (via artificial sea salt) in order to verify that the system functions in a field environment as well as it did in the lab.

Figure 2.1.25. *The LIBS optics holder mounted in the PRINSE robotic train. Operation of this system was tested once fully inserted into a simulated canister channel.*

As shown in Figure 2.1.26, the optics holder installed in the robotic train was able to successfully detect a concentration of 10 mg/m^2 Cl in a controlled environment. Both the blue and red line result from testing the same spot, which clearly demonstrates that nearly all Cl was removed from the test spot. The small spectral line near 837 nm most likely results from slight movement of the robotic car in between samples, meaning the test samples did not perfectly overlap.
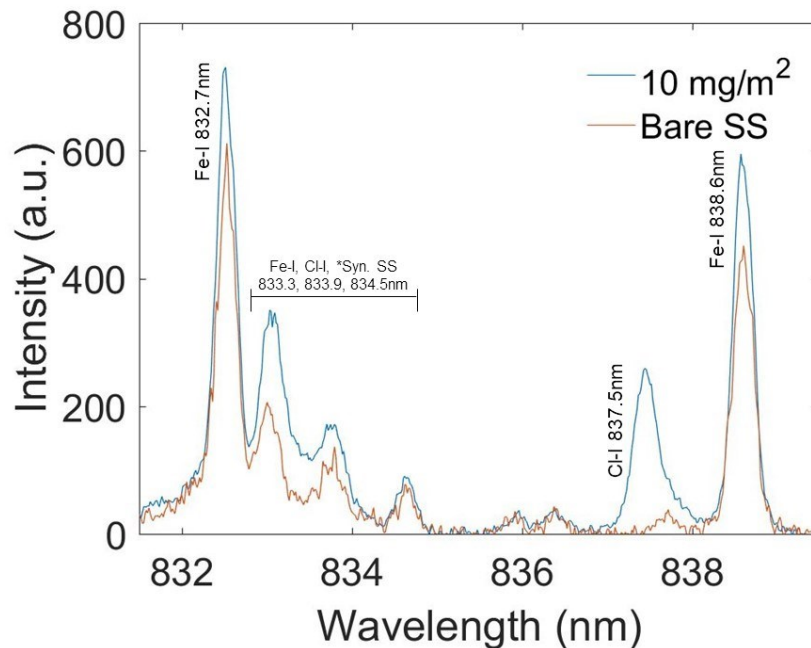
Figure 2.1.26. Test results of the final design of LIBS optics deployed by PRINSE system, verifying a chlorine concentration of 10 mg/m² on stainless steel is observable. Also shown is the result from a sample which chlorine has been removed, in which the Cl I peak is not present. The triple peaks between 833.3 nm and 834.5 nm are a convolution of iron, chlorine, and other elements present in the synthetic sea salt.

During the final testing, it was realized that the strain placed on the optical fibers running through the PRINSE cable bundle was not properly accounted for. Additional strain-relief is required inside the car holding the optics holder for reliable function. When the fiber is push/pulled at the final optics assembly, the fiber tip is moved from its optimal location. This can result in the fiber tip becoming damaged and the laser fiber needing to be re-cleaved before being operational again. Additionally, after hundreds of samples, the accumulation of plasma debris begins to reduce the laser energy reaching the target surface. This currently requires the optics to be removed and cleaned using standard techniques.

2.2 Nondestructive Inspection (NDI) of Stainless Steel Canister

The LIBS system described in the previous section enables in-situ assessment of whether the canister surface is in a potentially corrosive environment through the detection of chlorine. A possible corrosion process is that airborne chloride-bearing salts are deposited on the canister surface. Then when the humidity and temperature conditions permit, the chlorides go into solution and form an electrolyte. Surface pitting can occur. In the presence of a tensile driving acting in a susceptible material cracks can initiate from pits or other stress concentrators. This section describes the research and development of an ultrasonic guided wave-based NDI system designed to detect cracks, specifically stress corrosion cracks in the heat affected zone of welds. The noncontact coupling of electromagnetic acoustic transducers (EMATs) makes them well-suited for robotic inspection, thus EMATs are used to send and receive shear-horizontal (SH) waves. We will use EMATs in the pulse-echo mode to provide full NDI coverage of the full penetration fabrication welds of the DSCs.

2.2.1 Requirements

With the goal of having two opportunities to detect cracks before they penetrate through the DSC thickness, and assuming a five-year inspection interval, the minimum detectable crack was chosen to be a semi-circular surface breaking crack of radius 0.21" (5.3 mm). The requirements actually call for a machined notch instead of a crack to facilitate laboratory testing. The sensors housed in the robotic delivery system are designed to operate in temperatures up to 350 °F (177 °C) and gamma radiation doses of 27 krad/hr. These environment conditions have a significant effect on material selection for the sensory system. The full functions and requirements of the robotic inspection system are given in Section 1.3.

Cracks are expected to occur transverse to the weld-line based on: (i) nuclear plant operator's past experience with SCC, (ii) finite element simulations of thermal residual stresses in the HAZ, and (iii) residual stress measurements in a DSC mockup. However, there are also lower magnitude tensile residual stresses transverse to the weld, which could cause cracks to grow along the weld-line. Therefore, our NDI methods are designed to detect cracks oriented either transverse to a weld-line or along it.

2.2.2 Conceptual Plan

The robotic inspection system is designed for the Holtec HI-STORM 100 family of casks (see Figure 2.2.1) that include their multipurpose canister (MPC, previously referred as the DSC). All of the MPC models are nominally the same diameter and height, have a wall thickness of either 0.5" (12.7 mm) or 0.625" (15.9 mm), but vary to accommodate different basket geometries to hold the fuel rods. All MPCs are fabricated from austenitic stainless steel plates that are rolled and then welded as shown in Figure 2.2.1. Weld patterns vary from the one shown in Figure 2.2.1, many of the MPCs being fabricated now have the bottom weld and two full-height axial welds, but no circumferential weld. In earlier years the multipass full-penetration welds were not ground flush, but now they are typically ground flush. The overpack is steel-clad concrete and in many cases 16 guide channels are used to maintain alignment of the MPC inside the overpack as shown in Figure 2.2. 2. Generally speaking, the spacing between the channel and the MPC is too

small for sensors, requiring that the sensors be delivered vertically through the gaps between the channels. The channels stop short of the bottom of the cask.
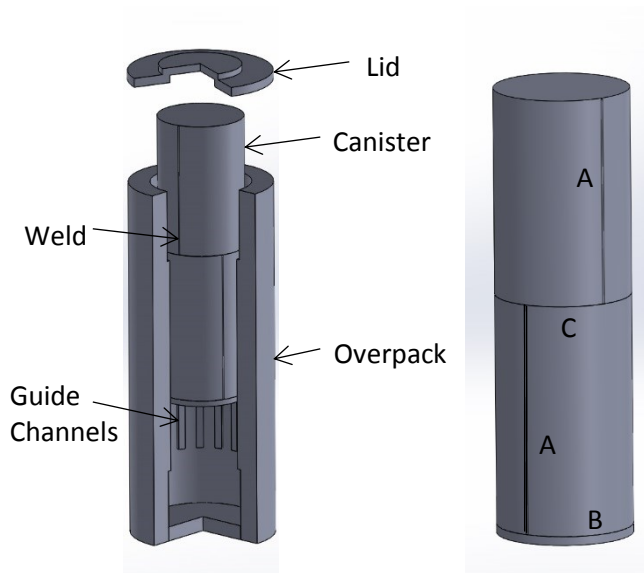
Figure 2.2.1. *Cut-away view of the Holtec HI-STORM 100 cask (left). Fabrication weld pattern for Holtec MPC; A = axial, B = bottom, C = circumferential (right).*

Figure 2.2.2. *Carbon steel guide channels on the steel clad interior of the HI-STORM overpack.*

The robotic system is inserted through an outlet vent in the overpack lid and staged on top of the MPC lid. It deploys the sensor train to the bottom of the MPC, sets the baseline, and then inspects the bottom weld as shown in Figure 2.2.3. It then raises the sensor train to inspect the circumferential weld, and then retracts the sensor train. The sensor train is then deployed between the adjacent set of guide channels and the process repeated. When the sensor train is in a gap near to the axial weld it inspects that weld on way up. The inspection uses the EMATs to send SH waves that function in a short-range pulse-echo mode to detect cracks in the HAZ of the

weld lines. If desired, this methodology could be used to inspect the entire MPC surface, however in this report we only consider the HAZ.

The weld line inspection sequence is described as:
1. Setup command center
2. Test delivery and sensor systems
3. Insert Delivery robot in exhaust vent and station it on the MPC lid
4. Position Delivery robot at perimeter of MPC lid to deploy Sensor cars (set i = 1)
5. Start lowering Sensor cars in between guide-channels i and i+1
6. Activate EMAT for pulse-echo in circumferential direction to search for axial weld in top half of MPC; Case A is that the axial weld is hidden behind an adjacent guide channel or in the adjacent guide channel gap (note that Case A occurs exactly twice, once from each side of the weld)
7. Activate EMAT for pulse-echo in circumferential direction to search for axial weld in bottom half of MPC; Case B is that the axial weld is hidden behind an adjacent guide channel or in the adjacent guide channel gap (note that Case B occurs exactly twice)
8. Set baseline at bottom of MPC
9. Micro-position EMAT above the bottom weld and acquire data for position i
10. If Case B then acquire data for axial weld continuously with EMAT during extraction of Sensor cars up to the circumferential weld
11. Move Sensor cars to HAZ below circumferential weld
12. Micro-position and acquire data for circumferential weld with EMAT for position i
13. Re-position to HAZ above circumferential weld
14. Micro-position and acquire data for circumferential weld with EMAT for position i
15. If Case A then re-position the Sensor cars at the circumferential weld and acquire data for axial weld continuously with EMAT during extraction of Sensor cars up to the top
16. Retract Sensor cars back into Delivery robot
17. Re-position Delivery robot on MPC lid for deployment of Sensor cars in gap between next set of guide-channels (increment the value of i = i+1)
18. Repeat steps 5-17 for the gaps between guide channels 2 and 3, then 3 and 4, etc. until all 16 gaps have been inspected
19. Remove Delivery robot through the exhaust vent. Make sure that no parts or debris from Delivery robot and Sensor cars are left on MPC lid
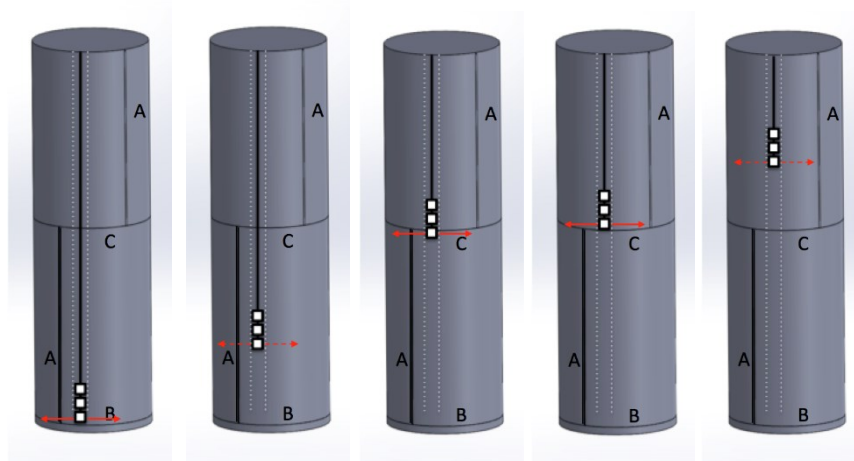
Figure 2.2.3*. Robotic inspection sequence of MPC weld lines from one gap between guide channels inside the overpack. Similar inspections are conducted from each of the 16 gaps. The welds are: A = axial, B = bottom, C = circumferential.*

2.2.3 Transducer Selection

This section is based largely on the article by Choi, Cho, and Lissenden in *Sensors* 17(5) 2017. The guidelines for transducer selection can be summarized as:

- must be deliverable by a robotic system;
- sufficiently small to fit into cargo bay of robot;
- do not require liquid couplant that could potentially degrade the canister over time;
- comprised of materials tolerant of the elevated temperature and gamma radiation environment;
- capable of sending and receiving ultrasonic guided waves that can provide 100% coverage of the canister weld lines;
- capable of sending and receiving shear-horizontal type guided waves that interact with cracks oriented transverse to, as well as parallel to the wave vector.

As far as we know, only electromagnetic acoustic transducers (EMATs) and magnetostrictive transducers (MSTs) meet these guidelines. Thus, the first task was to choose between EMATs and MSTs.

Transduction in periodic permanent magnet (PPM) EMATs is completely different from piezoelectric transduction, which requires a coupling medium between the transducer and the substrate. PPM EMATs can be effectively used to excite and receive a variety of types of ultrasonic waves, including SH waves in plates and torsional T(0,1) waves in pipes. Moreover, the noncontact nature of EMATs is ideal for robotic delivery. A pair of PPM EMATs, their dimensions, the layout of the permanent magnets and electric coil are shown in Figure 2.2.4. The transmitter and receiver are identical, each consisting of a periodic array of permanent magnets, a meander electric coil, and peripheral components. Importantly, they fit into the cargo bay of the robot.
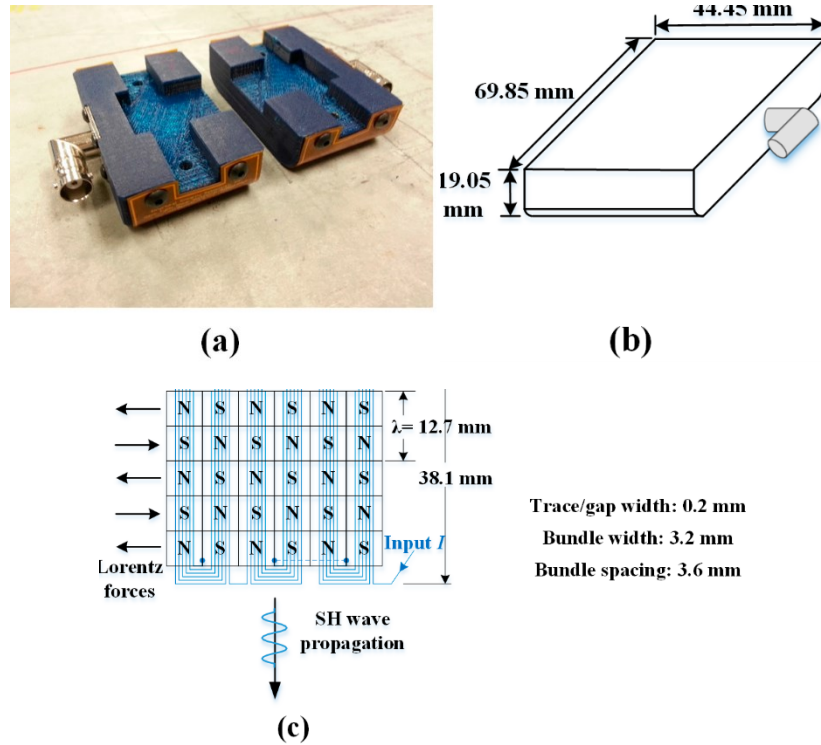
Figure 2.2.4. (a) Pair of PPM EMATs, (b) housing, and (c) layout of permanent magnets and electric coil.

The transduction principal for PPM EMATs is based on the Lorentz force, which is the cross product of the eddy currents and static magnetic field near the surface of the waveguide. Thus, the waveguide material must be an electrical conductor. The periodicity of the array of magnets determines the wavelength of the generated SH mode, while the direction of the electric coil fixes the polarity of the SH wave propagation. Though the transduction efficiency of PPM EMATs is lower than for typical piezoelectric and magnetostrictive transducers (MSTs), they offer noncontact transduction as well as suitable tolerance of radiation and high temperatures. Although the Lorentz force is larger in mild steel and aluminum, it is sufficiently large in stainless steel for NDT/NDI, even at high temperature.

MSTs provide higher efficiency in exciting and receiving SH waves than PPM EMATs, but they require a coupling medium. Each transducer comprises a magnet, a meandering electric coil, and a magnetostrictive foil such as remendur. Transduction with MSTs is based on the mechanical disturbance generated by strains associated with the motion of magnetic domains in the magnetostrictive foil, which is typically adhesively bonded to the sample surface. The wave in the foil is transmitted to the waveguide through the adhesive. However, in robotic inspection applications, the use of adhesively bonded foils is challenging at best. Therefore, dry frictional coupling between the foil and the substrate is investigated. A relatively large normal force is required to produce sufficient frictional forces to excite and receive SH waves. In dry storage casks the robot can apply normal force to the MST by a pneumatic piston or bladder restrained by the inside of the cask. The prototype MST, assembly of the MST, and layout of a permanent

magnet and a meander electric coil are shown in Figure 2.2.5. The transmitter and receiver both have the same dimensions and configuration, and fit into the cargo bay in the robot. The spatial period of the meander coil determines the wavelength of SH wave mode. Figure 2.2.5a shows the MST with an air bladder on top, which must fit on the robot and transmit the normal force to the cask.

Since SH waves are multimodal and dispersive, mode/frequency selection is important for successful NDI. From a signal processing perspective, it is desirable to excite a single mode, but often this is not possible given the finite size of the transducer. The selected mode should have good excitability/receivability with EMATs and MSTs as well as sensitivity to surface breaking cracks.
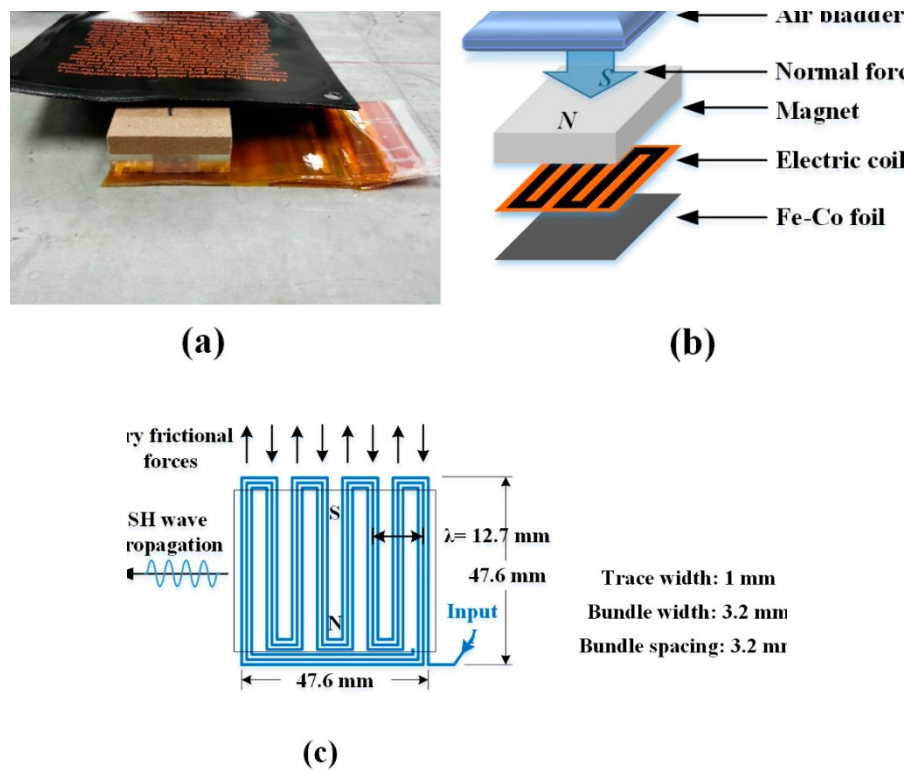
Figure 2.2.5. (a) MST prototype, (b) assembly of MST, and (c) layout of permanent magnet and meandering electric coil.

Propagating SH waves are given by the relationship between wave speed and frequency shown by dispersion curves. The SH mode phase velocity and group velocity dispersion curves for a 0.625" (15.9 mm) thick stainless steel plate shown in Figure 2.2.6 are based on a mass density of 8000 kg/m^3 and a measured shear wave speed of 3181 m/s. The fundamental mode, SH0, is often preferred because it is the one SH mode that is nondispersive. The blue lines in Figure 2.2.6a represent possible activation lines for EMATs and MSTs, and the slope of the activation line is the generated wavelength, which corresponds to the magnet spacing of the EMAT and the coil spacing of the MST. The intersection of the activation line and dispersion curves indicates the preferential excitation points for transducers having that wavelength. However, due to the finite

size of the transducer and the finite frequency bandwidth of the toneburst pulse sent to the transducer there is a zone of excitation, rather than just a point. Thus, it is common for a transducer to excite secondary modes in addition to the preferred mode due to the source influence.
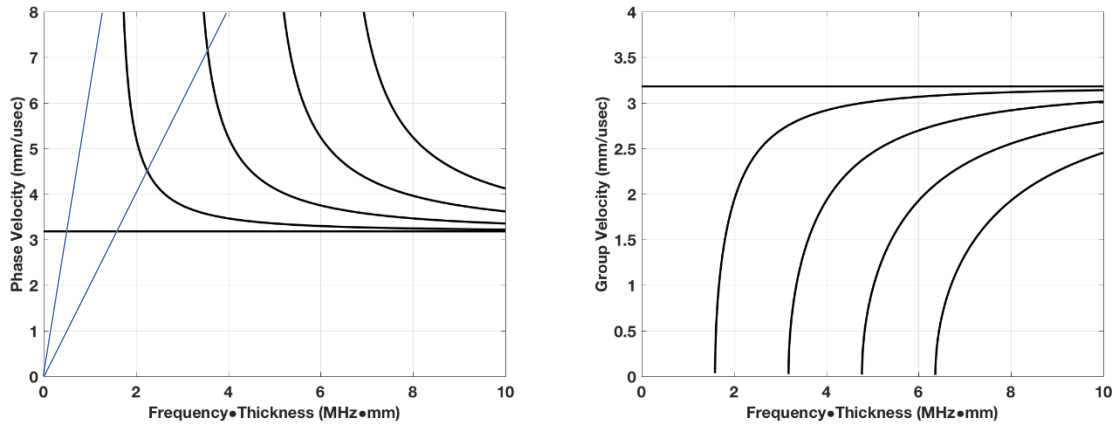
Figure 2.2.6. *(a) Phase and (b) group velocity dispersion curves for SH modes for stainless steel plate.*

In order to ensure excitation of a single SH mode it would be necessary to excite the SH0 mode below the lowest cutoff frequency, which would require a wavelength of at least 80 mm. This would require a very large transducer and result in low defect sensitivity. Thus, we selected a wavelength of 0.5" (12.7 mm) with an excitation frequency of 250 kHz as a compromise between transducer size, crack sensitivity, and the presence of multiple modes. At this wavelength and frequency, the SH0, SH1, and SH2 modes can propagate. If the propagation distance is relatively short, the wave packets for the different modes will not have time to separate given their similar group velocities. For the two plate thicknesses are investigated herein, the group velocities are:
0.5" (12.7 mm) thick: 3181, 2753, 0 m/s for SH0, SH1, SH2 respectively
0.625" (15.9 mm) thick: 3181, 2915, 1908 m/s for SH0, SH1, SH2 respectively.

The amplitudes of the SH0 and SH1 modes extracted from the EMAT and MST sent and received signals are shown in Figure 2.2.7. The waves propagated 14.2" (360 mm) in a 0.5" (12.7 mm) thick stainless steel plate. The waves generated and received by MSTs have an amplitude roughly 5.5 times larger than those generated and received by EMATs. However, the wave amplitude of the SH1 mode does not reach an asymptote for the normal forces applied, which would make amplitude-based detection difficult. Furthermore, since the MST transduction relies upon dry frictional coupling to the surface, there were concerns about the effect that surface debris on the MPC. Specifically, the concern is that debris would greatly reduce the coupling. Experiments were conducted using 850 μm diameter glass beads as surface debris and the results were dramatic. The debris increased the liftoff of the EMAT from zero to 850 μm, thus the amplitude was reduced by a factor of two. However, the presence of just a small number of glass beads eliminated the coupling of the MST receiver to the surface and no signal was received. These results were sufficient to conclude that EMATs should be selected as the transducers even though their signals

are significantly smaller than the MST signals. The two main drawbacks of the MSTs are: (i) they require a large normal force to be applied by the robotic system and (ii) they are ineffective when surface debris is present. Moreover, while the robot can apply a normal force, the wave amplitude is dependent on the force magnitude, which would be difficult to maintain. Also, while the HI-STORM casks provide a reaction force, other casks do not (e.g., NUHOMS).
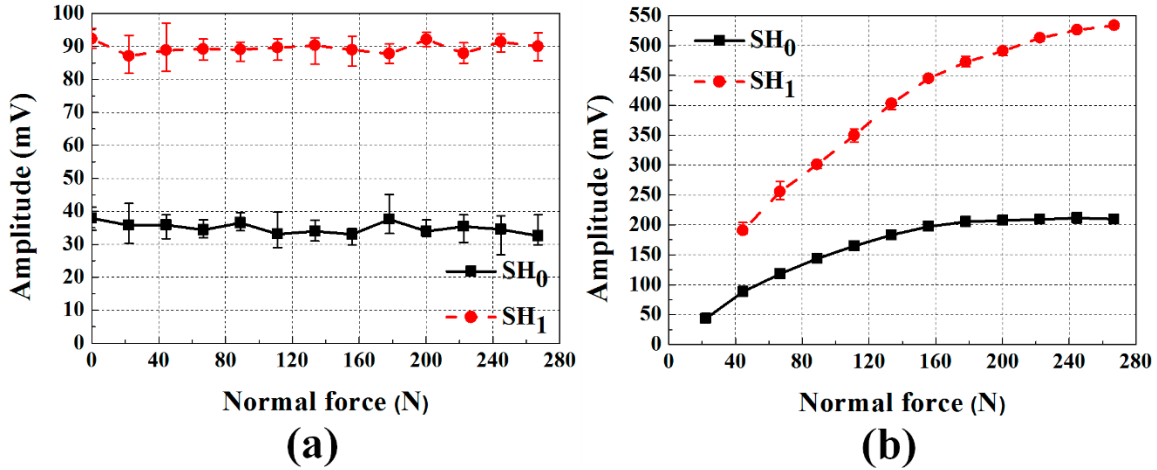
Figure 2.2.7. *Averaged peak amplitudes of SH0 and SH1 modes for: (a) EMATs and (b) MSTs as a function of the applied normal force.*

The directivity of the EMATs was measured with the help of a contact transducer as shown in Figure 2.2.8. The EMAT sends an SH wave that spreads out, while the receiving EMAT registers SH waves coming from a range of angles. For the transmitter, while a contact transducer was recording the maximum amplitude of the incoming SH waves, the EMAT transmitter generated SH waves from where the angle θ increased from 50 degrees to 130 degrees by every 1 degree. For the receiver directivity, the roles were switched and measurements repeated. The results were plotted in a polar diagram. The measured half-power beam width θ_{half} of the transmitter and receiver was 40 degrees. This angle is suitable to inspect the heat affected zone (HAZ) of the weld lines. Note that a trade-off exists between penetration power and directivity.
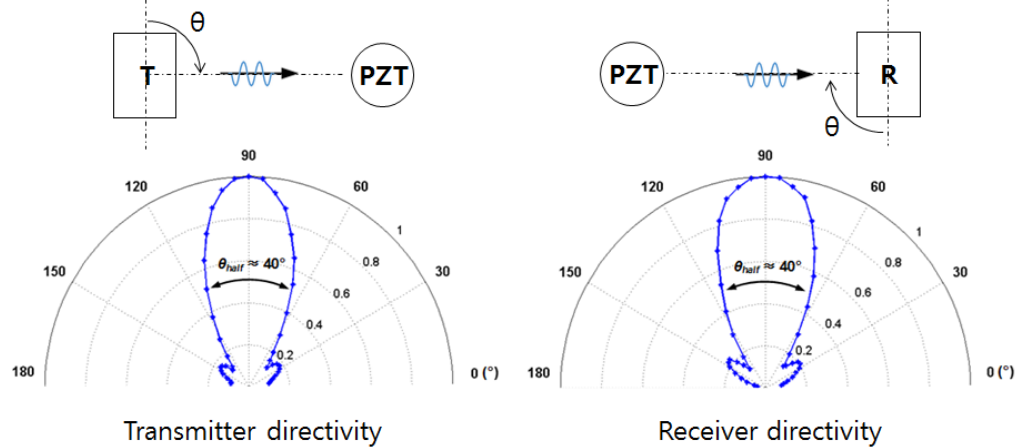
Figure 2.2.8. *The measured directivities of the EMATs at a distance of 200 mm.*

2.2.4 Robotic Deployment

The ultrasonic guided wave-based crack detection system is comprised of three parts:

- EMATs mounted in a robotic sensor car that goes into the cask;
- instrumentation located in the command center;
- cables inside the robot's tether that carry the electrical pulses between the command center and the EMATs.

This section describes the robotic deployment of the EMATs, as shown in Figures 2.2.9 and 2.2.10. A complete list of system components is provided in Section 2.2.5.

All data is acquired from the outer surface of the MPC from EMATs mounted within the 4.75" (121 mm) long by 5.125" (130 mm) wide by 1.25" (32 mm) high cargo bay of the front car of the train, which is lowered down the cylindrical surface of the MPC. The EMATs are located in the front car to ensure that the bottom weld can be inspected. While EMATs are noncontact transducers, to ensure strong and consistent signals zero liftoff is used; i.e., the EMAT will physically touch the canister. For an EMAT to generate waves in a waveguide, the material must be conducting so that eddy currents can be generated. Austenitic stainless steel is nonmagnetic but is electrically conductive. The consequences are that the ultrasonic signals are relatively small, but on the positive side the EMATs are easy to move along the surface because the magnetic force is small. Even though austenitic stainless steel is nonmagnetic, because the MPC has been rolled into its cylindrical shape there is sufficient martensite present to provide remnant magnetism. Furthermore, the welds often contain ferrite that makes them more magnetic than the base metal. The robotic system must provide sufficient force to prevent the EMATs from getting locked onto the MPC.
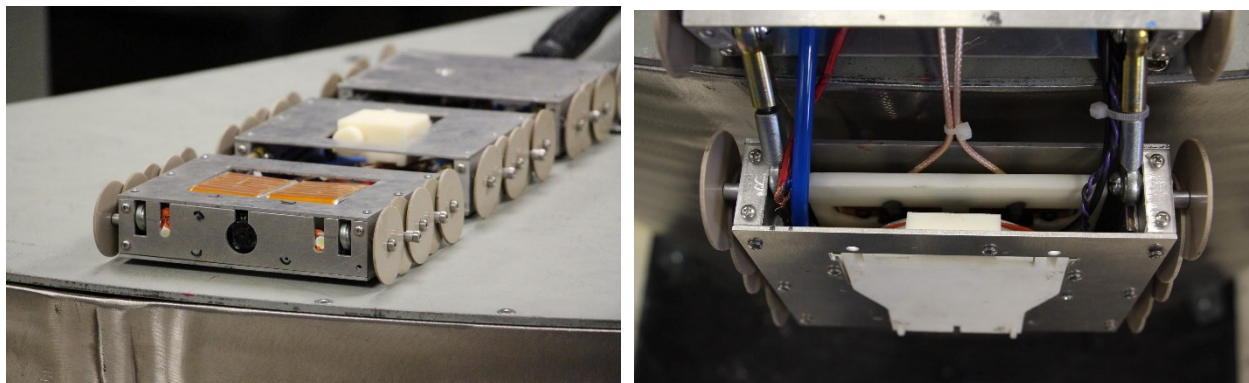
Figure 2.2.9. *Train of robotic cars, upside-down to see EMATs (on left) and then looking inside a car housing the EMATs (on right). The photo on the right shows the EMAT cables in the center, the pneumatic pivot for the EMAT extend/retract mechanism, and the pneumatically operated arm to apply reaction force to the inside of the overpack.*

A pneumatically operated actuation system extends the EMATs out of the car to make measurements. This eliminates the risk of the EMATs getting stuck on corners or magnetic materials during insertion and retraction. To ensure that EMAT liftoff is zero during measurements a pneumatically operated arm provides a reaction force on the inside of the

overpack. The default configuration of both the EMAT extension and reaction arm systems is 'in' to permit the train of sensor cars to be manually retracted in the event of a loss of power.

Two identical EMATs are mounted side-by-side because despite our best efforts, we were unable to eliminate ringing of the EMAT after an electrical signal had been sent to it. The ringing prevented the EMAT from functioning in pulse-echo mode for reflectors located nearby. Thus, side-by-side EMATs are used in pitch-catch mode. The EMATs are identical to enable switching their functionality from transmitter to receiver, and vice versa, by simply interchanging the cable connectors, and for simplicity. Due to the close proximity of the transmit and receive EMATs there were problems with electromagnetic interference in the received signal with some prototypes. In these cases, a thin sheet of soft ferromagnetic shielding alloy was placed between the EMATs. The shielding was not required in the final prototype, where the EMAT housing is aluminum.

The space constraints inside the cargo bay required us to locate the BNC cable connectors inside the tether, thus there is a short length of cable that is soldered directly to the EMAT. However, in early prototypes the BNC connector is located on the EMAT housing for convenience. The EMATs are installed into the sensor car via a mounting bracket. The geometry of the mounting bracket accounts for the curvature of the MPC. However, we found that the EMAT signals were best if the EMATs were allowed to self-adjust to the MPC surface due to the small magnetic attraction rather than be rigidly mounted to the bracket. Thus, the mounting screws should bottom out to leave a small range of motion.
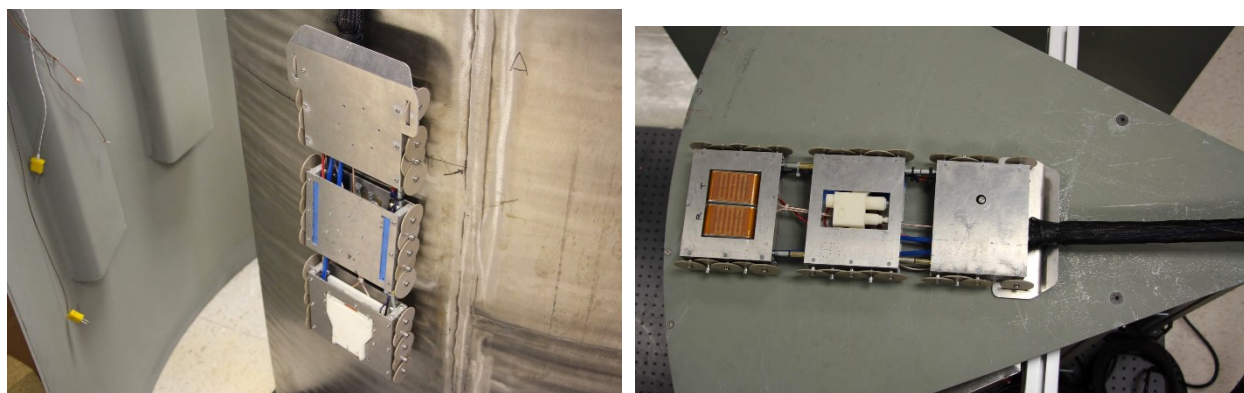
Figure 2.2.10. *Train of robot cars containing EMATs (front car), LIBS remote optics (middle car), and temperature probe and radiation sensor (back car).*

2.2.5 Inspection System Specifications
The equipment that comprises the crack detection system is specified below.
- Two identical EMATs are mounted inside the front sensor car, one is the transmitter and one is the receiver. Two EMAT pairs were fabricated that are nominally the same, with the exception of the magnets as described below.
  - 5x6 array of rare earth (NdFeB) magnets – 0.25" (6.35 mm) cubes
    - N52 – for operation up to 250°F

- N40UH – for operation up to 350°F
  - o Electrical coils (flexible printed circuit board); active element width is 1.5" (38 mm) and its dimension along the wave vector is 1.25" (32 mm), 3 loops with trace/gap width of 0.0079" (0.2 mm), bundle width of 0.125" (3.2 mm), and bundle spacing of 0.142" (3.6 mm)
  - o Aluminum housing dimensions: 0.5" (12.7 mm) thick by 1.75" (44.4 mm) wide by 2.75" (70.0 mm) long
  - o Novalco-based epoxy adhesive to bond magnets into the housing cavity
  - o two-sided polyimide tape to secure the electrical coils to the magnets
  - o PEEK wear-resistant tape (305 μm thick) bonded to the top of the electrical coils to act as a wear surface and protect the coils
- Two RG-316 coaxial cables 50' (15.24 m) long in the robot's tether, these cables are to be replaced by Axon polyimide FH cables (or equal) for use in a loaded cask (to resist elevated temperature and gamma radiation)
- Command center instrumentation
  - o Ritec TEM-128 transmitter matching network (12 nF and 2.6 μH)
  - o Ritec REMP-128 receiver matching network (11 nF and 2.7 μH) with 20 dB preamp
  - o Ritec GA-10000 gated amplifier (output power = 7.0)
  - o Olympus Preamp 5660B (40 dB)
  - o Kiwa 100-500 kHz bandpass filter
  - o National Instruments PXIe-1062Q chassis with PXIe-8360, PXI-5105, and PXI-5402 installed (used to send 5 cycle toneburst with 250 kHz central frequency and to digitize the received signal) controlled by Labview
  - o Dell laptop computer.

The instrumentation, see Figure 2.2.11, is typical of research laboratory setups but could be replaced by a hand-held system (Innerspec PowerBox H; Lynchburg, VA). The laptop computer uses a Labview VI to control the entire test via the NI PXIe-1062Q box through an MXI Express card. The NI box sends both a time gate and a signal to the Ritec Gated Amplifier 10000. The output of the gated amplifier goes through a matching network to the EMAT Transmitter. The signal from the EMAT Receiver goes through a matching network with a 20 dB amplification to a 40 dB preamp and then through a band pass filter before being digitized by the NI box. The Labview VI applies a bandpass filter [200-300] kHz and averaged 50 sets of data before recording. Data are acquired at a 60 MHz frequency.

Figure 2.2.11. Desktop command center instrumentation; Ritec amplifier, NI controller, laptop.

2.2.6 Notch Detection Capability

This section is based largely on the article by Choi, Cho, Lindsey and Lissenden in *Sensors* 18(193) 2018 and Choi, Cho, and Lissenden in *Nuclear Engineering Technology* 2018 (in-press). The EMATs were tested on a 12.7 mm thick 304 stainless steel welded plate having well-defined surface breaking notches near the HAZ to evaluate their notch sensitivity. Plate and notch dimensions are indicated in Figure 2.2.12. The plate contains three 75%-through-thickness notches implanted by electrical discharge machining having different orientations with respect to the weld line: 90˚, 0˚, and 45˚. The length-depth ratio of the rectangular notches is 2:1. Of the three notches, the 90˚ and 0˚ notches are of primary interest to us due to the direction of the thermal residual stress driving force for SCC.
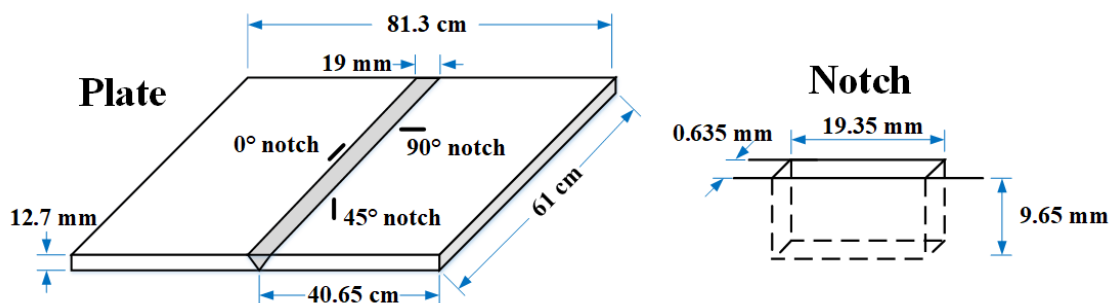
Figure 2.2.12. Plate and notch dimensions of a 12.7 mm thick 304 stainless steel welded plate having surface breaking notches.

A schematic of the experimental setup (which is a little different than that specified in section 2.2.5) to evaluate the EMAT notch sensitivity is shown in Figure 2.2.13. The RAM-5000-SNAP (Ritec, Warwick, MA, USA) is used to produce a five-cycle tone-burst electric signal with a 1200 V peak-to-peak voltage and a 250 kHz central frequency. The electric signal passes through a matching network (TEM-128, Ritec), and then to the transmitter to generate SH waves on the

plate. The acquired signal from the receiver goes through another matching network (REMP-128, RITEC) and a 30 dB pre-amplifier in the RAM-5000-SNAP. Then, the pre-amplified signal is displayed on an oscilloscope (MSO 2014, Tektronix, Beaverton, OR, USA) and recorded. For post-processing, a 500 kHz digital low-pass filter is applied to the recorded signal to eliminate high frequency noise.
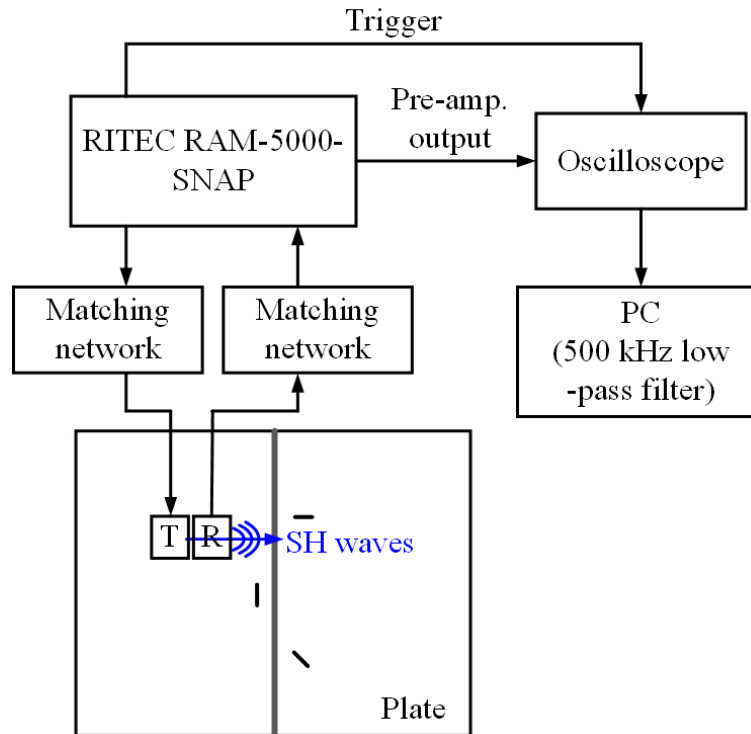
Figure 2.2.13. *Schematic of the experimental setup to evaluate EMAT's notch sensitivity.*

The notched plate inspection schemes and corresponding experimental setups are shown in Figure 2.2.14. Both the left and right sides of the weld line are inspected. The pair of EMATs is scanned in the direction parallel to the weld line maintaining a fixed distance between EMATs and the weld line to obtain B-scan images. The scan was performed from 10 to 50 cm with a step of 0.5 cm, based on the upper edge of the plate. Here, the locations of the 90° and 0° notches are 20 and 30 cm, respectively.
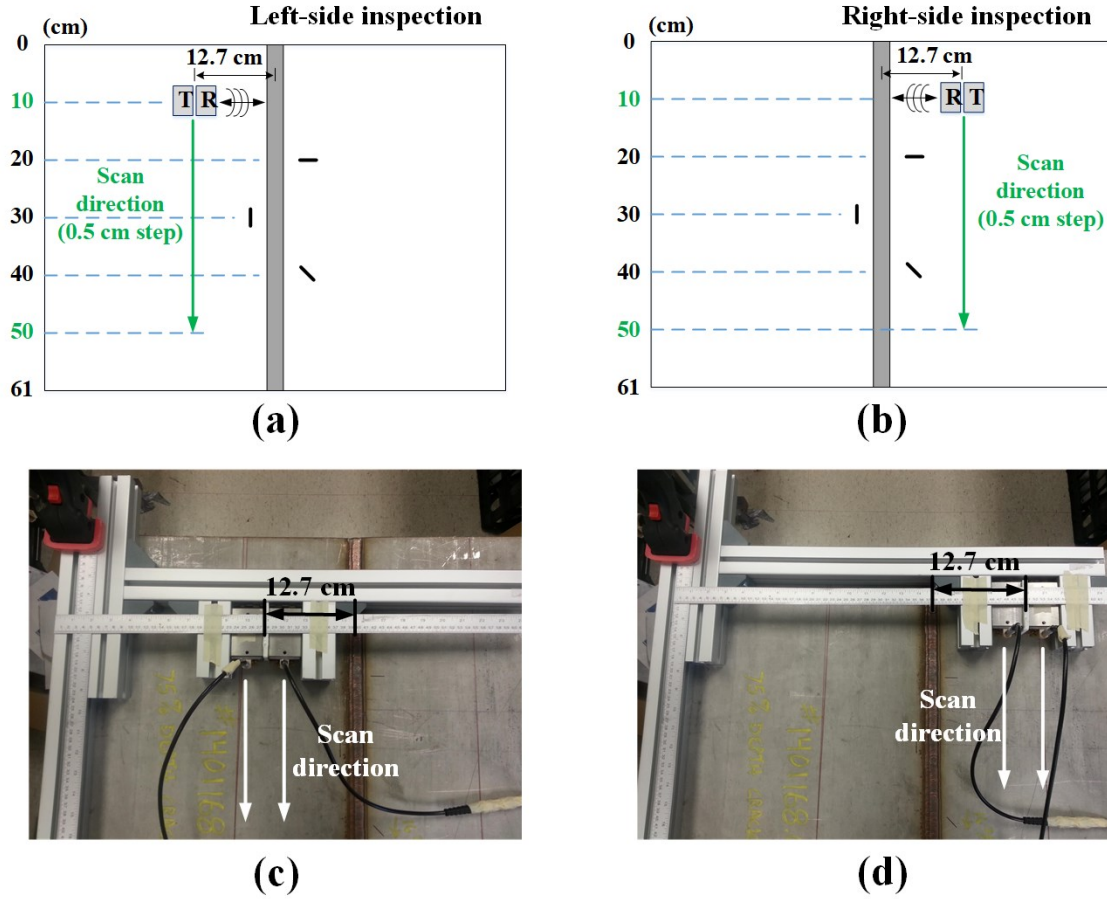
Figure 2.2.14. *Notched plate inspection schemes and corresponding experimental setups: (a) and (c) left-side inspection; and (b) and (d) right-side inspection.*

Figures 2.2.15(a) and (b) show the A-scans taken when the EMAT pair is located at the 20 cm position in the left and right-side inspections, respectively. In the left-side inspection, the 90˚ notch echo is not detected due to the following two phenomena: the scattering from the notch parallel to the wave vector is in general small and the small scattered waves may be severely attenuated as they pass through the weld. Meanwhile, the right-side signal shows clear notch echo arriving at about 100 μs. This result demonstrates that it is possible to detect the parallel notch with the EMATs if the SH waves do not pass through the weld. The waveform signals related to 0˚ notch detection measured at 30 cm position are shown in Figs. 2.2.15(c) and (d). The reflected waves from the notch are clearly observed at both left and right-side inspections. The 0˚ notch perpendicular to the wave vector reflected much more energy than the parallel notch.

B-scan images of the notch plate are shown in Fig. 2.2.16, where the Hilbert transformation was applied to each A-scan signal to obtain the envelope of the signal. The images display the absolute magnitudes of the enveloped signals in a color map. The waves arriving at approximately 110 μs are weld echoes. Though the echo amplitude varies with the scan position due to the non-uniformity of the weld quality, its arrival time is consistent. The echo from the 0˚ notch is clearly

shown before the weld echo in the left-side inspection, and after the weld echo in the right-side inspection. The 90˚ notch echo is also shown before the weld echo in the right-side inspection. However, the 45˚ notch was not detected since the notch deflection traveled off at a 45˚ angle and was not received by the EMAT. Overall, the experimental results show that the designed EMATs have good sensitivity to both notches, although the sensitivity to the parallel notch is certainly lower than that for the perpendicular notch.
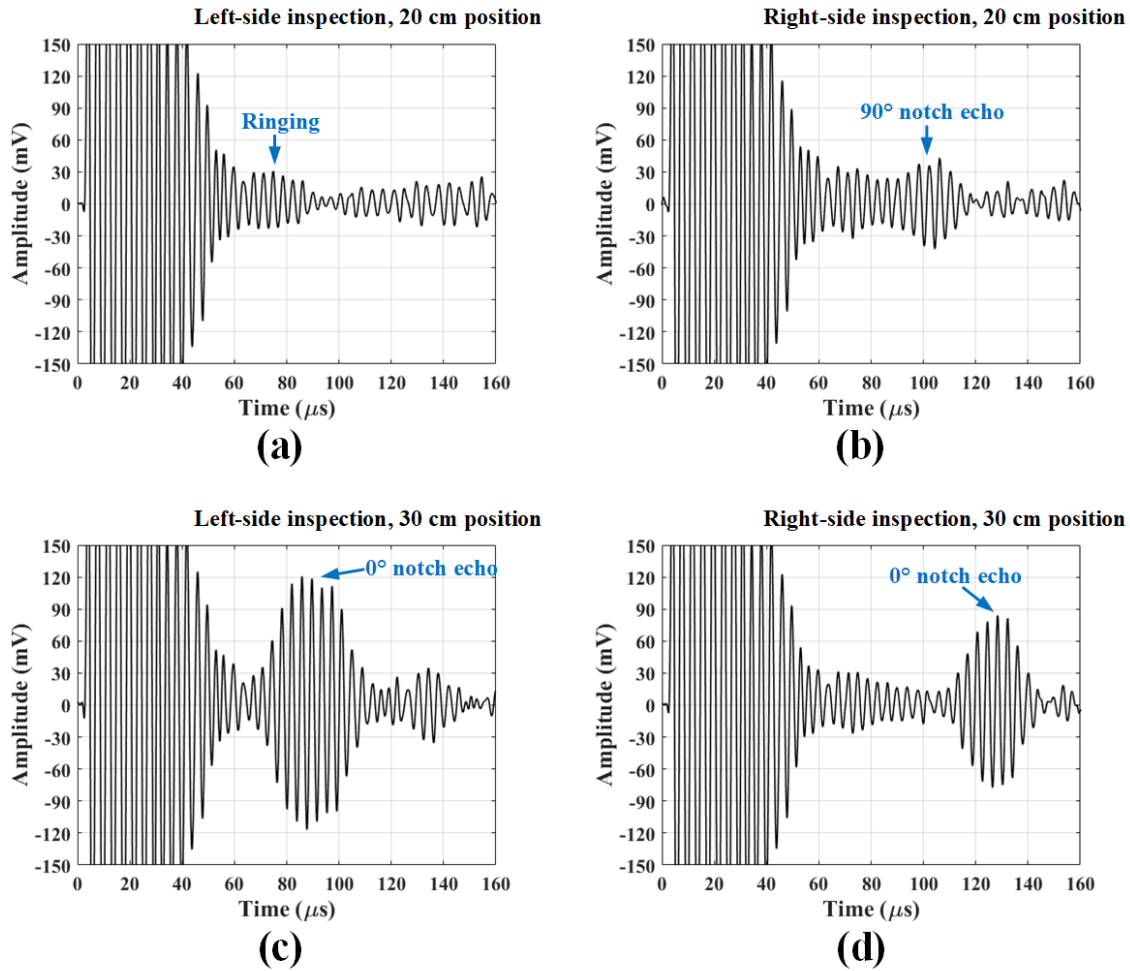
Figure 2.2.15. *The waveform signals taken when the EMAT pair is located at (a) and (b) 20 cm position; and (c) and (d) 30 cm position.*

Figure 2.2.16. *B-scan images of the notch plate at (a) left-side inspection; and (b) right-side inspection.*

The lab-scale canister mock-up shown in Fig. 2.2.17 was fabricated and used to evaluate the EMATs ability to excite and receive SH guided waves on the stainless steel canister using the proposed inspection methodology. The canister mock-up is made of 15.9 mm thick stainless steel and fabricated by submerged arc welding of three rectangular plates as per the HI-STORM 100S manufacturing process. Thus, three welds were made, which are axial, circumferential and bottom welds as shown in Fig. 2.2.17. Prior to rolling the welded plate to impart curvature, both surface attachments and weld caps were ground off.
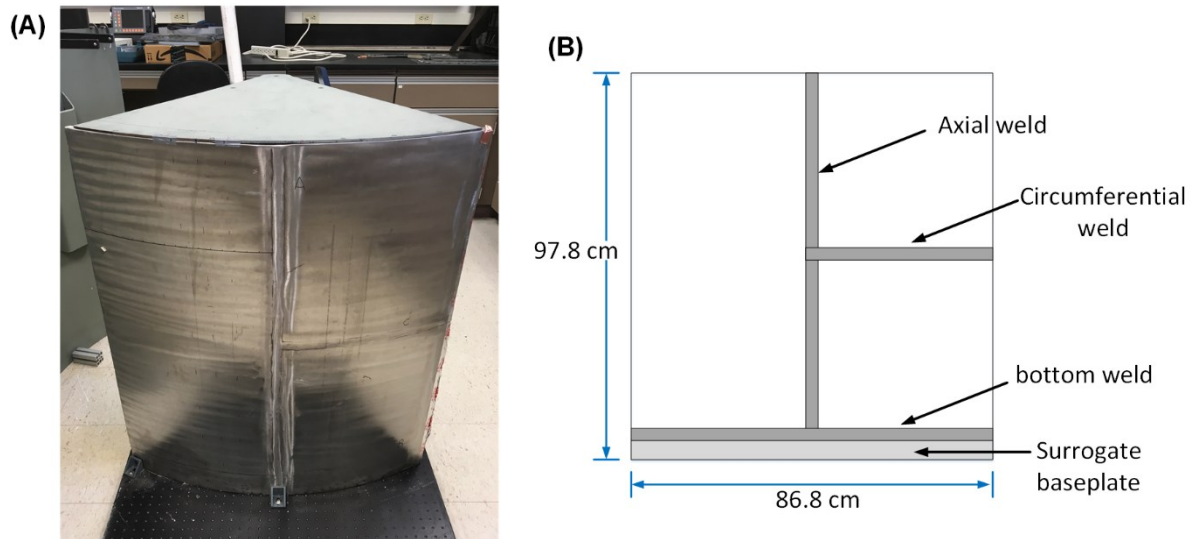
Figure 2.2.17. *(A) A photo and (B) schematic of the lab-scale canister mock-up having axial, circumferential and bottom welds fabricated by submerged arc welding.*

The inspection scheme for a lab-scale canister mock-up is shown in Fig. 2.2.18. In the canister inspection, the transmitter excites SH waves normal to the axial weld and the receiver picks up returning echoes from the weld. The purpose of this test is to determine whether it is possible to locate the axial welds under the proposed inspection methodology, and to acquire baseline data.

Both the left and right sides of the axial weld are inspected. The pair of EMATs is positioned on a vertical line 15 cm away from the axial weld and is scanned downward along the weld to obtain B-scan images. Initially it is located 10 cm away from the upper edge of the canister and moves down a total of 80 cm in increments of 1.25 cm. At each increment, the pulse-echo signal is recorded and used for B-scan imaging.
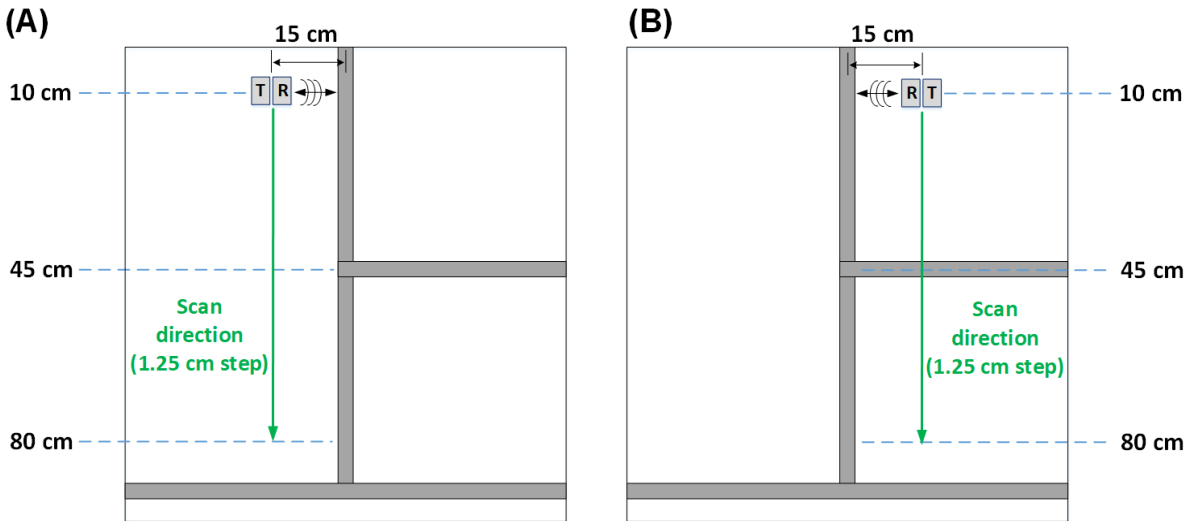
Figure 2.2.18. *Inspection schemes for a lab-scale canister mock-up at (a) left-side inspection and (b) right-side inspection.*

A typical pulse-echo signal taken when the pair of EMATs is located at 30 cm (from the top) in the left-side inspection is shown in Fig. 2.2.19. The weld echo is clearly observed by the first wave packet arriving between 110 and 130 μs. The echo includes both SH_0 and SH_1 mode reflections. The next packet arriving between 200 and 300 μs is the back-wall echo from the left edge of the canister mock-up, but we are not interested in this echo and it will not be present in the actual canister inspection.
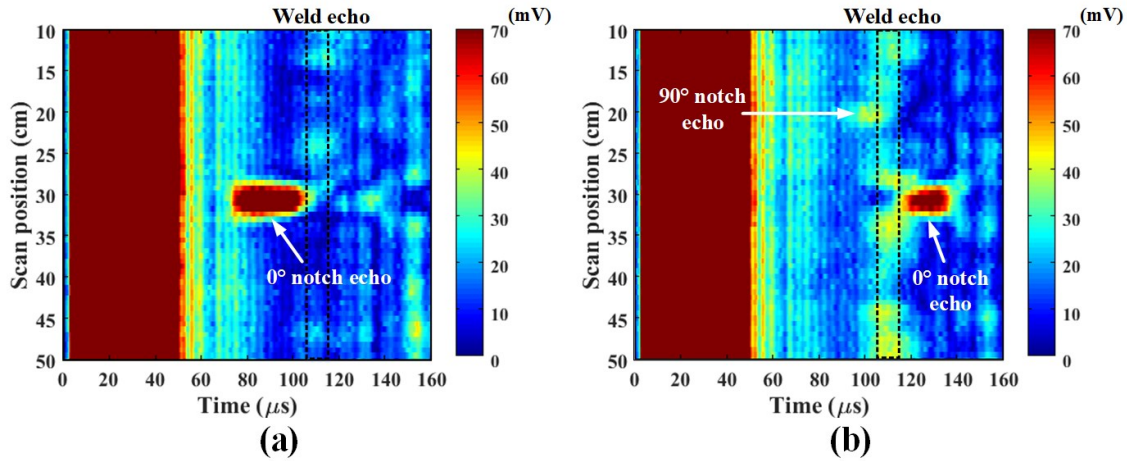
B-scan images of the canister mock-up are shown in Fig. 2.2.20, where the Hilbert transformation was applied to each A-scan signal to obtain the envelope of the signal. The images present the absolute voltage magnitudes of the enveloped signals in a color map. Both images clearly show indications of the weld echo between 110 and 130 μs, except where the circumferential weld interacts the axial weld at a y-position of 45 cm. The weld echo amplitude varies with the scan position due to the non-uniformity of the weld quality, but its arrival time is constant. The larger amplitude variability in the left-side inspection than in the right-side inspection suggests that the interface between the canister metal and the weld metal on the left side is more variable than on the right side. Knowing that the group velocity of the SH_1 mode, which is the dominant mode in the weld echo, is 2954 m/s as analyzed in group velocity dispersion curves in Fig. 2(B) and that initial time delay arising from the EMAT measurement system identified prior to this experiment is approximately 30 μs, the 125 μs time of flight at which the weld echo peak is measured corresponds to a round trip distance of 14 cm. This measured distance is in good agreement with the actual distance from the pair of EMATs to the weld interface in the canister mock-up

inspections. Consequently, the results in Fig. 2.2.20 clearly demonstrate that the axial weld can be detected and located by the SH wave-based pulse-echo method using EMATs.
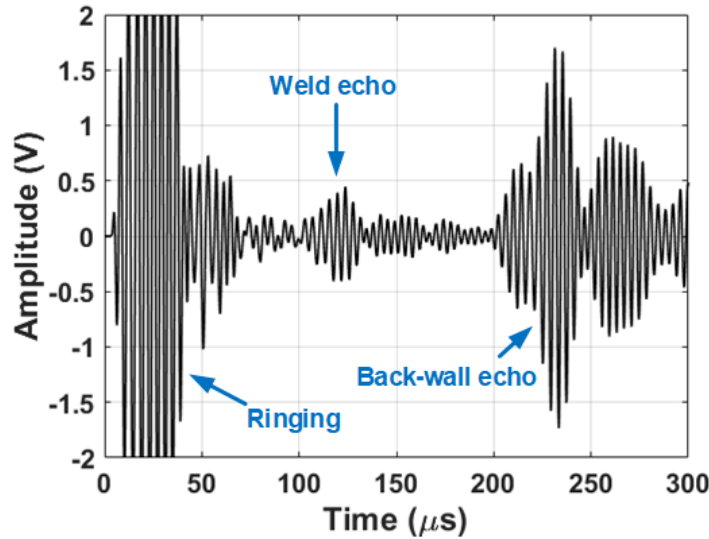
Figure 2.2.19. *A-scan taken when the pair of EMATs is located at 30 cm (from the top) in the left-side inspection.*
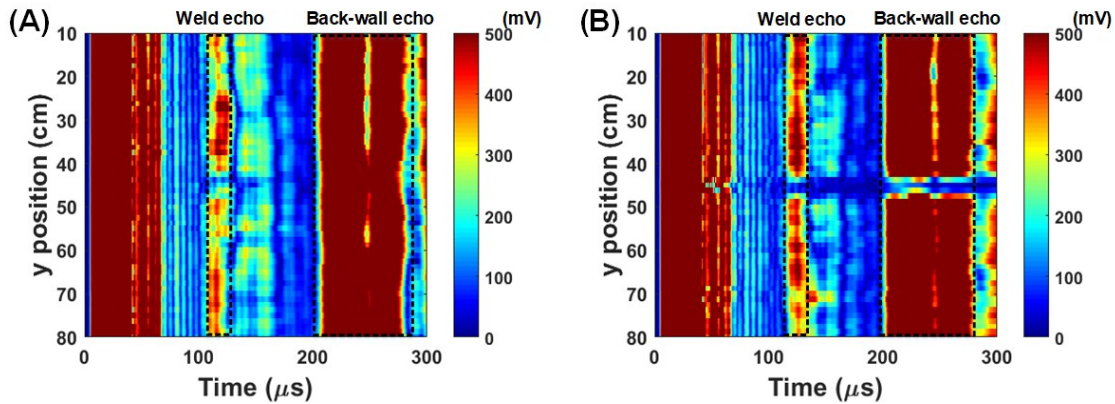
Figure 2.2.20. *B-scan images of the canister mock-up at (a) left-side inspection and (b) right-side inspection.*

To evaluate the capability of SH guided waves to detect cracks and to assess the distance range at which cracks can be detected, a 15.9 mm thick 304 stainless steel plate having well-defined surface breaking notches was prepared as shown in Fig. 2.2.21. Plate and notch dimensions are indicated in Figs. 2.2.21(A) and (B). The right end of the plate was cut as a chevron to divert the back-wall echoes in another direction. Two semi-elliptical surface notches, namely oriented perpendicular and parallel to the wave vector, were machined. They are 25%-through-thickness notches at their deepest point and the notch length-depth ratio is 2:1, which represents the minimum crack size that we aim to detect.
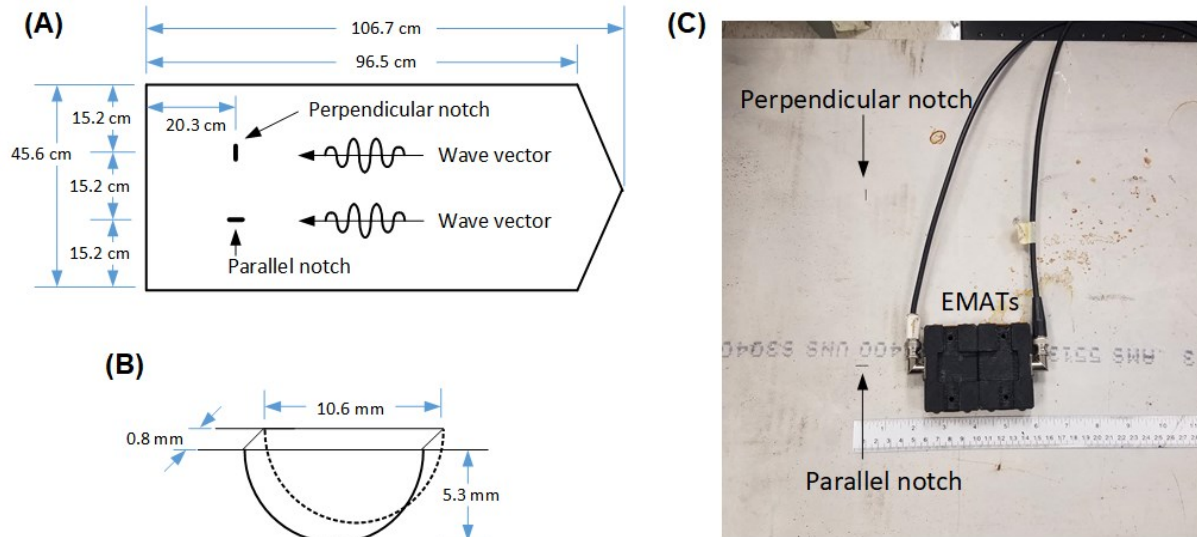
Figure 2.2.21. (a) Plate and (b) notch dimensions of a 15.9 mm thick 304 stainless steel plate having surface breaking notches oriented perpendicular or parallel to the wave vector direction indicated, and (c) a photo showing the EMAT arrangement for detecting the parallel notch.

Inspection schemes for the notched plate is shown in Fig. 2.2.22. The plate inspection is performed for one notch oriented perpendicular to the wave vector and one notch oriented parallel to the wave vector. For each notch, pulse-echo signals are examined from various distances ranging from 5 cm to 55 cm at 0.5 cm intervals to assess the distances from which the notches can be detected.
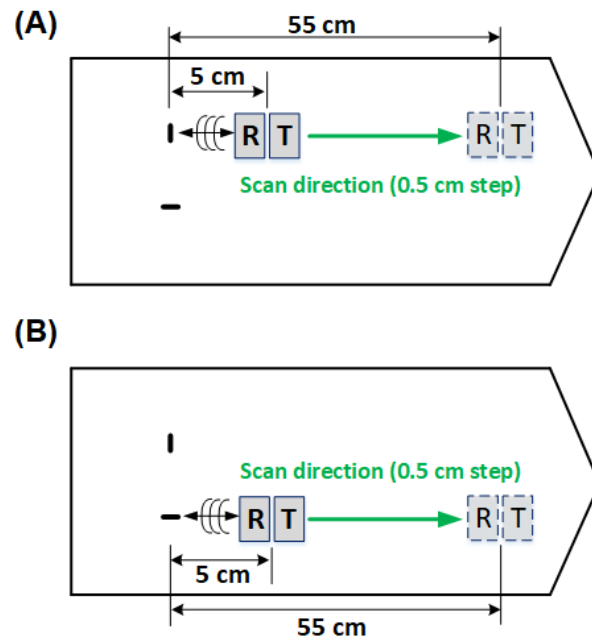
Figure 2.2.22. Inspection schemes for a stainless steel notched plate at (a) perpendicular notch detection and (b) parallel notch detection.

Figure 2.2.23 shows pulse-echo signals taken when the pair of EMATs is located 12 cm away from the perpendicular notch and the parallel notch. The notch echoes for both notches are clearly observed arriving at approximately 110 μs. A relatively large echo was received from the perpendicular notch, while the parallel notch created a smaller reflection.
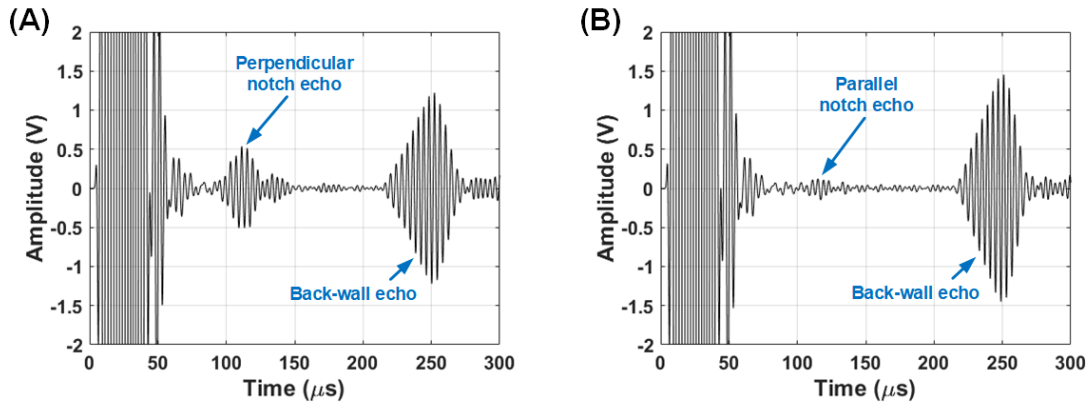
Figure 2.2.23. *A-scans taken when the pair of EMATs is located 12 cm away from (a) the perpendicular notch and (b) the parallel notch.*

A-scan signals measured at various distances from 5 to 55 cm for both notches are combined to plot the B-scan images in Fig. 2.2.24. The images were created by simply spatially stacking the A-scan signals enveloped by the Hilbert transformation. Note that the vertical red band prior to 80 μs is electromagnetic interference and that the diagonal red band centered at the positions of (200 μs, 5 cm) and (500 μs, 50 cm) is the echo from the plate end wall beyond the notches. A unique pattern in which the amplitude of perpendicular notch echoes vary periodically according to distance to the notch is observed in Fig. 2.2.24(a). This pattern was caused by the positive and negative interferences between the SH_0 and SH_1 modes that travel at the different group velocities identified in Fig. 2.2.24(b).
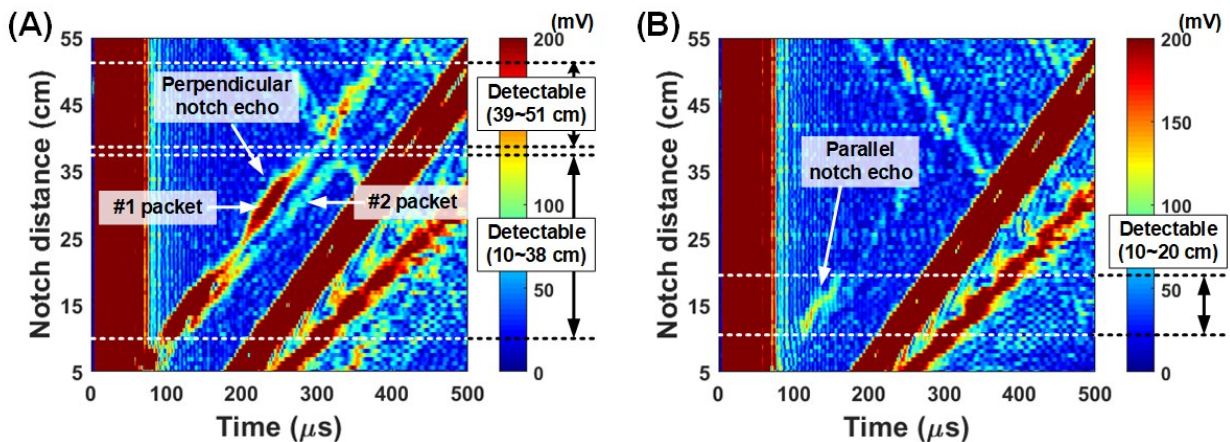
Figure 2.2.24. *B-scan images for (a) perpendicular notch detection and (b) parallel notch detection.*

To clearly identify the SH modes reflected from the perpendicular notch, supplemental measurements were conducted. Ten A-scan signals were collected while the transmitting EMAT was fixed at 30 cm away from the notch and the receiving EMAT was incrementally (2mm) reversed from where it had started, adjacent to the transmitting EMAT. Then, a two-dimensional fast Fourier transform was applied to all the A-scan signals. Figure 2.2.25 shows the frequency-phase velocity spectra for the #1 and #2 wave packets in Fig. 2.2.24(a). The #1 wave packet includes both SH_0 and SH_1 modes. However, since the amplitude of the SH_1 mode excited by the transmitting EMAT is higher than that of SH_0 mode, the SH_1 mode is dominant in the notch echoes. The #2 wave packet is the SH_2 mode with a higher frequency than the SH_0 and SH_1 modes. This higher mode was generated by mode conversions of incident SH_0 and SH_1 modes on the notch face.
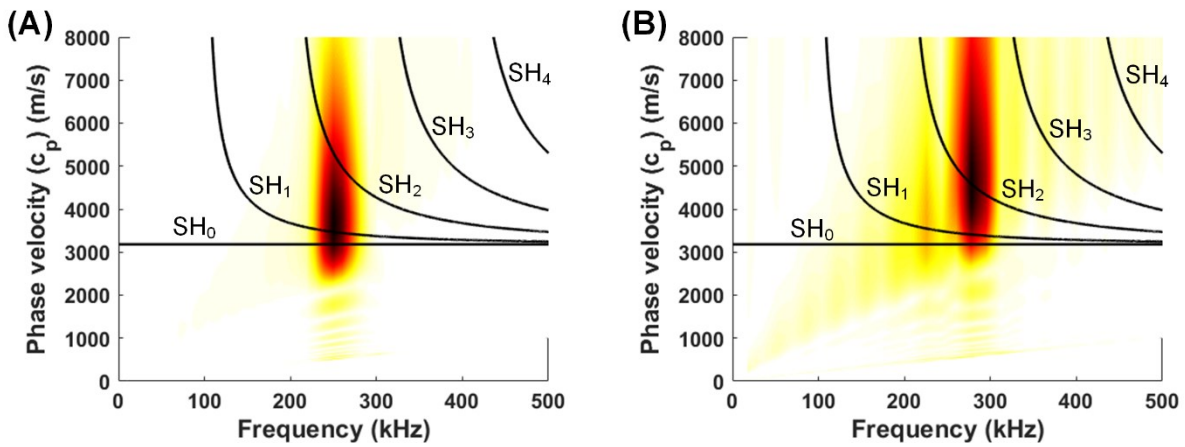
Figure 2.2.25. *Frequency-phase velocity spectra for (a) #1 and (b) #2 wave packets in Fig. 13(A).*

To assess the distances at which both notches are detectable, the signal-to-noise ratio (SNR) of the notch echoes was evaluated. The SNR was calculated from $20 \cdot \log_{10}[Signal(V) / Noise(V)]$, where the noise level was consersatively defined as the level of small bright spots randomly distributed in the B-scan images and the minimum SNR that determines a detectable notch echo was conservatively defined as 3.5 dB. For the perpendicular notch, there were two detectable ranges. The first range was from 10 to 38 cm, where the echo SNRs were 12.7 and 3.75 dB respectively. The second range was from 39 to 51 cm, where the echo SNRs were 5.15 and 6.36 dB, respectively. At the distance range from 38 to 39 cm, the echo SNR was less than 3.5 dB due to the negative interference between the SH_0 and SH_1 modes. Meanwhile, the detectable range for the parallel notch was significantly narrower than that of the perpendicular notch because of the smaller echo as identified in Figs. 2.2.23 and 2.2.24. The range for the parallel notch was from 10 to 20 cm, where the echo SNRs were 4.86 and 4.14 dB respectively.

Based on the detectable distances for notches oriented perpendicular or parallel to the wave vector analyzed from the B-scan images in Fig. 2.2.23 and knowing that the movement of a robotic sensor car is constrained to the gaps between guide channels, the NDI coverage for spent nuclear fuel storage canisters is mapped out in Fig. 2.2.26(a) for perpendicular cracks and in Fig. 2.2.26(b) for parallel cracks. The red, green, and blue regions represent the areas where cracks

can be detected when the delivery robot car (D) is deployed into the 1st, 2nd, and 3rd gap, respectively. Figure 2.2.26(a) shows that 100% coverage can be achieved for perpendicular cracks by robotic inspections in all 16 guide channel gaps and that the overlapping of coverage zones provides redundancy, which will improve the reliability of the inspection. On the other hand, Fig. 2.2.26(b) shows that cracks oriented parallel to the wave vector can only be detected when they are behind the guide channels. These cracks correspond to the circumferential cracks that grow parallel to the circumferential and bottom welds and also circumferential cracks that grow perpendicular to the axial welds. However, we reiterate that this is the result for the minimum crack size targeted for detection. Larger cracks will have a larger coverage zone. Alternatively, an eddy current array could be used between the guide channels to provide full coverage for circumferential cracks. Likewise, another supplementary solution to provide full coverage for circumferential cracks is to put a second EMAT pair oriented at 90 degrees to the first EMAT pair in another robot car.
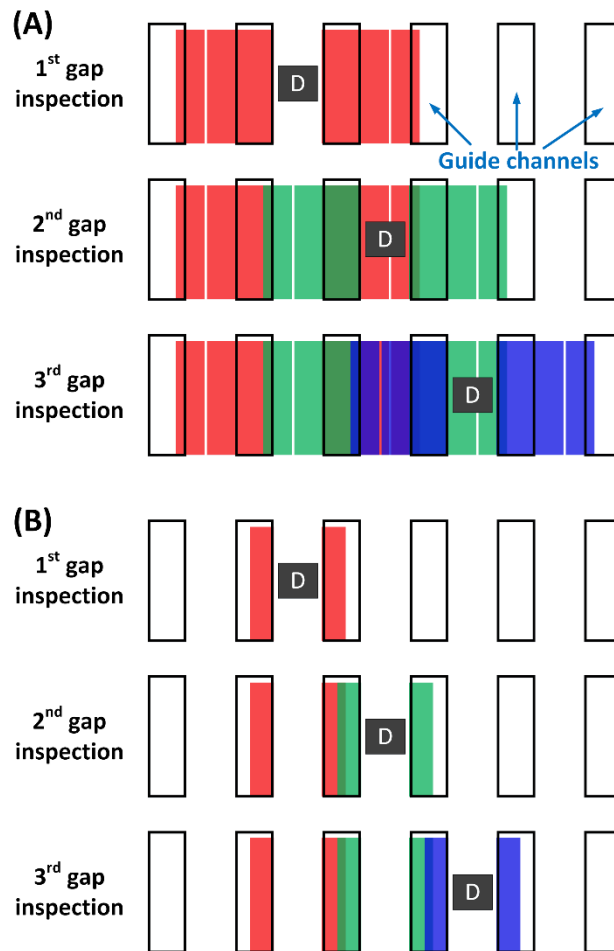
Figure 2.2.26. *Schematic of gap-by-gap canister NDI coverage for (a) perpendicular cracks and (b) parallel cracks. Red, green, and blue regions represent the areas where cracks can be detectable when the delivery robot car (indicated by the letter D) is deployed into the 1st, 2nd, and 3rd gap, respectively.*

2.2.7 Environmental Testing

2.2.7.1 Gamma radiation

This section is based largely on the article by Choi, Cho, Lindsey and Lissenden in *Sensors* 18(193) 2018. Accelerated gamma radiation tests were conducted on the primary EMAT components with no housing due the limited space inside the gamma cell at the Radiation Science and Engineering Center at the Pennsylvania State University. The test setup is shown in Figure 2.2.27. The transmitter and the receiver are separated to prevent mutual attraction of the magnets during testing. They are attached to a 6.35 mm thick and 177.8 mm long 304 stainless steel plate and the through-transmission mode is used. The ultrasonic test system and excitation parameters are the same as in the elevated temperature tests. The gamma cell provided a dose rate of 370 krad/hr from a cobalt-60 source. The test was conducted continuously for 16 hours, which produces a total dose of 5920 krad. This cumulative dose is equivalent to 219 hours of operation in a 27 krad/hr environment.
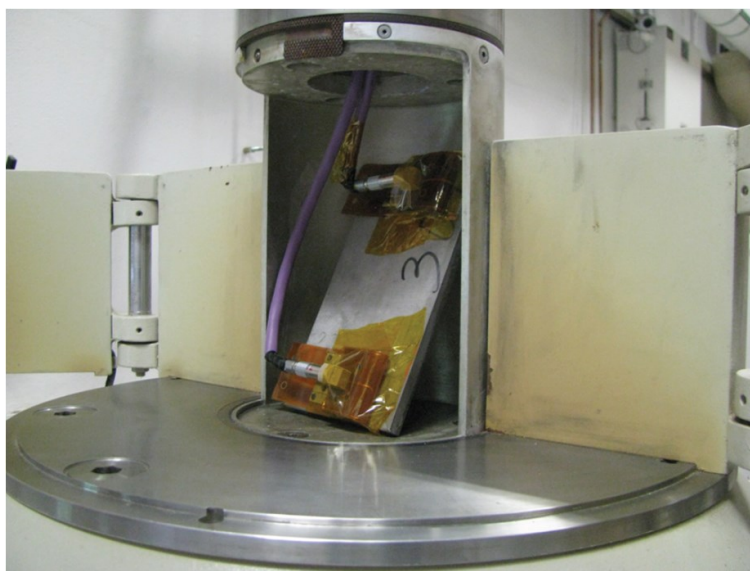
Figure 2.2.27. *Gamma radiation test setup in the gamma cell where the transmitter and the receiver are separately attached to both ends of a 6.35 mm thick 304 stainless steel plate, and employ the through-transmission mode.*

Typical SH wave signals collected at the beginning of the testing and after 16 hours of gamma radiation exposure are shown in Figure 2.2.28, where the signals are normalized with respect to the peak amplitude of the through-transmitted wave at the beginning of the testing. No meaningful changes in the peak amplitudes and waveforms as well as no abnormal noise are observed. A slightly longer ringing can be observed in these signals compared to the temperature testing signals. This is attributed to the absence of a sensor housing and ringing within the magnets. The normalized amplitudes of the incident wave as a function of the gamma dose are shown in Figure 2.2.29. A very slight amplitude reduction occurs initially, and then the normalized amplitude converges to approximately 0.98. The 2% reduction is significantly smaller than the reduced performance by elevated temperatures. These experimental results show reliable EMAT operation up to a total dose of 5920 krad and beyond.
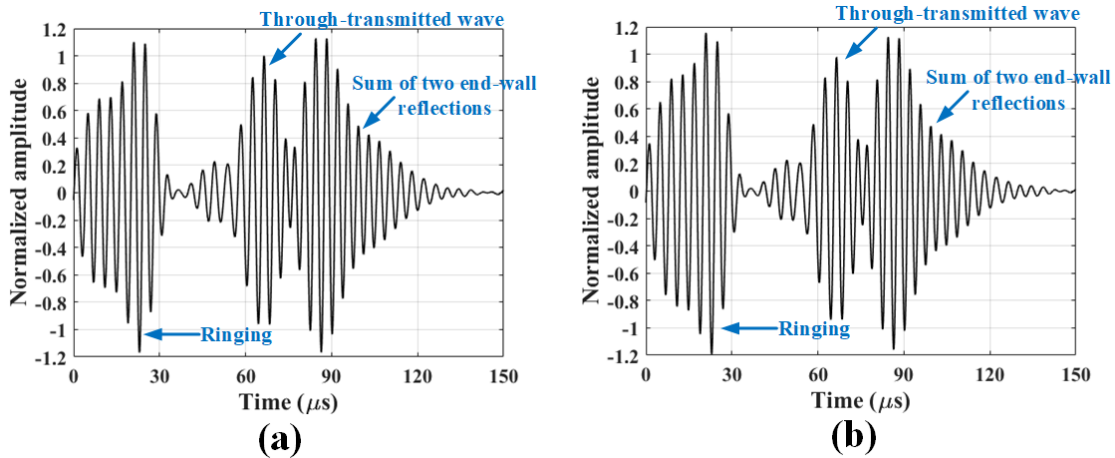
Figure 2.2.28. Normalized SH wave signals collected at (a) prior to exposure and (b) 16 hours of gamma radiation exposure.
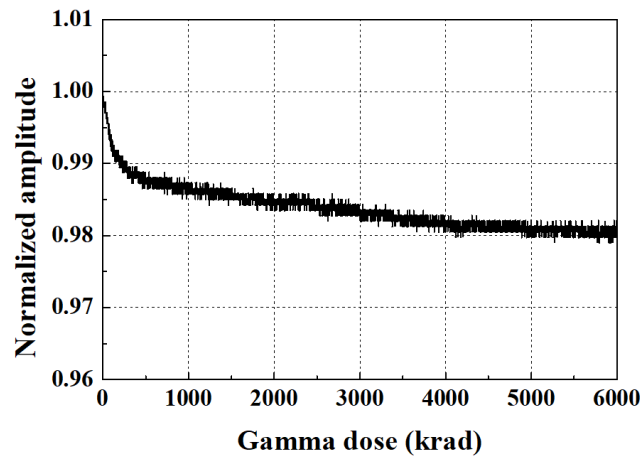
Figure 2.2.29. The normalized amplitudes of the incident wave as a function of gamma radiation dose.

2.2.7.2 Elevated temperature

Neodymium (NbFeB) magnets are sensitive to temperature. If heated above their maximum operating temperature they permanently lose a portion of their magnetic strength. If they are heated above their Curie temperature, they will lose all their magnetism. We observed that N52 grade neodymium magnets lose roughly 23% of their ultrasonic performance when heated to 350˚F, which motivated us to investigate alternative materials. In fact, there are various neodymium alloys with higher Curie temperatures than grade N52. Table 2.2.1 summarizes thermal characteristics of several readily available neodymium magnets. Considering that the maximum design temperature is 350˚F for our robotic inspection system, NUH grade neodymium may suffice for this project since its maximum operational temperature is listed as 356˚F. However, it should be noted that N40UH is the highest grade among NUH magnets and KJ Magnetics lists its magnetic strength is 12% less than N52 grade (N52: 14.8 kg, N40UH: 12.9 kg).

This lower magnetic strength can result in lower amplitude guided waves as a trade-off. Since magnetic strength is also dependent on the shape of the magnet as well as other factors, a performance evaluation is required for an accurate assessment.

Table 2.2.1. *Thermal characteristics of neodymium magnets* [https://www.kjmagnetics.com/specs.asp].

Material types	Max Operating Temp	Curie Temp
N	176˚F (80˚C)	590˚F (310˚C)
NM	212˚F (100˚C)	644˚F (340˚C)
NH	248˚F (120˚C)	644˚F (340˚C)
NSH	302˚F (150˚C)	644˚F (340˚C)
NUH	356˚F (180˚C)	662˚F (350˚C)
NEH	392˚F (200˚C)	662˚F (350˚C)

We purchased N40UH grade magnets (1/4" x 1/4" x 1/4" cubes) from KJ Magnetics and fabricated a new set of aluminum (Al 6061-T6) housings. Figure 2.2.30 shows photos of the new EMATs in their mounting bracket. RG-316 coax cables were directly soldered on the flexible electric coils. The cables were adhesively fixed on the cradle to provide strain-relieve for the soldered joint. The coax cable is joined to the coax cable in the tether by BNC connectors.
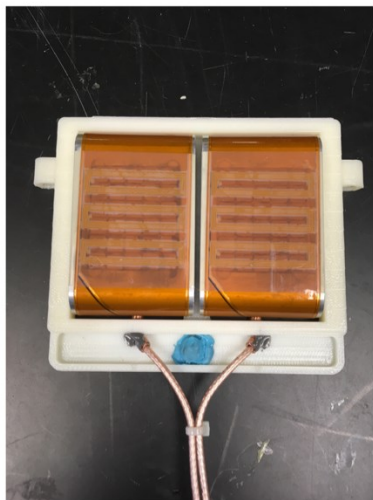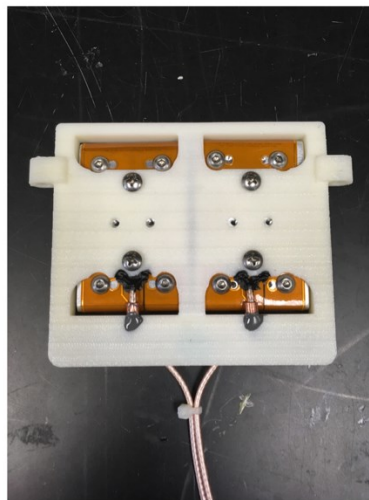
(a)   (b)

Figure 2.2.30. *Photos of the new EMATs with N40UH grade neodymium magnets mounted in a cradle: (a) bottom view showing the meandering coil PCB of the EMATs, (b) top view showing the attachments.*

The performance change at room temperature was evaluated by conducting measurements on echoes from the perpendicular notch in the 15.9 mm thick stainless steel plate used in results described in section 2.2.6. Figure 2.2.31 shows the experimental setup. The distance between the center of EMATs (transmitter/receiver) and the perpendicular notch was set to be 178 mm

and fixtures were constructed to minimize variation between measurements. 1440 Vpp, 5 cycle, 250kHz toneburst pulses were excited into the transmitting EMAT (T) and then A-scan signals were acquired by the receiving EMAT (R) for each EMAT pair with N40UH and N52 magnets. All other instruments (digitizer, pre-amplifier, matching box, etc.) were kept the same.
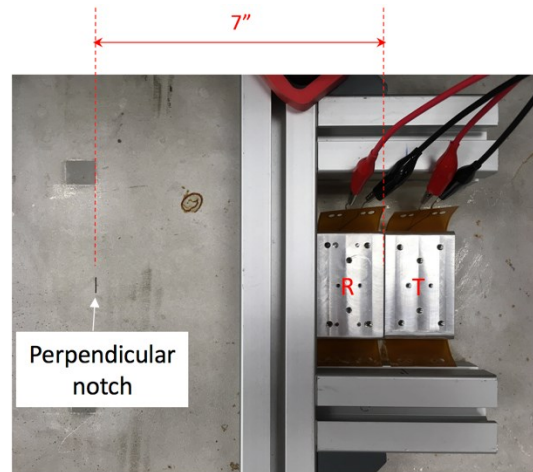
Figure 2.2.31. *Experimental setup to compare the ultrasonic performance of N40UH and N52 grade magnets.*

Figure 2.2.32 shows the A-scan signals taken by those EMAT pairs on the notched stainless steel plate. In terms of signal strength, the peak amplitude of the notch echo was decreased by 13.9% when N40UH grade magnets were used, which corresponds well to their difference in magnetic strength given above (12%). The overall quality of signals experienced negligible degradation. To reiterate, these measurements were made at room temperature, after heating cycles. A comparison between the N52 and N40UH magnets is provided in Figure 2.2.33, where the magnetic pull force and the amplitude of a notch echo are shown.
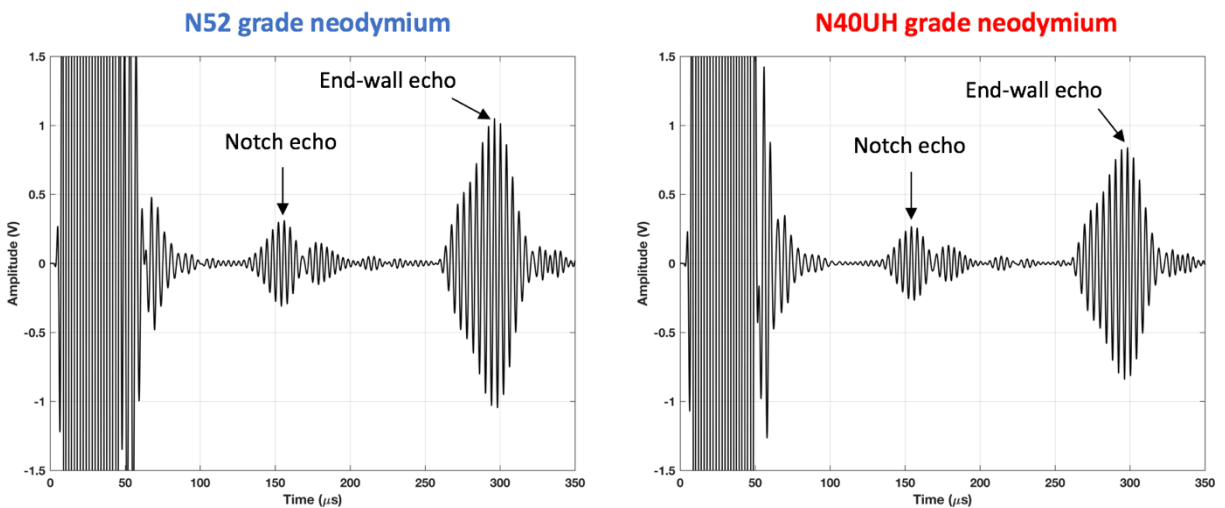
(a)   (b)

Figure 2.2.32. *A-scan signals taken by EMATs with two different grades of neodymium magnets: (a) N52 grade, (b) N40UH grade. The SNR of the notch echo calculated based on the noise floor between 200 ~ 250 us were 15.8 and 14.1 dB for N52 and N40UH, respectively.*
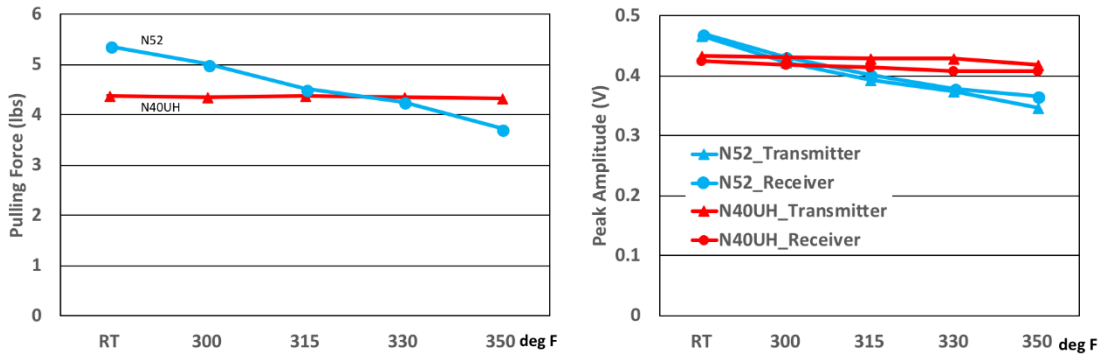
Figure 2.2.33. *A-scan signals taken by EMATs with two different grades of neodymium magnets: (a) N52 grade, (b) N40UH grade. The SNR of the notch echo calculated based on the noise floor between 200 ~ 250 us were 15.8 and 14.1 dB for N52 and N40UH, respectively.*

2.2.8 Laboratory Mockup Testing

To demonstrate the ability of the EMAT system to function on realistic geometry at elevated temperature, we had Holtec fabricate a mockup for our use at Penn State as shown in Figure 2.2.34. It represents a section of an MPC in an overpack. The shell structure is 15.9 mm thick stainless steel and fabricated by welding three rectangular plates as per the HI-STORM 100S manufacturing process (submerged arc welding process). This shell structure was also used for the final demonstration that will be described in section 2.2.12.
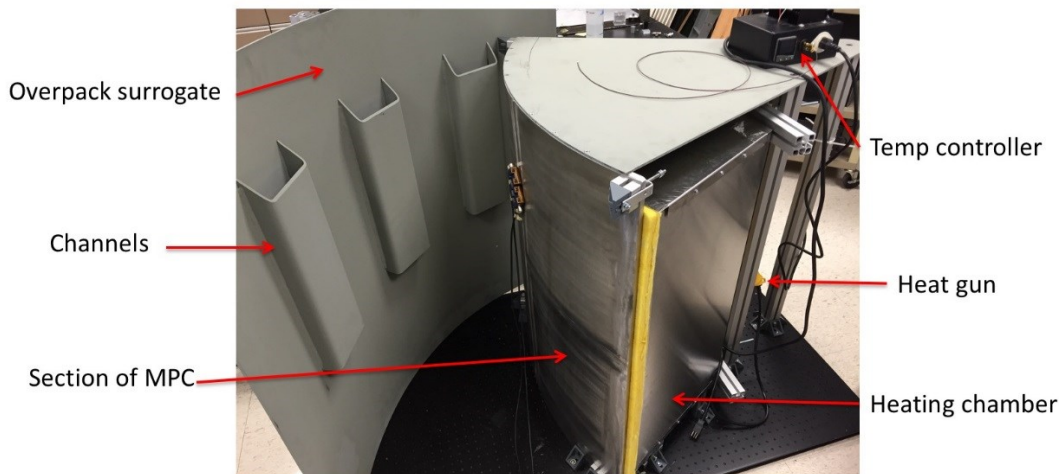
Figure 2.2.34. *The laboratory mockup at Penn State with heating chamber.*

For thermal testing, a heating chamber was attached to the concave side and two heat guns were used to achieve the desired surface temperature, which was measured by three thermocouples spot-welded at heights of 76 mm (3"), 533 mm (21"), and 787 mm (31") from the bottom as

shown in Figure 2.2.35a. We learned from preliminary testing that the maximum surface temperature is 533 mm (21") from the bottom. In addition, two semi-elliptical notches in the shell were created. Figure 2.2.35a also shows the locations and orientations of the notches in the heat affected zone of the welds. The sizes of Notch A and Notch B are 19.8 x 3.4 mm (0.781 x 0.135") and 21.9 x 3.4 mm (0.864 x 0.133") (i.e., surface length x maximum depth), respectively. Notches A and B are located in the heat affected zone of the axial weld and the bottom weld respectively. Notch A passes through the weld metal and the shell, while Notch B is along the fusion line between the weld metal and the shell. For each set of measurements, the maximum surface temperature at the height of 533 mm (21") was held at 70F, 250F, 300F, and then 350F while circumferential pulse-echo measurements were made with the EMATs containing the N40UH magnets. This scan path was selected to examine Notch B. The same instruments were used as described in the section 2.2.5 except we replaced the Ritec GA-1000 gated amplifier with Ritec RAM-5000.
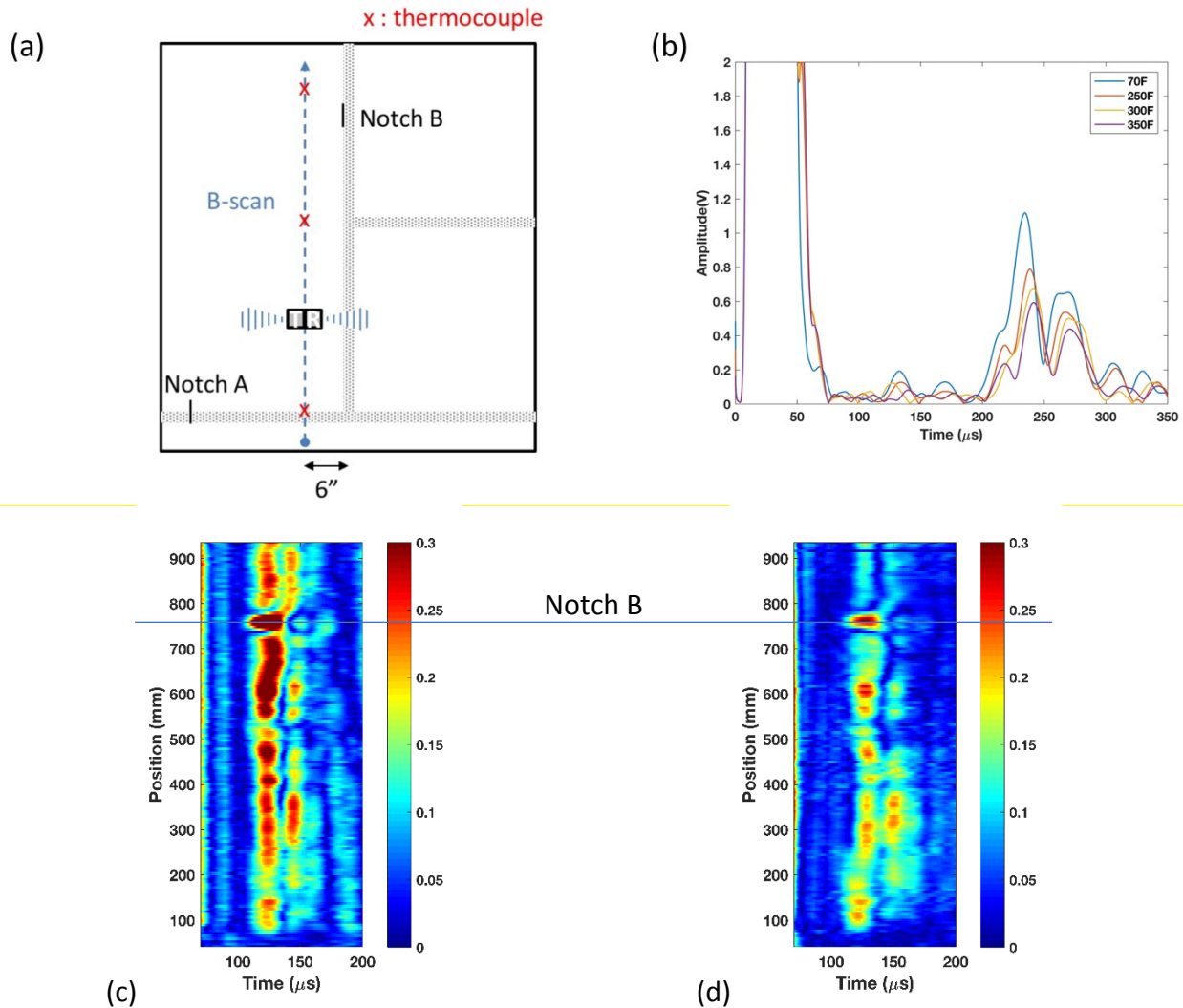
Figure 2.2.35. (a) Schematic of the B-scan setup, (b) Hilbert transformed A-scan signals collected for the different temperatures, (c) B-scan at 70F, and (d) B-scan at 350F. Identified temperature is at a height of 533 mm (21").

Figure 2.2.35b shows the Hilbert transform of the A-scans taken for the all temperatures at a height of 533 mm (21"). The peaks between 100-150 μs indicate the weld echo and its amplitude decreased from 0.19 V to 0.08 V as the temperature increased from 70F to 350F. The decrease in amplitude is due to the effect of temperature on the EMAT magnets as well as the change in the stainless steel shell. Additionally, the end-wall echo peaks between 200-250 μs illustrate the decreasing wave speed with temperature associated with the decreasing shear modulus. The B-scan results are provided in Figures 2.2.35c and 2.2.35d for 70F and 350F, respectively. It is apparent that the EMATs with N40UH magnets can detect notches in the weld at temperatures up to 350F. In fact, at elevated temperature it is easier to distinguish the notch echo from the weld echo than it is at room temperature.

2.2.9 Results on Holtec MPC

2.2.9.1 Measurement of magnetic force between EMATs and MPC surface

While we conducted various tests on the MPCs (Holtec multipurpose canister) at Holtec Manufacturing Division (HMD), one important observation was the unexpected significant magnetic force between the EMATs and the MPC shell. The MPC that we tested was constructed of 304L austenite stainless steel. The shell is 0.5" thick and was welded to a baseplate. The MPC had two full height axial welds, but no circumferential weld. All weld caps had been ground off and the interface between weld and base metal was difficult to see by eye, which in fact motivated us to check the magnetic forces at several key spots around the MPC surface using a hand-held neodymium magnet. In descending order the magnetic forces were: the axial weld, the shell, the bottom weld, and the baseplate. An interesting observation was that the bottom weld was less magnetic than the shell, while the axial weld was more magnetic than the shell. The magnetic force between EMATs and MPCs is a critical factor that affects the EMAT retraction mechanism being developed by the delivery team. The retraction mechanism relies on the restoring force of spring coils, provided that the magnetic force is no greater than that of the coils. Accordingly, we measured the force between the EMATs and the MPC shell as shown in Fig. 2.2.36.
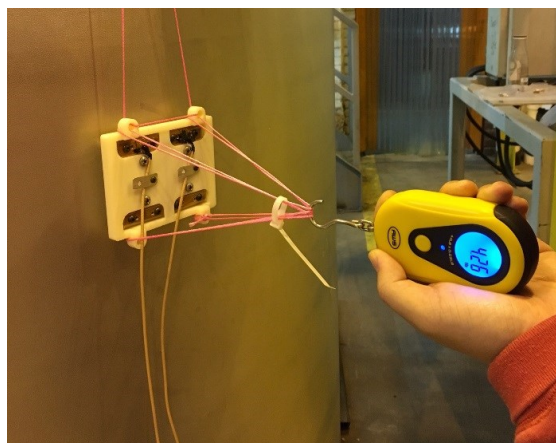
Figure 2.2.36. *Measurement of the magnetic force between the EMATs and the MPC shell. The maximum measured force at several spots was 5 lbs.*

While the EMATs were stuck to the MPC surface, we slowly increased the normal force to the EMATs and recorded the maximum reading before they separated. In order to gain confidence in the measurement, we tried a number of times at several spots. The recorded values varied from 3.5 to 5.0 lbs, which is a significant amount of force considering the fact that the MPC is austenitic stainless steel, which is known to be nonmagnetic. Based on literature review and discussions with professional colleagues, the force is due to a small portion of the austenite phase being transformed into martensitic during plastic deformation associated with the rolling operation. The γ-austenitic phase is intrinsically non-ferromagnetic and it dominates in austenitic stainless steel as the name suggests. However, when it is subject to tensile plastic strain, γ-austenitic phase can transform to α-martensitic phase especially at the places where slip bands prevail. The α-martensitic phase is known to be more ferromagnetic than the γ-austenitic phase. Due to this magnetic property mismatch, quantitative martensitic phase analyses are often conducted by measuring the magnetic field. Therefore, the martensitic phase could develop near the outer surface during rolling and it could introduce magnetism. Conservatively, we assume that the deformation induced magnetism is common for all canisters (even though it is not exhibited by the mockup at Penn State, which was also fabricated by Holtec). In order to overcome the challenges posed by this new finding, the delivery team developed a new EMAT extension and retraction mechanism.

2.2.9.2 Evaluation of weld echoes at incremental distances

The second test we conducted during the HMD visit was evaluating ultrasonic echoes from the axial weld at incrementally larger distances. This test aimed to determine from how far away the EMATs could be from the axial weld to locate it. As shown in Fig. 2.2.37, at a given height from the bottom, the EMATs were initially placed at 102 mm (4") away from the axial weld and repositioned up to 1016 mm (40") away in 51 mm (2") increments. At each position, fifty pulse-echo measurements were made and the obtained waveform signals were averaged (i.e. time synchronous averaging) to reduce background noise, which resulted a high signal-to-noise ratio. In total 19 averaged A-scan signals were acquired at each height. We examined four different heights to capture the variation in weld echoes.
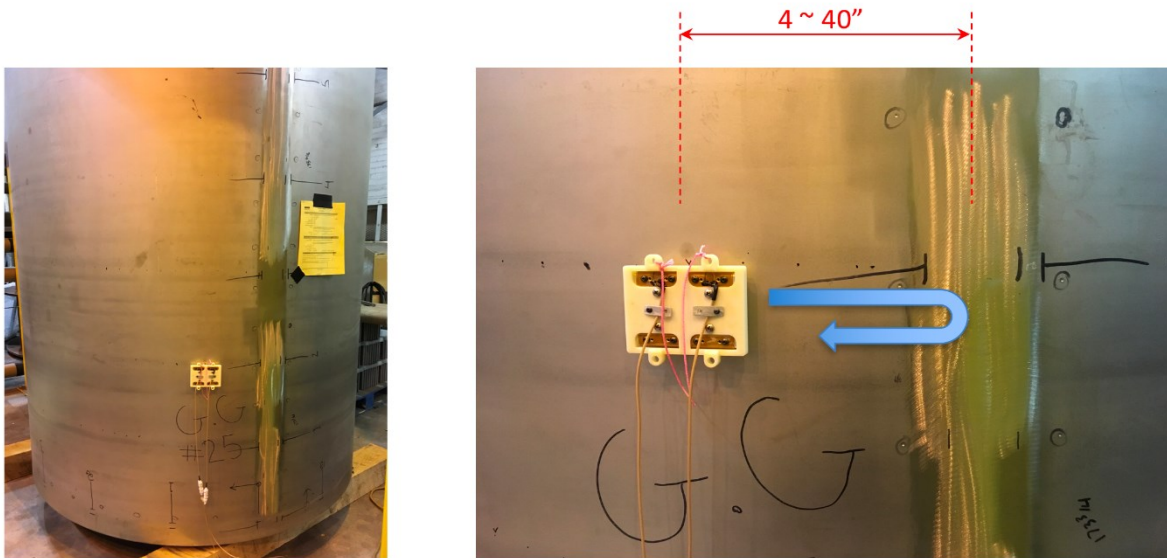
(a)   (b)

Figure 2.2.37. *(a) The EMATs stayed in contact with the MPC by the magnetic force, (b) the EMATs took pulse-echo measurements from the axial weld at distances from 102-1016 mm (4-40").*

Figure 2.2.38 shows 6 averaged A-scan signals obtained at a height of 1.346 m (53"). Clearly, we were able to identify an SH1 mode echo from the axial weld. The arrival time of the SH1 mode increased linearly with the setback of the EMATs. The measured group velocity was 2.93 mm/usec, which is very close to the theoretically calculated value, 2.85 mm/µs. Because the parameters relevant to pulse generation and reception, e.g. the pulse generation duration and delays, will be constant during an inspection, it should not be too difficult to locate the axial weld from the sensor car.
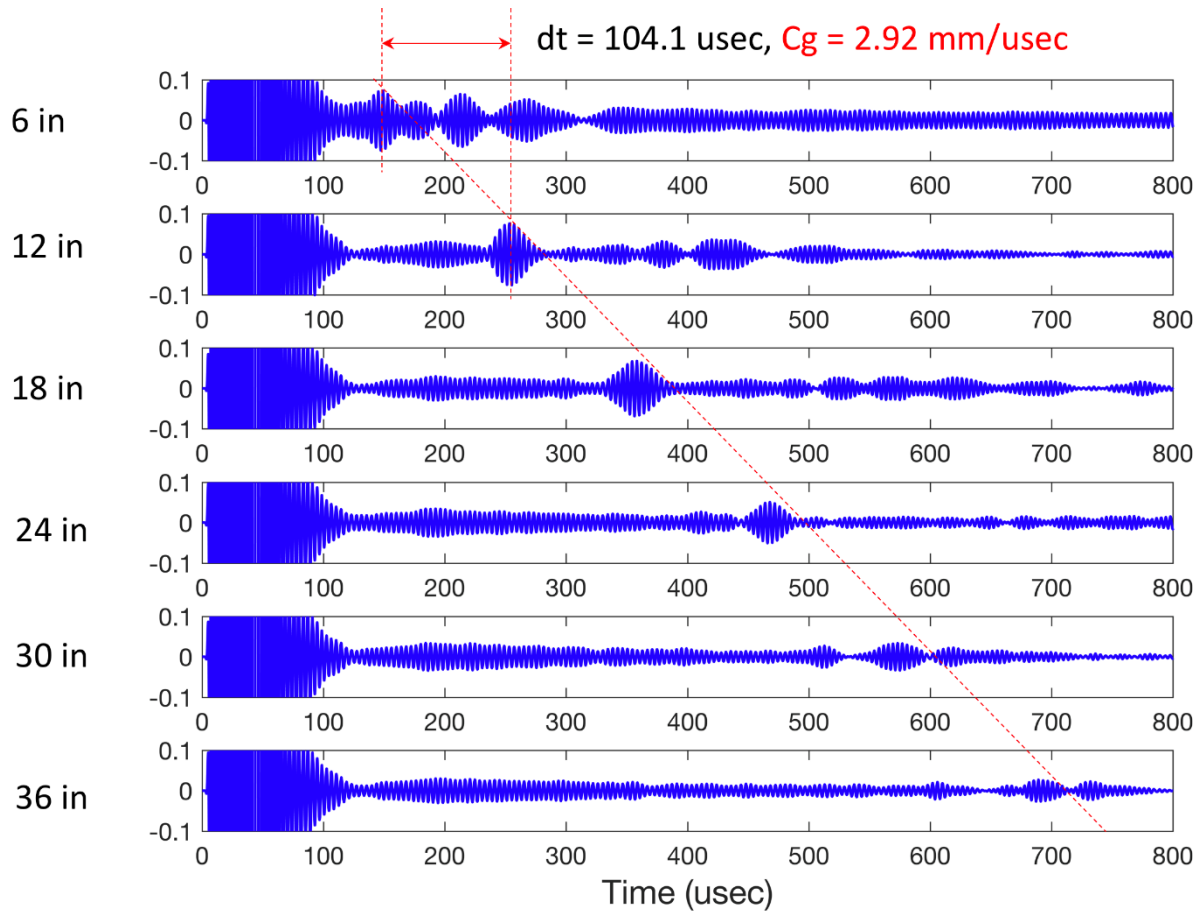
Figure 2.2.38. *A-scan waveforms taken at distances ranging from 152-914 mm (6-36") from the axial weld. The SH1 mode is identified by a red dashed line.*

However, it should be noted that there exists variation along the axial weld. Figure 2.2.39 shows two A-scan waveform signals taken from different heights (1.016 and 1.346 m) but the same 457 mm (18") distance from the weld. The peak amplitudes of the returning SH1 mode differed by approximately 50%. Assuming negligible differences in the other conditions relevant to EMAT measurements, this difference is attributed to variability in the weld fusion process. The variability in weld echoes is better highlighted in B-scans shown in Fig. 2.2.40. Each B-scan is constructed by stacking all the A-scan signals so that the horizontal axis and the vertical axis of the plot indicate the time and the circumferential distances, respectively, while the colormap represents the intensity of the Hilbert transformation. As indicated by the arrows the extension of the returning SH1 mode is quite different one from the other. At the 1.346 m height, the weld may be identified 711 mm (28") away, while at the 1.016 m height it may only be identified within 457 mm (18"). However, both of these are sufficient, as we only need to find it within 357 mm (14") of the weld.

(a)   (b)
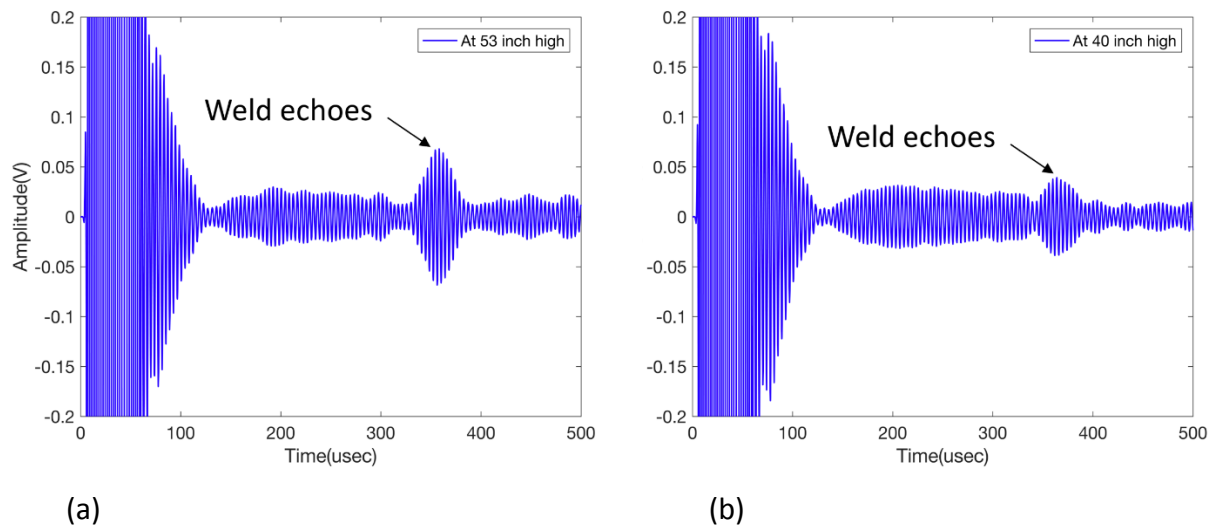
Figure 2.2.39. *A-scan signals for EMAT 18" from axial weld: (a) 1.346 m (53") height, (b) 1.016 m (40") height. The weld echo amplitude varies by roughly 50%.*

(a)   (b)
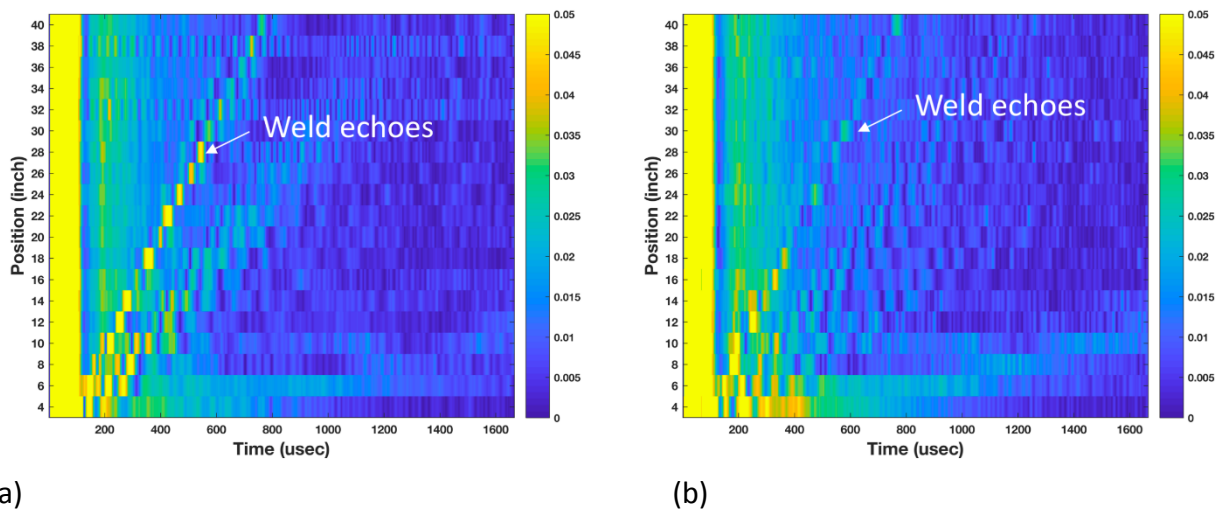
Figure 2.2.40. *B-scans showing axial weld echoes at heights of (a) 1.346 m (53") and (b) 1.016 m (40").*

A-scans were recorded for much longer durations to determine whether SH waves traveling around the circumference of the canister are measurable. Figure 2.2.41 shows that the wrap-around signals from the SH0 and SH1 wave modes are apparent for 4 laps around the canister. While the wrap-around signals are apparent, no weld echoes are seen in the A-scans recorded at three different axial positions, thus indicating that most of the wave energy is transmitted through the weld, rather than reflected by it. Further study would reveal whether scattering from SCC is sufficient for crack detection.
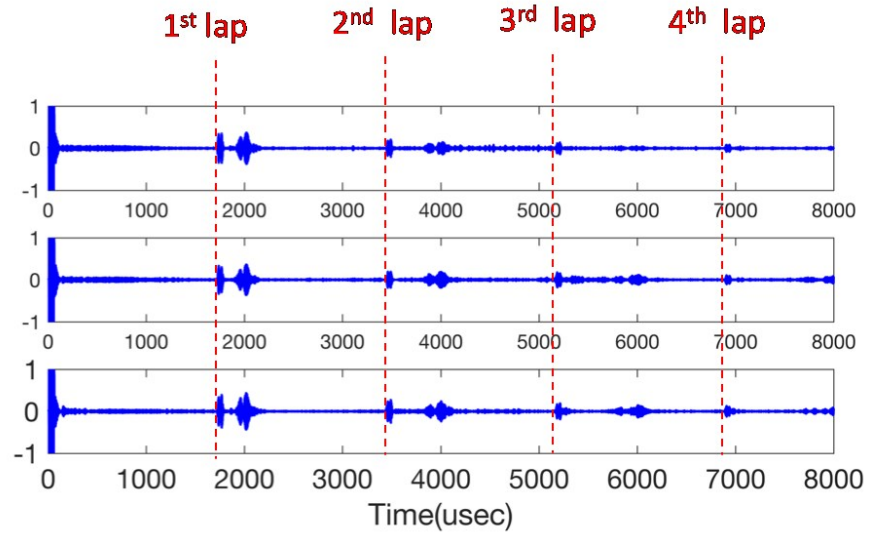
Figure 2.2.41. *SH0 and SH1 waves travel around the MPC circumference many times.*

2.2.10 Results of Blind Tests on Canister Mockup

This section describes benchmarking the EMATs. Testing is conducted on welded stainless steel mockups containing artificially implanted defects at the Pacific Northwest National Laboratory (PNNL). The defects are intended to be representative of stress corrosion cracks. The first mockup is a welded plate with crack-like defects implanted by a localized thermal fatigue process intended to create branched cracks. The second mockup is full-diameter partial-height cylinder implanted with closed crack-like defects. The inspection of the cylinder was done in a blind fashion, i.e., the inspector did not know where the defects are located. Test results were assessed by PNNL personnel who know where the defects are located.

Guided waves were selected for nondestructive inspection of cracks in the canister for a number of reasons:

- they enable full volumetric inspection of weld lines even though access to many of the welds is blocked by guide channels inside the overpack;
- shear horizontal (SH) guided waves are 3-dimensional, making possible detection of cracks oriented parallel, as well as perpendicular to the wave vector direction;
- SH waves are efficiently generated and received by electromagnetic acoustic transducers (EMATs), which are noncontact devices that are well-suited for robotic inspection and are comprised of materials that tolerate elevated temperatures and gamma radiation.

While guided wave inspection of pipelines is becoming more common, and standards for the use of guided wave technology are under development for the American Society for Nondestructive Testing (ASNT), it will be very beneficial to benchmark the capability of the robotic inspection system for crack detection relative to more conventional techniques such as bulk wave ultrasonics and eddy current methods. Initially, we planned to do this benchmarking on standard specimens with artificial defects due to the lack of realistic samples for dry storage canisters. However, during the course of the project our colleague Ryan Meyer at Pacific Northwest

National Laboratory (PNNL) acquired a full diameter partial-length mockup of a canister given financial support from the NRC. We received permission to reallocate some of our project funds to seed realistic defects into this canister mockup with the intent of using it to assess the effectiveness of the robotic inspection system that we are developing. After our project is completed it will remain valuable to the community for assessment of other inspection systems and methods as they develop.

A meeting was held at EPRI in Charlotte on June 14, 2016 to plan the implantation of defects in the mockup structure. Stress corrosion cracks (SCC) in stainless steel typically exhibit branching and can be intra- or trans-granular or both. EPRI reactor experience is that SCC are tightly closed. Meeting participants agreed that simulation of branched and closed cracks of controlled length is extremely difficult, risky, and expensive. Therefore, the consensus decision was made to focus on closed cracks of controlled length and depth without branching. A vendor was contracted to implant closed cracks into the canister mockup in the heat affected zone of the weld lines. The cracks are to have a range of sizes, a 2:1 length to depth ratio, and are oriented either along the weld or transverse to it. Since the cracks are tightly closed they are not visible by eye. Therefore, blind nondestructive testing is possible and PNNL/NRC would like to keep the flaw locations, orientations, and sizes secret so that the mockup can be used repeatedly for blind tests to provide a rigorous test of nondestructive inspection transducers, instrumentation, and methods. Therefore, in this report the flaw specifics are not provided.

PNNL also has a flat plate with a weld having seeded flaws of various sizes that were created using a thermal fatigue procedure that results in branched cracks. These cracks are not closed and sizes and locations will be divulged.

2.2.10.1 Test Structures

Welded Plate

A photo of the welded plate structure with thermal fatigue cracks is shown in Fig. 2.2.42. The nominally flat 304 stainless steel plate is 0.5" thick by 24" long and 16.75" wide. The weld is located 6" from the left edge of the plate. The cracks are located in the weld fusion line on the right side of the weld and are 0.185", 0.275", 0.500", and 0.800" long. These cracks are 20, 30, 50, and 80% through the wall thickness respectively. The bottom crack tip of each crack is located 3.125", 6.385", 9.635", and 13.135" from the bottom of the plate, respectively.

Canister Mockup

The shell shown in Fig. 2.2.43 mocks up the dry storage canister used in the NUHOMS (horizontal axis) cask. It is 68" in diameter and 60" long, and was fabricated by the vendor who makes the real canisters. There is a full circumferential weld and two axial welds (48" and 12" long) that are ground flush. A stiffening ring has been added to each end to provide stability. The canister is positioned with its axis in the vertical direction and circumferential weld near the top as shown in Fig. 2.2.43 in order for us to simulate inspection of a vertical axis HI-STORM cask with our robotic inspection system. In addition to the implanted (closed crack) defects there are four EDM notches in the vicinity of welds: 0.5" and 0.125" long perpendicular to, and along the short axial

weld respectively, and 0.125" and 0.5" long perpendicular to, and along the circumferential weld, respectively.
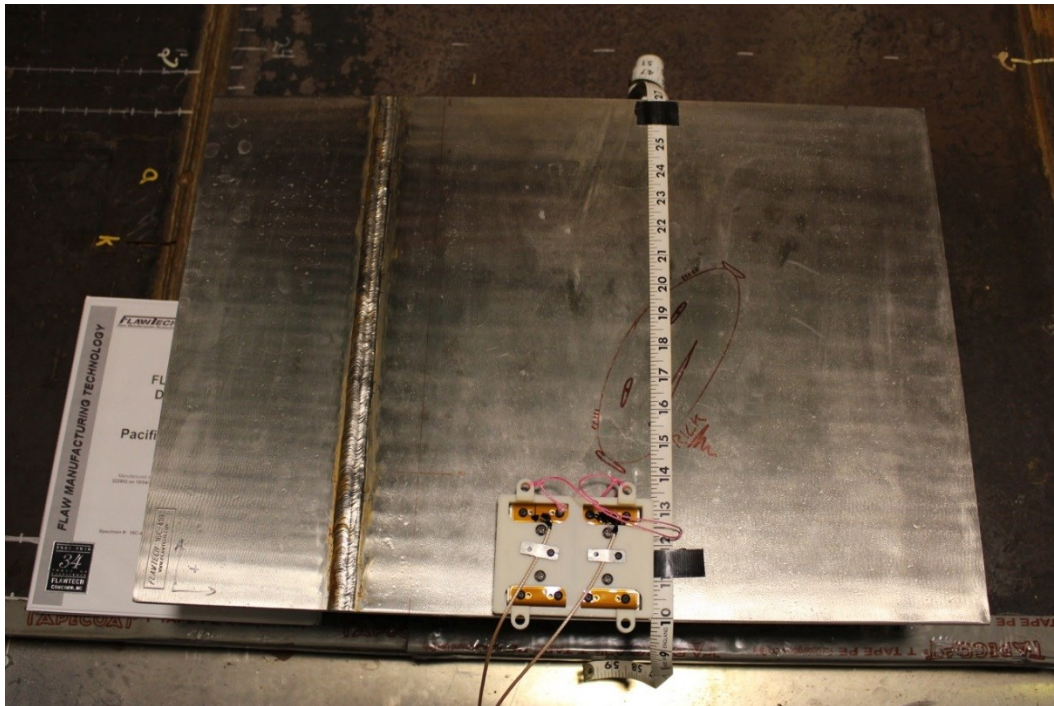
Figure 2.2.42. *Stainless steel plate with weld and thermal fatigue induced cracks in HAZ.*

Figure 2.2.43. *Full-diameter partial height canister mockup with EMAT pair on the right side of the 4 ft long axial weld.*

2.2.10.2 Electromagnetic acoustic transmitters (EMATs) and instrumentation

The EMATs and instrumentation are described in Section 2.2.5. The robotic inspection system was not brought to PNNL, but an arduino-controlled stepper motor was setup to accurately position the EMATs and automate data acquisition. The bracket is suspended by a yoke connected to a tracked rubber cable that extends over the gear of the stepper motor and then supports a counterweight hanging inside the canister. A bubble level is used to ensure the bracket is straight as shown in Fig. 2.2.44. Unfortunately, the stepper motor generated electrical noise that ruined the EMAT signals even though the system worked fine on the Penn State mockup. Therefore, the EMATs were positioned manually by turning the stepper motor gear 45 degrees, which corresponded to 5 mm.
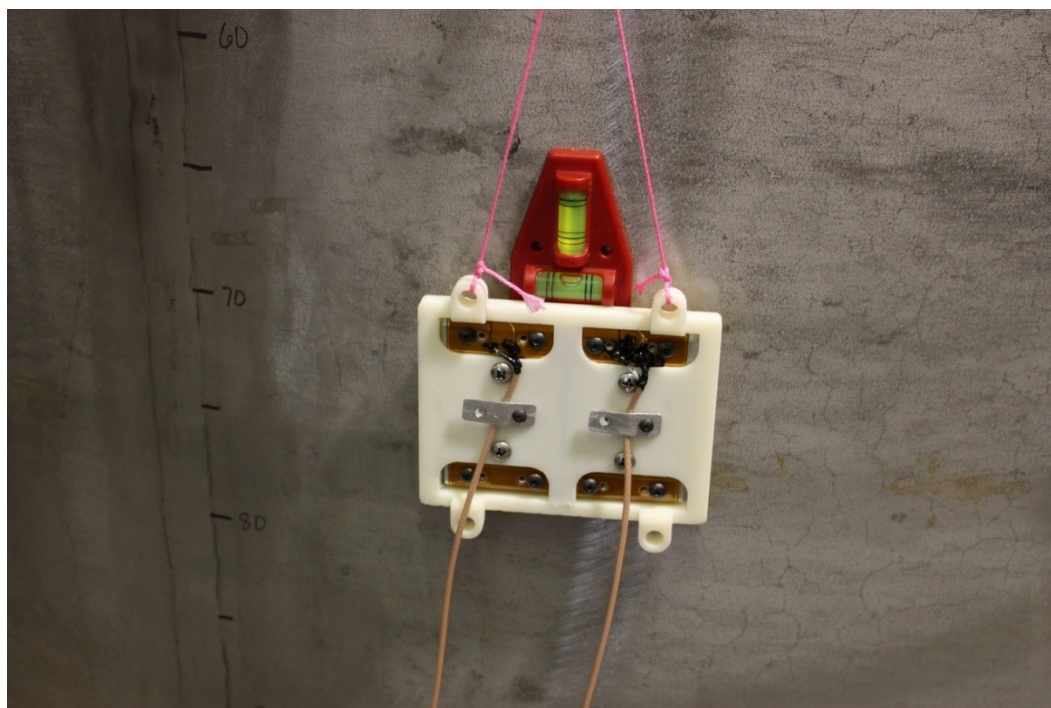
Figure 2.2.44. EMAT pair in mounting bracket for robotic inspection system.

2.2.10.3 Inspection Methodology

Welded Plate

Due to the limited size of the plate the EMAT bracket was scanned only along two different lines. Scans were made by moving the EMAT bracket in 0.25" increments as measured by a ruler placed adjacent to the EMAT bracket. Altogether, 3 scans were made; the first used a flexible ruler (see Fig. 2.2.42) that could not be used as a straight edge for EMAT movement, so that inspection was repeated with a steel ruler as a guide. The centerline of the EMAT pair was first 6.5" and then 16" from the weld centerline. For each scan, a B-scan can be compiled from the 55 A-scans acquired. For robotic inspections the EMATs are designed to be flush with the surface (i.e., zero liftoff), therefore the EMAT bracket is designed for the canister curvature. For the EMATs to function properly on the nominally flat plate, pressure was applied to the back of the bracket to push the EMATs flush with the plate surface. Inevitable finger pressure variations result in amplitude

variation of the received waves. This amplitude variation can be eliminated by normalizing the A-scan with respect to the backwall echo of the SH1 mode. When the EMATs are at 6.5" the echoes from each backwall arrive at nearly the same time, but when the EMATs are at 16" the echo from the backwall near the EMAT arrives when the electromagnetic interference is present (and thus is not observed).

Canister Mockup

While the flaw locations in the mockup are known to PNNL, they were unknown to the Penn State team. It was decided in advance to conduct the inspection blind, i.e., without knowing where the flaws were implanted. Therefore, the developed canister NDI methodology could be followed. In a 0.5" thick stainless steel plate two modes will propagate: SH0 and SH1. The wave structure of the SH1 makes it the dominant mode.

Canister NDI will entail (1) creating a B-scan along the axial welds and (2) assessing A-scans acquired from the 16 gaps between guide channels inside the HI-STORM 100 cask. For the canister mockup the EMATs are moved in 5 mm (~0.2 in) increments along the axial welds and across the circumferential weld.

The nondestructive inspection of the canister included:
- 443 A-scans along the 48" long axial weld;
- 93 A-scans along the 12" long axial weld;
- 192 A-scans from 8 positions along the circumferential weld (35 cm (~13.8 in) apart, except at the 48" axial weld), see Fig. 2.2.45;
- EMAT bracket was rotated 90 degrees in order to send waves in the axial direction at selected locations;
- The duration of the A-scan was increased to 9500 µs in order to record wrap-around signals at six different locations;
- The EMAT bracket was moved progressively further from the axial weld to assess from how far away the axial weld can be located.
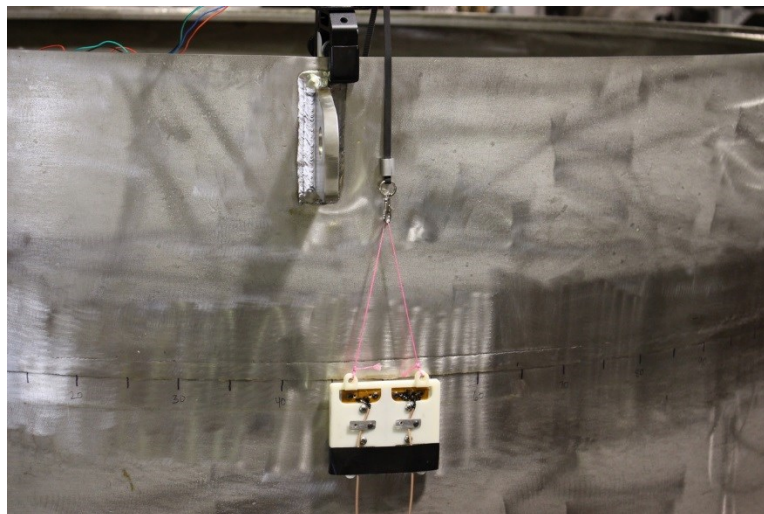
Figure 2.2.45. EMAT mounting bracket positioned below the circumferential weld.

2.2.10.4 Results

The inspection results are shown in Milestone M3 report. In order for the mockup to remain usable for future blind testing as planned, the locations of 'indications' are not reported herein. The detailed findings have been sent to PNNL in order for the inspection accuracy to be assessed. The term 'indications' is used to describe what are believed to be echoes from the implanted flaws.

An example defect indication is shown in Fig. 2.2.46. The indications are summarized in Table 2.2.2, which has been edited from a data sheet containing detailed location information. There are some important points regarding the inspection:

1. Inspection time was very limited. The inspection was planned to take two days, but setup was delayed by the equipment inspection, which took place later than scheduled. Time was lost trouble-shooting the problem with electrical noise from the stepper motor intended to automate measurements. Ultimately, manual measurements were made, which required more time to acquire data. Therefore, we were not able to inspect all of the circumferential weld line. We did inspect the full length of both axial welds.
2. Some of the implanted flaws may have been smaller than the threshold size for which the EMAT inspection system was developed. Our functions and requirements document specifies that semi-elliptical EDM notches larger than 0.42" by 0.21" be detected.
3. Sending SH waves in the axial direction would have provided redundancy and improved the confidence level of whether an indication is a flaw.
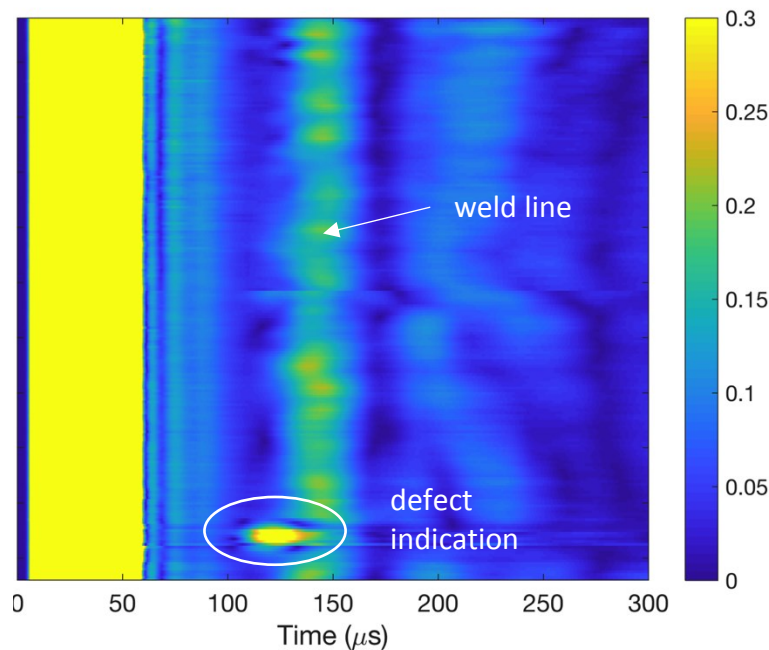
***Figure 2.2.46**. B-scan along weld showing a clear defect indication.*

Table 2.2.2. *Blind test results on DSC mockup.*

Defect No	Amp dB	Comments
1	20.1	The indication is received from outside the weld metal, but in the heat affected zone (HAZ). The large signal-to-noise ratio (SNR) suggests that this is a crack parallel to the weld line. An indication is received from three different B-scans. CONFIDENCE LEVEL: High
2	8.1	Relatively weak indication obtained from one B-scan; if this is a defect, it is in the HAZ outside of the weld metal. Most likely, this possible defect is oriented transverse to the weld. No redundant data are available. CONFIDENCE LEVEL: Moderate
3	13.3	Relatively weak indication obtained from scans taken from both sides of a weld. There are also indications from other scans. The indications are low and positions do not exactly coincide, but since six A-scans indicate that there could be a defect at this location it would be helpful to send waves in the axial direction to gather more information. CONFIDENCE LEVEL: Moderate
4	20.0	There are multiple indications of this defect from scans taken in both circumferential and axial directions. One of the indications has a high SNR that suggests a crack oriented transverse to the weld line. CONFIDENCE LEVEL: High
5	25.2	Scans from both sides of the weld line exhibit strong weld reflections, although the reflection varies along the weld line. One (or more) of these indications could be a defect in the weld, but there is a reasonable probability that this large weld echo is just variability in the weld. CONFIDENCE LEVEL: Moderate
6	8.6	A scan along the circumferential weld line contained an echo that could be a defect. The fact that another scan of this same region from a different location does not indicate this defect, makes it more likely that the indication in question is not a defect. CONFIDENCE LEVEL: Low
7	10.0	Indications from two scans along the circumferential weld enable locating the possible defect. CONFIDENCE LEVEL: Moderate
8	13.3	Two scans along the circumferential weld indicate this potential defect is located in the HAZ above the weld. CONFIDENCE LEVEL: Moderate

The blind inspection results are:
- Detected 100% of flaws larger than our threshold
- Detected 50% of flaws near the threshold
    - However, we mis-located one
    - One flaw was indicated, but not identified as a flaw because we had to re-position the EMATs, but did not go back and acquire new data
- Detected 50% of flaws smaller than the threshold
- Detected 50% of flaws much smaller than the threshold

Lessons learned/confirmed:
- Cracks oriented parallel to the SH wave vector are more challenging to detect
- Redundancy is highly desirable
- Prefer to send waves in both circumferential and axial directions (and/or add EC array sensor)

2.2.10.5 Conclusions

Nondestructive inspection methods to detect stress corrosion cracking in canisters that store spent nuclear fuel were conducted on a canister mockup at PNNL. The pulse-echo mode of inspection using electromagnetic acoustic transducers was used in the same way that is made possible by a robotic delivery system (i.e., the PRINSE system – proactive robotic inspection of nuclear storage enclosures system being researched/developed/designed in our NEUP Integrated Research Project) for dry storage casks at an independent spent fuel storage installation. The robotic inspection system is designed to be capable of inspecting 100% of the weld lines in the canister by using shear-horizontal waves. The blind inspection of the canister mockup at PNNL revealed 8 indications of possible flaws, none of which were visible by eye. Based on the signal-to-noise ratio of the indication, and sometimes redundant data, a confidence level of High/Moderate/Low was assigned to each indication. In the near future PNNL will fingerprint the mockup to characterize the implanted flaws, and once this is completed we will issue an addendum to this report that assesses the accuracy of our inspection results.

2.2.11 PRINSE Deployment at Holtec HMD

The signals received by the EMAT are highly amplified, which makes electrical noise a potential issue due to the other electrical components in the robotic inspection system and other nearby systems in the field. Electrical noise problems occurred during field testing at the Holtec Manufacturing Division (HMD) and had to be solved, because the EMAT signals were completely overwhelmed by the noise.

Within a laboratory environment at Penn State, the canister NDI and delivery teams conducted an in-depth investigation on the instrumentation of the entire equipment and circuitry. The first tests confirmed that the noise levels observed in the field could be repeated in the lab environment, with the same amplitudes, by operating heavy equipment around the equipment. It was found that the noise sensitivity was high enough that measurements would be unusable without noise correction, even without heavy equipment in nearby operation.

The noise investigation first examined whether electromagnetic coupling along the length of the tether was allowing cross-wire communication from one device to another within the tether. By removing the EMAT cables from the tether completely, it was found that noise would still occur even with the EMAT cables in isolation from the rest of the system. Even so, the coax cables were rerouted in twisted-pair fashion to prevent this noise type from interfering in the future. We also installed a ferrite clamp on the receiving cable to further reduce EMI noise that may be traveling along the conductor of the EMAT wiring.

The lack of inter-wire interference sources suggested that the noise source was due to the use of multiple grounding locations within the overall system. The problem was correlated to the operation of the winch motors, and it was determined that high energy EMI generated by the switched-mode control of the motors needed to be properly shunted to ground to prevent interference on the EMAT signal ground. Implementing a star grounding scheme using the DAQ as the star point accomplished this. Thus, all electrical signals within the entire delivery system are referenced from the ground of the EMAT measurement. This choice was made because the signal ground used by the EMAT amplifiers is hard-wired to the instrumentation casing, which is connected to earth ground.

The approach of using the star-grounded system immediately attenuated nearly all noise on the system, to a level nearly identical to using the EMATs independently of the robotic delivery system. Thus, to suppress the noise, an additional grounding wire was run in each of the three tethers (car train, winch plate, insertion arm frame) to provide the ability to connect each of the three subsystems to the grounding terminals of the NI system. This additional grounding circuit greatly contributed to the noise reduction, allowing very clear measurements from the EMAT in all tests thereafter. Moreover, when the connections to this grounding point were intentionally broken, the noise could be immediately repeated at levels equivalent to the HMD tests, suggesting that this noise path was the primary issue discovered at HMD.

2.2.12 PRINSE Deployment at Test Track
A-scan and B-scan of notches

We successfully demonstrated remote EMAT delivery and detection of machined notches in the presence of invited guests during the final live demonstration at Test Track. For this testing, the EMATs having N52 grade magnets and a 5/8" thick aluminum housing were installed into the first sensor car. The delivery system was equipped with the noise suppression measures discussed in the previous section. The LabVIEW VI communicated with the master robot OS via a network cable so that it can obtain synchronized time stamps and the winch motor encoding information for precise positioning. Figure 2.2.47 shows a photo of the sensor cars deployed onto the steel canister mockup during the demonstration.

Figure 2.2.47. *The sensor cars deployed onto the stainless steel canister mock up during the final technology demonstration at Test Track.*

For demonstrating the ability of the EMAT system to detect stress corrosion cracking (SCC), we created two semi-elliptical notches in the canister mockup that was fabricated by Holtec. Figure 2.2.48a shows the locations and orientations of the notches in the heat affected zone of the welds and the EMAT scan path. The sizes of Notch A and Notch B are 0.781" x 0.135" and 0.864" x 0.133" (length x maximum depth) respectively. Notches A and B are located in the heat affected zone of the axial weld and the bottom weld respectively. Notch A passes through the weld metal and the shell, while Notch B is along the fusion line between the weld metal and the shell. These locations and orientations are what is expected from potential SCC. B-scans were obtained along the vertical path indicated in Figure 2.2.48a. The path was chosen to demonstrate the real inspection capability of guided waves (SH waves) sent and received by the EMATs, and that they are able to interrogate both sides of the sensor car. It was also intended to separate anticipated notch echoes from the end-wall echoes, which will not exist in a real canister because it is a closed cylinder. A post-processed B-scan of the collected data during the demonstration is shown in Figure 2.2.48b. Both Notch A and B were detected by the received echoes shown in Figure 2.2.48b. Note that the travel distances marked on the y-axis were acquired from the winch motor encoder via the robot OS network. In this single scan, the NDI system interrogated more than 525 in^2 and detected the defects located along two different weld lines.

Figure 2.2.48. *(a) Schematic of remote EMAT measurement during the final technology demonstration at Test Track, and (b) a post-processed B-scan plot of the EMAT inspection data.*

2.3 Nondestructive Inspection (NDI) of Concrete Overpack

Two different approaches for nondestructive evaluation (NDE) of horizontal and vertical types of concrete overpack systems are developed. A fully contactless air-coupled scanning ultrasonic test platform and a frequency-wavenumber (f-k) domain data analysis method are proposed for horizontal concrete overpack systems. Analysis, numerical simulation and experimental results demonstrate that distributed cracks in concrete can be detected and cracked regions localized within a scanned region of concrete. In a separate effort, a semi-coupled test platform and a guided wave attenuation-based data analysis method are proposed for vertical overpack systems. Analysis, numerical simulation and experimental results show that the bonding conditions of steel-concrete interfaces can be quantitatively characterized using the proposed guided wave signal analysis scheme.

2.3.1 Background and objective

Dry storage systems (DSS) for spent nuclear fuels, which had originally been designed for relatively short term interim use, are expected to be in service much longer than for what they were initially designed. The Nuclear Regulatory Commission (NRC) has identified concrete degradation in overpack systems as one of the potential issues for safe long-term storage of spent nuclear fuels [1]. The vertical and horizontal overpack systems are subjected to a variety of damage mechanisms and environmental loads, resulting in possible deterioration during their service life.

Vertical overpack systems are typically steel-clad concrete structures, where a steel cladding layer is directly attached to an underlying concrete bulk. Chloride ingress and carbonation of concrete can cause corrosion of the steel cladding layer [2,3] and other mechanisms, for example freezing-thawing cycles and alkali-silica reactivity (ASR) can lead to deterioration of the underlying concrete [2]. A combination of repeated exposures of degradation mechanisms can result in disbond damage of the steel-concrete interfaces. Horizontal concrete overpack systems typically are bare concrete structures that are directly exposed to environmental loads and a variety of physical and chemical deterioration mechanisms such as freezing-thawing cycles, wetting and drying, and ASR [2,3]. As a result, distributed microcracking can initiate within the near-surface region of the concrete, and the damage manifests over the remaining service life unless properly repaired.

It is difficult to detect the potential damage that can initiate at sub-surface locations of vertical and horizontal overpack systems from the outer surface. Hence, the utility of visual inspection to concrete overpack systems is limited. The objective of this research is to develop NDI systems that can detect, characterize and visualize the damage in concrete overpack systems.

2.3.2 NDI system development for horizontal overpack systems

To develop an NDE system for horizontal overpack systems, analytical modeling, numerical simulation and experimental validation studies were carried out.

2.3.2.1 Fully contactless air-coupled scanning ultrasound measurement system

To obtain high-quality leaky ultrasonic surface wave signals from concrete elements, an eight-channel MEMS ultrasonic sensor array (MUSA) and signal conditioning (SC) circuit have been developed. Printed circuit boards (PCBs) for the MUSA board and the SC board are shown in **Figure 2.3.1(a)**. Eight individual MEMS ultrasonic sensor components (Knowles Acoustics, SPM0404UD5) are attached to the MUSA board. The MUSA board is stacked on the SC board.

The SC board comprises of a power supplying unit, DC removal filters, and pre-amplifying units. The power supplying unit has a voltage regulator that provides stable 3.3 V and is connected with a 3.7V Li-Po battery. The regulated DC voltage (3.3 V) is provided to the MUSA board and the SC board. The DC removal filters are the first-order RC high-pass filters with the cut-off frequency of 500 Hz that is far below ultrasonic frequencies of interest. Pre-amplifying units have two-stage operational amplifiers with gain-adjusting resistors. The nominal gain is set to be 10 at each step so that the total gain becomes 100 times.

An automated two-dimensional scanner has been configured (**Figure 2.3.1(b)**) for rapid collection of a large number of ultrasonic data. The scanning system is based on stepper motors that are controlled electrically using GRBL firmware. The speed of scanning operation and spatial resolution are adjustable and various scanning patterns can be achieved. To achieve a certain scanning pattern, a text-based code is generated and sent to the controller using Universal G-code installed on a controlling computer. The developed sensor boards are integrated into the automated scanner.
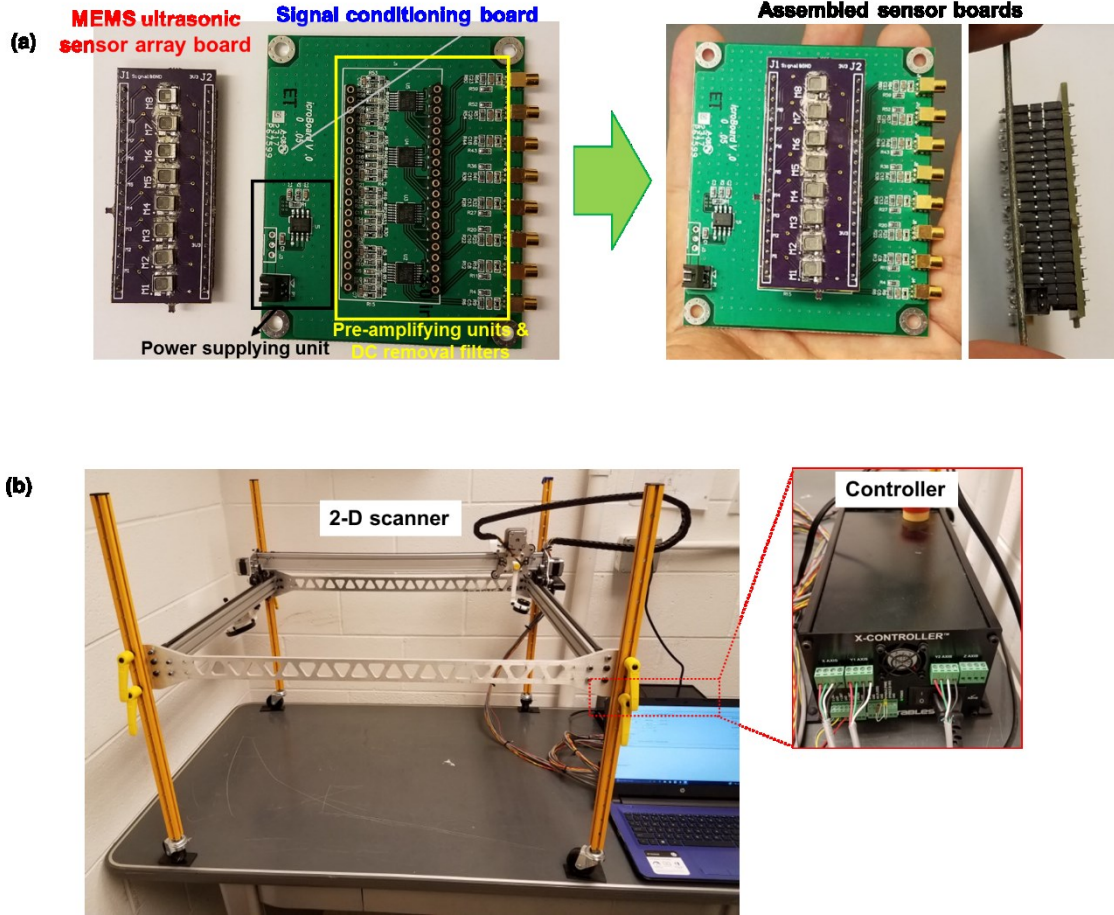
Figure 2.3.1. *The developed ultrasonic scanning system: a) MEMS ultrasonic sensor array board and signal conditioning board and b) motorized scanner and controller unit.*

2.3.2.2 Data analysis method: extraction of crack-induced multiple and local scattering components

A frequency-wavenumber (*f-k*) domain signal filtering technique was developed to enhance the detection of cracking damage in concrete. The overview of the signal processing procedure of the proposed approach is illustrated in **Figure 2.3.2**. Once the raw surface wave time signal set $s(t,x)$ is obtained through scanning measurements, a 2-D discrete Fourier transform (FT) is applied to convert the signal set from *t-x* to *f-k* domains

$$\bar{S}(f,k) = \int_{-\infty}^{\infty}\int_{-\infty}^{\infty} s(t,x)e^{-i2\pi(ft+kx)}dxdt, \tag{2.3.1}$$

where $\bar{S}(f,k)$ is the converted *f-k* domain surface wavefield. Then, $\bar{S}(f,k)$ is decomposed into incoherent scattering $\bar{S}_{ISC}(f,k)$ and coherent forward propagating $\bar{S}_{FW}(f,k)$ wavefields by multiplying the filtering masks $M_{ISC}(f,k)$ and $M_{CF}(f,k)$ respectively through

$$\overline{S}_{ISC}(f,k) = \overline{S}(f,k) M_{ISC}(f,k) \tag{2.3.2}$$

and

$$\overline{S}_{CF}(f,k) = \overline{S}(f,k) M_{CF}(f,k). \tag{2.3.3}$$

Note that $M_{ISC}(f,k)$ includes the *f-k* region caused by local scatter from a single crack as well as incoherent multiple scatter from distributed crack regions. Hence, both single crack and distributed multiple cracks can be detected. The two decomposed wavefields are then re-converted into *t-x* domain using an inverse 2-D FT through

$$s_{ISC}(t,x) = \int_{-\infty}^{\infty}\int_{-\infty}^{\infty} \overline{S}_{ISC}(f,k) e^{i2\pi(ft+kx)} dk df \tag{2.3.4}$$

and

$$s_{CF}(t,x) = \int_{-\infty}^{\infty}\int_{-\infty}^{\infty} \overline{S}_{CF}(f,k) e^{i2\pi(ft+kx)} dk df. \tag{2.3.5}$$

Then, the time-cumulative energies to time T for both filtered wavefields, $E_{ISC}(x)$ and $E_{CF}(x)$ are obtained as

$$E_{ISC}(x) = \int_{0}^{T} \left[s_{ISC}(t,x) \right]^2 dt \tag{2.3.6}$$

and

$$E_{CF}(x) = \int_{0}^{T} \left[s_{CF}(t,x) \right]^2 dt. \tag{2.3.7}$$

Finally, the normalized scattering energy $E_N(x)$ is computed as:

$$E_N(x) = \frac{E_{ISC}(x)}{E_{CF}(x)}. \tag{2.3.8}$$
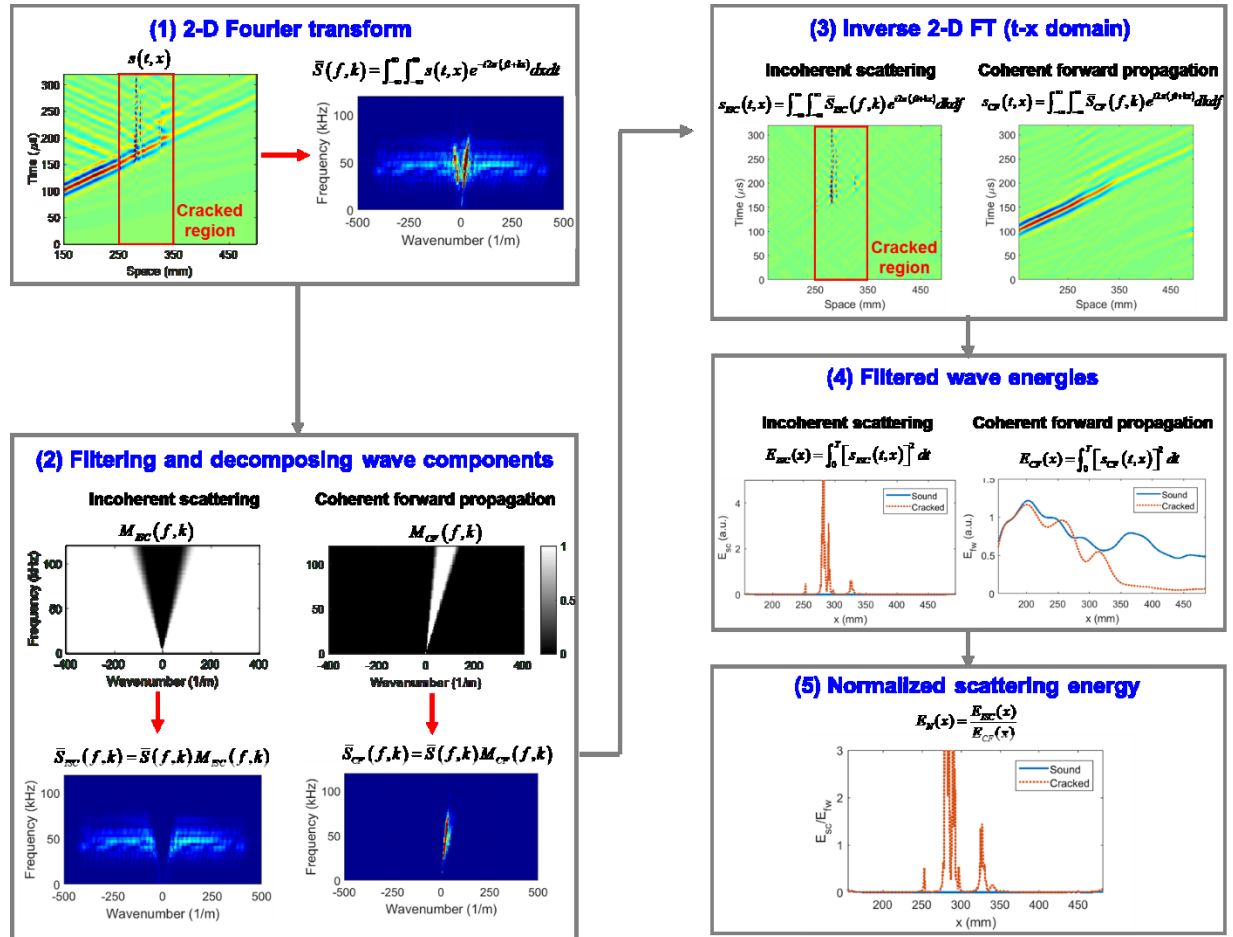
Figure 2.3.2. *Overview of the signal processing procedure to extract incoherent multiple scattering wave components and compute normalized scattering energy.*

2.3.2.3 Analytical modeling and analysis

To investigate the scattered wavefields set up by multiple scatterers, the analytical solution for a one-dimensional (1-D) multiple point scatterer model is created using Born series expansion. The 1-D model is illustrated in Fig. 2.3.3. The general 1-D equation of motion for a linear elastic medium is given by

$$\rho(x)\frac{\partial^2 u(x,t)}{\partial t^2} - \frac{\partial}{\partial x}\left[E(x)\frac{\partial u(x,t)}{\partial x}\right] = f(x,t), \qquad (2.3.9)$$

where $u(x, t)$ and $f(x, t)$ are the displacement field and the forcing function as a function of space ($x \in (-\infty, \infty)$) and time ($t \in [0, \infty)$), respectively, and $\rho(x)$ and $E(x)$ are the space-varying mass density and elastic modulus, respectively. Here, E is assumed to be constant throughout the entire spatial domain. The point-scatterers are modeled by locally reducing mass density with respect to the homogenous background mass density ρ, expressed as

$$\rho(x) = \rho\left[1 - \varepsilon\sum_{j=1}^{N}\delta(x - x_j)\right],$$ (2.3.10)

where ε ($0 < \varepsilon < 1$) is the density reduction factor that can have an arbitrary value between 0 and 1, $\delta(.)$ the Dirac delta function, x_j the position of the jth point-scatterer and N the total number of point-scatterers. Taking into account a time-harmonic concentrated force acting at $x = 0$, $f(x,t) = \delta(x)e^{-i\omega t}$, and substituting Eq. (2.3.10) into Eq. (2.3.9), the Green's function of the medium under harmonic loading, $G(x)e^{-i\omega t}$, is sought and the equation of motion is then expressed as

$$-\omega^2\rho G(x) - E\frac{\partial^2 G(x)}{\partial x^2} = \delta(x) - \omega^2\rho\varepsilon\left[\sum_{j=1}^{n}\delta(x - x_j)\right]G(x).$$ (2.3.11)

Here, the time-harmonic oscillation term with the angular frequency ω, $e^{-i\omega t}$, is cancelled out and the original partial differential equation reduces to the ordinary differential equation shown in Eq. (2.3.11). The first term on the right hand side in Eq. (2.3.11), $\delta(x)$, represents the concentrated force acting at $x = 0$ that sets up the incident wavefield $G_0(x)$. The second term on the right hand side introduced by the point-scatterers can be considered as the secondary forcing function that sets up the scattered wavefield $G_{sc}(x)$. Then, the full wavefield $G(x)$ can be expressed as the superposition of $G_0(x)$ and $G_{sc}(x)$.

$G_0(x)$ can be obtained by solving Eq. (2.3.11) without consideration of the secondary forcing term, given by [4]

$$G_0(x) = \frac{i}{2\rho c_0^2 k_0}e^{ik_0|x|},$$ (2.3.12)

where k_0 and c_0 are the wavenumber and wave speed respectively for the bare medium without scatterers expressed as ω/c_0 and $\sqrt{E/\rho}$. $G(x)$ is then obtained by taking the convolution integral of the force terms with respect to $G_0(x)$

$$G(x) = \int_{-\infty}^{\infty}G_0(x - \xi)\delta(\zeta)d\xi - \omega^2\rho\varepsilon\int_{-\infty}^{\infty}G_0(x - \xi)\left[\sum_{i=1}^{n}\delta(\xi - x_i)\right]G(\xi)d\xi.$$ (2.3.13)

Finally, the implicit solution is obtained by performing the integrations

$$G(x) = G_0(x) + G_{sc}(x)$$
$$= G_0(x) - \omega^2\rho\varepsilon\sum_{i=1}^{N}G(x_i)G_0(x - x_i)$$ (2.3.14)

Because of the implicit nature of Eq. (2.3.14), $G(x)$ can only be numerically computed by iteration. For a weak single scatterer case, the first iteration approximates $G(x_i)$ on the right hand side as

$G_0(x_i)$, which provides a good estimate of $G(x)$. This first order approximate solution is called the (first) Born approximation, which is given by

$$G_1(x) = G_0(x) - \omega^2 \rho \varepsilon \sum_{i=1}^{N} G_0(x_i) G_0(x - x_i).$$ (2.3.15)

However, the first order Born approximation does not take into account the interaction between each scatterer, and hence multiple scattering effects are neglected. In this study, a higher order Born series expansion is sought to consider the multiple scattering effects of the point scatterers.

The Mth order Born series expansion solution is given by

$$G_M(x) = G_0(x) - \omega^2 \rho \varepsilon \sum_{i=1}^{N} G_{M-1}(x_i) G_0(x - x_i),$$ (2.3.16)

where $G_{M-1}(x)$ is the $(M-1)^{th}$ order Born series expansion solution. Iteration is carried out until a convergent solution is obtained. Finally, the time-harmonic wavefield solution to Eq. (2.3.9) is obtained by multiplying the harmonic oscillator to the convergent solution

$$u(x,t) = G(x)e^{-i\omega t} = G_M(x)e^{-i\omega t}.$$ (2.3.17)
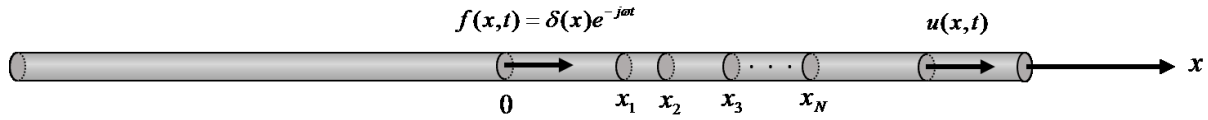
Figure 2.3.3. *Illustration of the 1-D multiple point-scatterer model.*

The obtained analytical solution and the proposed data analysis method were numerically evaluated. The 1-D model illustrated in **Figure 2.3.3** where n point-scatterers are shown. For generality, normalized position (x/λ) and time (tc/λ) are considered, where λ and c are the wavelength and wave velocity of the incident wave. **Figure 2.3.4(a)** shows the time-harmonic wave response for the total wavefield. Its decomposed wavefields, incident and scattered wavefields, are seen in **Figures 2.3.4 (b)** and **(c)**, respectively. The location of the scatterers are indicated in the figures. The scattered wavefield seen in **Figures 2.3.4(c)** reveals that the three scatterers generate forward- and back-scattered waves that are indicated as wave rays with positive and negative slopes, respectively. Moreover, non-propagating local resonance occurs within the scatterer region as seen in **Figure 2.3.4(c)**.
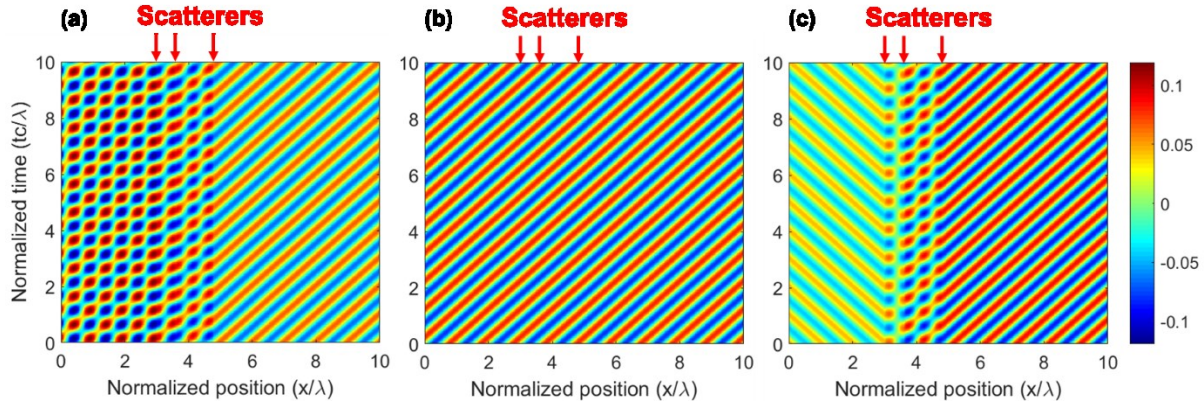
Figure 2.3.4 *Time-harmonic wave responses for the case of three scatterers: (a) total wavefield, (b) incident wavefield and (c) scattered wavefield. Three scatterers are located at x/λ = 3, x/λ = 3.6 and x/λ = 4.8.*

To localize the scatterers, the proposed high-wavenumber filtering approach was applied to the total wavefield seen in **Figure 2.3.4(a)**. The filtered wavefield is shown in **Figure 2.3.5(a).** The location of the scatterers and the source that is not identified in the total wavefield is clearly visualized after high-wavenumber filtering as seen in **Figure 2.3.5(a)**. **Figure 2.3.5(b)** shows the total energy density (*T*) of the scattered waves computed as

$$T = K + V = 2K = \rho \omega^2 \left| G_{sc}(x) \right|^2 , \qquad (2.3.18)$$

where *K* and *V* are the kinetic and potential energy densities of the scattered waves, respectively. G_{sc} is the high-wavenumber filtered Green' function. Similar to the filtered wavefield, the location of the scatterers and source is well identified that are not in the total wavefield. This analytical demonstration validates the potential of the proposed high-wavenumber filtering approach in localizing multiple scatterers such as distributed damage.
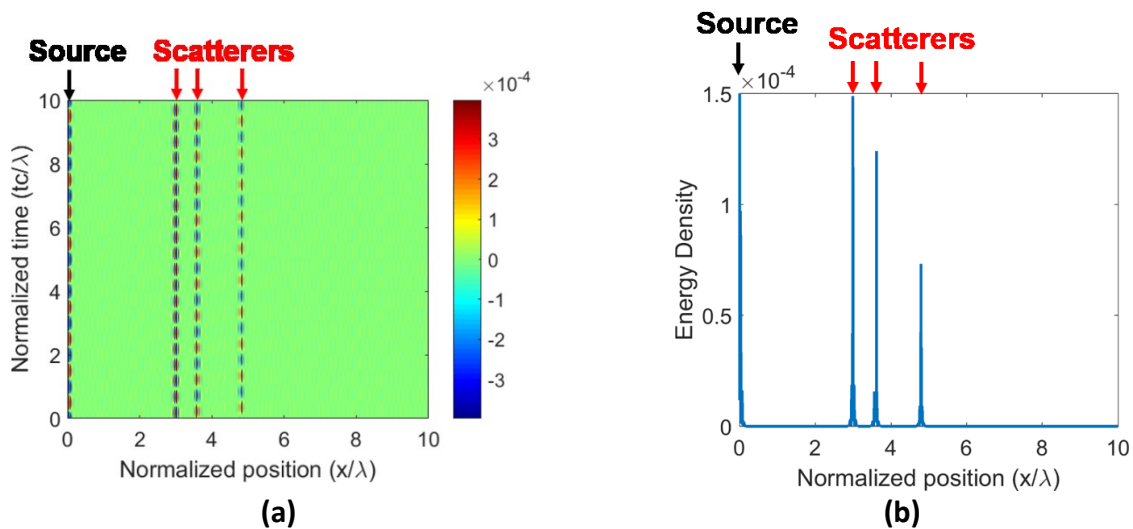
Figure 2.3.5. *High-wavenumber scattered wave responses: (a) filtered wavefield and (b) energy density.*

2.3.2.4 Numerical simulations

Two-dimensional (2-D) linear elastic plane strain dynamic finite element (FE) simulation was performed using the Abaqus/Standard solver (Dassault Systems) to understand the effects of distributed cracking in concrete on surface wave propagation and scattering. The following simulation model cases were considered: sound mortar, sound concrete, damaged concrete with different crack volumes and damaged concrete with a single surface-breaking crack.

Error! Reference source not found. The overall structure of the numerical models is seen in **Figure .3.6(a)**. A semi-infinite half-space was simulated using absorbing layers with increased damping (ALID) [5,6]. 2-D 1 mm plane strain elements were used throughout the entire region. The excitation force was applied at the left edge (x = 0) of the region of interest with properties shown in **Figure 2.3.6(a).** To selectively generate ultrasonic surface waves as incident waves, the spatial distribution of the force amplitude was designed to follow the wave structure of the surface wave. A 5-cycle tone burst signal with a center frequency of 50 kHz was used as the input signal. An example mass density distribution of the region of interest is shown in **Figure 2.3.6(b)**. Concrete was modeled as a heterogeneous solid with the combination of homogeneous background medium (mortar) and randomly distributed coarse aggregates. The coarse aggregate particles were modeled as random ellipses with various aspect ratios. Young's modulus distribution was also similarly defined. Poisson ratio was uniformly set to be 0.26 throughout the region of interest. For each damaged concrete model, a localized cracked region is defined and cracks were modeled by assigning vanishingly small mass density and Young's modulus values to certain elements. The localized cracked region for the damaged concrete models are illustrated in **Figure 2.3.6(c)**. Three distributed crack cases with different crack volume ratio (CVR) and a single surface-breaking crack case were considered. CVR is defined as

$$CVR\ [\%] = \frac{N_{crack}}{N_{total}} \times 100 \tag{2.3.19}$$

where N_{crack} and N_{total} are the number of the crack elements and that of the total elements within the localized cracked region, respectively. To simulate linear scanning measurement, the corresponding surface wave responses were obtained at 0.8 µs of time step across 350 spatial points at 1 mm spacing along the top surface from x = 150 to 499 mm.
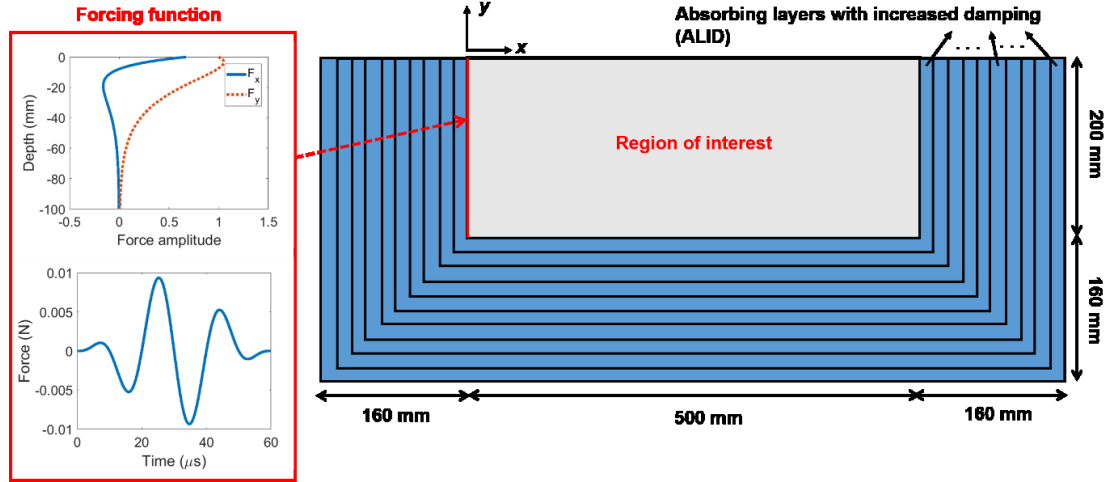
(a)
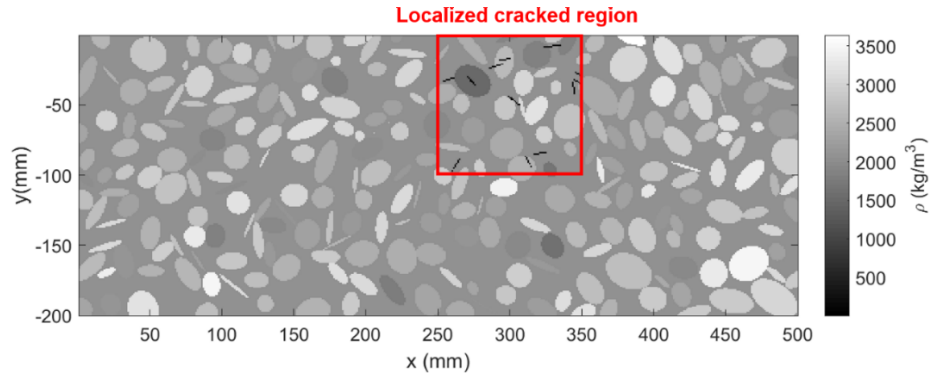
(b)
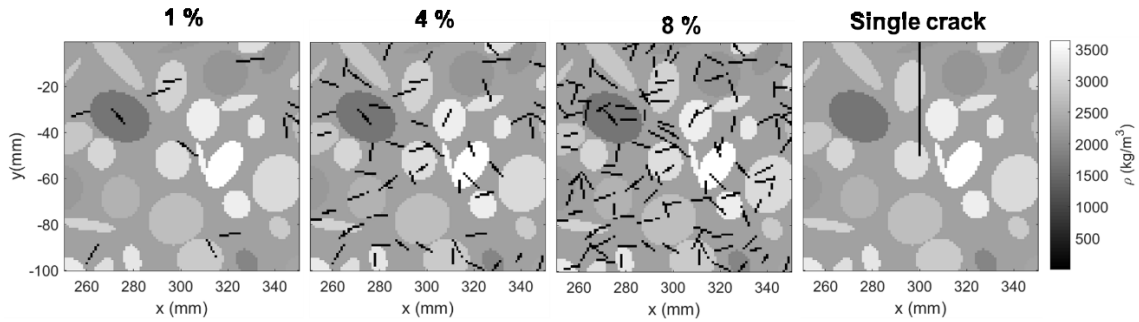
(c)

Figure 2.3.6. Configuration of numerical model of 2-D discrete random medium (simulated concrete): (a) overall structure of the numerical model, (b) an example mass density distribution of the region of interest and (c) localized cracked region for the damaged concrete models.

Figure 2.3.7 shows the time-space (*t-x*) domain signals from all the model cases. For the sound concrete case shown in **Figure 2.3.7(b)**, both coherent forward (indicated as CF) propagating and back-scattered (indicated as BS) surface waves are seen, while only coherent forward propagating waves are seen in the mortar case shown in **Figure 2.3.7(a)**. The back-scattered waves shown in the sound concrete case are set up by the coarse aggregate network. **Figures**

2.3.7 (c) to **(e)** show *t-x* domain signals from damaged concrete with 1%, 4% and 8% of CVR. The localized cracked region, *x* = 250 mm to 350 mm, is indicated in each *t-x* domain signal. In addition to the coherent forward propagating and back-scattered waves, incoherent multiple scattering (indicated as IMS) waves are seen within the cracked region for the damaged concrete case with 4 % CVR shown in **Figure 2.3.7(d)**. Incoherent multiple scattering is more clearly observed as the CVR increases, as seen in **Figure 2.3.7(e)**. At certain regions, very strong interactions between cracks occur, resulting in local resonances. For the case of the single surface-breaking crack shown in **Figure 2.3.7(f)**, local scattering is observed at the crack location.
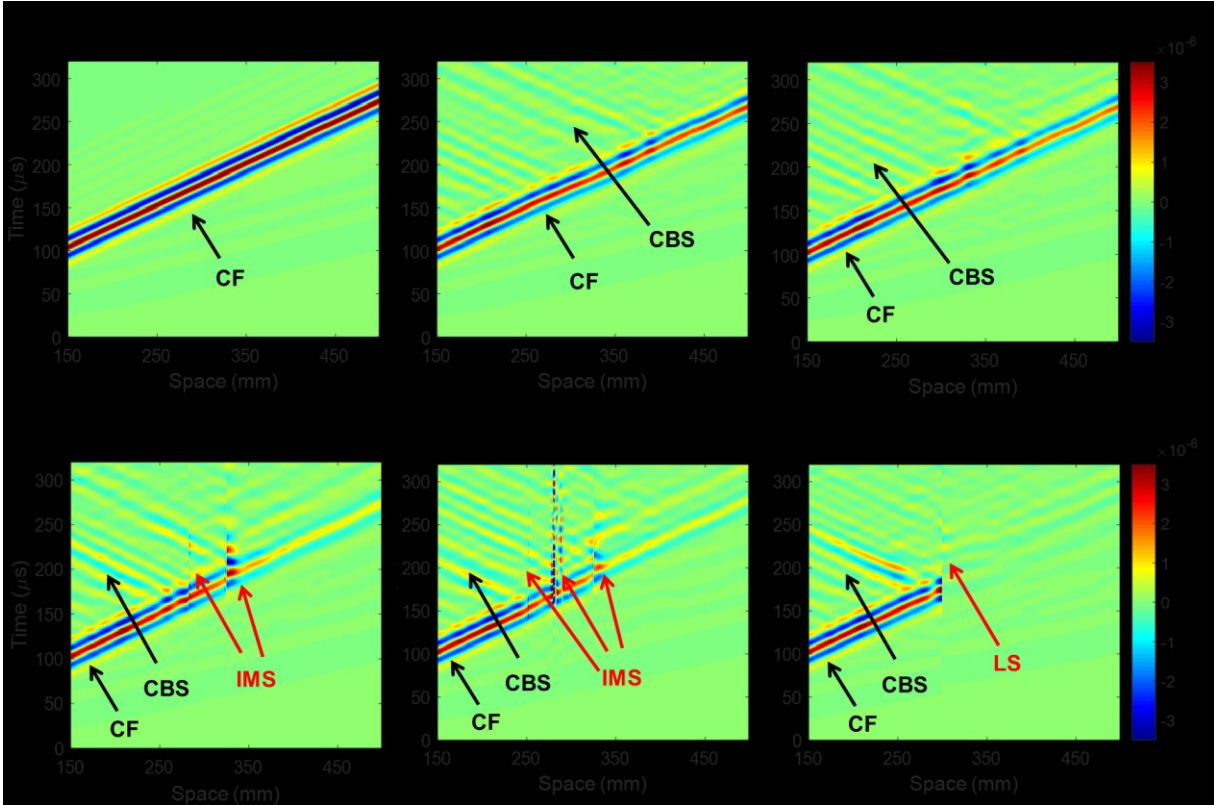
Figure 2.3.7. Time-space (t-x) domain signals obtained from the top surface of the simulated concrete models: cases for (a) mortar, (b) sound concrete, (c) damaged concrete (1 % CVR), (d) damaged concrete (4 % CVR), (e) damaged concrete (8 % CVR), and (f) damaged concrete (single crack).

To better understand the scattered wave fields set up by localized cracked regions in concrete, frequency-wavenumber (*f-k*) analysis was carried out. Tukey windows were applied to the original *t-x* domain signals in space to isolate the localized region before computing the 2-D FT. **Figures 2.3.8 (a) to (d)** show the *f-k* domain magnitude spectra for all the simulation cases. In the mortar case shown in **Figure 2.3.8(a)**, only the coherent forward propagating wave components are seen, while coherent back-scattered wave components are also observed in the sound concrete case shown in **Figure 2.3.8(b)**. For the damaged concrete with distributed cracks, the magnitude spectra become broader as the crack volume increases, as seen in **Figures 2.3.8 (c)** to

(e). This wavenumber broadening phenomenon results from incoherent multiple scattering wave components set up by the distributed crack network. For the single crack concrete case, the *f-k* magnitude spectrum exhibits is only slightly broader than that of the sound concrete case, resulting from the local scattering near the crack location. The simulation results shown in **Figures 2.3.7** and **2.3.8** demonstrate that incoherent multiple scatter and local scatter are unique features caused by the presence of cracking in concrete.
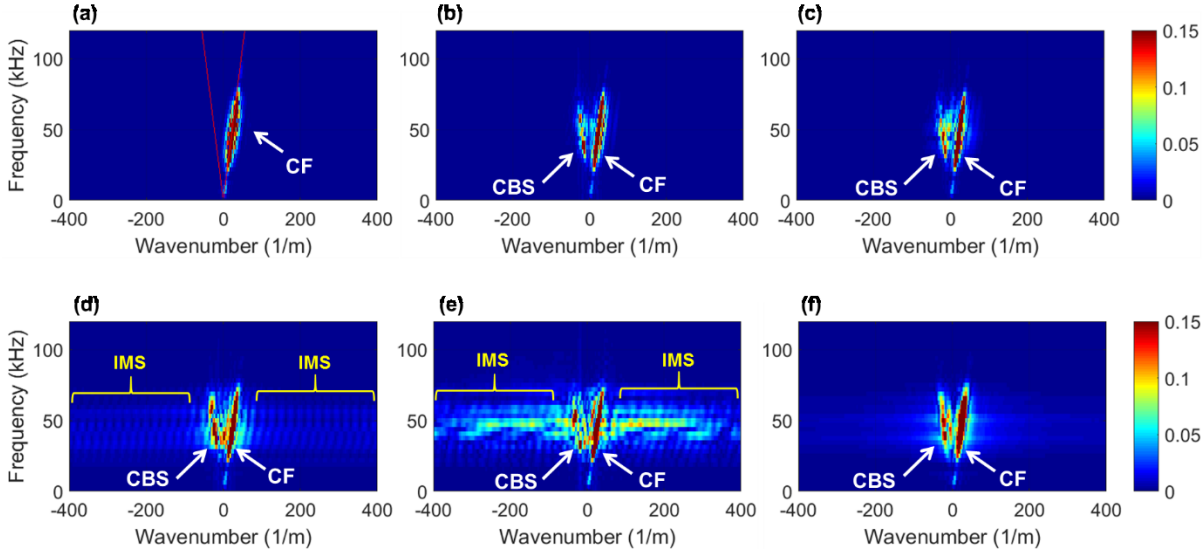
Figure 2.3.8. Frequency-wavenumber (f-k) domain magnitude spectra from simulated concrete models: cases for (a) mortar, (b) sound concrete, (c) damaged concrete (1 % CVR), (d) damaged concrete (4 % CVR), (e) damaged concrete (8 % CVR), and (f) damaged concrete (single crack).

To numerically verify the proposed signal processing scheme, the *f-k* domain signal filtering approach described in **Figure 2.3.2** was applied to numerical simulation data. **Figure 2.3.9(a)** shows E_N computed for all the six simulation cases. The damaged concrete cases show high E_N values within the cracked region. To check the sensitivity of the proposed technique in low-level damage, E_N values for the cases of mortar, sound concrete and the lowest damaged concrete (1 % of CVR) are compared in **Figure 2.3.9(b)**. The sound mortar case shows E_N values nearly zero over the inspection region. Although the sound concrete case shows E_N values slightly larger than those values of the mortar case, the E_N values from the sound concrete case are still close to zero. However, the 1 % CVR case exhibits much higher E_N values within the cracked region, clearly distinguishable from the sound concrete case. The results demonstrate the potential of the proposed approach to characterize cracking damage in concrete.
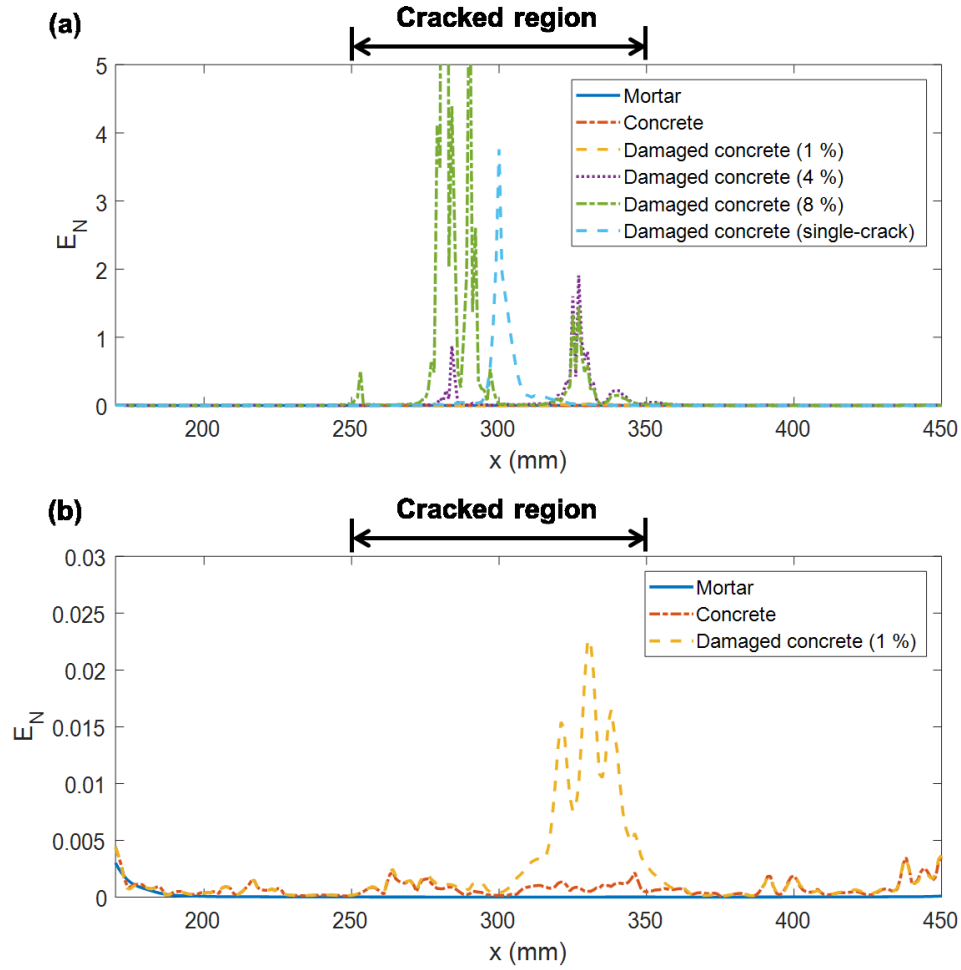
Figure 2.3.9. *Spatial distribution of normalized incoherent scattered wave energy $E_N(x)$: (a) all the simulation cases and (b) the cases for mortar, sound concrete and damaged concrete with 1 % CVR.*

2.3.2.5 Laboratory-scale experimental validation

An experimental investigation was performed to verify the feasibility of the proposed *f-k* domain signal filtering approach. **Figure 2.3.10(a)** shows the experimental setup for fully contactless ultrasonic tests. An air-coupled ultrasonic sender (Series 600, SensComp Inc.) having a center frequency of 50 kHz generated surface waves in concrete specimens. The corresponding wave responses were measured by an air-coupled MEMS ultrasonic receiver (SPM0404UD5, Knowles Electronics Corp.) that was scanned across 121 spatial points at a spacing of 2.5 mm. To improve signal-to-noise ratio, the time signals were measured 100 times at each measurement position and then time averaged. **Figure 2.3.10(b)** shows three tested concrete specimens having different extents of simulated cracking content by volume: (1) sound concrete (0% plastic fiber content by volume), (2) damaged concrete with low crack volume (0.3%) and (3) damaged concrete with high crack volume (0.6%).
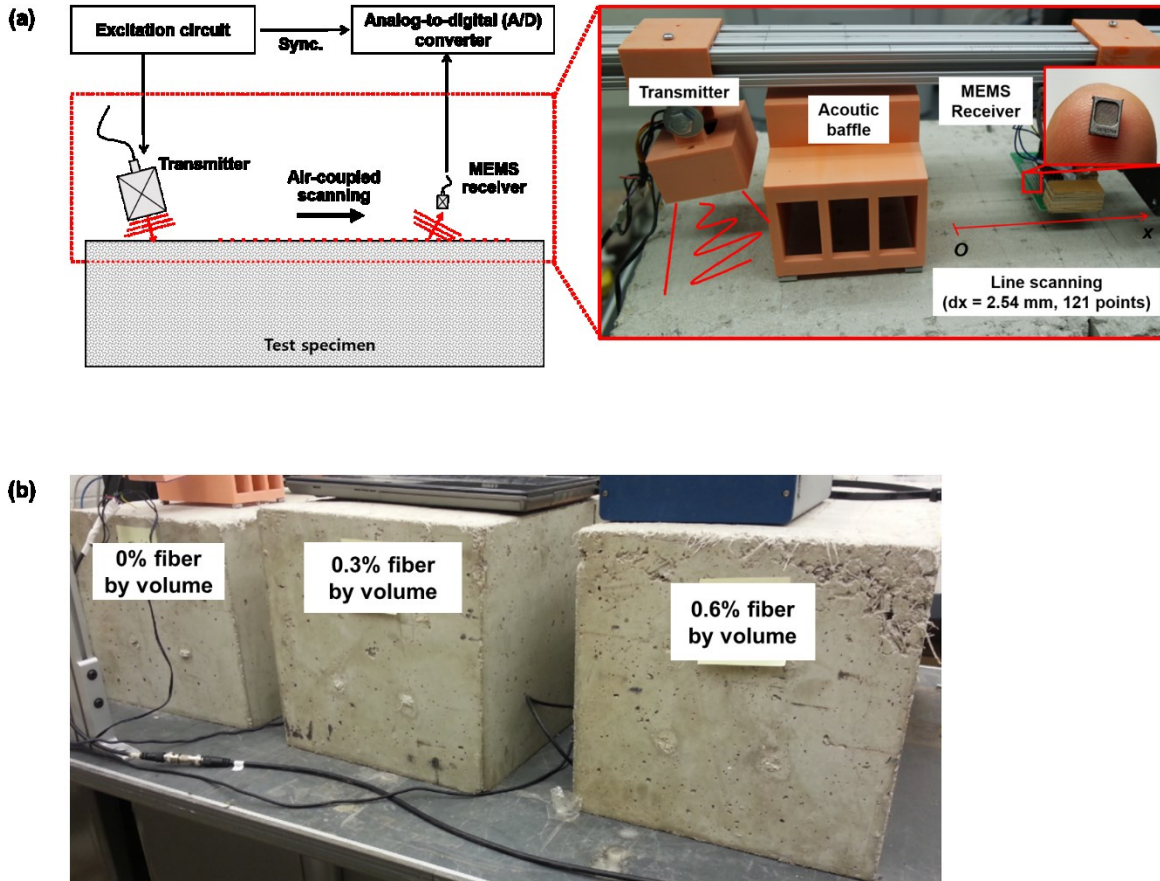
Figure 2.3.10. *Experimental setup: (a) contactless leaky ultrasound measurement setup and (b) concrete samples with simulated cracking damage.*

The t-x domain signals obtained from the three concrete specimens are shown in **Figure 2.3.11**. In the sound concrete case, seen in **Figure 2.3.11(a)**, the majority of wave components are coherent forward propagating waves. In the t-x domain signal for the low volume simulated crack case seen in **Figure 2.3.11(b)**, less coherent surface wave energy is presented across measurement space compared with the sound concrete case. The high volume simulated crack case shown in **Figure 2.3.11(c)** shows incoherent wave scattering patterns and disrupted wave rays across measurement space.

The proposed *f-k* filtering approach was applied to the experimental data. **Figure 2.3.12** shows the spatial distribution of the incoherent scattered wave energy (E_N) for all the specimens. Similar to the simulation results shown in **Figure 2.3.9**, higher E_N values are seen for the two cases of concrete specimens with fiber content, while the sound concrete case (0% fiber) shows E_N values nearly zero throughout the scanned area. These experimental results demonstrate the feasibility of the proposed *f-k* domain signal filtering approach to characterize distributed cracking in concrete.
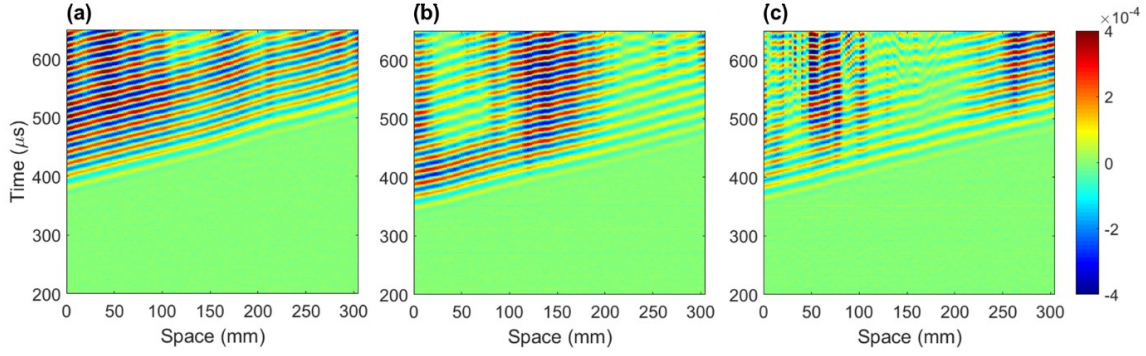
Figure 2.3.11. *T-x domain signals obtained from the three concrete specimens: (a) sound concrete, (b) concrete with low crack volume (0.3% fibers by volume) and (c) concrete with high crack volume (0.6% fibers by volume).*
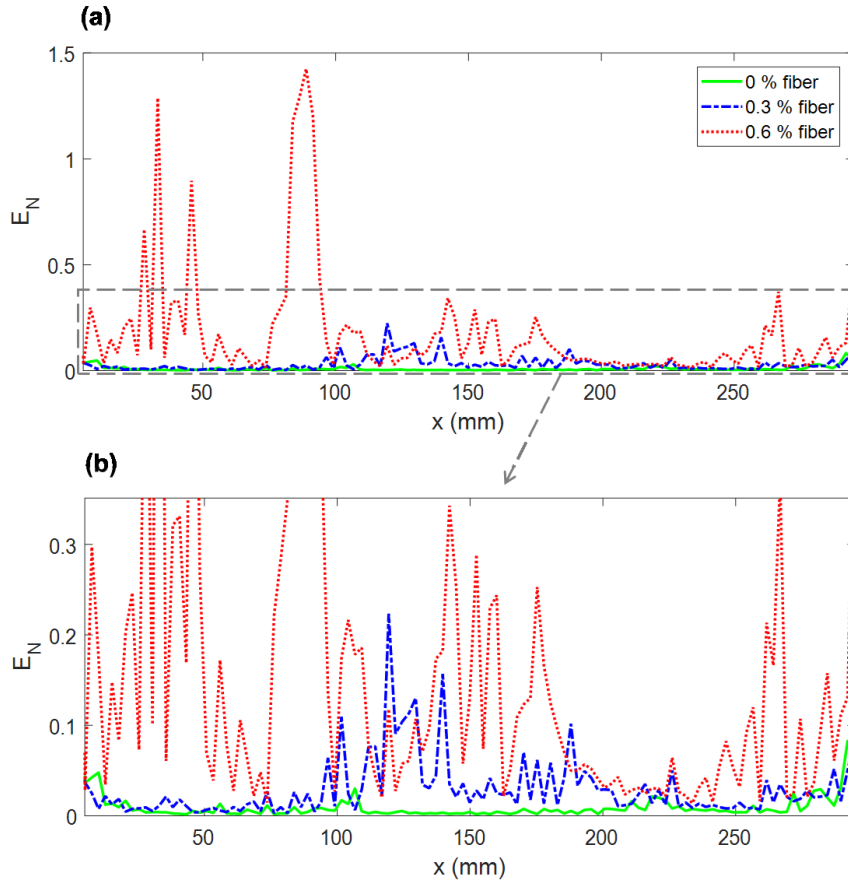
Figure 2.3.12. *Spatial distribution of normalized incoherent scattered wave energy (E_N) for all the concrete samples (a). A zoom-in plot of E_N is shown in (b).*

2.3.2.6 Large-scale experimental validation

The proposed approach was applied to large-scale concrete samples housed at the testbed of National Institute of Standards and Technology (NIST) under ASR-promoting environments. The four tested concrete samples are seen in **Figure 2.3.13(a)**. The control sample includes non-

reactive aggregate, reactive samples 1 and 3 relatively high reactive aggregate in a similar level, and Reactive sample 2 low-reactivity aggregate. These different levels of aggregate reactivity provide the evidence that the control sample may have no damage, while Reactive sample 1 to 3 ASR-induced damage with respect to the level of aggregate reactivity.

The automated contactless scanning ultrasound measurement system was applied to the top surface of each sample as seen in **Figure 2.3.13(b)**. The scanning area of each sample is shown in **Figures 2.3.14 (a)** to **(d)**. A whole scanning area (197.5 mm x 161 mm) is sub-divided into three sub-scan areas, and dense line scanning measurements were performed within a sub-scan area using the 8-channel MEMS receiver array as shown in **Figure 2.3.14(e)**. Hence, total 24 line scan data sets were obtained from each sample. To monitor the progress of ASR damage, ultrasonic data sets were obtained at three different dates: July 2017, September 2017 and March 2018.
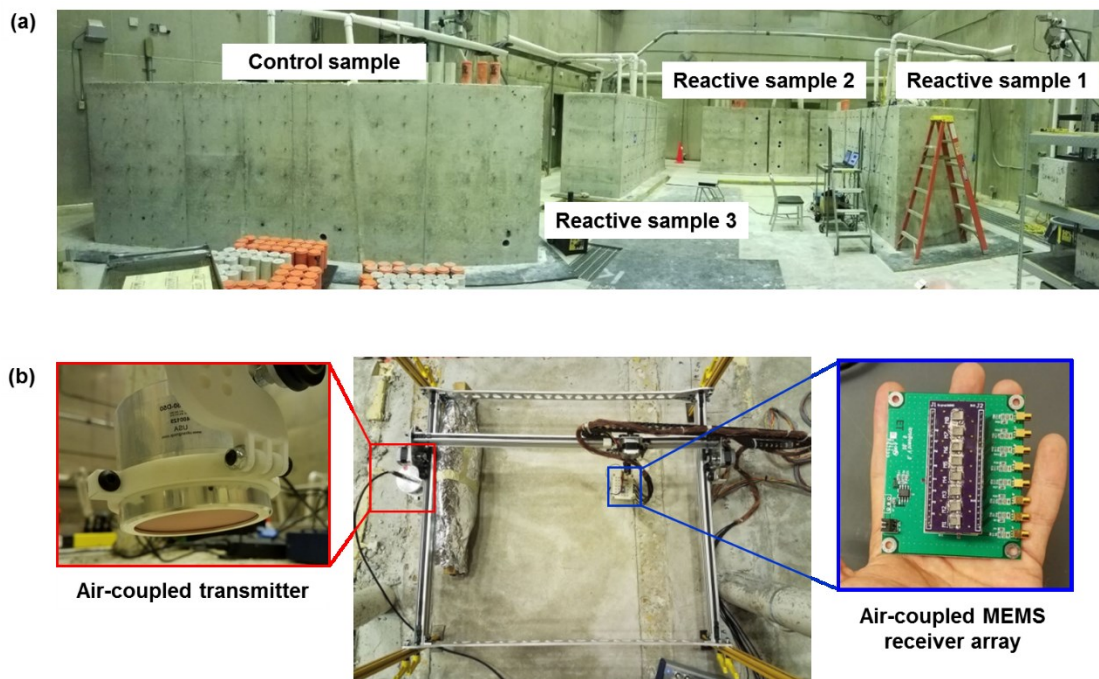
Figure 2.3.13. *Experimental setup for the large-scale testing: (a) concrete samples including aggregates with different reactivity and (b) the automated contactless scanning ultrasound measurement setup.*
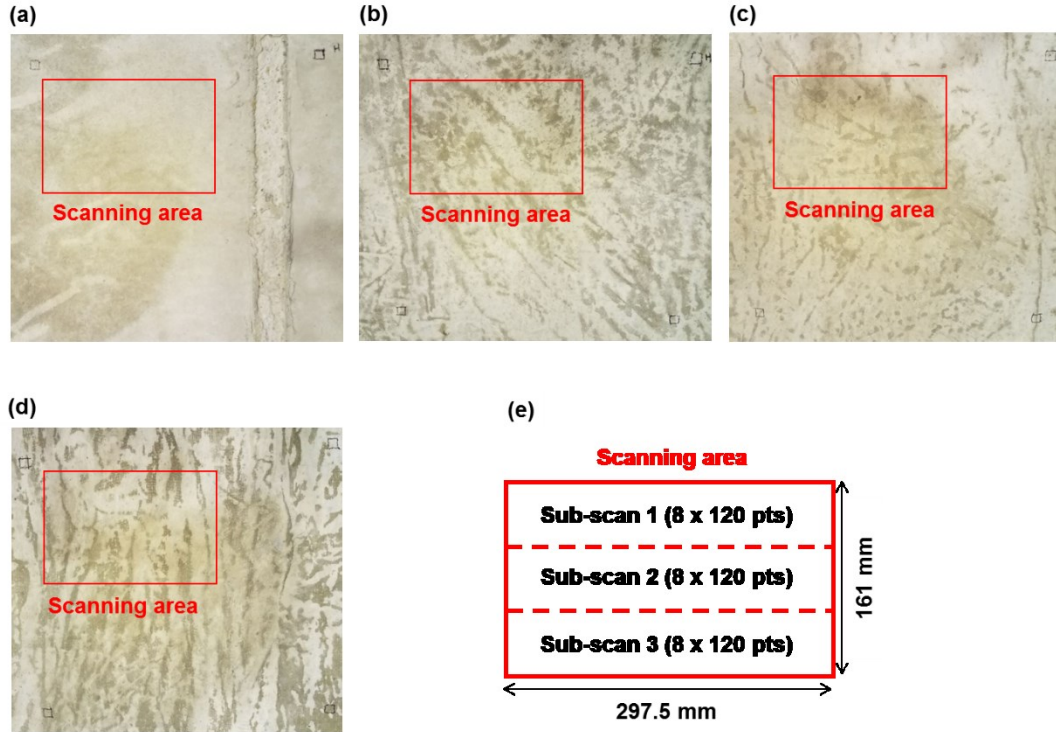
Figure 2.3.14 Scanning area of each concrete sample: (a) Control sample, (b) Reactive sample 1, (c) Reactive sample 2, (d) Reactive sample 3, and (e) the dimension of each scanning area. Three sub-scanning operations were performed within a scanning area, and each sub-scan area includes 8 x 120 spatial sampling points.

The normalized scattered energy (E_N) maps for the four inspected concrete samples are seen in **Figure 2.3.15**. **Figures 2.3.15 (a)** to **(c)** show E_N maps for control sample computed using the three data sets collected in July 2017, September 2017 and March 2018, respectively. Similarly, **Figures 2.3.15 (d)** to **(f)** show E_N maps for Reactive sample 1, **Figures 2.3.15 (g)** to **(i)** for Reactive sample 2 and **Figures 2.3.15 (i)** to **(l)** for Reactive sample 3. In each E_N map, red color represents high scattered energy level, while blue color low level. The E_N maps of Control sample seen in **Figures 2.3.15 (a)** to **(c)** present low E_N level close to zero for all the time instances, implying low likelihood of ASR damage within the scanning area. For the case of Reactive sample 1, slightly higher E_N level than Control sample is seen in the July 2017 data (**Figures 2.3.15 (d)**), and significantly higher E_N level is seen in September 2017 and March 2018 data sets shown in **Figures 2.3.15 (e)** and **(f)**. The high E_N values within the scanning area reveal high likelihood of damage caused by expansion of ASR products. The case of Reactive sample 2 shows relatively high E_N values in some locations within the scanning area as seen in **Figures 2.3.15 (g)** to **(i)**. However, the overall EN level is lower than the other reactive samples possibly due to the lower reactivity aggregate than other two reactive samples. For the case of Reactive sample 3 seen in **Figures 2.3.15 (j)** to **(l)**, high E_N values are presented across the overall region of the scanning area, similar to the case of Reactive sample 1. These large-scale experimental results demonstrate the feasibility of the proposed approach in detecting and localizing distributed damage in real-world concrete applications.
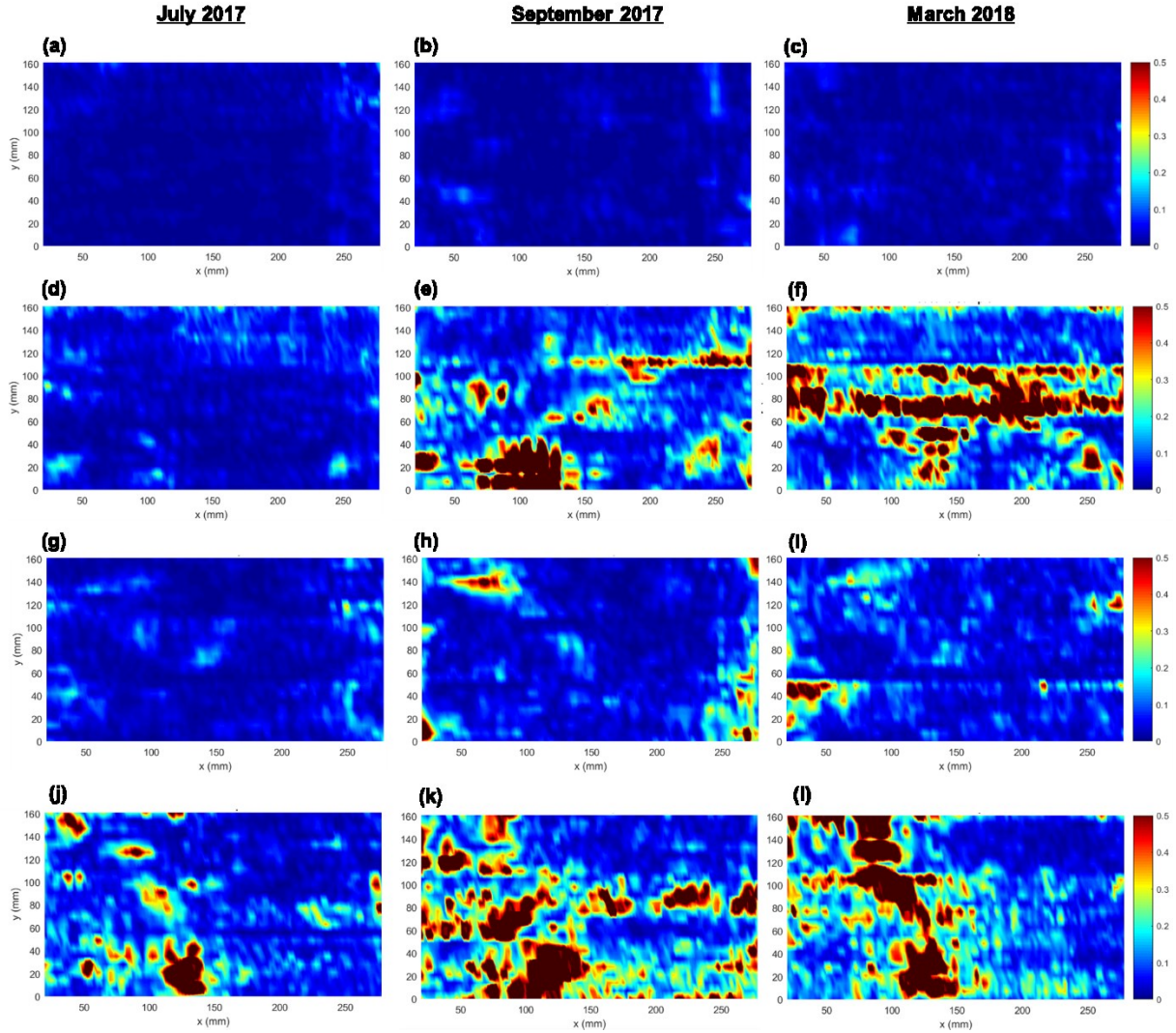
Figure 2.3.15. *Normalized scattered energy (E_N) maps for the four concrete samples: Control sample (a to c), Reactive sample 1 (d to f), Reactive sample 2 (g to i), and Reactive sample 3 (j to l). The left column maps were computed using the data collected in July 2017, the middle column maps September 2017, and the right column March 2018.*

2.3.3 NDI system development for vertical overpack sytems

To develop an NDE system for the vertical overpack systems, analytical modeling, numerical simulation and experimental studies were carried out.

2.3.3.1 Analytical modeling

The modal solutions for guided waves propagating in multi-layered media can be obtained using matrix-based techniques [7–11]. In this study, the global matrix technique [9–11] was used to model guided wave propagation in steel-clad concrete structures with well bonded, weakly bonded and completely disbonded interfaces. In this technique, each layer is represented by a 4 x 4 layer matrix that is a function of elastic material properties, thickness of each finite layer,

frequency (f) and complex-valued wavenumber (k). By satisfying boundary conditions at each layer interface, all the layer matrices are assembled into a system matrix (S). Note that S should be singular for the multi-layer model to have modal solutions. The characteristic equation for the modal solutions is therefore given by

$$F(f,k) = \det[S] = 0.$$ (2.3.20)

Once the modal solutions are obtained, unique characteristics, such as phase velocities and attenuation of the guided waves in multi-layered media, can be identified. Detailed descriptions of the global matrix technique can be found in our publication [12] and elsewhere [9,10].

Figure 2.3.16 shows configurations of analytical models for guided waves in the steel cladding layer with well bonded, weakly bonded and completely disbonded interfaces respectively. The guided waves propagating in the steel-cladding that is well bonded to the underlying concrete shown in **Figure 2.3.16(a)** were assumed to behave as guided waves in a single-layered half-space, where the acoustic impedance (Z) of the top layer (steel-cladding) is greater than that of the underlying half-space (concrete). The case of weakly bonded steel-cladding is modeled as a double-layered half-space, where a thin interfacial layer is placed between the steel cladding and the underlying concrete half-space. This interfacial layer represents the bond between steel and concrete, where the Z value of this interfacial layer is lower in value than those of the steel layer and underlying concrete. A decrease in steel-concrete interface bond condition is simulated by a decrease in Z value of the interfacial layer. The guided waves propagating in the completely disbonded steel-cladding layer shown in **Figure 2.3.16(c)** are assumed to behave as Lamb waves (plate waves) in a traction-free steel plate.

The global matrix equations can be solved to derive real and complex-valued wavenumbers across a range of frequencies for a given set of layer thicknesses and elastic properties. The phase velocity (c_{ph}) of a given wave mode can then be determined by

$$c_{ph} = \frac{\omega}{\mathrm{Re}[k_x]},$$ (2.3.21)

and the attenuation (α) in dB/m by

$$\alpha = -20\log_{10} e^{-\mathrm{Im}[k_x]},$$ (2.3.22)
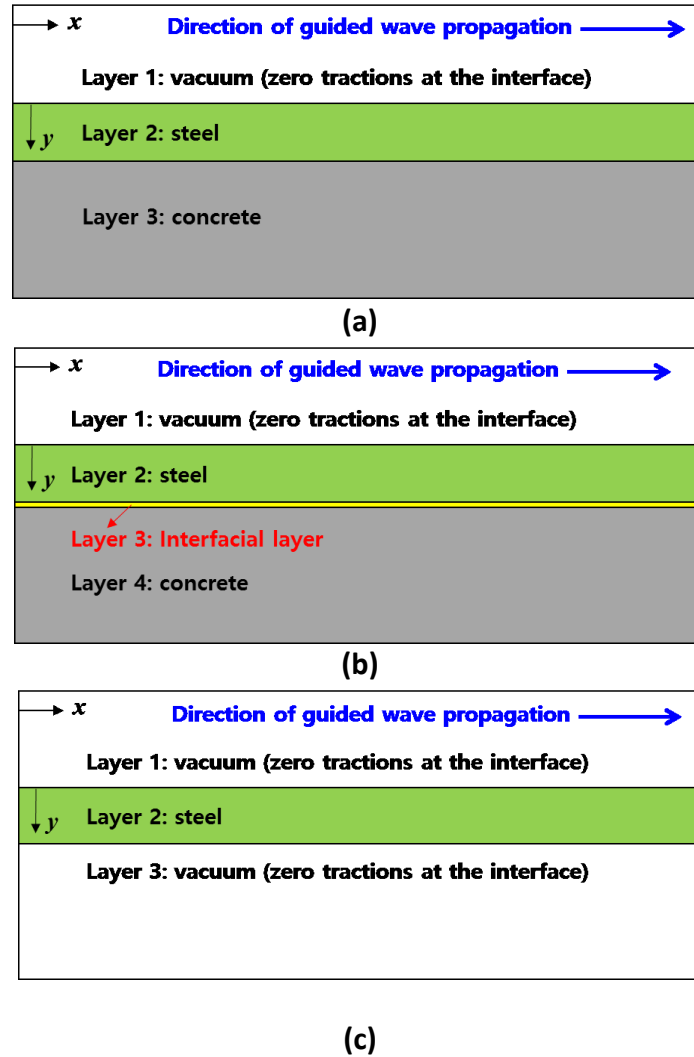
Figure 2.3.16. *Configurations of analytical models for guided waves in a steel cladding layer: (a) well bonded, (b) weakly bonded and (c) completely disbonded interface cases.*

where Re[k_x] and Im[k_x] represent the real and imaginary components of k_x, respectively. Note that the physical mechanism of the attenuation is the leakage of the given guided wave mode into the adjacent half-spaces [11]. The contributions to attenuation from material damping and grain scattering are not considered in this analysis because these effects are negligible for steel at the ultrasonic frequencies employed in the work. However, geometric spreading does have an influence on amplitude decay of guided waves. Nevertheless, this effect is compensated for within the signal processing approach employed, which is described in section 2.3.3.3 The material properties for all the layers assumed in the calculations are shown in **Table 2.3.1**. The thicknesses of the steel cladding and the interfacial layers are 19 mm and 2 mm, respectively.

Table 2.3.1. Material properties of layered models.

		P-wave velocity [m/s]	S-wave velocity [m/s]	Density [kg/m³]
Steel		5800	3100	7850
Concrete		4066	2490	2400
Interfacial layer	Case 1	4066	2490	2400
	Case 2	3659.4	2241	2400
	Case 3	3252.8	1992	2400
	Case 4	2846.2	1743	2400
	Case 5	2439.6	1494	2400
	Case 6	2033	1245	2400
	Case 7	1626.4	996	2400
	Case 8	1219.8	747	2400
	Case 9	813.2	498	2400
	Case 10	406.6	249	2400
	Case 11	40.66	24.9	2400
	Case 12	0	0	2400

Figure 2.3.17 shows the modal solutions obtained by the global matrix technique for the well bonded, weakly bonded and disbonded steel-cladding cases shown in **Figure 2.3.16**. Here, only the fundamental symmetric (S0) and the anti-symmetric (A0) guided wave modes are displayed for simplicity. In the figure, 'Good' and 'Free' represent well bonded and completely disbonded cases respectively. '0.6Z', '0.4Z' and '0.2Z' represent weakly bonded cases, where Z of the interfacial layers is 60, 40 and 20 percent of Z of the underlying concrete respectively. As seen in **Figure 2.3.17(a)**, little distinction between the well bonded, weakly bonded and disbonded cases can be made from the real wavenumber data. This result suggests that conventional ultrasonic wave approaches based on wave phase or group velocity analysis would not be effective for characterizing steel-concrete interface bonding conditions.

However, much greater distinction is observed in the imaginary wavenumber responses, as shown in **Figure 2.3.17(b)**. No attenuation was observed for both the S0 and A0 modes in the completely disbonded case, while nontrivial attenuation is observed for both modes in the well bonded and weakly bonded steel cladding cases. Furthermore, the S0 mode shows greater attenuation than the A0 mode in the well bonded and the weakly bonded cases. The attenuation of the S0 mode drastically increases as the frequency increases beyond 100 kHz. It can be seen that S0 mode attenuation consistently and monotonically decreases within the frequency region indicated in the box shown in **Figure 2.3.17(b)**, as Z of the interfacial layer decreases. To illustrate this behavior more closely, the S0 mode attenuation at 125 kHz under varying Z of the interfacial layer is shown in **Figure 2.3.18**. The reduction of interfacial layer Z value represents weakening of steel-concrete interface bond where 100% reduction in Z represents the completely disbonded case. These analytical results indicate that the attenuation behavior of the S0 mode has potential to quantitatively characterize interface bonding conditions of steel-clad concrete structures. A frequency of 125 kHz was selected because it exhibits the highest sensitivity to bond condition

changes, as indicated by the attenuation behaviors shown in **Figure 2.3.17**. The excitation frequencies in numerical simulations and experiments are also set to be 125 kHz in order to study interface bond characterization. In case that an inappropriate frequency is selected, for example 25 kHz, the attenuation behavior of the S0 mode cannot sensitively distinguish the interface bond condition as indicated by the attenuation behaviors shown in **Figure 2.3.17**.
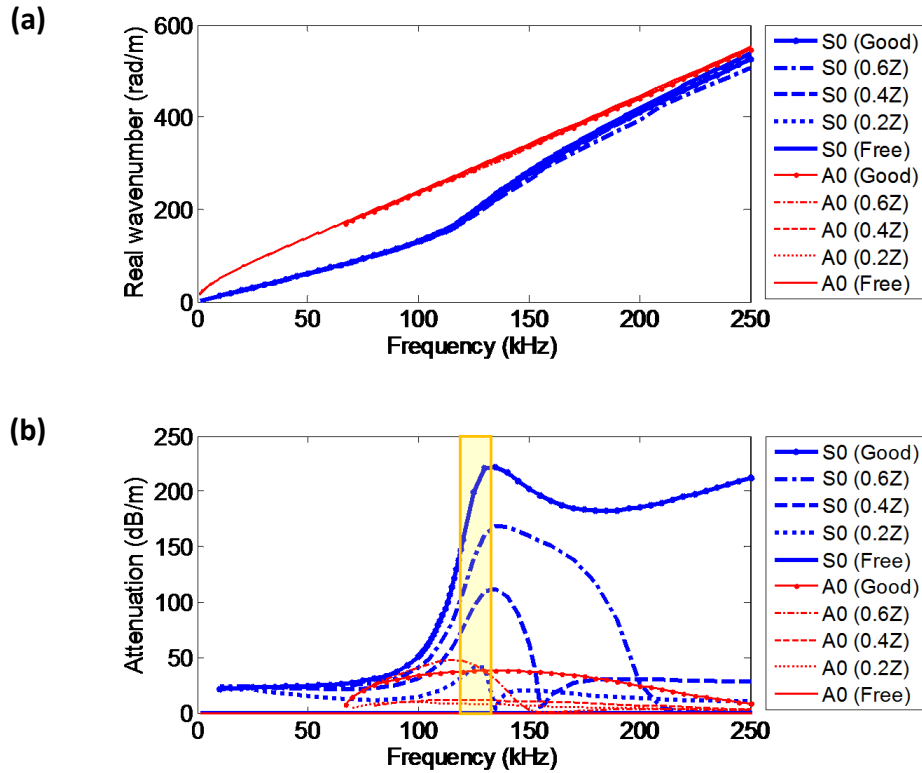
Figure 2.3.17. *Theoretical modal solutions under various interface bonding conditions obtained by the global matrix technique: (a) real wavenumbers and (b) imaginary wavenumbers (attenuation).*
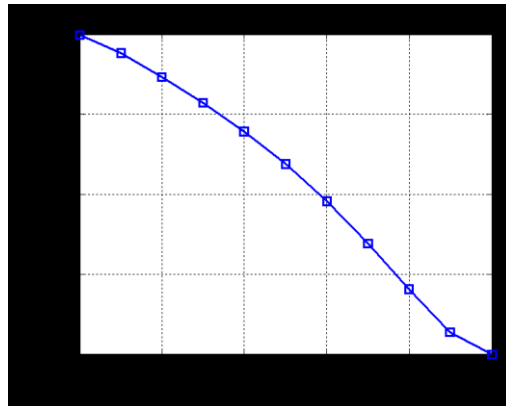
Figure. 2.3.18. *Analytical prediction of S0 mode attenuation at 125 kHz as a function of gradual reduction in acoustic impedance (Z) of the interfacial layer.*

2.3.3.2 Signal processing to extract attenuation characteristics of guided wave modes

Although S0 mode attenuation shows potential to characterize steel-concrete interface bonding conditions, it is difficult in practice to extract this characteristic from the full guided wave signal. This difficulty arises from the fact that guided waves in the steel cladding layer show multi-modal and dispersive characteristics [10,4], and furthermore attenuation is an amplitude-related property that is very sensitive to experimental parameters such as receiver-specimen coupling condition. To address these issues, we propose a signal processing scheme to extract a dimensionless damage index, normalized S0 mode magnitude, that reflects the attenuation characteristics of the S0 mode but at the same time is not meaningfully influenced by variations in experimental parameters. The signal processing scheme is based on frequency-wavenumber (f-k) domain signal analysis.

Figure 2.3.19 shows an overview of the signal processing scheme to extract the normalized S0 mode magnitude A_{S0}^N from the obtained guided wave signal set. First, raw guided wave field $s(t,x)$ time-space (t-x) domain data are obtained from a series of ultrasonic scan measurements. Next, Hanning windowing and zero-padding in the x-domain are applied to $s(t,x)$ to improve k-domain resolution. A two-dimensional (2-D) Fourier transform (FT) is then applied to the windowed and zero-padded wave field $s_W(t,x)$ to convert the signal set from the t-x domain to the f-k domain though

$$\overline{S}(f,k) = \int_{-\infty}^{\infty}\int_{-\infty}^{\infty} s_W(t,x)e^{-i2\pi(ft+kx)}dxdt \cdot \tag{2.3.23}$$

Note that individual guided wave modes that are poorly separated in t-, t-x and f-domains are clearly distinguished in the f-k domain, and thus the S0 mode can readily be identified. Next, the wavenumber spectrum at the center frequency (f_C) of excitation $\overline{S}(f_C,k)$ is extracted from the magnitude spectrum in the f-k domain. A_{S0}^N is computed as

$$A_{S0}^N = \frac{A_{S0}}{A_{A0}}, \tag{2.3.24}$$

where A_{S0} and A_{A0} are the maximum magnitudes of the S0 and the A0 modes respectively in $\overline{S}(f_C,k)$. The normalization expressed in Eq. (2.3.24) enables muting of the effects of signal variation caused by other experimental parameters, under the following assumptions: (1) variations in other experimental parameters influence both the S0 and A0 mode amplitudes to the same degree; (2) the A0 mode amplitude is insensitive to the interface bonding conditions; and (3) amplitude attenuation caused by geometric spreading can be compensated by the amplitude normalization process used in the signal processing scheme. With this approach, high A_{S0}^N value represents low S0 mode attenuation associated with weak steel-concrete bond, while low A_{S0}^N value represents the high S0 mode attenuation associated with strong bond. Note that

A_{S0}^N has absolute meaning, where values close to 0 represent well bonded condition, while those close to 2.3 represent poor condition.
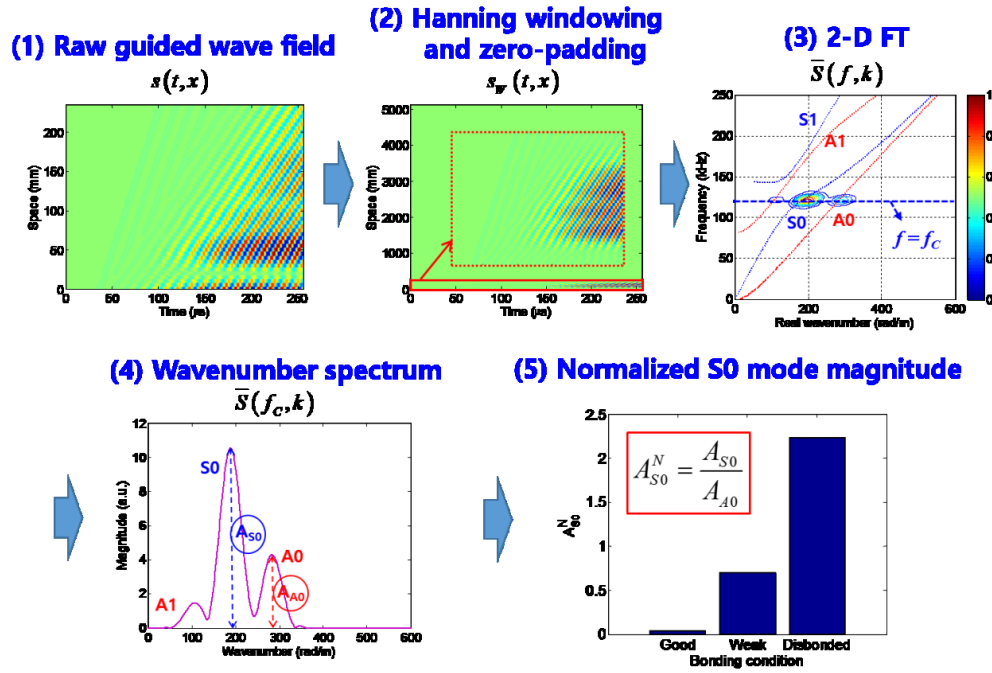
Figure 2.3.19. *Overview of the procedure to compute normalized S0 mode magnitude.*

2.3.3.3 Numerical simulation

Dynamic finite element (FE) simulation was carried out using the dynamic explicit solver in Abaqus (Dassault Systems) to investigate the effects of the steel-concrete interface bond condition on the guided wave propagation characteristics in the steel cladding layer and to verify the signal processing scheme described in Section 2.3.3.2.

The structure of the FE simulation model is shown in **Figure 2.3.20**. Four layers are modeled: (1) an air half-space (indicated by blue color), (2) a 19 mm-thick steel cladding layer (green), (3) a 2 mm-thick interfacial layer (yellow) and (4) a concrete half-space (gray). Although the full model was used in the simulations, only data from the region of interest shown in the magnified view in **Figure 2.3.20** were considered in the analysis. Each layer was configured to be perfectly bonded to the neighboring layers. All the layers are assumed to be composed of linearly elastic, isotropic and homogeneous materials. The material properties used in the analysis are shown in **Table 2.3.1**. 2-D four-node plane strain elements (CPE4R) were used throughout this model. The element size was 0.5 mm throughout the steel cladding and interfacial layers. For the air layer, 0.5 mm elements were used for the region within a vertical distance of 20 mm from the top surface of the steel cladding layer. The element size was then gradually increased from 0.5 mm to 2 mm in a size-graded configuration as a function of distance within the region of 20 mm to 70 mm vertical distance from the top surface of the steel cladding. Two-mm elements were used for the remaining region of the air layer. A similar graded element size distribution was

employed for the concrete layer as a function of vertical distance from the bottom of the interfacial layer. Specifically, 0.5 mm elements were used throughout the region within a vertical distance of 20 mm from the bottom surface of the interfacial layer. Then, element size gradually increased from 0.5 mm to 2 mm within the region defined by 20 mm to 70 mm vertical distance from the bottom of the interfacial layer. Two-mm elements were used for the remaining region of the concrete layer. Incremental interface deterioration was modeled by controlling the value of Z of the interface layer. A distributed pressure was applied to the air layer near the steel cladding surface using 20-cycle tone burst input with a center frequency of 125 kHz. The incident angle from air to the steel surface was set 4.9 °, which is the critical angle of the S0 Lamb wave mode at 125 kHz in a free steel plate in air. The resulting guided wave responses were obtained on the surface of the steel cladding at 48 locations with 5 mm spacing between sensed points, indicated by yellow dots in **Figure 2.3.20**. The time step used in the dynamic explicit solver was 0.5 µs.

Figure 2.3.20. *Overall structure of numerical finite element simulation model (top), and detail of region of interest (bottom).*

The sensitivity of the S0 and A0 modes to steel-concrete interface bonding conditions were evaluated in the *f-k* domain. **Figure 2.3.21** shows the *f-k* domain magnitude spectra for well bonded, weakly bonded and disbonded conditions. In the weakly bonded case, *Z* of the interface layer is 20 percent of that of the underlying concrete. The *f-k* domain magnitude spectra were normalized by the maximum spectral magnitude of the well bonded interface case. Within each spectrum, red color represents high spectral magnitude and blue color low magnitude. Theoretical Lamb wave mode solutions, which assume only real-valued wavenumbers, are overlaid on the *f-k* domain spectra to aid in identification of individual guided wave modes. In the well bonded interface case shown in **Figure 2.3.21(a)**, only the A0 mode is seen in the *f-k* domain magnitude spectrum, while the S0 mode is negligible because of its high attenuation owing to leakage into the concrete. The weak bond case shown in Figure **2.3.21(b)** shows higher S0 mode magnitude than the well bonded interface case, while the A0 mode magnitudes are similar between the two cases. In the disbonded case shown in **Figure 2.3.21(c)**, the greatest S0 mode magnitude is seen, while the A0 mode magnitude is still similar to other cases. These results show good agreement with the analytical results, demonstrating that the behavior of the S0 mode is sensitive to steel-concrete interface bonding conditions while the A0 mode is largely unaffected.
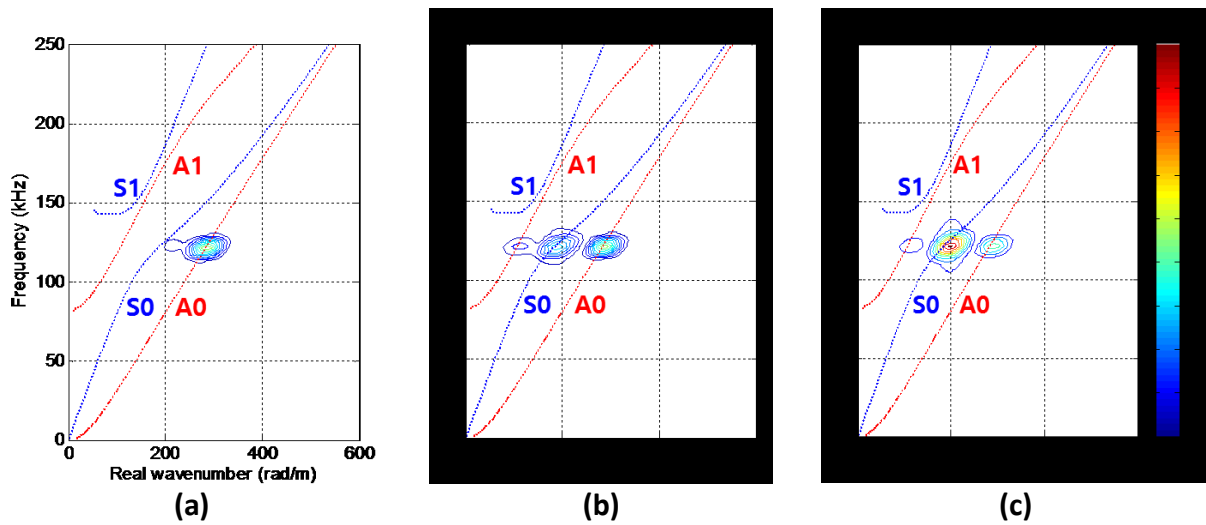
Figure 2.3.21. *F-k domain spectra from finite element simulation data for (a) well-bonded, (b) weekly bonded (80% reduction in Z) and (c) fully disbonded interfaces. Expected Lamb mode behavior in steel plate indicated by dotted lines.*

To quantitatively characterize the interface condition, the proposed signal processing technique described in Section 2.3.3.2 was applied to the guided wave signal sets obtained by the numerical simulation. The normalized S0 mode magnitude A_{S0}^{N} at 125 kHz presented as a function of percent decrease in *Z* of the interfacial layer is shown in **Figure 2.3.22**. A_{S0}^{N} monotonically increases as *Z* of the interfacial layer gradually decreases. Note that a strong correlation between the numerical simulation results A_{S0}^{N} and the analytical results of the S0 mode attenuation shown in **Figure 2.3.18** is seen: the S0 mode attenuation gradually decreases as *Z* of the interface layer decreases, while A_{S0}^{N} gradually increases as the interface *Z* decreases. These results demonstrate

that A_{S0}^N represents the attenuation behavior of the S0 mode owing to changes in the interface bond condition in a quantitative fashion.
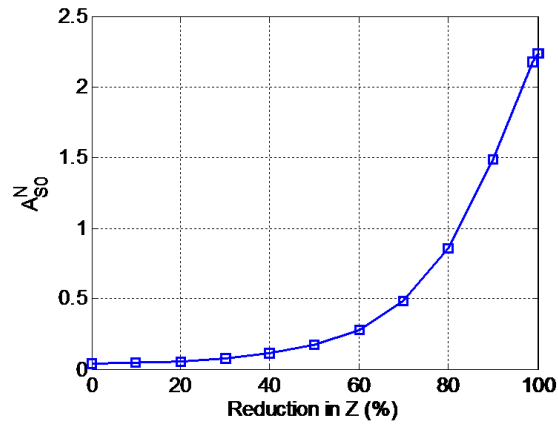

Figure 2.3.22. *Normalized S0 mode magnitude as a function of reduction in Z of the interfacial layer.*

2.3.3.4 Experimental validation

A series of experiments were carried out to investigate the feasibility of the proposed approach. The air-coupled ultrasonic test setup is shown in **Figure 2.3.23(a)**. A scanning air-coupled ultrasonic transmitter (AT120, Airmar Technology Corp.) generated guided waves at 48 different positions along a line with a 5 mm spacing between excitation points; the test configuration is shown in the magnified view in **Figure 2.3.23(a)**. The center frequency of the excitation was 125 kHz. The corresponding guided wave responses were measured by a contact-type accelerometer receiver (352B10, PCB Piezotronics Inc.). Through the concept of linear reciprocity, this test configuration with moving excitation locations and fixed sensing location is equivalent to the one of fixed excitation and moving sensing positions that is represented in the numerical simulation (**Figure 2.3.23**). An excitation circuit (T1, Airmar Technology Corp.) was used to derive the air-coupled transmitter, and a signal conditioner (PCB 442c04, PCB Piezotronics Inc.) to amplify analog signals measured by the receiver. The measured guided wave signals were digitized using an analog-to-digital (A/D) converter (NI USB-6366, National Instrument Inc.) at a sampling rate of 2 MS/s. To improve signal-to-noise ratio, time signals were measured 50 times at each scanning position and then time averaged.

The tested steel-clad concrete specimens that represent different interface conditions are shown in **Figure 2.3.23(b)**. Specimen A was prepared without any foreign materials at the interface to simulate a well bonded steel-concrete interface. Furthermore, half of the surface of Specimen A has a roughened surface, while the other half remains smooth as shown in **Figure 2.3.23(b)**. Specimens B and C have thin Styrofoam pieces attached on the interface with low and high spatial densities respectively to simulate lower and higher degrees of weakened interface. Specimen D has oil and dirt at the interface so that the entire interface should be weak. Specimen E is a traction-free steel plate that represents a fully disbonded interface. All the five steel plates in the

prepared specimens have the same dimensions (533 mm x 152 mm x 19 mm) and nominal material properties. In preparation of underlying concrete layers for Specimens A to D, fresh concrete was directly poured onto the steel plates placed on the bottom of concrete prism molds. Note that all the four underlying concrete layers for Specimens A to D were prepared in a same day with the same mixture batch using material component proportions shown in **Table 2.3.2**.

(a)

(b)
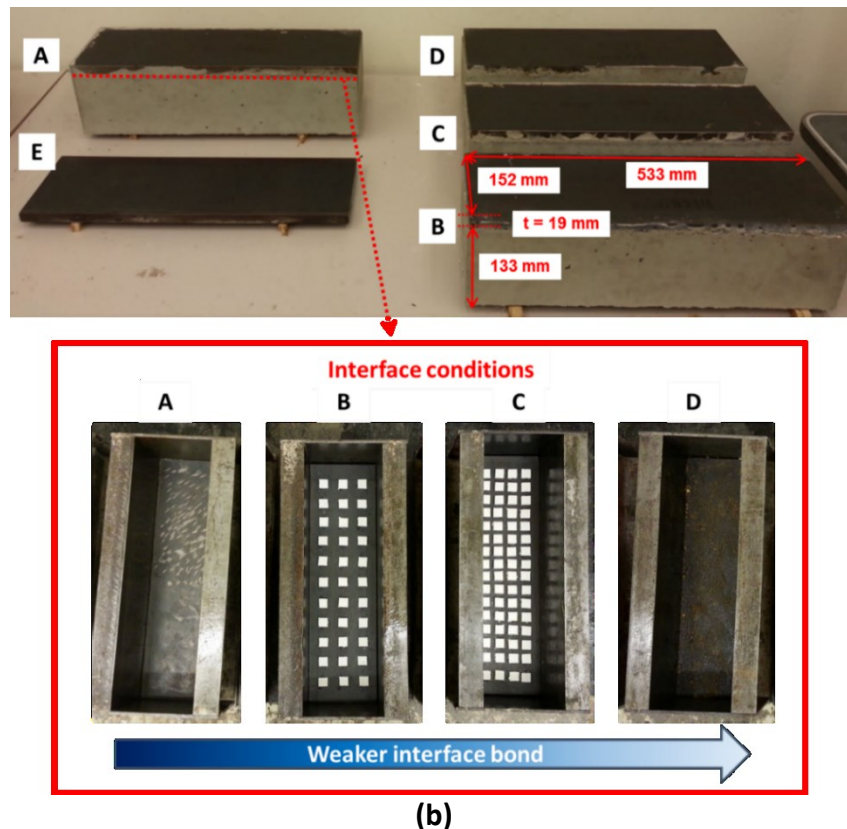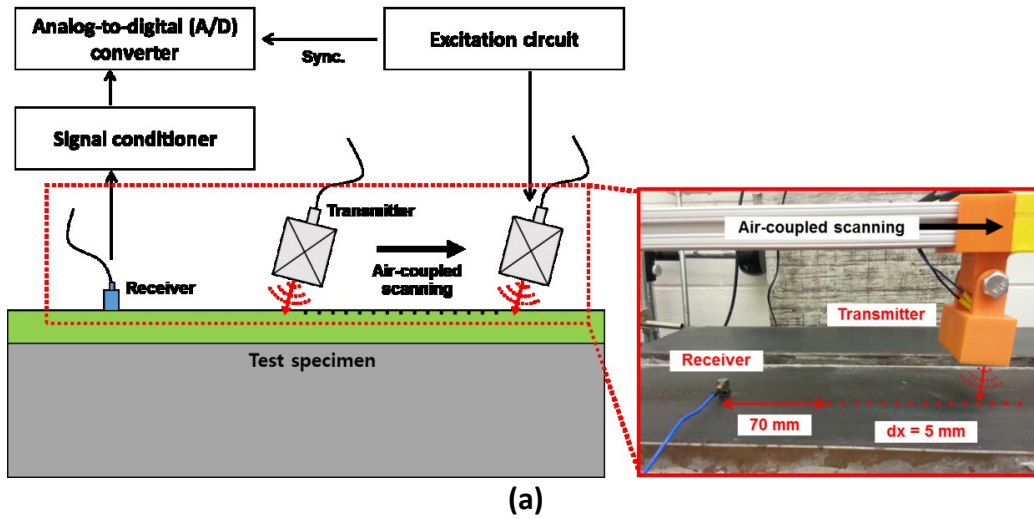
Figure 2.3.23. *Experimental setup: (a) a schematic illustration of the air-coupled ultrasonic scanning setup and (b) specimens with different interface bonding conditions.*

**Table 2.3.2**. *Mix design proportion for underlying concrete layers.*

Contents	Unit weight [kg/m³]
Water	192.7
Cement	406.5
Fly ash	71.7
Coarse aggregate*	953.5
Fine aggregate	663.5

*The nominal maximum aggregate size is 25.4 mm.

The *f-k* domain magnitude spectra for all specimens are shown in Figure **2.3.24**. The magnitude spectra were normalized by the maximum spectral value in the case of Specimen A. Individual guided wave modes are clearly isolated and identified in *f-k* domain. Similar to the numerical simulation results shown in **Figure 2.3.21**, the nominally well bonded interface case (Specimen A) shown in **Figure 2.3.24(a)** shows the lowest S0 mode magnitude, while the weakly bonded cases (Specimens B to D) and the disbonded case (Specimen E) show higher S0 mode magnitudes. The A0 mode magnitudes do not vary much for different interface bonding conditions. These results show a good agreement with the numerical simulation results in that the S0 mode behavior shows high sensitivity to steel-concrete interface bonding conditions while the A0 mode is largely unaffected.

The normalized S0 mode magnitude A_{S0}^N for three repeated tests at 125 kHz for all the specimens, is shown in **Figure 2.3.25(a)**. To investigate the experimental repeatability, A_{S0}^N values obtained from three repeated tests with completely reset test setups (transmitter and receiver re-installed) for each measurement are displayed. As shown in **Figure 2.3.25(a)**, A_{S0}^N values obtained from each specimen show good repeatability with only relatively minor variation. In **Figure 2.3.25(b)**, the average A_{S0}^N of three repeated tests for each specimen is shown along with the numerical predictions of A_{S0}^N for the well bonded (zero percent reduction in Z) and fully disbonded cases (100 percent reduction in Z) shown in **Figure 2.3.22**. The A_{S0}^N value for the disbonded case obtained from experiment (Specimen E) shows good agreement with the numerical prediction. Specimen A, which represents a nominally well bonded interface, shows the lowest A_{S0}^N value on average, and Specimen E, the fully disbonded interface, the highest value. Specimens B to D, which represent partially bonded interfaces with incrementally weaker bonding conditions, show increasing A_{S0}^N values similar to the numerical simulation results shown in **Figure 2.3.22**. These results demonstrate that the dimensionless damage index A_{S0}^N obtained

by the proposed signal processing scheme enables quantitative characterization of steel-concrete interface bonding conditions. However, the experimentally obtained A_{S0}^{N} value for Specimen A is higher than that numerically predicted for the well bonded condition (zero percent reduction in *Z*), although the specimen was designed to represent a well bonded interface. We assert that this discrepancy between experimental and numerical simulation results are caused by a non-perfect, weakened interface bond in Specimen A, especially in the region where the steel plate surface is smooth.
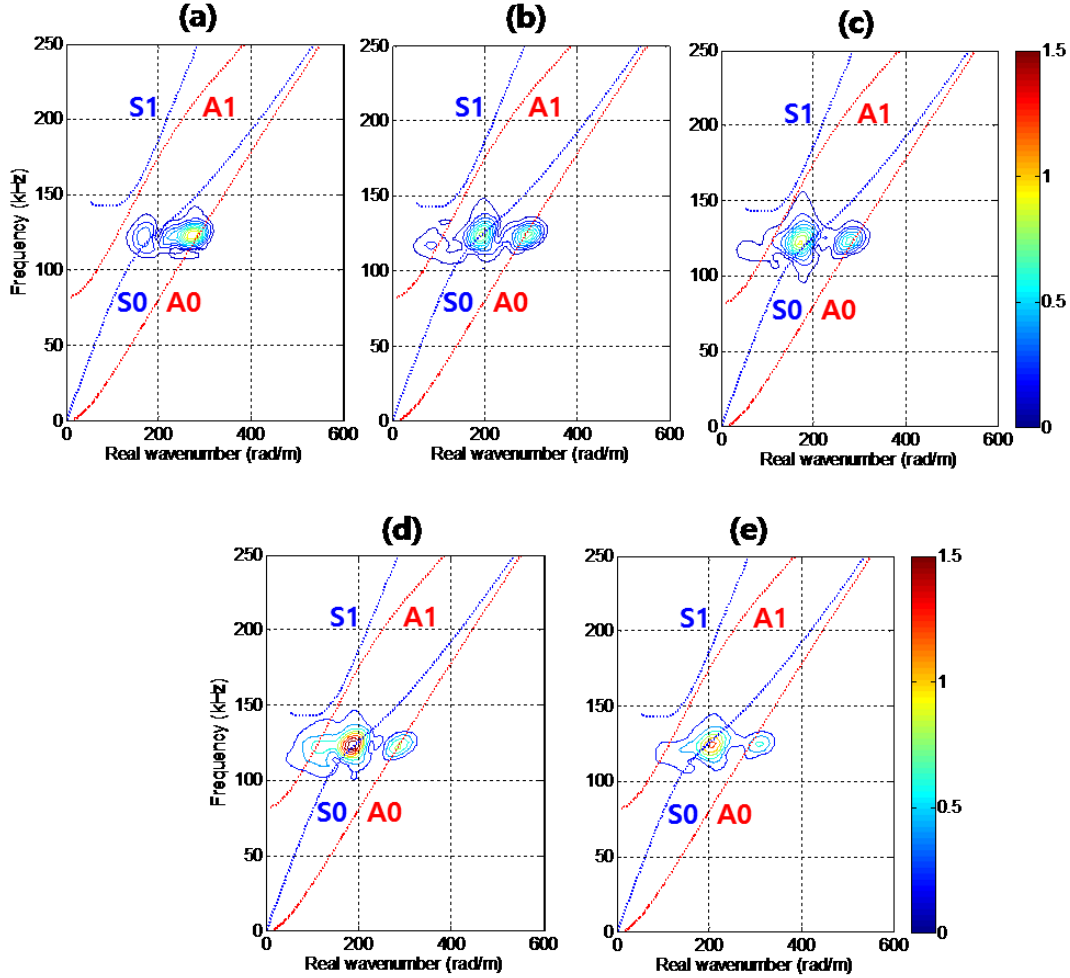
Figure 2.3.24. *F-k domain magnitude spectra for specimens (a) A, (b) B, (c) C, (d) D and (e) E.*
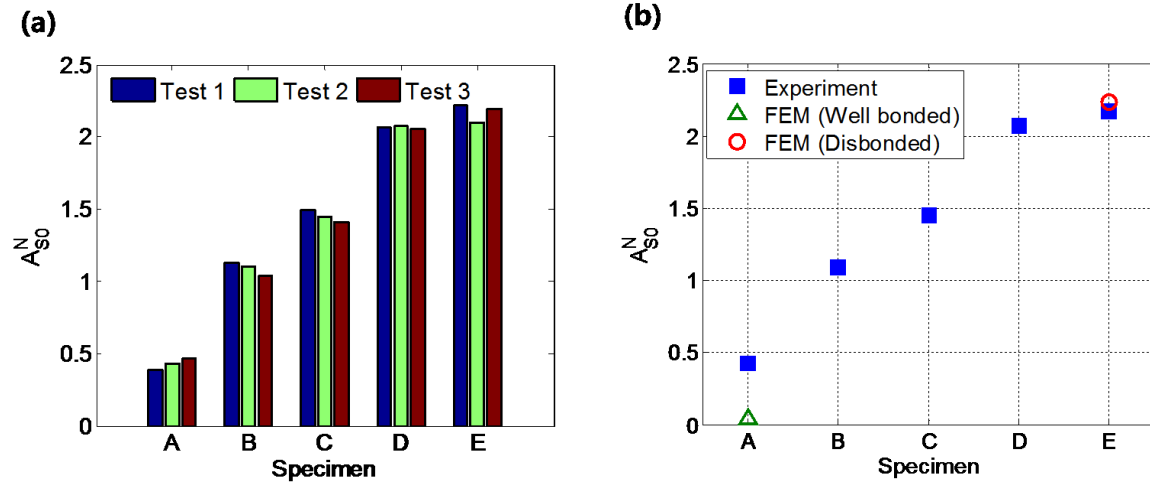
Figure 2.3.25. *Normalized S0 mode magnitude* A_{S0}^{N} *for the five specimens (a), and average experimental data (b) where numerical predictions for the well bonded (A) and fully disbonded (E) cases are indicated with hollow symbols.*

2.3.4 References

[1] Nuclear Regulatory Commision (NRC), Premature degradation of spent fuel storage cask structures and components from environmental moisture, 2013.

[2] ACI Committee 349, Evaluation of existing nuclear safety-related concrete structures, 2002.

[3] S. Johnson, Degradation mechanisms and inspection techniques for concrete structures in dry storage systems for spent nuclear fuel, Palo Alto, CA, 2015.

[4] K.F. Graff, Wave motion in elastic solids, Dover Publications Inc., New York, 1975.

[5] M.B. Drozdz, Efficient finite element modelling of ultrasound in elastic media, Mech. Eng. (2008) 1–220.

[6] P. Rajagopal, M. Drozdz, E.A. Skelton, M.J.S. Lowe, R. V Craster, On the use of absorbing layers to simulate the propagation of elastic waves in unbounded isotropic media using commercially available Finite Element packages, NDT E Int. 51 (2012) 30–40. doi:10.1016/j.ndteint.2012.04.001.

[7] W.T. Thomson, Transmission of elastic waves through a stratified solid medium, J. Appl. Phys. 21 (1950) 89–93. doi:10.1063/1.1699629.

[8] N.A. Haskell, Dispersion of surface waves on multilayered media, Bull. Seismol. Soc. Am. 43 (1953) 17–34.

[9] L. Knopoff, A matrix method for elastic wave problems, Bull. Seismol. Soc. Am. 54 (1964) 431–438.

[10] M.J.S. Lowe, Matrix techniques for modeling ultrasonic waves in multilayered media, IEEE Trans. Ultrason. Ferroelectr. Freq. Control. 42 (1995) 525–542. doi:10.1109/58.393096.

[11] N. Ryden, M.J.S. Lowe, Guided wave propagation in three-layer pavement structures, J. Acoust. Soc. Am. 116 (2004) 2902. doi:10.1121/1.1808223.

[12] H. Song, J.S. Popovics, Characterization of steel-concrete interface bonding conditions

using attenuation characteristics of guided waves, Cem. Concr. Compos. 83 (2017) 111–124. doi:10.1016/j.cemconcomp.2017.07.001.

2.4 Sensor Delivery System

This section describes the design, construction, and testing of the robotic sensor delivery system. The system is capable of entering the dry storage cask, maneuvering around the interior of the cask, taking measurements of the storage canister, and then exiting the cask for retrieval and reuse. The integrated sensors include Laser Induced Breakdown Spectroscopy (LIBS), Electromagnetic Active Transducers (EMATs), temperature measurement probes, and a Geiger-Muller counter, allowing characterization of the canister surface degradation, material composition, weld quality, temperature, and radiation. The system is controlled remotely through a computer Graphical User Interface (GUI) and integrates measurements from all sensors through a local area network. The system is designed for fault-robust recovery from the cask, and to prevent operator exposure to radiation. Although all elements are discussed, the primary focus of this this section is to present and discuss the design elements specific to the robotic delivery system.

The description of the sensory delivery system presented in the following subsections is a summary of a significant body of prior work. This work ranges from development of the initial system concept and dimensional analysis, to a working prototype with integrated sensors capable of taking measurements on an in-use canister. Throughout the development, mock-up systems were developed that ranged from a transparent representation of the annulus spacing around a cask to study wedging and jamming of the robot, to a full-height 1:1 scale MPC mock up for demonstration purposes.

2.4.1 Requirements

The application focus of the sensor delivery system is on the inspection of vertical dry storage canisters. While the focus is specifically on the HI-STORM 100S vertical cask architecture, the general inspection requirements are similar for other storage architectures.

The general functional requirements of the inspection system are as follows:
- The robot must fit through the outlet vent of the HI-STORM 100S and down the ventilation channels formed between the MPC and the overpack;
- The robot must navigate through the vent and into a desired ventilation channel;
- The robot construction must enable, without significant redesign, the ability to operate with all functional sensors at the higher operational temperatures of the dry-storage containment;
- The robot must enable, without significant redesign, the operation for the longest inspection duration – estimated to be 8 hours – with little performance loss, in an extreme radiation environment (estimated to be 27 krad/hr);
- The robot must be easily retrieved in the event of sensor or power failure, and leave no material behind in the canister nor damage the canister in any way;
- The robot must support, place, integrate and operate necessary sensor systems for comprehensive canister and overpack inspection.

2.4.2 Prior work by others related to robotic canister inspection

Existing cask inspection technologies depend on the configuration of the cask. Bolted casks have testing ports used to measure pressure changes between the inner and outer lids in order to monitor the cask for potential leaks [1]. Welded casks, like the HI-STORM series, have the testing ports sealed after initial manufacturer testing, and do not retain any ports for later monitoring during storage; it is assumed the two welded lids will together prevent any leakage [1]. Successful interior surveys of vertical casks were performed in 2004 and 2007 using miniature borescopes with radiation-resistant cameras and radiation sensors (Figure 2.4.1).
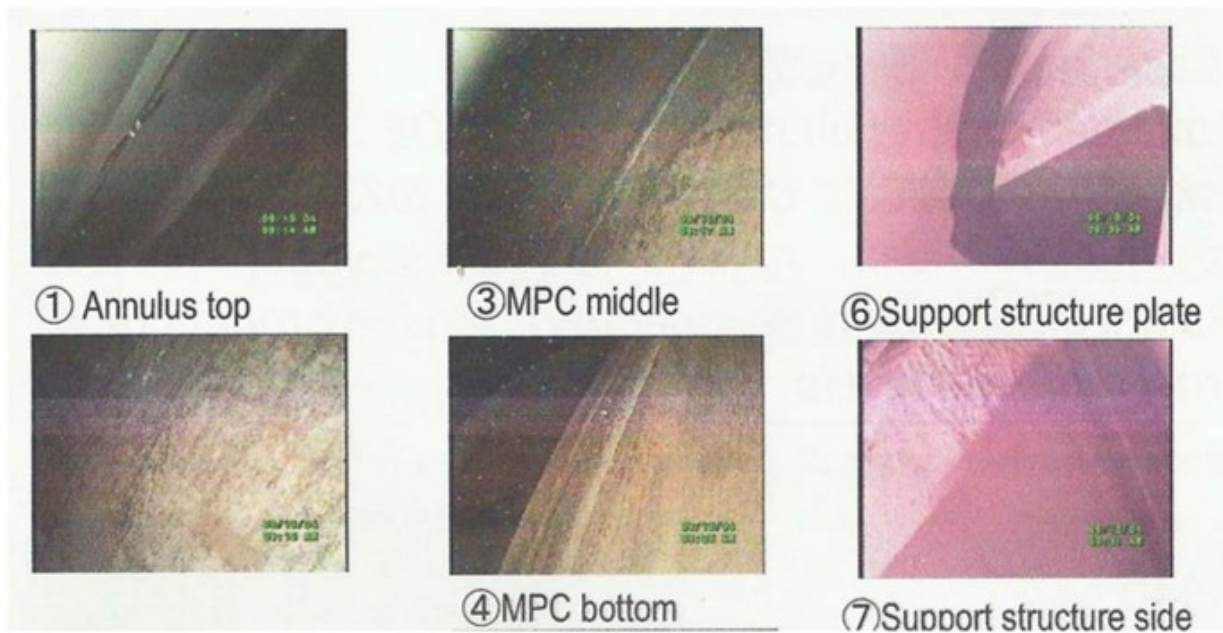
Figure 2.4.1. *Images from borescope visual survey in a vertical cask system, obtained by CRIEPI workers in collaboration with INL investigators, after [1].*

2.4.3 Development of the robotic delivery system concept

Due to the cost of developing temperature- and radiation-resistant stand-alone robotic systems, the inspection system was conceptualized even in the proposal stage as a guided wand. This decision allows power, data storage, and guidance systems to be located outside the cask. In the thesis work as part of the project, McNelly developed the guided wand concept into a hybrid robotic system, implementing designs from both wand and autonomous robot systems [2]. The hybrid design concept consisted of semi-autonomous cars containing sensors that would traverse the ventilation channel, and a guidable arm to deliver the sensor cars to the entrance of the ventilation channel.

2.4.3.1 Dimensional analysis of sensor cars

The dimensions of the ventilation channel has the largest impact on the sensor design, as all the desired sensors must fit within the small space of the channel. Additionally, the cars containing the sensors are constrained in size not just by the dimensions of the channel itself, but also the

fact that the sensor cars must traverse across the MPC and make a 90 degree turn into the ventilation channel (see Figure 2.4.2).

(a) Insertion   (b) Extraction
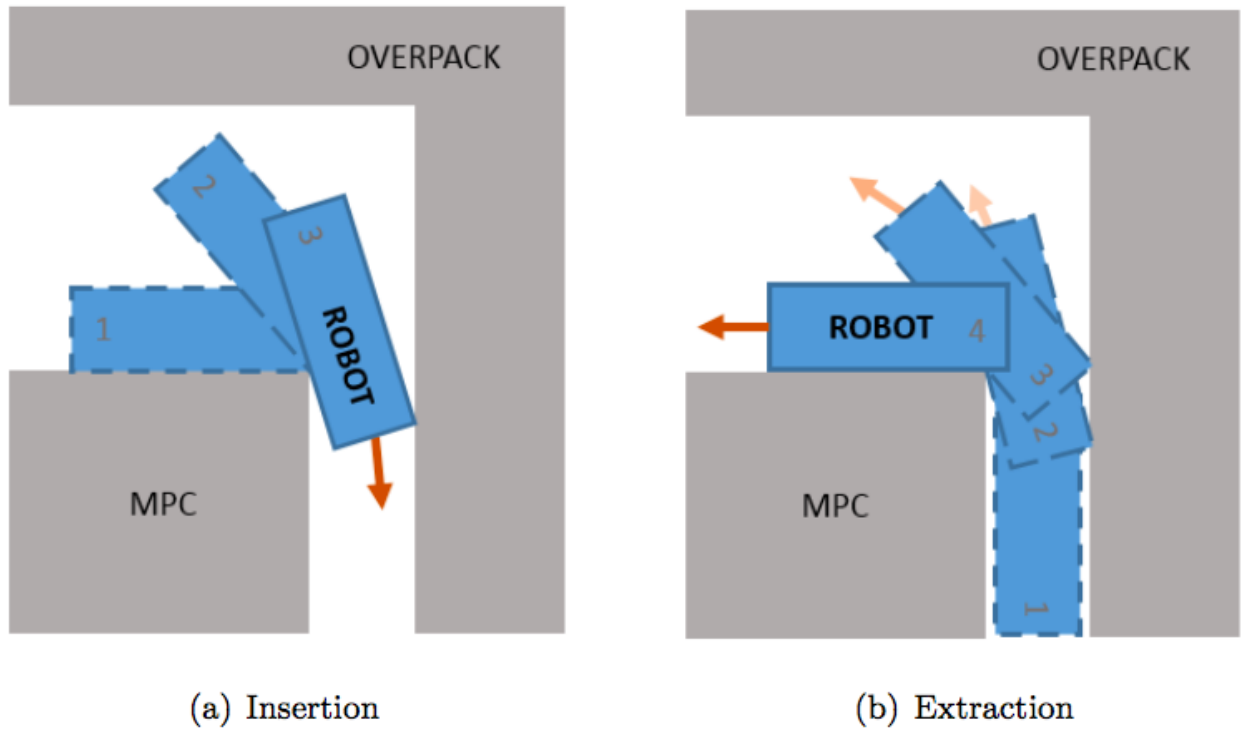
Figure 2.4.2. *Insertion and Extraction of robot sensor cars, after [2].*

2.4.3.2 Wedging and Jamming Analysis

The sensor car train is most susceptible to getting stuck when entering and exiting the ventilation channel (Figure 2.4.3). Starting with the dimensions of the ventilation channel as provided by Holtec, McNelly determined the maximum sensor car external dimensions that could enter the channel by adapting the wedging and jamming analysis typically used for peg-in-hole assembly of parts [2].
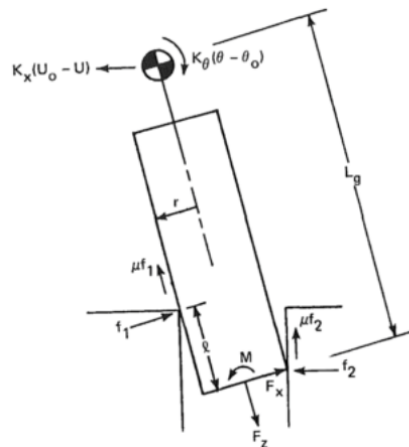
Figure 2.4.3. *Diagram of forces and moments on the peg-in-hole problem during two-point-contact, after [3].*

Wedging and jamming are two situations in which the peg becomes stuck in the hole. Jamming is defined as the condition in which the forces and moments acting on the peg are in the wrong proportions, preventing movement [3]. Wedging, in contrast, is caused by the geometry and deformation of the parts involved in assembly [3]. Due to friction between the hole and the peg that is being inserted into it, the peg may become wedged or jammed in the hole during assembly. The ability of the peg to become jammed or wedged is dependent on its geometry, the geometry of the hole, and the forces involved in assembly (see Figure 2.4.3).
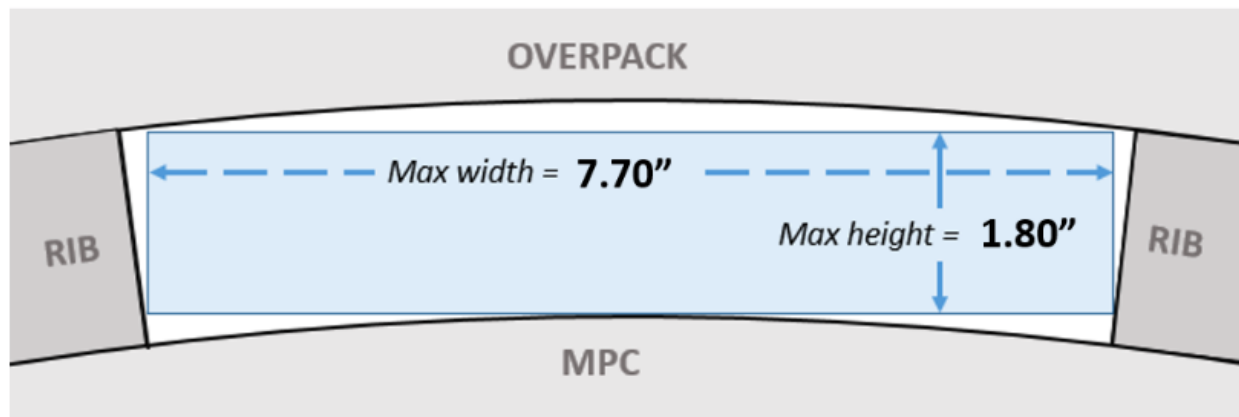
Figure 2.4.4. Maximum available rectangular space based on cask geometry, after [2].

Similarly, due to friction between the surfaces of the sensor robot and the MPC or overpack, the sensor car could become wedged or jammed. The peg-in-hole problem was applied to the sensor robot to determine an optimal geometry for the sensor robot to prevent wedging or jamming within the cask. The sensor cars needed to be sized to prevent jamming during both insertion and extraction, and the forces on the cars are different in each situation.

For the wedging and jamming analysis, McNelly simplified the vent channel clearance to be rectangular (Figure 2.4.4), and assumed the sensor car to be a rectangular prism. The maximum angle of insertion was then calculated according to sensor car height and width (Figure 2.4.5).
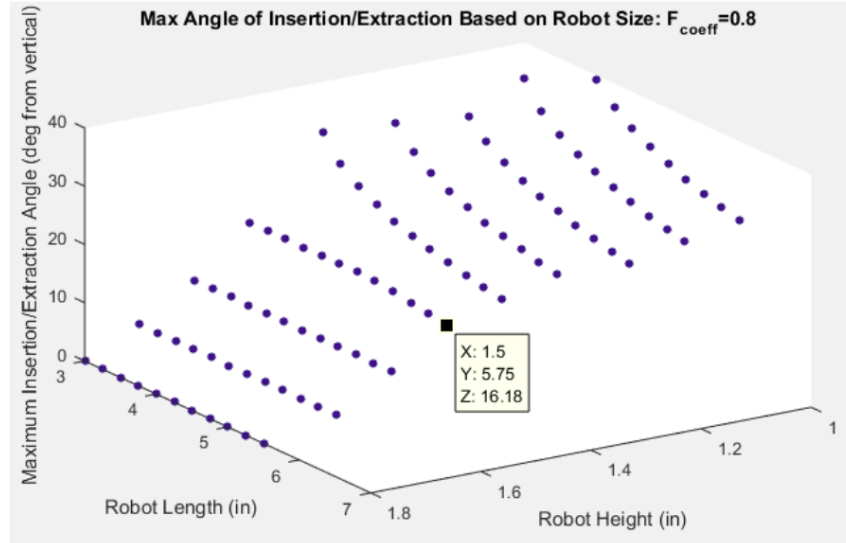
Figure 2.4.5. *3D plot of sensor car insertion angle versus sensor car height and length to avoid wedging and jamming, after [2].*

Choosing an insertion angle of 15 degrees from vertical, the optimal calculated external height and width that would prevent both wedging and jamming is shown in Figure 2.4.6.

height - length - width
1.50" x 5.75" x 7.00"
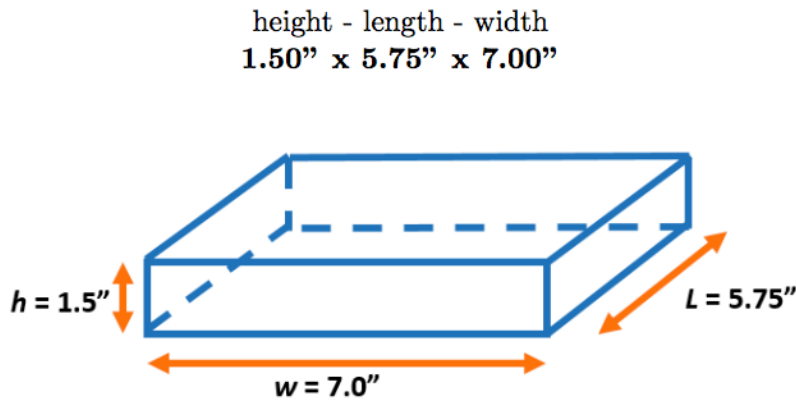
Figure 2.4.6. *Maximum sensor package external dimensions, from McNelly dimensional wedging and jamming analysis, after [2].*

Layered wheels were added to the concept design to reduce friction between the sensor cars and the surfaces they touch, and to prevent scratching or other damage to the MPC (Figure 2.4.7). With the maximum outer dimensions of the sensor car determined, it became clear that multiple cars tethered together in a "train" would be required to provide enough internal space to house all of the desired sensors. This complicates the peg-in-hole problem into a multi-peg system; however, since the jamming calculations exist as a function of force direction and coefficient of friction, it was assumed that linking sensor cars would not have a drastic effect on jamming [2].
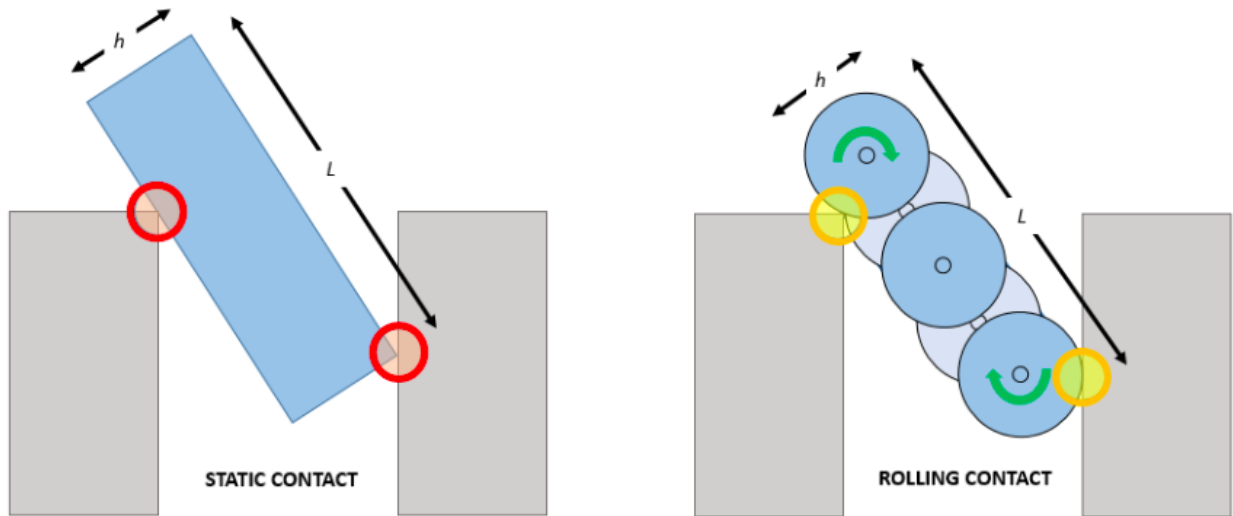
Figure 2.4.7*. Wheels were added to the sensor car to reduce friction and prevent damage to surfaces, after [2].*

Physical prototypes of the robot were constructed with 1:1 scale, and tested within a simulated mock-up of the annulus space. Experiments using this mock-up confirmed the wedging and jamming calculations gave correct predictions for both jamming/wedging conditions and for jam- and wedge-free situations.

2.4.3.3 Delivery Arm Concept

Two different methods of delivering the robot to the ventilation channel were explored in McNelly's thesis work [2] – the first was a navigable, self-propelled robotic sensor car, and the second was a passive sensor car delivered using a mechanical arm. Using the mechanical arm, the sensor robot would be delivered to the ventilation channel, and the arm would rotate around the center of the MPC to position the robot above different ventilation channels (Figure 2.4.8) [2].
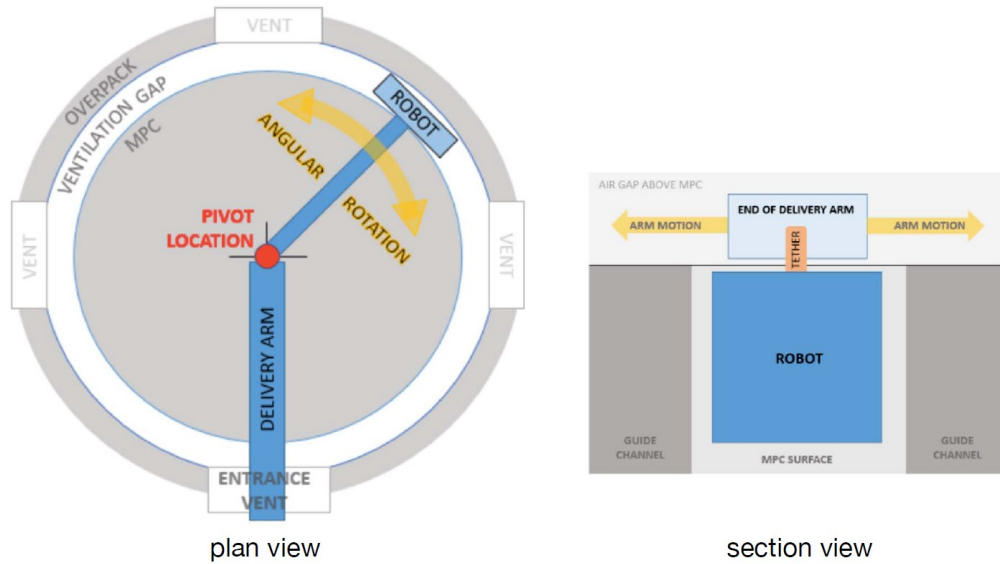
Figure 2.4.8. A diagram of initial delivery arm concept showing the arm insertion and pivoting to different ventilation channels, after [2].

The end of the delivery arm was conceptualized to have a rounded to allow for gravity-assisted sensor car insertion into the ventilation channel. This shape, generally called the arm "hump", was based on the previously-decided insertion angle of 15 degrees from vertical (Figure 2.4.9). Both active tilting mechanisms and passive ramps were considered (Figure 2.4.10).
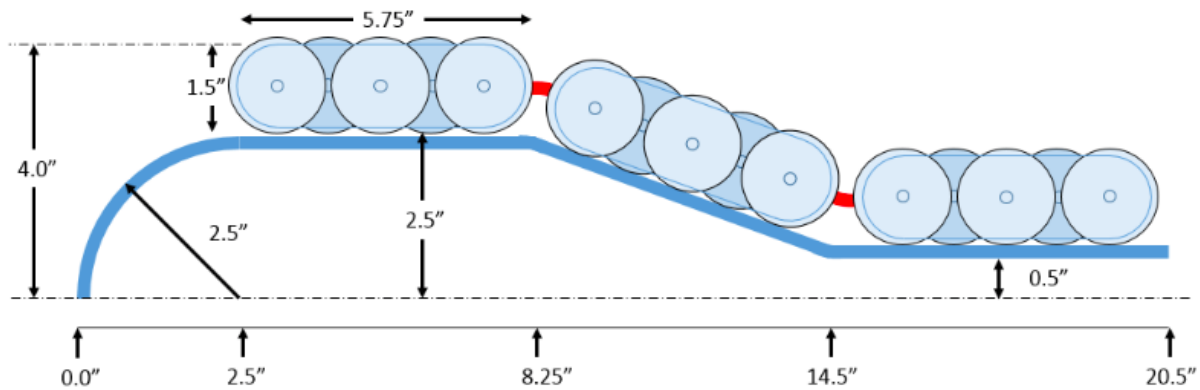
Figure 2.4.9. Diagram of initial delivery arm concept from McNelly [2], showing it shaped to allow gravity to assist in sensor car insertion into the ventilation channel.
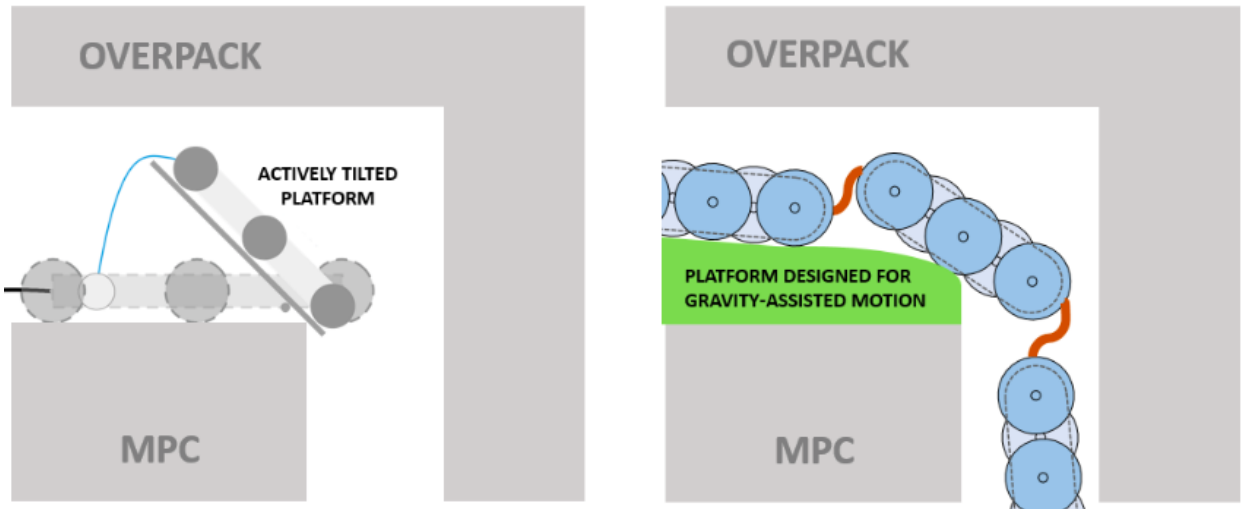
Figure 2.4.10. Two possible mechanisms considered to achieve sensor car insertion angle requirements of 15 degrees.

2.4.3.4 Entering the Cask

The ventilation opening to the cask is located in the cask lid, twenty feet above the ground. McNelly proposed locating the robot system on a support scaffold, with the control center and operator located on the ground (Figure 2.4.11).
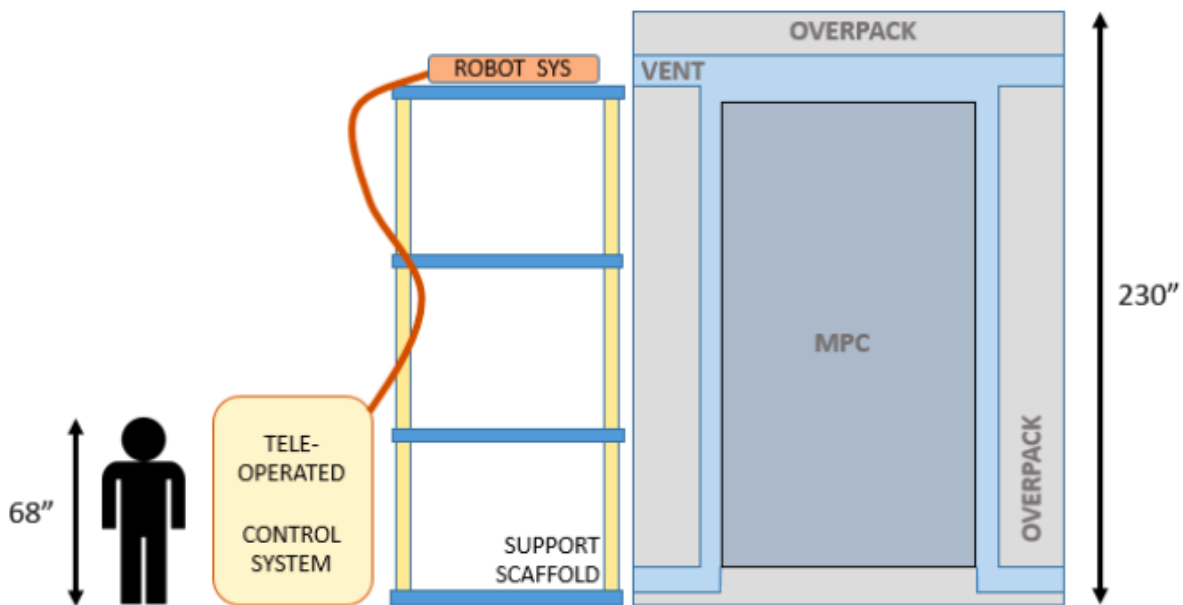
Figure 2.4.11. Diagram of cask entry concept, showing support scaffold and operator control center, after [2].

2.4.3.5 Radiation Limits Assumed for Robotic Development

As part of the preliminary work on this project, the modeling team at South Carolina led by Dr. Knight built an analytical model of the interior of the HI-STORM 100 cask to model the radiation emitted by the spent nuclear waste stored in the canister [4]. The radiation model was built using

code packages ORIGEN-ARP and MCNP based on dimensions from the Holtec drawings (Figure 2.4.12).
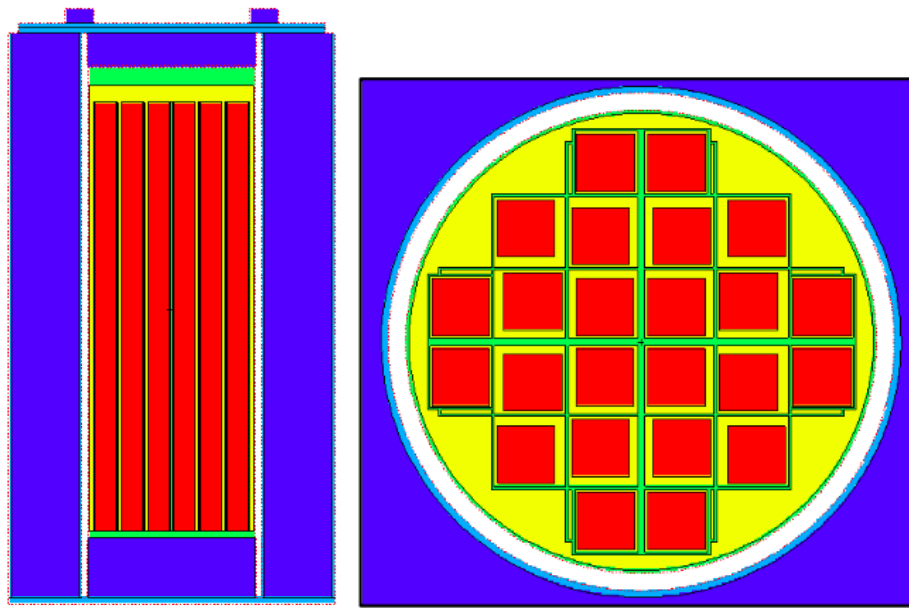
Figure 2.4.12. *Cross section and top view and of HI-STORM 100 METCOM canister model built in MCNP for radiation modeling, showing baskets that hold the spent fuel rods, after [4].*

Both the total neutron flux and photon flux on the outer wall of the MPC, along with the Cobalt activation dose equivalent, were estimated using the analytical models [4]. The resulting values are shown in Table 2.4.1.

Table 2.4.1. *Values obtained from radiation modeling*

Total neutron flux:	6.78×10^6	$1/cm^2$-sec
Total photon flux:	3.45×10^{13}	$1/cm^2$-sec
Dose equivalent:	1.87×10^{-7}	mrem/hr

2.4.3.6 Dry Cask Storage Thermal Characterization

As part of the preliminary work on this project, Knight et al. also built an analytical model of the interior of the HI-STORM 100 cask to model the interior temperature of the cask [4]. The thermal model was built using Cycle 3 and 4 of Cobra-SFS, and included friction factors and drag losses when determining the heat transfer from the natural ventilation of the inlet and outlet vents on the overpack and the conduction through the overpack material. Knight's team also modeled the radiative heat transfer inside the cask using a separate program called RADGEN [4]. The Cobra-SFS code used was specifically designed and validated at the Pacific Northwest National Laboratory (PNNL) for analysis of spent nuclear fuel storage [4].

Running at a total power of 34 kW, which corresponds to the maximum power output (i.e. hottest) that the spent fuel rods will be stored in the canister, the Peak Clad Temperature (PCT) of the fuel rods inside the canister was calculated to be 667.9 F (353.3 C) [5]. However, the more

relevant value to the sensor robot is the air temperature inside the cask between the MPC and overpack. The MPC surface temperatures were calculated at a range of heat decay loads from the fuel rods (Figure 2.4.13). These calculations were then used to determine the maximum canister temperature after a period of cool down years after loaded into the canister, for a variety of heat decay loads (Figure 2.4.14).
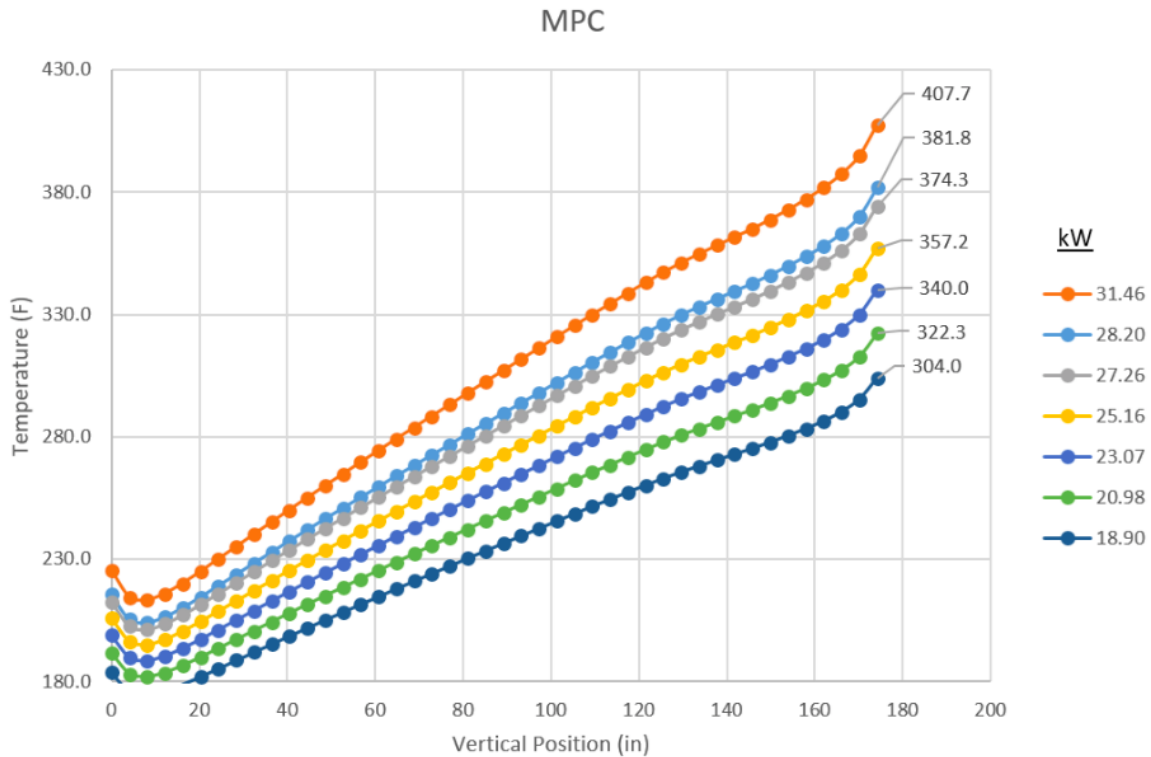
Figure 2.4.13. *MPC surface temperature versus height for various fuel rod decay heat loads, after [6].*
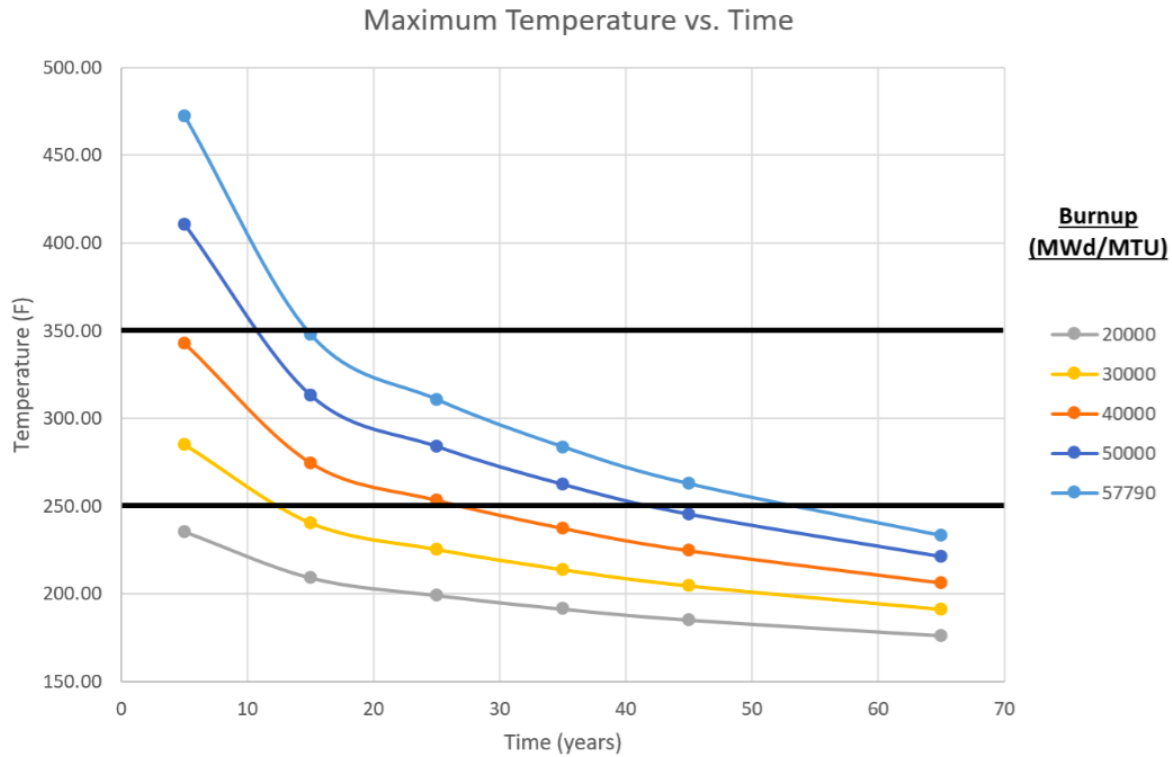
Figure 2.4.14. *Maximum MPC surface temperature versus cooldown time (in years) for various fuel rod decay heat loads, after [6].*

2.4.4 Design Constraints

The inspection system must operate under a large number of different constraints. To understand the full requirements and interactions between each constraint, it was helpful to first approach each constraint individually. However, with the large number of dimensional, thermal, material, and operational constraints, it was likely that a design meeting one constraint would not fulfill another. For example, most teleoperated robots use servo motors or other electronic actuators. The heat and radiation inside the cask, however, prevents the use of electric motors without thick shielding and active cooling. Some pipe inspection robots have used magnetic wheels to allow them to climb up and down vertical steel surfaces [7], but this could scratch or damage the MPC surface and could not be used. The combination of high temperature and high radiation also further restricts the materials suitable for use inside the cask, compared to just one or the other. When two or more constraints intersected, the most-limiting constraint was typically analyzed and designed for first. To stay within budget and time constraints, any components that could achieve the temperature and radiation requirements, but would require custom manufacturing to do so, had to be bought off-the-shelf instead. The systems were designed such that the constraints would be met, after the placeholder components were replaced. The following subsections explain each constraint for the robotic system design in detail, including how the constraint affected the ultimate design choices for the final design.

2.4.4.1 High Temperature Operational Requirements

Previous sections characterized the relationship between interior temperature versus the cask age after initial loading, and these relationships defined the operational temperature goals for the robotic design. The project teams focused on three levels of cask interior temperatures: 350F was the hottest possible temperature at which an inspection would take place. 180F was the temperature of the canisters most at risk of salt deliquesce, and 250F was an intermediate temperature between these two extremes. The lowest temperature of 180F was still at the upper limit of military-spec high-temperature electronics, and higher temperatures were understood to require some form of active cooling for any electronics to be viable. Any materials to be used inside the canister must be resistant to the highest temperatures involved, which is hereafter assumed to be 350F.

2.4.4.2 Radiation-based Material Restrictions

Besides producing heat, the spent fuel rods also emit radiation, again described in prior sections. Because of the ability of gamma radiation to damage electrical components and particular plastics, the high gamma radiation levels restricted the available materials to be used inside the cask. Due to the high temperature and radiation levels inside the cask, typical plastic bearing surfaces, such as Polytetrafluoroethylene (PTFE, and also known by the brand name Teflon) or Ultra-high-molecular-weight polyethylene (UHMW) were not useable. The two plastic options were found that met the environmental restrictions – Polyether ether ketone (PEEK) and Polyetherimide (PEI, or under the brand name Ultem). Both are rated for continuous use at high temperatures (340F for PEI and 480F for PEEK [8]) and have resistance to gamma radiation. Although PEI has slightly lower performance, it can be 3D printed by specialized machines. All plastics used on areas of the system that would enter the cask were made from PEEK or PEI; or for 3D printed parts, printing was done using a PLA placeholder for budget reasons.

Additionally, neutron activation was considered as a potential problem for some materials selected for the robotic system. Cobalt, for example, common in many magnets – and therefore also common in electric motors and actuators – is known to become radioactive itself when it undergoes neutron capture. For this reason, the designs for the robotic system minimized the use of Cobalt-based magnets and similar materials which could be susceptible to gamma and/or neutron radiation.

2.4.4.3 Preventing Damage to Canister and Recovering Robot

A key requirement in the design of the robotic inspection system is that it cause no damage the canister during inspection. The project advisory board gave each project team a list of guidelines to ensure that the inspection is truly non-destructive. Since the system was being designed specifically to the dimensional constraints of the Holtec HI-STORM 100S cask system, Holtec also provided suggestions to prevent the system from physically damaging the canister during inspection. Carbon steel, for example, is known to damage the stainless steel surface of the MPC, and a scratch or gouge from a carbon steel part could eventually lead to corrosion and SCC in the canister.

To ensure compliance with manufacturer recommendations to prevent damage to the canister, all designs followed the allowed material list provided by Holtec and the advisory board. Specifically, no carbon steel, PTFE, or PVC was used to construct any parts of the system that would enter the cask. Aluminum was used for the main structural elements of the delivery arm, vent mount, and sensor cars, and surfaces that would contact the MPC or cask were PEEK or PEI to prevent scratches.

The deposition of any parts during inspection, left inside the cask after inspection, would also qualify as damaging the cask. So the inspection system included the requirement that it must never drop any parts, no matter how small. The robot needs to be designed with minimal part count in mind, and also take precautions, such as safety wire, against screws or nuts coming loose during operation.

Besides not leaving small parts behind, the entire system was designed to be manually removable in case of power failure or mechanical error, and be robust enough to not break during this passive-removal process.

2.4.4.4 Space Constraints

As shown in the previous wedging and jamming analysis work done for this project, the overall dimensions of the robot train was constrained by the gap between the canister and the interior of the overpack. Additional constraints are imposed to the rest of the robotic system due to the cask entrance geometry, as well as the geometry of the space between the overpack and the cask.

2.4.4.4.1 Constraints to Cask Entrance

The ventilation opening is the first dimensional constraint encountered by the system during an inspection. Since the vent opening is the only means of access to the inside of the cask, the delivery arm and sensor train be sized to fit through the opening. Working from the Holtec dimensioned drawings openly available on the internet (Figures 2.4.15 and 2.4.16), the ventilation opening of the HI-STORM 100S Version B is nominally 25" wide by 6" tall.
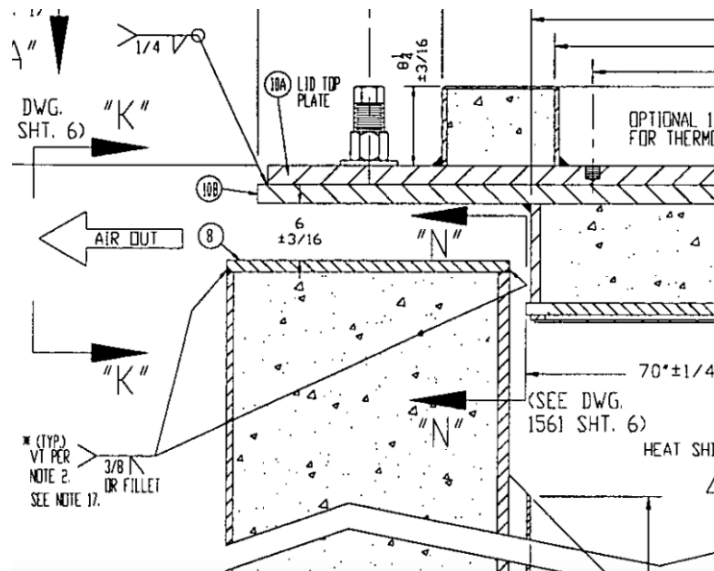
Figure 2.4.15. Section view of ventilation opening from Holtec drawings.
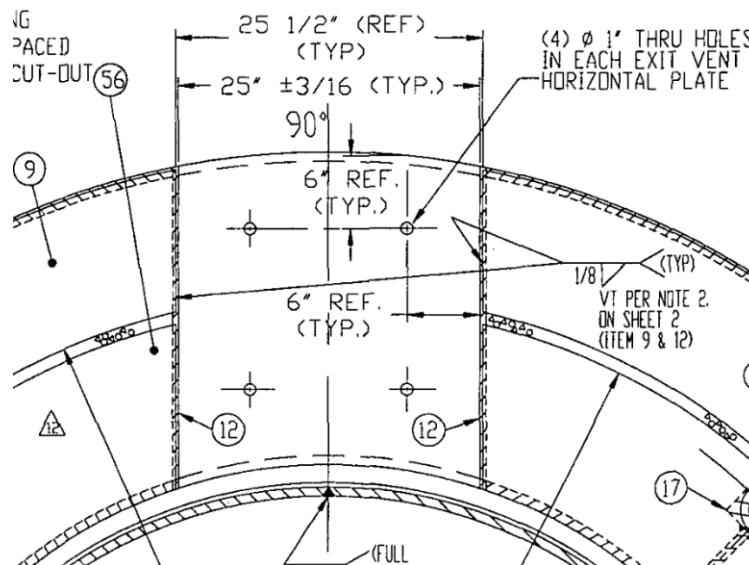
Figures 2.4.16. Top view of ventilation opening from Holtec drawings.

The steel vent piece used in the cask's vent system was provided by Holtec, and incorporated into the mockup for testing. The ventilation opening restricts the dimensions of the components of the inspection system that need to enter the cask.

2.4.4.4.2 Constraints while Taking Measurements

In order to take measurements of the MPC surface, the robot train and sensors must fit in the gap between the MPC and overpack interior. The distance from the top of the MPC to the overpack lid is variable from 6" to 18", depending on the height of the MPC (Figure 2.4.17).
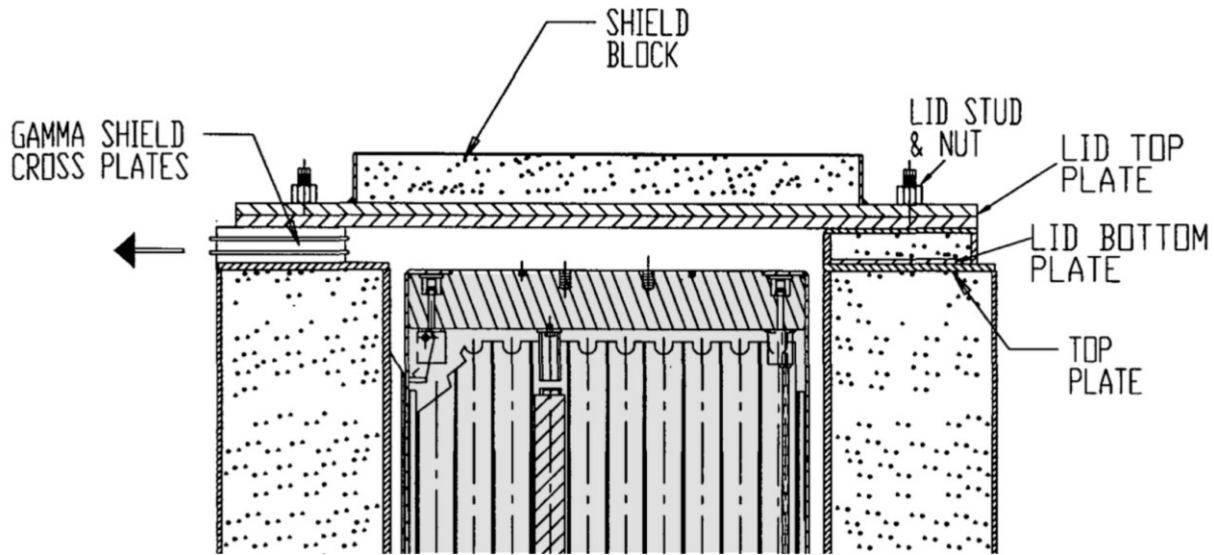
Figure 2.4.17. *Section view of top of MPC to overpack gap from Holtec drawings.*
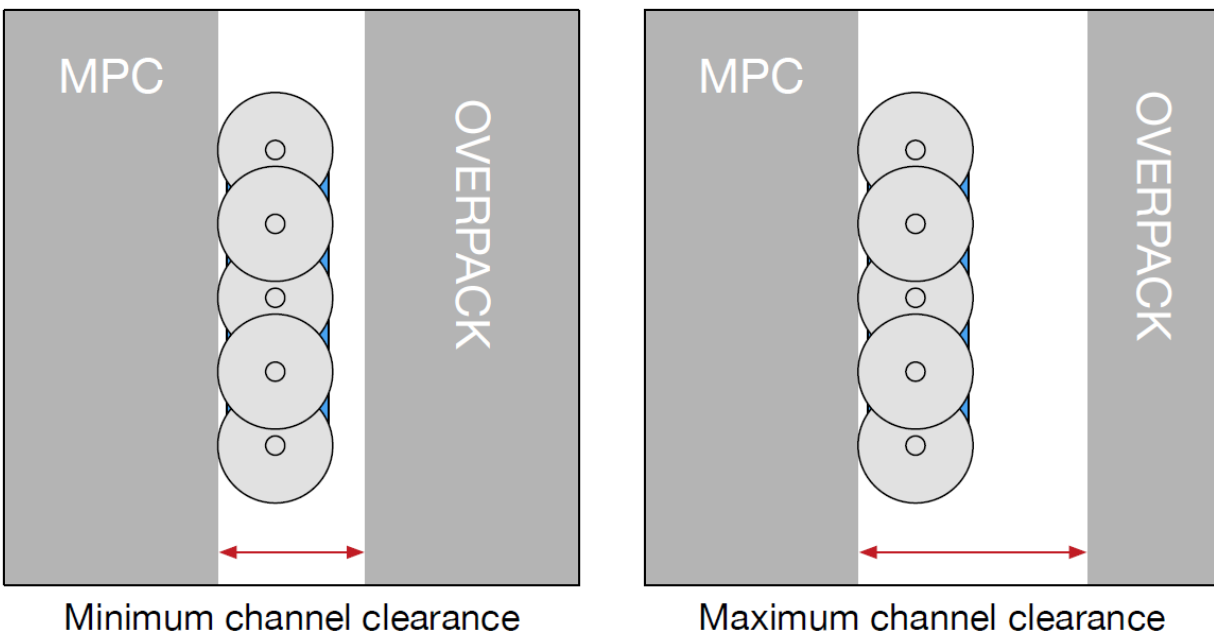
Figure 2.4.18. *Cross section diagram of sensor car in channel showing variable channel width.*

While lowered into the ventilation channel, the robot has even less space. The clearance between the overpack and MPC can range from 2" to 3.4". The guide channels in the overpack restrict the position of the MPC within the overpack, but the cask may not necessarily be centered and concentric with the overpack, making the clearance in each vent channel different. The HI-STORM 100S has rectangular guide channels (Figure 2.4.19), while the HI-STORM 100S Version B has circular guide channels.
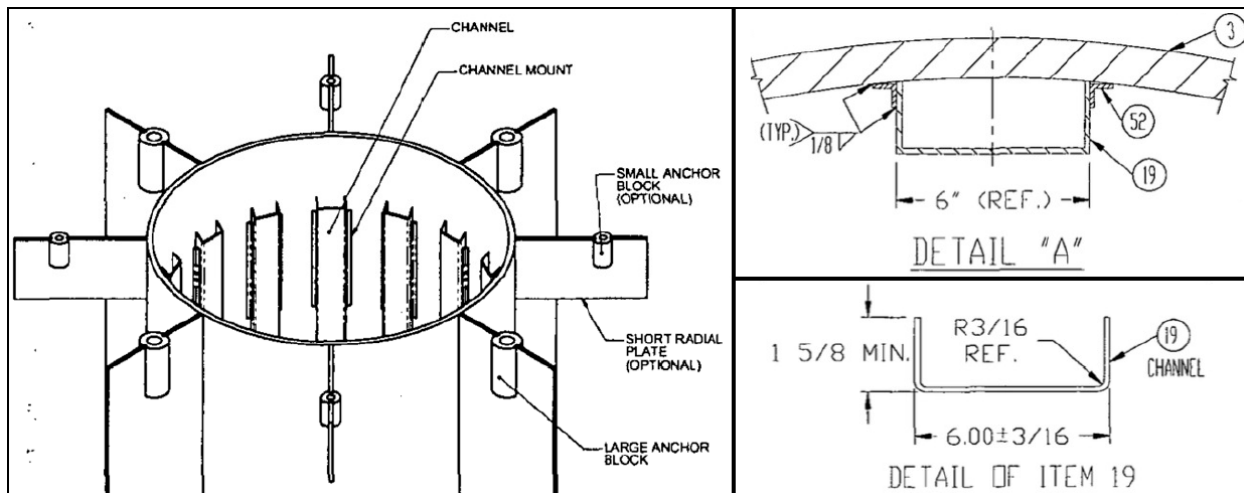
***Figure 2.4.19**. Isometric and detail views of rectangular HI-STORM 100S overpack channel guides from Holtec drawings.*

2.4.4.4.3 Constraints while entering the ventilation channel

Looking down into the ventilation channel, the sensor car train has an arc-shaped opening to fit through as described in previous sections. However, when looking at a cross-sectional view of the cask interior, it can be seen that the sensor car train must traverse a 90 degree bend to enter the ventilation channel during insertion and extraction (Figure 2.4.20).

2.4.4.5 Operating without Line-of-sight

Due to the limited space and harsh environment within the canister, the system must be operated remotely. This brings its own set of challenges to controlling, powering, and localizing the sensor robot. For power and communications, the robot must be tethered to the control center. The tether must be flexible enough to traverse the same path as the robot cars, and it must be small enough in diameter to not constrain the sensor cars' movement. The tether must also be long enough for a full insertion – running from the bottom of the ventilation channel, to the top of the MPC, out of the cask vent, and back down to the control center (Figure 2.4.20) requires a minimum tether length of 50'. Any power or data cables in the tether must be sized appropriately to operate at this length.

Additionally, because the system uses remote sensors and actuators, the system was designed to be capable of manual recovery. Every actuator was designed to "fail closed" – or, in other words, return to its retracted position when power is lost. Additionally, the shape of all components was designed such that the system can be pulled out of the cask by hand, and be durable enough to survive this manual recovery
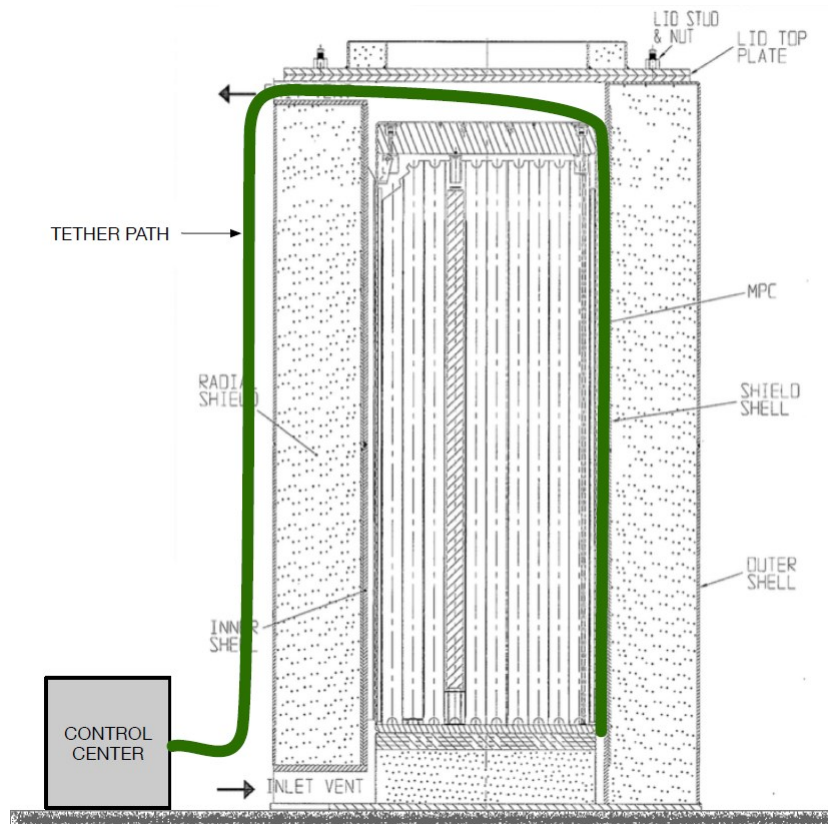
Figure 2.4.20. *Path of data and power tether (green) from control center, through cask, and to sensor robot.*

To take useful measurements and accurately maneuver the system, the operator must know the location of the system inside the cask. This localization can be performed using a combination of camera images and other sensors, such as wheel encoders or inertial measurement units. Because of the complex cask geometry, the system requires multiple cameras to keep track of each component, and the live images from each camera must be easily monitored by the operator. Any other sensor data used for localization needs to be presented to the operator as well, to be used for both live operation of the system and later analysis of the sensor measurements.

The biggest challenge the robot delivery sub-team found in operating the remote robot with no direct line of sight was in accurately determining the position of the robot. The data obtained for the robot car position was split up into two purposes: real-time data displayed to the operator, and precise data stored for post-inspection sensor analysis. The operator can use an approximate position and orientation of the robot shown in real-time to maneuver the robot inside the cask, but for the sensor measurements to be useful, more accurate positional data was recorded while measurements are being taken. Helpfully, these more precise positional data can be extracted and analyzed later, and do not need to be displayed in real time. The sensor car telemetry came from the winch encoders, and the video came from three separate cameras: the front-facing camera on the first sensor car, the downward-facing camera on the end of the delivery arm, and the camera on the vent mount showing the top of the MPC. Both sensor car telemetry and images

from in-cask cameras were designed to be displayed in real-time to aid the operator during inspections, and recorded for later use.

Not only is the interior of the cask inaccessible, but it is also too radioactive for an operator to have any direct contact with the inspection system during in-field use. Because of this, the components of the inspection system that will be inside the cask must be controlled remotely, and be robust enough to continue operation (or at a minimum, allow for retrieval) in case of operator or mechanical errors. Typically, remotely-operated robots will use small servo motors to maneuver and actuate sensors, but more specialized robots can use pneumatic or cable actuators. As described in later sections, pneumatic actuators were designed and fabricated for in-car sensor actuation due to the radiation levels affecting conventional electoral actuators.

Other aspects of the system also require actuation or remote control by the operator. The delivery arm pivot must be controlled to align the sensor cars with the ventilation channel, and the sensor cars themselves need assistance entering the ventilation channel. Both of these functions were achieved using remote cable actuation, again described in later sections. The use of remote cables again alleviated the concern about radiation or thermal influences on the motion or retrieval of the robot delivery system.

2.4.4.6 Sensor support
2.4.4.6.1 Carrying and transporting sensors
The sensor cars have been designed first to ensure they fit within the space constraints of the cask, and second around taking accurate measurements of the canister. All aspects of the system have taken into account how the design may affect the ability of the sensors to gather accurate data. For example, the EMATs house strong rare earth magnets, and must be kept clear from ferrous metals and sensitive electronics. The EMATs themselves were very sensitive to electromagnetic interference, which showed up in field and lab measurements as noise. The sensor car and delivery arm design needed to operate with the additional weight of the sensors and related actuators. The cask geometry constrained the dimensions of the sensor cars, and the sensor car geometry constrained the final allowable dimensions for the sensors held within. The EMATs imposed additional constraints on the robot design to avoid ferrous materials and electrical cables near the sensors.

2.4.4.6.2 Sensor Size Constraints
Once the sensor car final dimensions were decided by the robot delivery sub-team, these constraints were shared with the sensor development teams, so that each had a dimensional goal to design towards. All desired sensors, and the accessories required to acquire accurate data, needed to fit within the sensor cars. This meant miniaturizing not only the EMATS, LIBS, Geiger-Mueller, cameras, and thermocouples, but also the mechanisms to actuate each. Development of the miniaturized sensors and sensor actuators happened in parallel. The sensor teams were given a 4" long x 3" wide x 1.2" tall space within the sensor car chassis in which to fit the sensors, and were also provided the 3D SolidWorks model of the sensor car chassis as it was updated throughout the project.

2.4.4.6.3 Positional accuracy requirements

In order to safely operate the system, the operator of the inspection system needs to know the sensor car location within the ventilation channel. The vertical position of the sensor car also needed a minimum level of accuracy to obtain useful data from the sensor measurements. During development, the EMAT sensor team determined that measurements taken every 1/4" while traversing vertically up the MPC would provide the best coverage of the canister weld lines, but steps as large as 1/2" would be acceptable for characterizing the canister. The LIBS measurements required no specific step size, as long as the same location on the cask was not ablated more than once. It was also decided that the sensor cars should be able to return to a specific location in the ventilation channel, with accuracy matching that of the step size.

The positional accuracy goal of the system was a 1/2" step size based on the sensor requirements, both for distances between each measurement, and for the ability to travel down the channel and stop at a certain point. This imposed the constraint that the winch, delivery arm, and sensor car system design could not add more than 1/2" absolute error into the sensor car location measurement, with a precision of ½" as well. The field tests showed that the accuracy goal of ½" could be achieved but only with calibration to a reference weld line, and if this calibration was performed correctly, the accuracy could be as small as 1/16" one-sigma accuracy. The precision of motion was limited by the flexibility of the guide cables, which was found to be approximately 1/16" to 1/32". In other words, with correct calibration, the accuracy was limited by the precision, and both were limited by the mechanical flexure in the long cables used to winch the robot up and down the canister surface.

2.4.4.6.4 Radiation shielding requirements

Where possible, radiation-sensitive components in the system were shielded. Boxes with sealed walls incorporating lead shot were designed for the in-cask cameras mounted on the delivery arm and vent mount. The small size of the sensor cars, however, prevented any meaningful shielding for the sensor electronics; this required sensitive components, such as the front facing camera in the first sensor car, to instead be considered disposable. These disposable elements were designed to be easily replaced once damaged beyond usability. Radiation-resistant electronics were available via COTS suppliers, but were found too costly to fit within the budget of the project; in such situations, lower-cost COTS electronics were used, particularly the camera systems, that could be replaced later, as necessary, for high-radiation performance.

2.4.4.7 Time Constraints

To minimize the exposure of operators to excessive radiation, the inspection time needed be as short as possible. This constraint also included designing the system operation as a whole to minimize operator exposure to radiation. The goal suggested by the advisory board early in the project was one cask inspection per 8-hour day, including set-up, data collection, and tear down. Assuming one hour each for set-up and tear down, this corresponded to 22 minutes to inspect each of the 16 ventilation channels. The set-up, operation, and tear down of the robotic system needed to stay within these time constraints. Field testing, discussed in later sections, showed

that a precise scan of a single ventilation channel using the EMAT sensors could be done in roughly 10 to 15 minutes, including deployment and retrieval.

To minimize operator exposure to radiation while inserting the system into the cask, the design allows the operator to install the system into the vent rapidly, and thereafter stay fully below the shine path of the ventilation opening. After insertion in the cask, the design relies on cameras instead of direct operator line-of-sight.

2.4.4.8 Robot and Delivery System Packaging and Testing

As the sensors were integrated into the robot, the packaging space of the robot became a critical factor. To understand potential packaging options, the interior layout of the sensor robot cars was accurately modeled in 3D, and updated with each iteration of the design of the LIBS and EMATs (Figure 2.4.21). Note: additional CAD drawings of the robot system can be found in the Appendices.
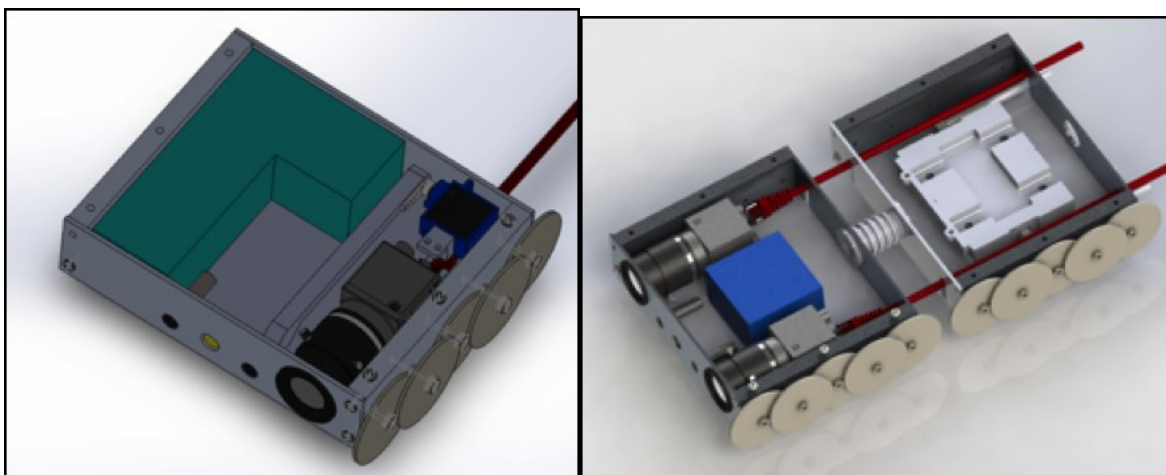
Figure 2.4.21. Early stage CAD space planning showing the front car with a camera and a version of the LIBS (left), and the first two cars with stereo cameras and prototype EMATs (right).

During the packaging process, a 3D model of the HI-STORM 100S cask was made to check clearances for the sensor car when inspecting the bottom circumferential weld. With the locations of the bottom circumferential weld and the EMATs car as shown in Figure 2.4.22, the bottom ventilation opening in some of the channels restricts the vertical motion of the sensor robot. Because of this, inspecting the weld in these channels required placement of the EMATs in the front car.
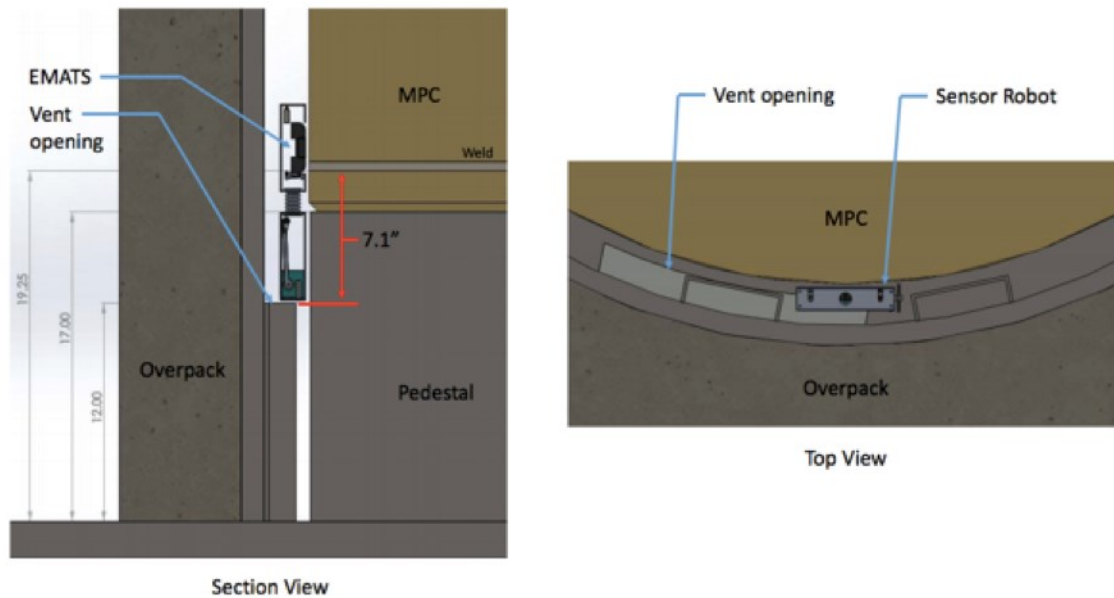
Figure 2.4.22. *Section and plan view of the sensor robot in the channels restricted by the bottom vent opening.*

2.4.4.9 Material Performance at Elevated Temperatures

To determine the integrity of the robot design while in the high-temperature cask environment, a sensor car with PEEK wheels was tested at high temperature (Figure 2.4.23). The car was placed in an oven and heated to 350 degrees Fahrenheit for 30 minutes. While in the oven and with a 5 lb weight placed on top of the car to represent the mass of the equipment inside the car, it was still able to roll freely, showing no significant deformation of the PEEK wheels at temperature.

Figure 2.4.23. *Car chassis with PEEK wheels used for thermal testing*

2.4.5 Sensor Actuation

2.4.5.1 Sensor Actuation Requirements and Design Intent

The three main sensors featured in the inspection system – EMATS, LIBS, and temperature probe – all require direct contact with the canister surface in order to take reliable and accurate measurements. Safely transporting and operating the sensors to inspection sites within a working canister is the main goal that the robotic inspection systems needed to fulfill. To both protect the sensors and to prevent the cars from getting wedged or jammed, it was determined early on in the project [2] that each sensor needed to retract back into the car chassis when not taking measurements. The sensors must also be extended out of the car and pushed up against the MPC surface to take measurements. Any actuator design must also "fail closed" – if power is lost, or some other error occurs, the sensor needs to retract into the car chassis to allow for manual retrieval of the sensor cars.

Initial designs and test builds for sensor actuation mechanisms relied on micro servo motors. After mixed results using servo motors, a custom pneumatic actuation method was prototyped and integrated into the sensor cars. This design process is explained in the sections that follow for each sensor separately, as each sensor type has its own distinct requirements.

2.4.5.1.1 EMATS Actuation Requirements

Because of the strong magnets inside the EMAT sensors, they are especially susceptible to attaching to a magnetic surface. To ensure that the sensor robot does not get hung up or stuck in the ventilation channel, which is made of a magnetic steel material, the EMATs are designed to deploy only when measurements are being taken. The EMATs are retracted inside the body of the sensor robot car at all other times. In case of power failure, the EMATs deployment mechanism is designed to fail closed and automatically retract. Additionally, the two EMATs require good, centered contact with the curved surface of the MPC for accurate measurements. The actuator holds the EMAT sensors along an arc that, assuming the robot is aligned with the canister, causes the sensors to have a flush contact with the curved MPC surface.

2.4.5.1.2 LIBS Actuation Requirements

In comparison to the EMAT sensors, the LIBS optics are not magnetic, and are therefore less likely to jam the cars in the vent channel. However, the LIBS optics are fragile and need to be precisely aligned. To prevent damage to the LIBS optics, the sensor is deployed only when measurements are being taken and be retracted inside the body of the sensor robot car at all other times. The LIBS requires just one point of contact on the MPC surface, and is close to the centerline of the car so that the sensor pushing up against the MPC does not impart any torque on the sensor cars. The fiber optic cables connecting to the optics are fragile, and have a limited bending radius.

2.4.5.1.3 Temperature Probe Actuation Requirements

The temperature probe requires a single point of contact on the MPC similar to the LIBS system. However, unlike the EMATS and LIBS, the reading obtained from the temperature probe depends on the force pressing the probe against the surface. Since the metal tip of the temperature probe

could scratch or damage the canister surface, it is retracted when not taking measurements. Like the LIBS, the probe is close to the centerline of the car to prevent any torque on the sensor cars.
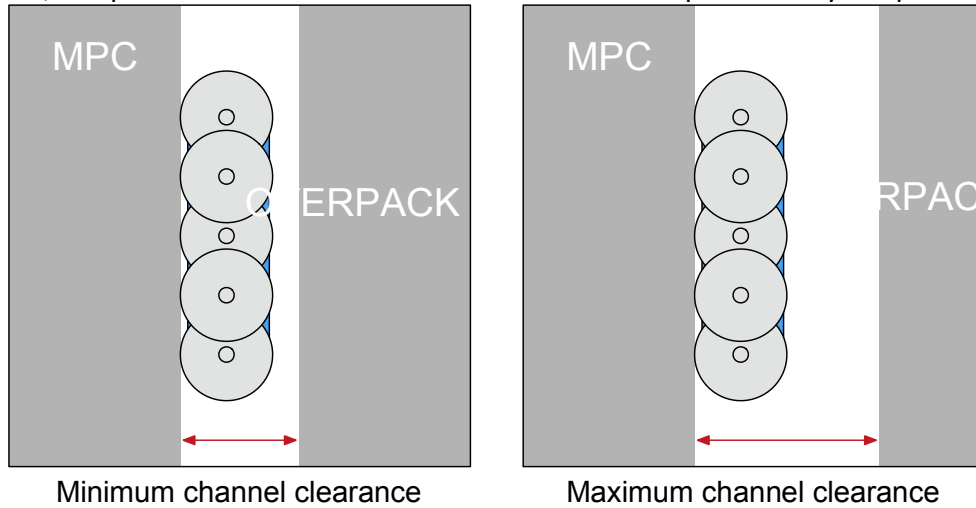
Figure 2.4.24. *Cross section diagram of sensor car in channel, showing channel clearance range*

2.4.5.1.4 Stabilization and Holding Force Mechanism
While the sensor cars are inside the ventilation channel, the cars may not necessarily be touching the vertical surface of the MPC. The sensor robot needs to be stabilized and pressed against the MPC, both for accuracy of position estimates and to ensure valid sensor measurements. Additionally, the surface temperature sensor requires a holding force to keep sufficient surface contact with the side of the MPC. Like the previously discussed sensor actuators themselves, the stabilization mechanism fails closed to prevent the sensor cars from getting jammed inside the cask. As described in previous sections, the ventilation channel clearance can range from 2" to 3.4" (Figure 2.4.24), and the stabilizing arms are designed to work throughout the whole range of channel dimensions.

2.4.5.2 Servo Motor Actuation Development
2.4.5.2.1 Stabilizing arm prototype development
To achieve the required holding force against the MPC, an arm mechanism was designed to extend from the robot to the overpack surface (Figure 2.4.25). The first proof-of-concept prototype of this stabilizing mechanism consisted of two servomotor-controlled arms that rotated outwards to push against the overpack walls (Figure 2.4.26). The stabilizing arms and wheels were 3D printed PLA plastic, mounted directly to the micro-scale servo motors. The motors were then mounted in an empty prototype robot chassis for testing in the ventilation channel mock-up. After testing that the stabilizing arms held the robot against the MPC securely, work began on a new version with smaller servo motors, incorporating the EMAT sensor actuator into the same car.

retracted — extended
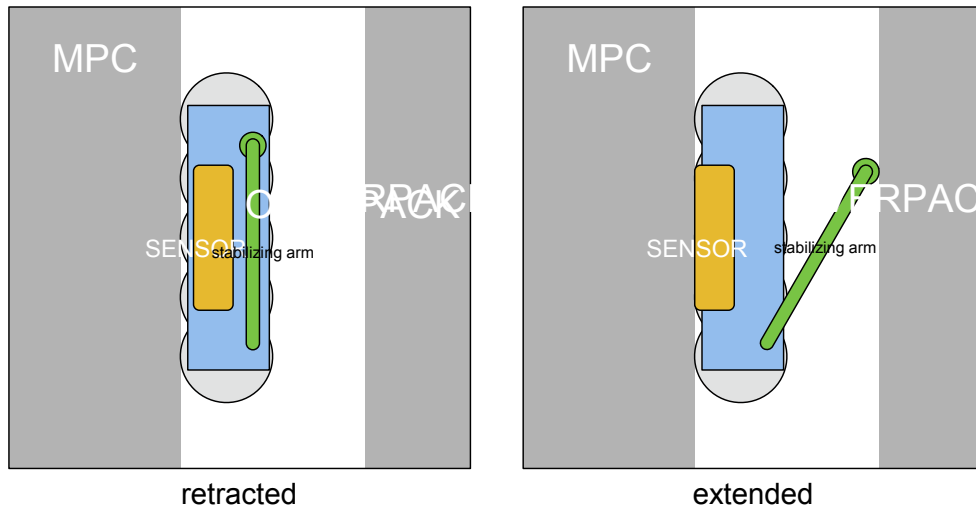
Figure 2.4.25. *Cross section diagram of sensor car in channel, showing sensor and stabilizing arm concept*

Figure 2.4.26. *The first prototype stabilizing arms and servomotors*

2.4.5.2.2 EMAT sensor deployment

The first proof of concept prototype for the sensor actuation mechanisms was for the EMAT sensors. The EMAT sensors are deployed only when measurements are being taken, and retracted inside the body of the sensor robot car at all other times. In case of power failure, the EMATs deployment mechanism is designed to fail closed and automatically retract.

The first version consisted of a sliding bracket which held the two EMAT sensors. The bracket (Figure 2.4.27) was 3D printed out of PLA, and slid vertically on 4 steel dowel pins mounted inside the robot body. A compression spring was fit around each dowel pin and provided the return force to ensure the mechanism failed closed. The springs were sized to overcome the magnetic attraction force of the EMATs on the weld of a steel plate with a representative weld, which was measured to be 5.9 N (1.3 lbf).
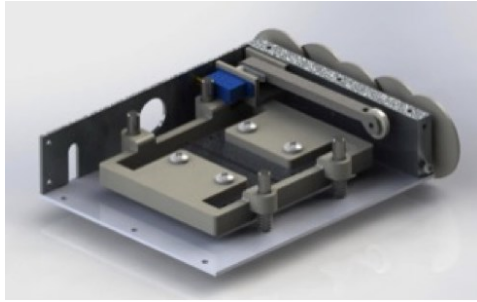
(a) CAD render of the
EMATs within the sensor car
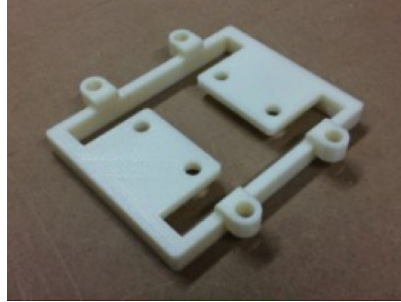
(b) first 3D printed prototype of the
EMAT bracket

Figure 2.4.27. Initial prototype of EMATs servo motor actuation

The bracket design was modified to fit the aluminum-bodied EMAT sensor to be used for measurements. The final dimensions of the aluminum EMAT sensor with flying leads were slightly larger than the 3D printed plastic EMAT sensors used earlier in the project (Figure 2.4.28).

The bracket also had space to mount a piece of electromagnetic shielding material between the two sensors. A rotating cam mounted to a micro servo (Figure 2.4.29) pushed the whole assembly up and down. This design gave a usable range of 0.25", which is enough to pull the EMATs entirely inside the robot body and extend the EMAT sensors past the wheels.
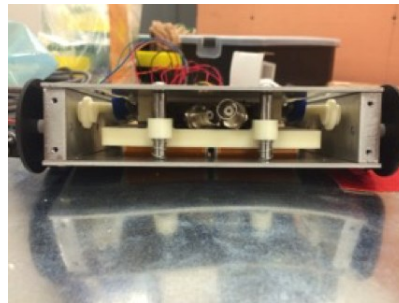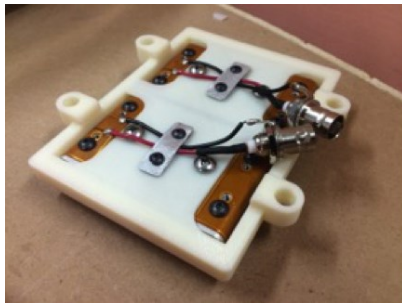
Figure 2.4.28. The V2 bracket for the aluminum EMAT sensor mounted in the sensor car
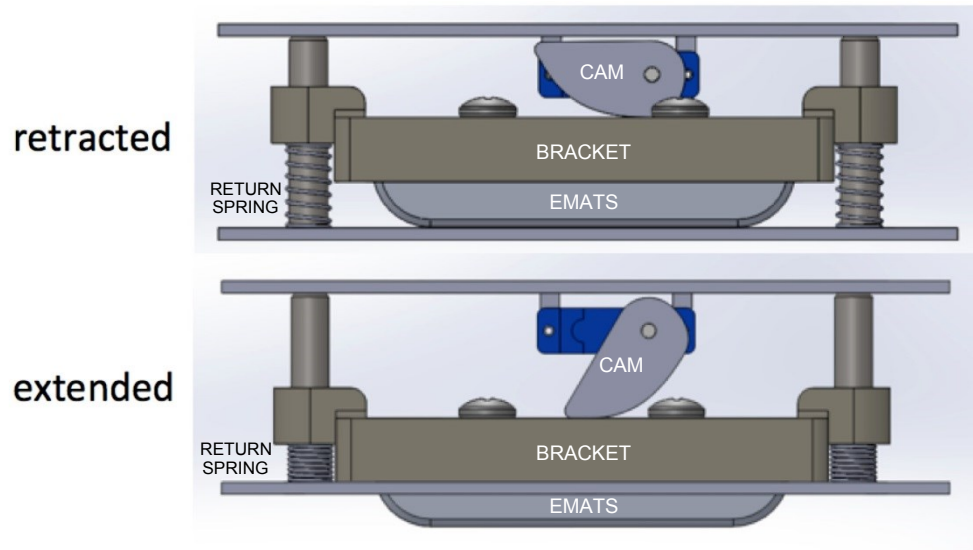
Figure 2.4.29. *Section views of EMAT deployment with sliding bracket and rotating cam*

2.4.5.2.3 Combining EMAT sensor deployment and stabilizing arms

To integrate the stabilizing arms and EMAT sensor deployment into the same car, smaller nano-scale servo motors were selected. After modeling the new EMAT sensor bracket, stabilizing arms, and servo bracket in Solidworks, the components were 3D printed out of PLA plastic. The servo bracket was designed to hold all four servos (one for each stabilizing arm, and two for the EMATS) securely to the top plate of the sensor car chassis (Figure 2.4.30).

EMATS servo bracket isometric view

EMATS servo bracket view, in car chassis with stabilizing arms and cams attached
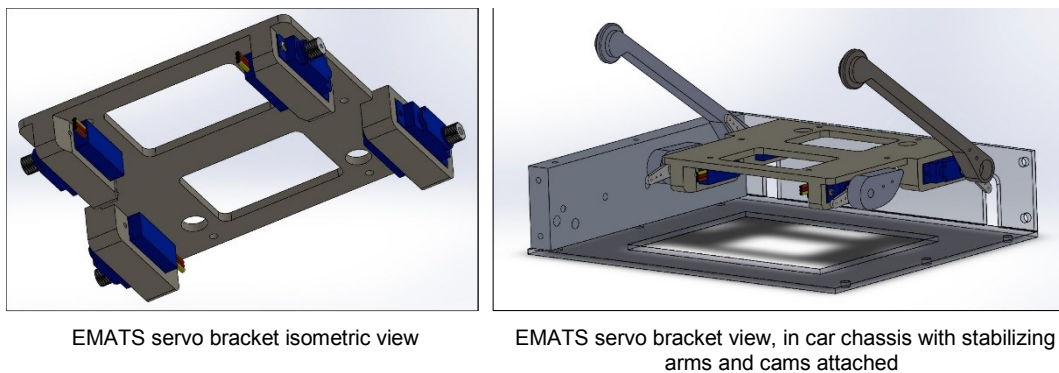
Figure 2.4.30. *The servo bracket 3D model*

For the EMAT sensors, no specific holding force was required as long as contact is made between the sensor and surface. The stabilizing arms themselves were designed with a captive wheel to reduce the number of parts. Similarly to the first prototype, each arm was directly mounted to the servo that rotates it. Isometric and dimensioned drawings of these components can be found in Van Sant's thesis [9]. The design could be printed out of PEEK for temperature resistance.
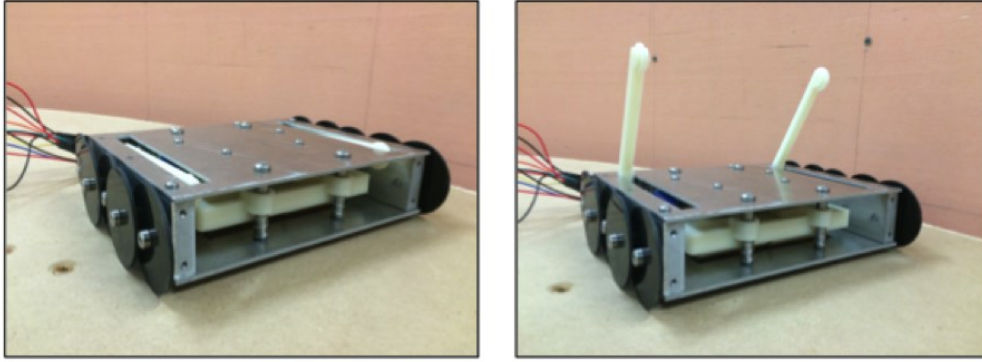
Figure 2.4.31. *Two views showing the stabilizing arms retracted and extended*

2.4.5.2.4 Servo motor actuator control

The servomotors were controlled by an Arduino microcontroller mounted in a box located at the main power supply for the winch. The code to run the microcontroller is in Appendix B.1 of Van Sant's thesis [9]. The box had one toggle switch for extending the stabilizing arms, one for the EMAT sensors, and one for the sensor car lighting power, and LED indicators for each. Power for the servos and lighting was provided on separate circuits to prevent the lighting from dimming when the servos were in use. The servo power and control signals were sent to the car through a Cat 5 Ethernet cable with twisted pair conductors and ground to minimize noise in the servo signal from the long 50' cable length.

2.4.5.2.5 Testing and taking sensor measurements with servo actuation

To test the actuated EMAT sensors in a situation similar to a real inspection, both the winch (described in later sections) and the sensor cars were set up on the metal MPC mockup used by the EMAT sensor team. This allowed the EMAT sensor team to take EMAT measurements while the winch moved the sensor cars at a constant velocity along the side of the MPC. The positional data from the winch motor encoder was recorded in Robot Operating System (ROS), and saved with respect to the absolute time recorded by the computer's CPU. This data was then combined with the EMAT sensor data to get an accurate map of the EMAT sensor measurements as the car moved along the MPC. Both B-scan and A-scan measurements were taken at multiple positions of the overpack.

However, while taking the EMAT sensor measurements with the sensor car and winch system, multiple issues with the sensor actuation design were found. Since the EMAT sensors are very sensitive, electromagnetic interference from the servo control signals was seen in the EMAT measurements. This noise was determined to be caused by the cables connecting the servos to the microcontroller running alongside the EMATS signal cables in the data tether. With the design constraints of the robot's data tether, this interference was unavoidable without heavily shielding the EMATS cables. Additionally, although they had metal gears, the servos had a short lifespan

and burnt out or broke gear teeth due to the stresses of repeatedly holding the EMAT sensors near their maximum rated torque while taking measurements.

2.4.5.3 Pneumatic Actuation Development

The reliability and electromagnetic noise issues with the use of servo motors within the robot were deemed unacceptable for meeting the design goals of the robotic inspection system. The noise added to the EMAT sensor measurements from the servo signal cables reduced the accuracy and ability of the EMAT sensor measurements for cask surface characterization to nearly an unusable level. The servo motor's lack of durability reduced the number of measurements that the system could make before needing repair, slowing down the inspection process and increasing the time required to inspect each cask. Because the deployment of each sensor merely requires an on/off motion change, pneumatics were next considered for actuation.

2.4.5.3.1 Intent and proof of concept

The key factor in using pneumatic operation, assuming the actuation is successful, is to remove the noise source affecting the EMAT sensor measurements, and drastically improve the durability of the system. As a proof of concept, a thin sheet of silicone rubber was sandwiched underneath the lid of a PVC junction box (Figure 2.4.32). A hole cut in the lid allowed the silicone rubber to expand when the inside of the box was pressurized. An air hose connector threaded into the junction box provided a connection to an air compressor and pneumatic valve to turn the actuator on and off.
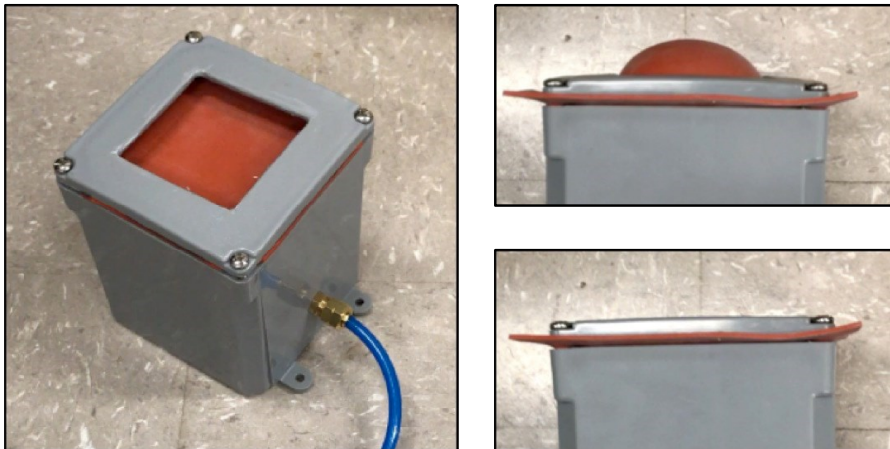
Figure 2.4.32. *Pneumatic actuator proof of concept prototype at 25psi; top view, extended and contracted*

With this proof of concept complete, the actuator design was miniaturized to fit within the sensor car. The top and bottom pieces of the actuator body were waterjet cut out of 0.080" aluminum, with multiple pieces of silicone rubber clamped in between, holding the 6mm air hose in place (Figure 2.4.33). Once assembled inside the sensor car, the new actuator was capable of pushing the EMAT sensors downward against the MPC with a contact force proportional to the supply air pressure (Figure 2.4.34). Dimensioned drawings of the miniaturized actuator are shown in Appendix A.4 in Van Sant's thesis [9].
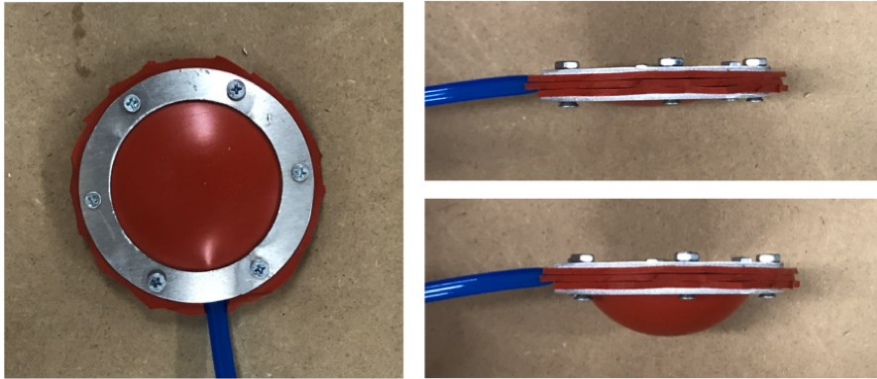
Figure 2.4.33. Miniaturized pneumatic actuator at 25psi; top view, extended and contracted
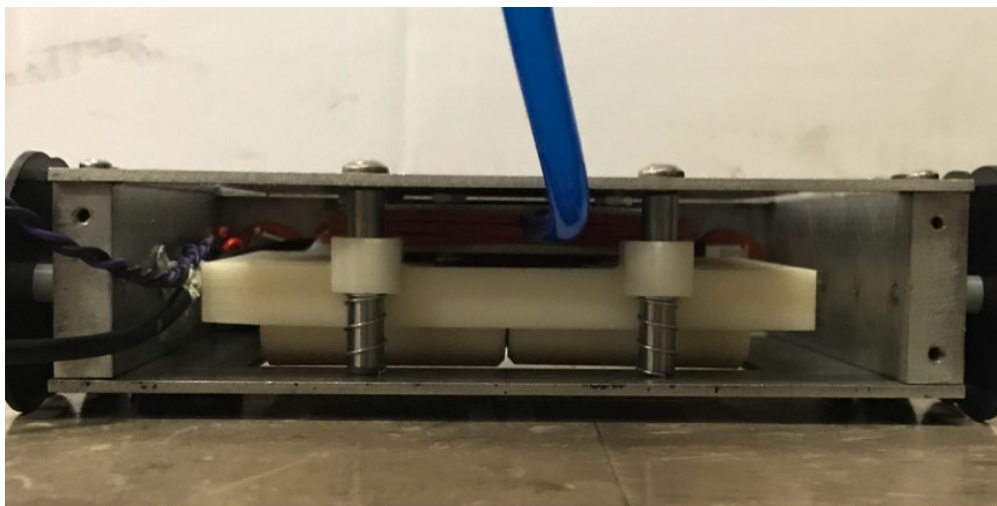
Figure 2.4.34. Miniaturized pneumatic actuator inside EMAT sensor car

2.4.5.3.2 Integration into EMAT sensor car

After the initial miniaturizing of the proof of concept actuator design, a double-sided actuator was designed and integrated into the EMAT sensor car to extend both the EMAT sensors and the delivery arms at the same time using the same supply air. This allowed the team to reduce the number of air hoses within the robot tether. A diagram of this actuator design is shown in Figure 2.4.35. The actuator consists of 4 separate 3D printed parts assembled together with the silicone rubber gaskets. The air hose connects into the hollow side of the main part, which allows air to travel through a channel and expand the silicone rubber outwards, pressing against the EMAT sensor bracket on one side and the stabilizing arm on the other side. Two separate silicone rubber gaskets are clamped to the main actuator part, and secured in place with small screws. The stabilizing arm pivots on shoulder screws that thread into the top clamping portion of the actuator assembly, and has two torsion springs to return the arm to its closed position. The stabilizing arm has captive wheels to press against the overpack (Figure 2.4.36). As in the previous version, the EMAT sensor bracket slides up and down on metal posts and returns to its retracted position by springs on each post. The main actuator part attaches to the top panel of the car chassis with small screws, anchoring the whole actuator assembly in place. Dimensioned drawings of each actuator part can be found in Appendix A.4 in Van Sant's thesis [9].
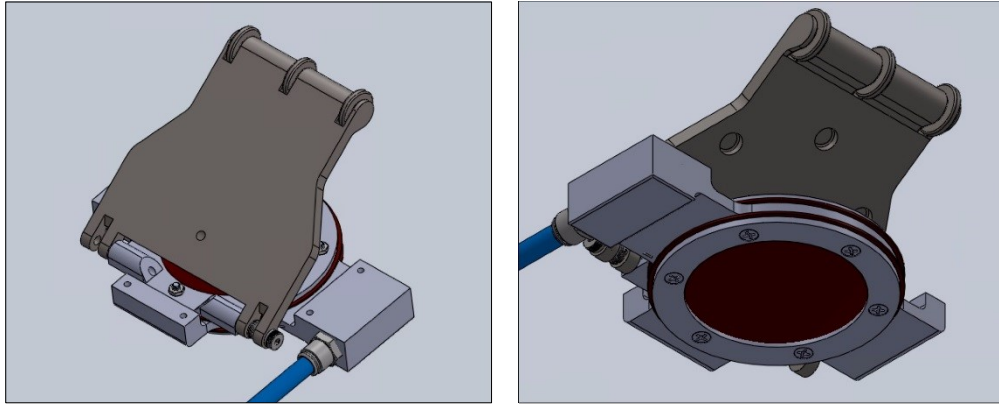
Figure 2.4.35. *Isometric top and bottom view of 3D Solidworks model used to print pneumatic actuator, showing stabilizing arm (dark grey), air hose connection (blue), and the silicone rubber gaskets (red) sandwiched between the three actuator body pieces (light grey)*

(a) retracted   (b) extended

Figure 2.4.36. *3D printed pneumatically actuated EMATS stabilizing arms and actuator mounted in robot car chassis*

From the May 10, 2017 Holtec visit, the robotics sub-team learned that the fielded MPC is much more magnetic than the mock-up section of MPC used for testing with the EMATS team, the EMAT sensor actuator was redesigned to retract with greater force. After measuring the magnetic force between the EMAT sensor and MPC at Holtec to be around 22 N (5 lbf), a mockup was constructed with the same force by layering aluminum sheets over the top of a steel sheet. The new actuator design pivoted the EMAT sensor down onto the MPC instead of sliding along metal posts, allowing stronger return springs (Figure 5.14). Using the mock up for testing with different strength springs, the new actuator was able to retract the EMATS from the surface with as much as 31.1 N (7 lbf) of force between the EMATS and the surface.
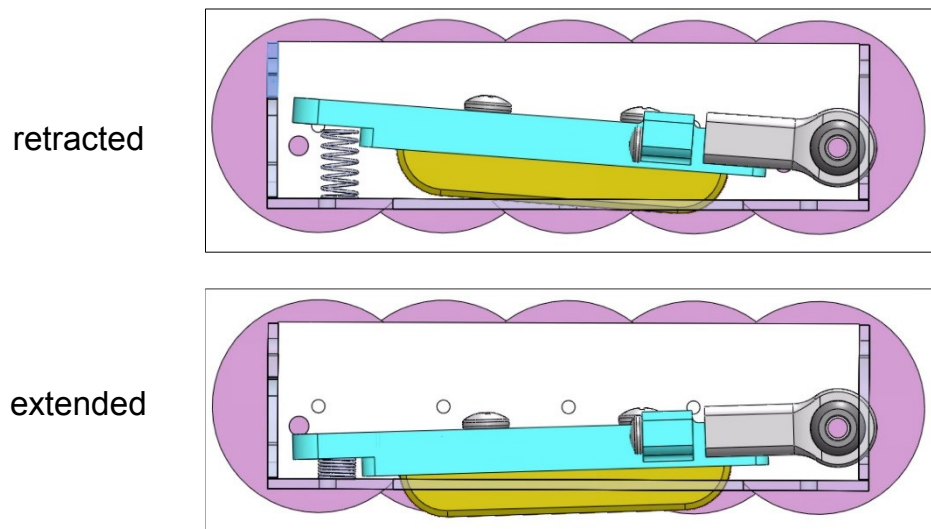
Figure 2.4.37. *CAD cross section of pivoting pneumatic actuator, showing EMAT sensor (yellow), EMAT bracket (blue), and robot car wheels (pink)*

2.4.5.3.3 LIBS actuation

Once the pneumatic actuator concept and prototypes were developed for the EMAT sensors, the miniaturized actuator was adapted to fit in the LIBS car. The bottom of the LIBS actuator was waterjet cut out of 0.050" aluminum, and sized to fully surround the LIBS optics holder. The bottom ring and the layers of silicon gasket were then screwed directly into the top panel of the car, with the 6mm air hose clamped in between (Figure 2.4.38).

After receiving the LIBS optics holder design from the LIBS team, the holder designed was modified to work with the actuator. Two "wings" on either side of the optics holder attached to two rod ends, allowing the whole optics assembly to pivot up and down (Figure 2.4.38). The bottom panel of the robot chassis was modified to allow the LIBS optics to extend outside the car chassis. Two compression springs attached to the side wings of the optics holder provided the force to retract the optics holder back into the car. The whole optics holder assembly was 3D printed and was quickly removable from the car chassis. This design allowed the LIBS team at University of Michigan to locally print their own parts to assemble the optics, and easily swap in the assembled optics into the sensor car for testing when visiting Penn State.
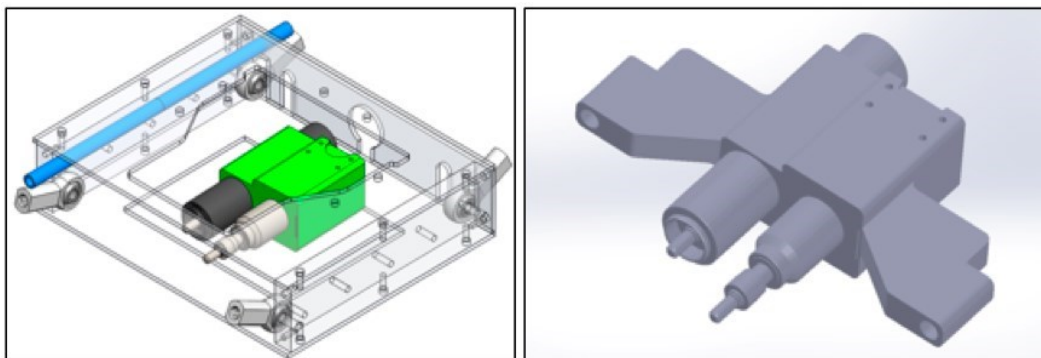
Figure 2.4.38. *LIBS optics holder CAD model in car and optics holder modified for actuation*

The LIBS optics were larger than the EMAT sensors, and did not leave enough space within the sensor car to house the double-sided actuator and stabilizing arm assembly. However, after testing the system on the full-height MPC mock up with the LIBS team, it was determined that the stabilizing arms on the EMAT sensor car provided enough force that the LIBS car did not need its own stabilization, and the LIBS system was capable of taking measurements on the mock-up without the stabilizing arms.
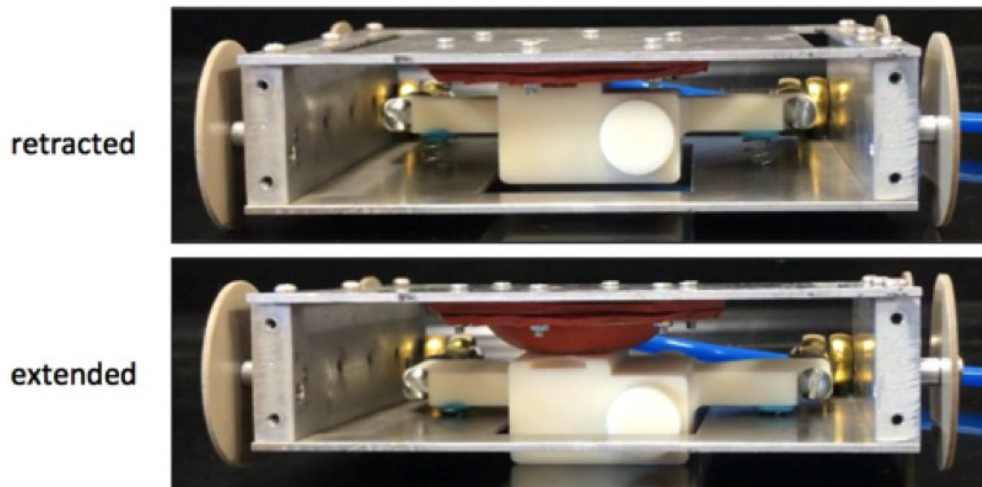
Figure 2.4.39. *LIBS actuator installed in car chassis, extended and retracted*

2.4.5.3.4 Thermocouple actuation

The thermocouple pneumatic actuator followed the same design as the LIBS optics holder – the aluminum ring, silicone gasket, and air hose were attached directly to the top panel of the robot chassis. The thermocouple probe itself was mounted inside a stainless steel tube, bent at a 90 degree angle (Figure 2.4.40). The end of the tube was mounted to a pivoting plastic block, which was then attached to the side chassis of the robot car, allowing the thermocouple tube to pivot downward and touch the surface of the MPC to take measurements (Figure 2.4.39). The thermocouple wires connected at the pivoting plastic mounting block, and ran through the data tether back to the control center. The thermocouple "tapper" was spring loaded to return to its retracted position.
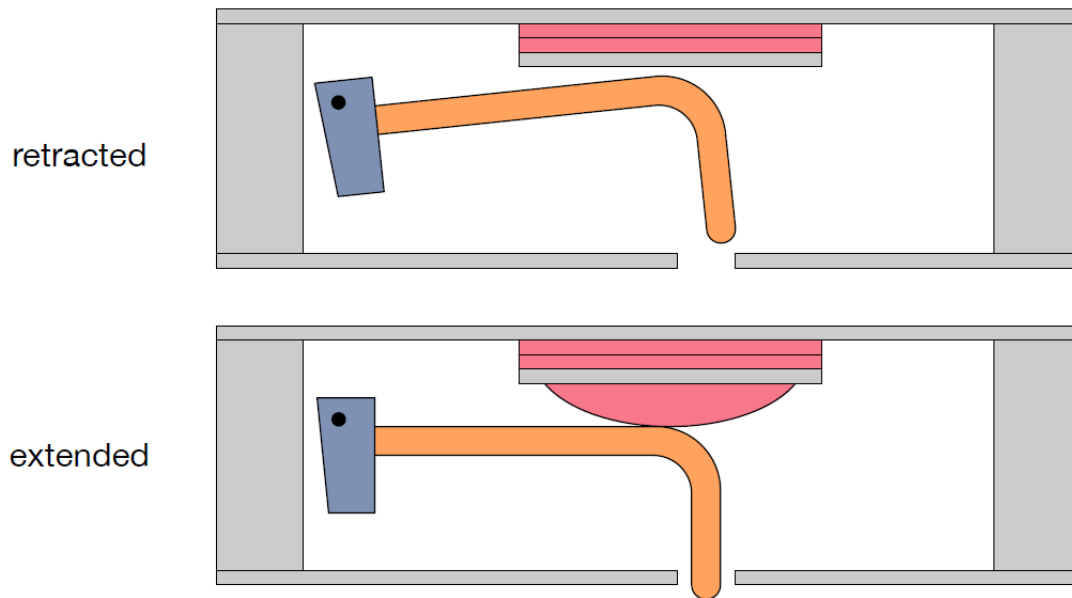
Figure 2.4.39. *Thermocouple (orange) actuator concept diagram shown extended and retracted*
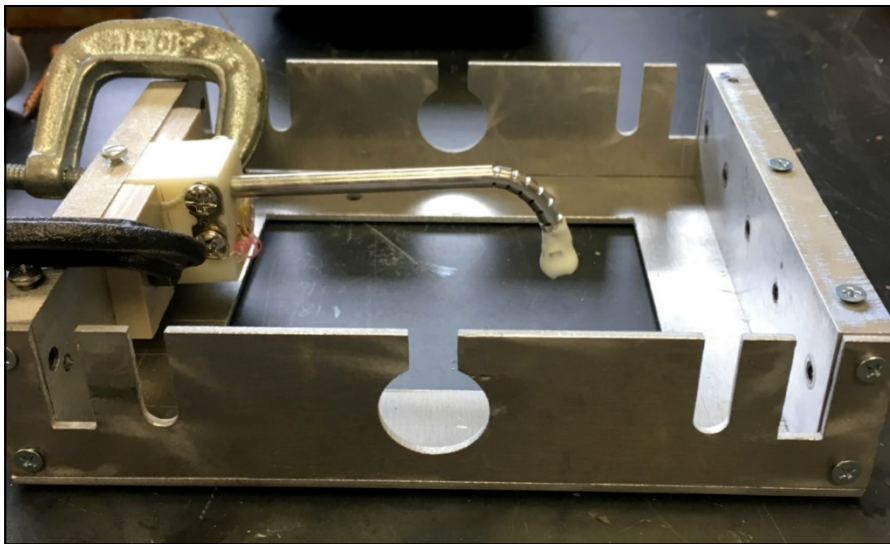
Figure 2.4.40. *Constructed thermocouple actuator mounted in car, with top panel removed*

2.4.6 System Design Process

2.4.6.1 Introduction

The robotic inspection system consists of four main components that operate together: the sensor robot, the delivery arm, the delivery winch, and a command and control center. The sensor robot houses all sensors within a compact body that meets the environmental constraints

within the cask. The delivery arm acts as a mechanism both to insert the sensor robot into the cask and to guide the robot when entering and exiting the ventilation channel. The winch raises and lowers the robot within the channel and tracks the robot's position. The command and control center provides power to the robot as well as a computer-based driving interface to the operator.

This section describes the iterative design process of the vent mount, winch assembly, delivery arm and cameras, and the robot sensor train. The field tests of these prototypes and the in-lab MPC mock-ups used to test the prototypes are also described in this section. A team of both graduate and undergraduate researchers from Penn State collaborated on the design and fabrication of the components of the system as described in this chapter, and the members included Bobby Leary, Jen Bracken, Franz Card, Mike Gehrsitz, Matthew Ng, John Ominski, Noah Shandelman, Yewon Hwang, and Chris Velez.

2.4.6.2 Vent Anchor Mechanism and Mount

2.4.6.2.1 Initial Concept and First Prototype

The initial concept prototype for the vent anchor and winch assembly was built for both in-lab positional accuracy testing and field testing at McGuire Nuclear Station in May 2016. The vent mount structure was build out of 80-20 extruded aluminum bar. The overall shape resembled an upside down "L", with the winch on the bottom next to the cask ventilation opening, and the top of the structure sitting on top of the cask lid, and weighted to secure the whole assembly on top of the cask (Figure 2.4.41).
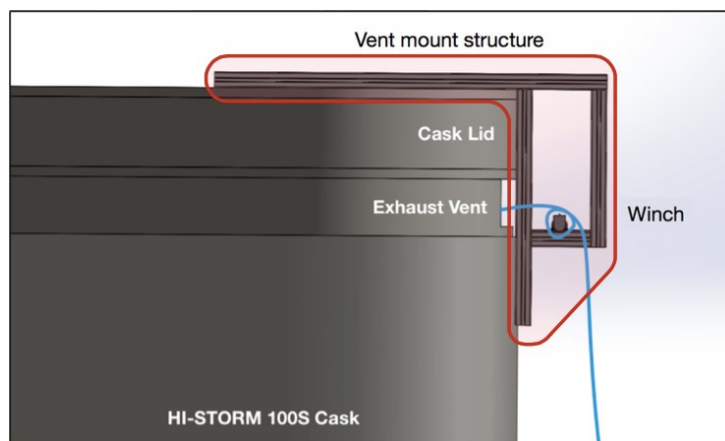
Figure 2.4.41. *Side view diagram of winch installed on cask*

2.4.6.2.2 First Vent Mount Prototype

After the team's May 2016 visit to McGuire Nuclear Station, we recognized the need to securely mount the system to the cask. During the February 8, 2017 visit to Holtec Manufacturing, the delivery group was given a section of the steel that reinforces the ventilation opening in the overpack. This piece was incorporated into the in-lab cask mockup, and using the new, more accurate ventilation opening, a mechanism was developed to hold the winch system inside the vent when mounted to the cask. Compared to early versions of the winch system, which sat on top of the overpack, mounting inside the vent opening is safer and more secure, and allowed for

a smaller, lighter overall structure. The design had two extensions that slide into the vent opening, with a four-bar mechanism to "lock" the structure in place (Figure 2.4.42).
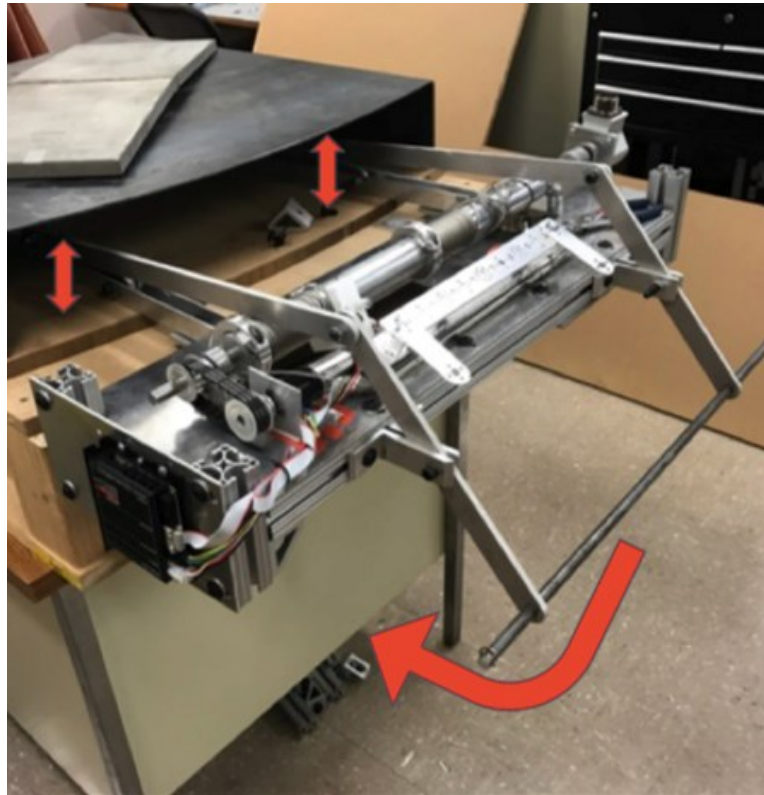
Figure 2.4.42. *Operation of the mechanism to hold the winch system in the vent opening*

The operator controlled the locking mechanism by pushing a main lever, which then locked in position where it could be secured with zip-ties to prevent accidental removal. The extensions inside the cask had hooks on the end to further guard against accidental removal. After testing the insertion and removal of the vent anchor assembly, the hook design was replaced with wheels to allow the extensions to more easily roll into the vent, and then drop over the edge of the overpack interior to hold the structure in place. The wheel design (Figure 2.4.43) allowed for a smoother insertion and retrieval of the winch system from the vent opening.

Figure 2.4.43. *Wheels on end of extension into vent opening*

2.4.6.2.3 Second Version Improvements

The second vent anchor prototype improved the build quality and operator usability of the vent anchor. The design had two extensions that slide into the vent opening and lock the structure in place by expanding both vertically and horizontally, as seen in Figure 2.4.44. All contact points between the vent anchor and the cask vent itself were acrylic plastic, acting as a placeholder the PEEK to be used in the final version. The plastic wheels on the bottom of the anchor again allowed for a smooth insertion and retrieval of the winch system from the vent opening.

Figure 2.4.44. *Vent anchor assembly inserted in vent opening*

Instead of the zip-ties used on the first prototype, the operator locked the mount in the vent by tightening a lead screw for each four-bar locking mechanism (Figure 2.4.45). There were two linkages on each side of the vent mount assembly – one extended upwards to lock against the top of the ventilation opening, and one expanded horizontally to lock against the side wall of the ventilation opening. As the screw is tightened, the four-bar mechanism expands and locks the vent anchor in place until the operator loosens the screw. Using a wireless driver, all four locks could be tightened in about 20 seconds, limiting the operator's exposure to the vent opening.
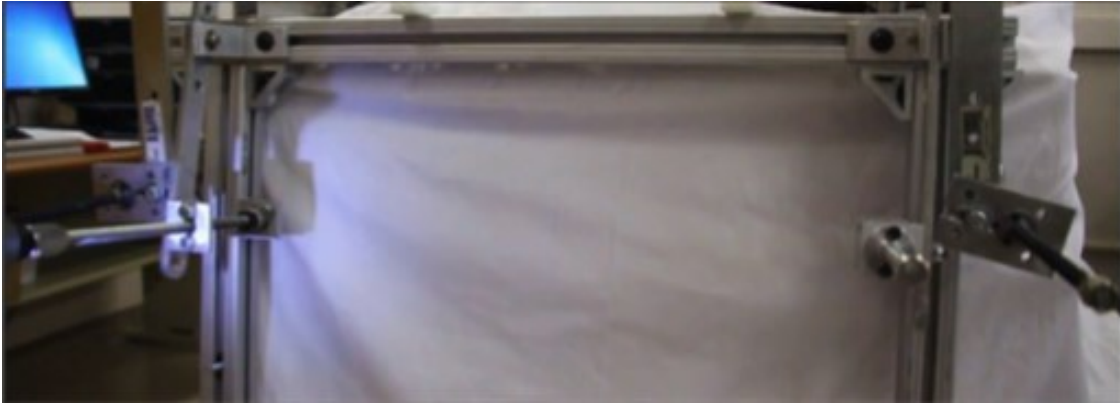
Figure 2.4.45. *View of the 4 locking lead screws*

To make the vent anchor lighter and easier to insert into the vent opening, the winch and vent anchor were divided into separate modular units. The vent anchor is inserted and locked in place first, and the winch is then attached on to it, keeping the down the weight of individual parts lifted by the operator. The 80-20 structure was replaced with a single aluminum plate to reduce weight and part count, and to allow the winch assembly to "lock-on" to the vent anchor during insertion. An aluminum hook on the top of the winch assembly inserts into a square hole on the vent anchor, and two toggle clamps on the bottom of the winch assembly secure it in place (Figure 2.4.46).
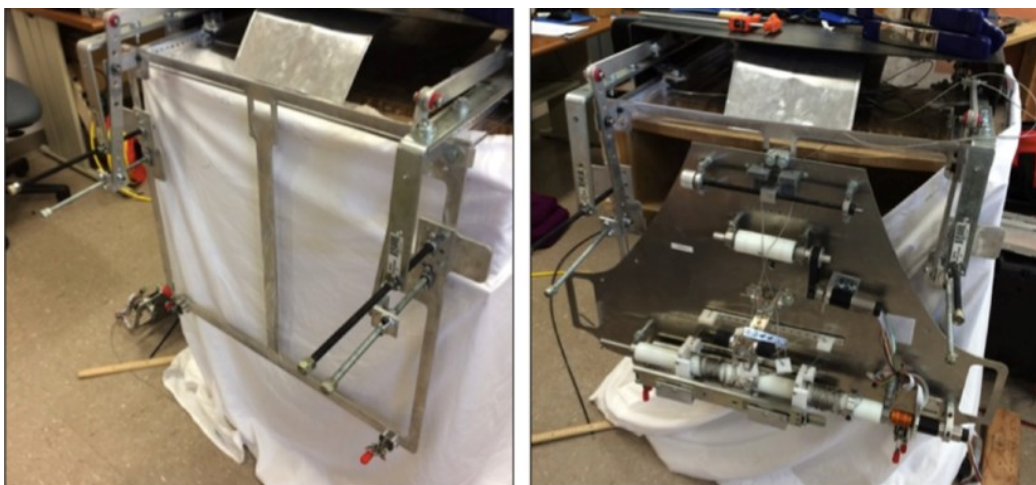
Figure 2.4.46. *The vent mount plate with and without the winch attached*

2.4.6.3 The Winch Design

2.4.6.3.1 Initial Concept

McNelly outlined the concept for a gravity-assisted sensor car insertion into the ventilation channel, and suggested using cables to support the weight of the sensor car train while in the channel [McNelly 2015]. In this concept, a winch-inspired mechanism outside the cask would pull in and let out the support cables, allowing the sensor cars to scale the MPC.

2.4.6.3.2 First Winch Prototype

The first winch system prototype had a motor-powered spool for the robot support cables and was assembled as part of the 80-20 vent mount assembly described in Section 2.4.6.2.1. The Maxon-branded motor included an integrated optical encoder to read the rotation of the motor, and a second optical encoder was mounted to the cable spool shaft to directly read the rotation of the spool, for redundancy. The cables connected to the sensor robot wound around the spool and connected to counterweights to support the weight of the sensor robot when it is in the channel, and to give a visual representation of where the robot is in the channel. The winch structure also contained the electronics needed for the motor and optical encoder, and was connected to a laptop computer to control the motor. Real-time images from the sensor robot cameras were also shown on this computer to aid the operators during the cask inspection. The winch and sensor robot were also connected to a power supply system that can run off a 12V battery or 120V wall supply. The power supply system had a built-in fault safety such that disconnection of wall supply power would cause seamless switch-over to battery power, and reconnection of wall supply power would recharge onboard batteries while seamlessly switching back to the wall power source.
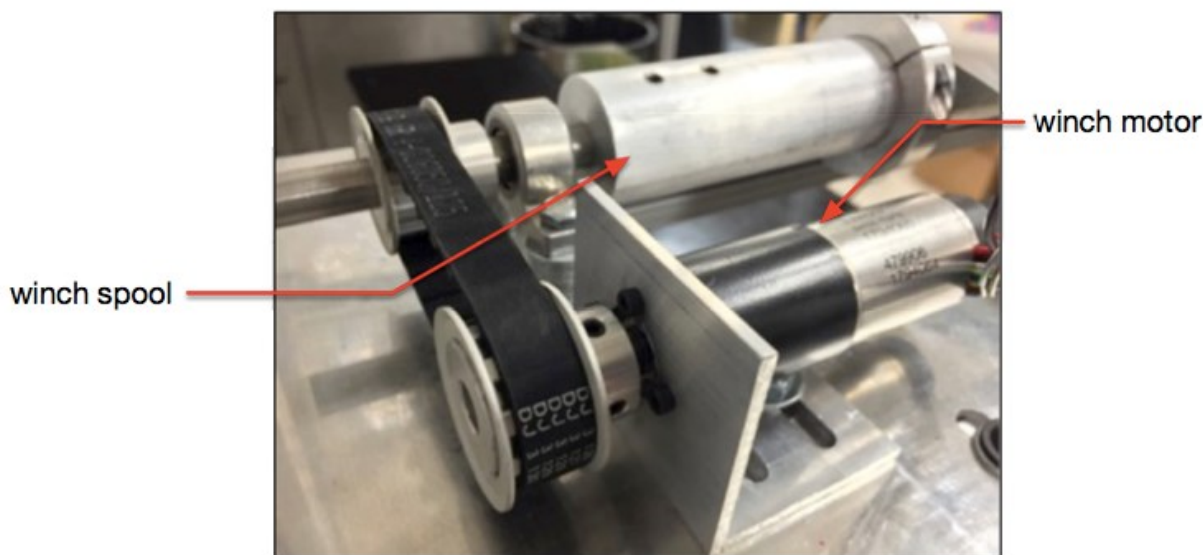
Figure 2.4.47. *Winch motor connected to cable spool shaft with pulley and belt*

The motor was indirectly connected to the spool with a belt and pulley system (Figure 2.4.47), which provided a fail-safe by slipping if the sensor robot happens to become jammed or wedged in the channel during inspection. The steel support cables connected to the robot were designed

to hold 10 times the weight of the robot for a large factor of safety. The delivery arm passed over the spool and in between the two support cables (Figure 2.4.48).
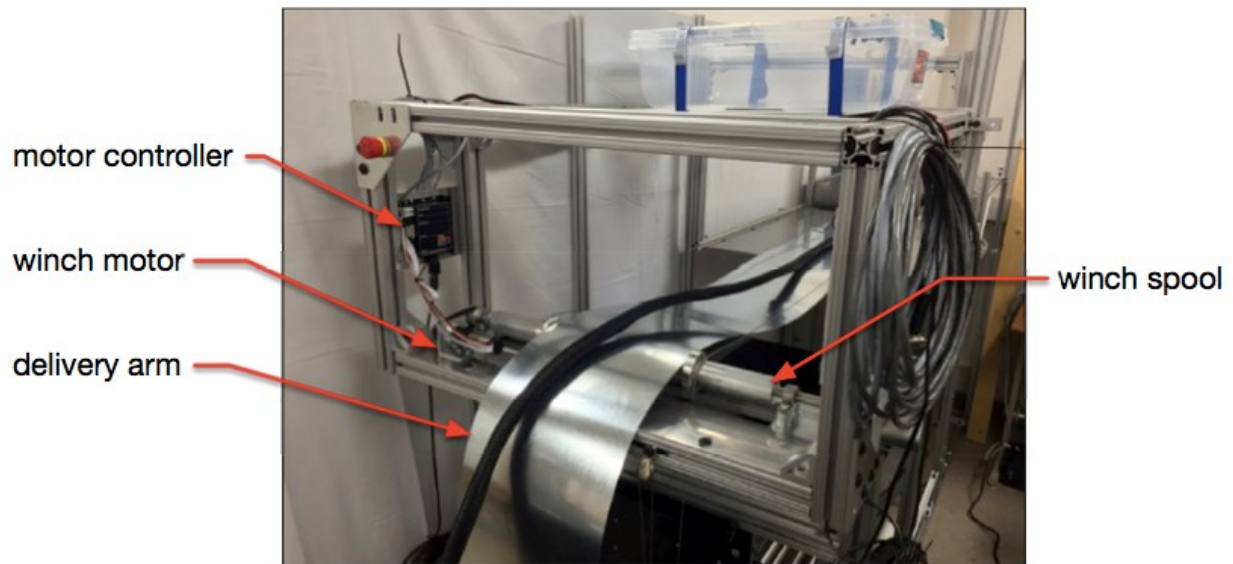
Figure 2.4.48. *Delivery arm passing over the winch spool, set up on an early version of the cask mock up*

2.4.6.3.3 Second Prototype with Lead-Follower Motors

To prepare for the May 10, 2016 Holtec Manufacturing visit, significant updates were made to the winch design. While the previous winch prototype worked well once the sensor robot was inside the ventilation channel, tests showed that the winch had trouble spooling out unless constant tension was kept on the support cables, which complicated the robot insertion into the canister itself. To create this constant tension, a second motor was incorporated into the winch system to pull on the main cable spool (Figure 2.4.6.49).
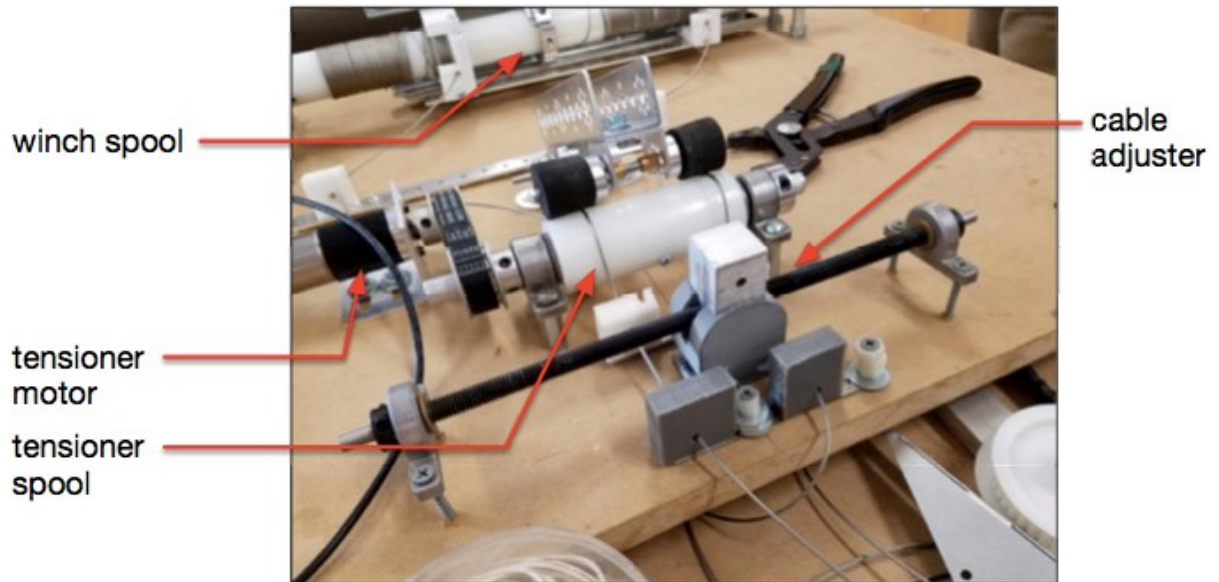
Figure 2.4.49. *Prototype tensioner motor and spool mechanism*

The tensioner spool was changed to ABS plastic to prevent any electrical noise between the motor and cable, and the cable was held snug against the spool with two rubber wheels. The motor and controller are the same Maxon models used for the main spool. The Robot Operating System (ROS) code for controlling the motors from the operator computer was updated to set up the two motors in a lead-follow situation – when the winch spooled out, the tensioner motor was set to run faster than the main spool, creating constant tension on the spooled cable. When the winch spooled in, the tensioner motor ran slightly slower than the main spool. The cable guides were constructed out of slippery UHMW polyethylene, and were mounted to sliding horizontal guides to follow the cable as it wrapped around the spool (Figure 2.4.50). The guides were spring-loaded to press against the cable coils to ensure the cable wrapped neatly around the spool with no gaps between each coil.
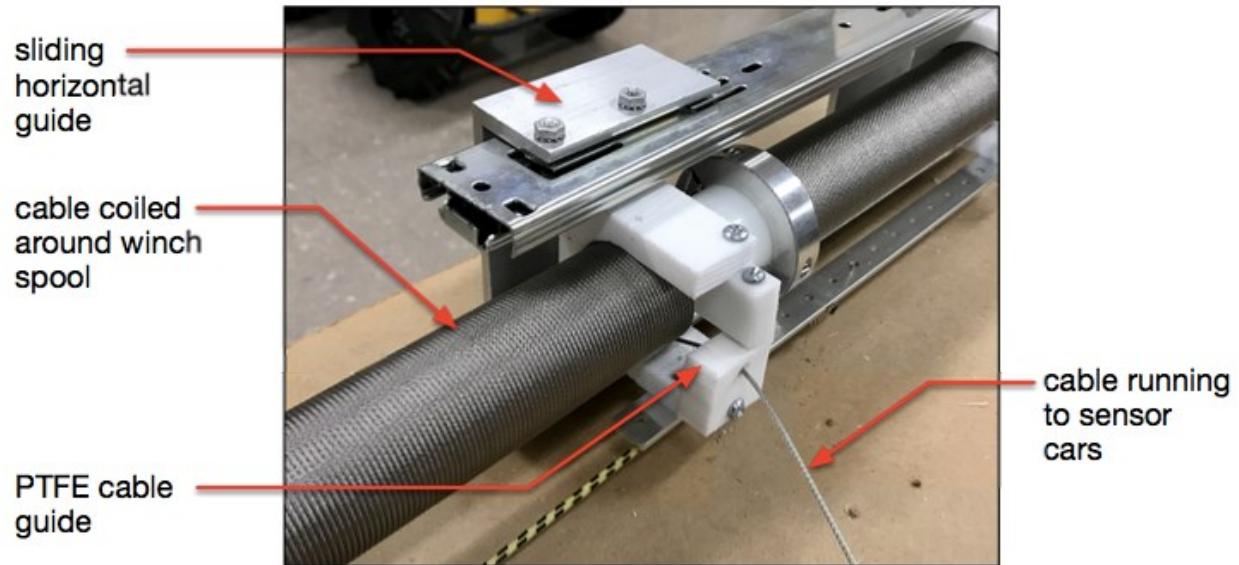
Figure 2.4.50. *View of winch cable guide*

The dual-motor winch design was initially built and prototyped on a MDF board for ease of mounting and relocating parts. After the setup was completed and tested, the winch mechanisms were mounted to a lightweight aluminum panel (Figures 2.4.51 and 2.4.52). During testing, it was observed that the belt driving the spool shaft was sensitive to tension adjustments and could sometimes slip on the pulley. To reduce part count and improve reliability, the belt drive connection between the motor and spool shaft was modified to a direct, inline connection (Figure 2.4.53).
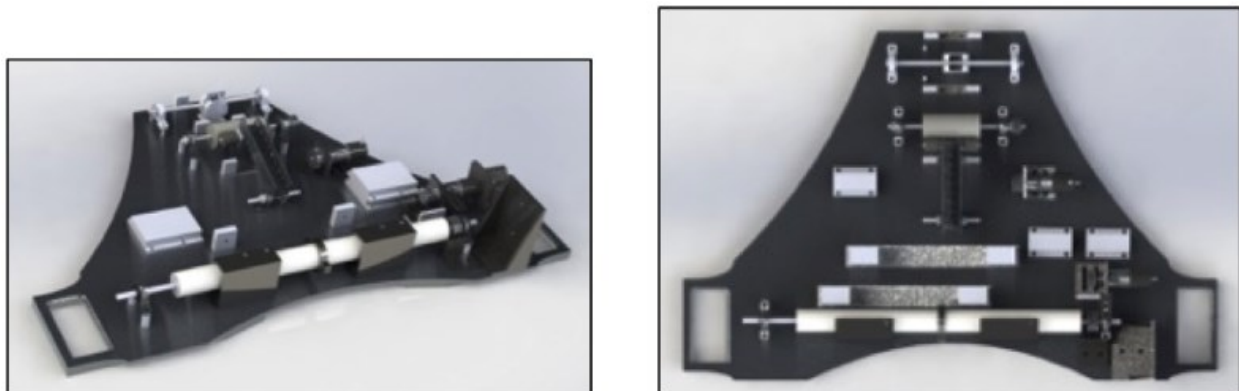
Figure 2.4.51. *CAD visualization of winch assembly from different angles*
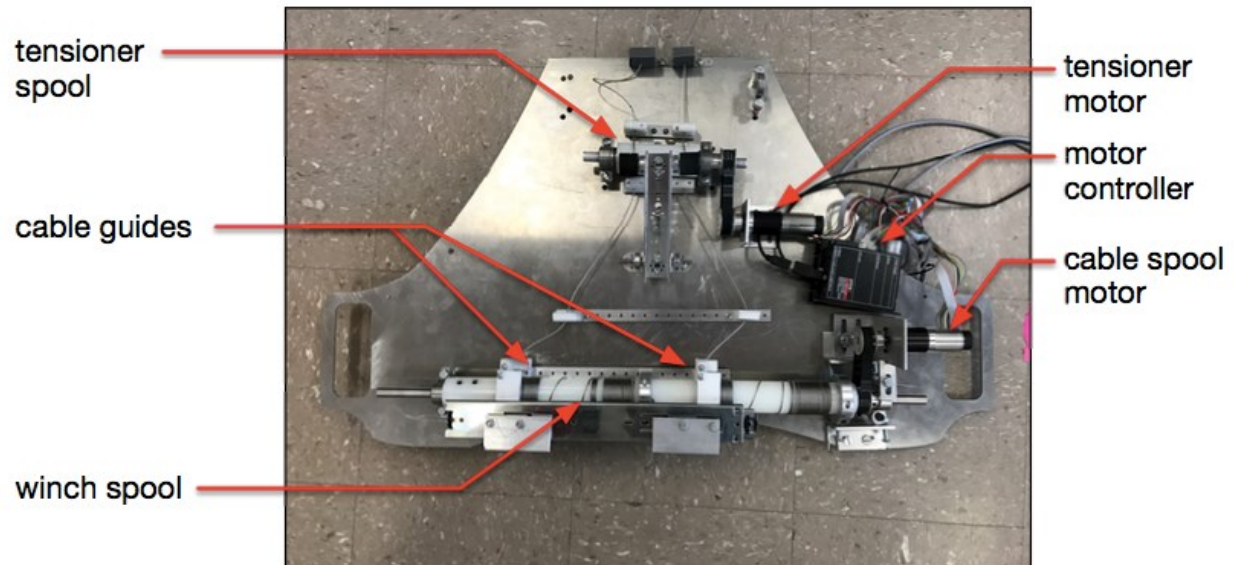
Figure 2.4.52. *Winch assembly on aluminum backing plate*
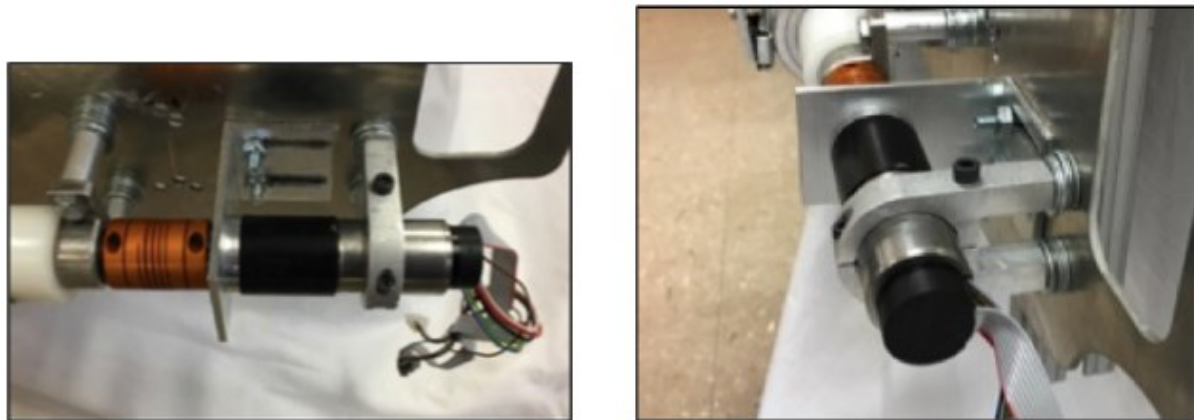
Figure 2.4.53. *Main winch motor direct mounted to spool shaft*

2.4.6.3.4 Decoupling the Winch from the Vent Mount

As described in the vent anchor section, the winch assembly was a separate module from the vent anchor to make it easier for the operator to insert the vent anchor into the vent opening. The winch panel had a metal hook on the back, which the operator fit into a hole on the vent anchor assembly. Once the winch panel is fit in place, the operator latches two toggle clamps on the winch panel to lock the two modules together (Figure 2.4.54).
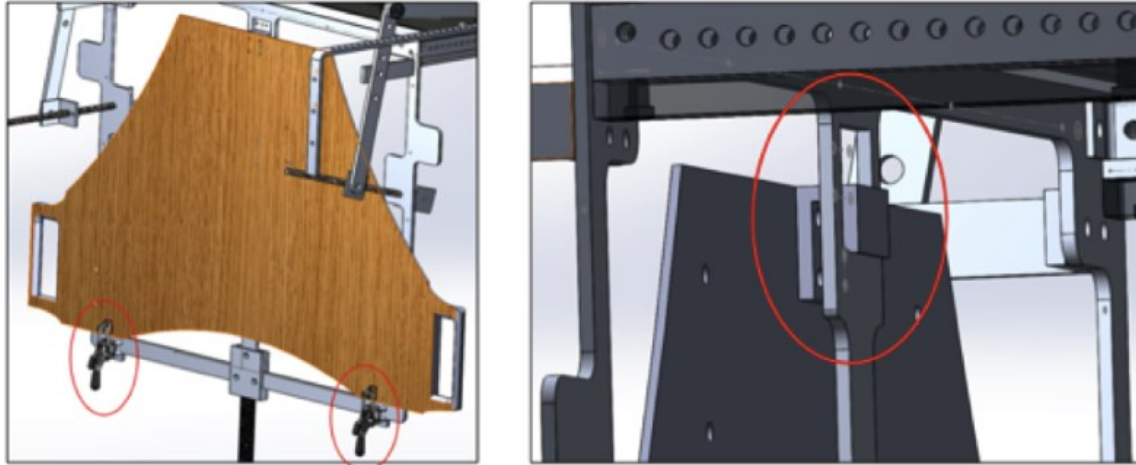
Figure 2.4.54. *CAD visualization of the hook and latches on the winch assembly*

2.4.6.3.5 Adding Cable Tensioning Arms

During testing, it was found that the lead-follower motor arrangement limited the maximum speed of the winch, and still did not satisfactorily guide the cable onto the spool when retracting the cables, as the tension on the support cables varied with the location of the sensor robot. Spring-loaded cable tensioning arms were installed to replace the lead-follower motor set-up (Figure 2.4.55).
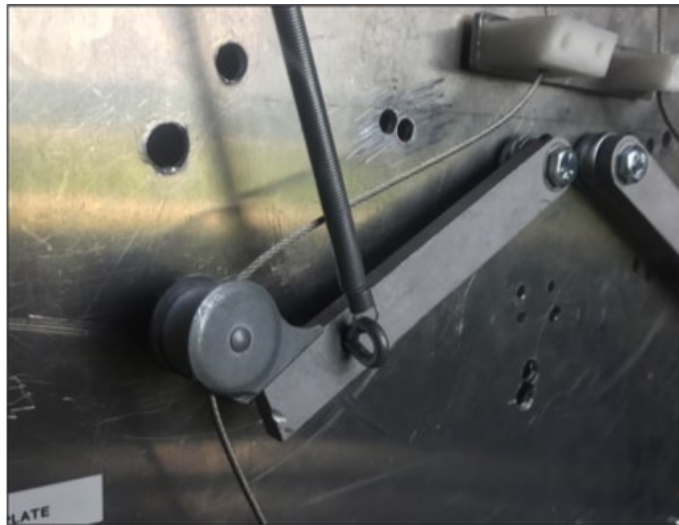
Figure 2.4.55. *Tensioner arm mechanism*

Since the angle of the tensioning arms corresponded to the tension in the cable, the operator could quickly visually estimate the cable tension. Potentiometers mounted to the axle of the arms could measure and record the arm angle. A motor operated cable guide was built using a 8mm lead screw to better guide the cable back onto the spool when reeling in. The cable runs through a Teflon guide, which is attached to a nut on the lead screw. As the motor rotates and turns the lead screw, the cable guide translates along the length of the spool (Figure 2.4.56).
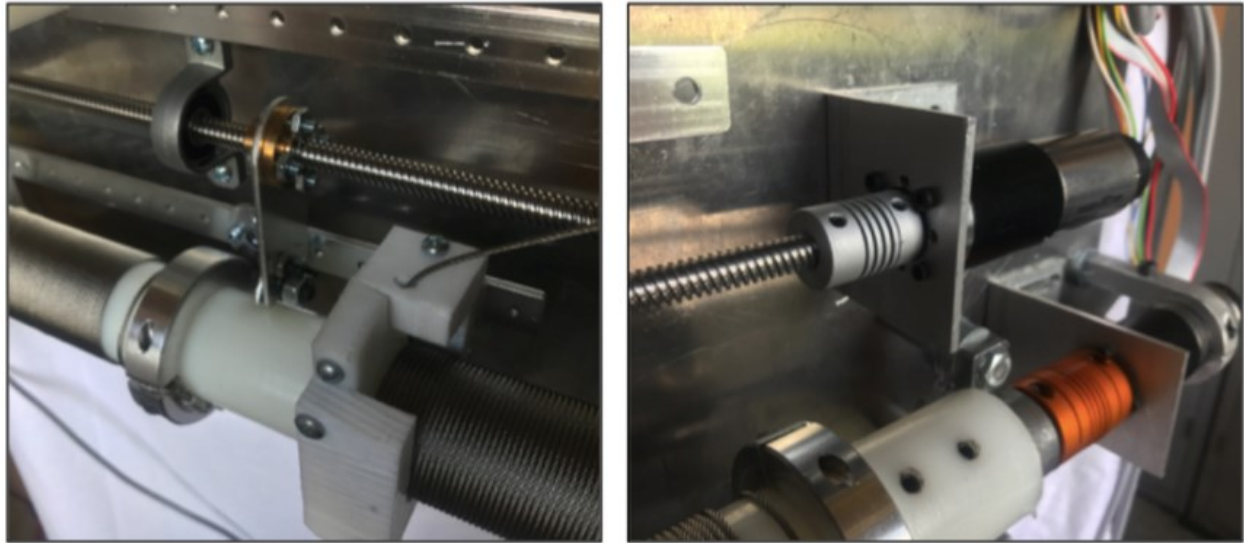
Figure 2.4.56. *Motorized cable guide mechanism*

Using readings from the encoder mounted to the cable spool, the cable guide motor controller was programmed in ROS to rotate at a speed proportional to the main spool speed, guiding the winch cable onto the spool neatly and precisely. The controller ROS code was also modified to allow the operator to adjust the offset of the cable guide as needed, using the left joystick.

The winch cables were modified to run through full housing from the end of the winch assembly, along the delivery arm, and into a housing stop on the back of the sensor train garage. The full housing run ensured that the cable length does not change as the delivery arm is moved around or pivoted. Since the robot train was permanently connected to the winch by the winch cables, and the robot train was housed in the garage on the delivery arm, the delivery arm and winch cannot be separated while the system is prepped for inspection. The end of the delivery arm was attached to a rotating cylinder at the top of the winch baseplate.

2.4.6.4 Delivery Arm
2.4.6.4.1 Initial Concept
Two different methods of delivering the robot to the ventilation channel were explored in McNelly – first, a navigable, self-propelled robotic sensor car, and second, a passive sensor car delivered using a mechanical arm. Using the mechanical arm, the sensor robot would be delivered to the ventilation channel, and the arm would rotate around the center of the MPC to position the robot above different ventilation channels (Figure 2.4.57). The end of the delivery arm would be shaped to allow for gravity-assisted sensor car insertion into the ventilation channel (Figure 2.4.58).
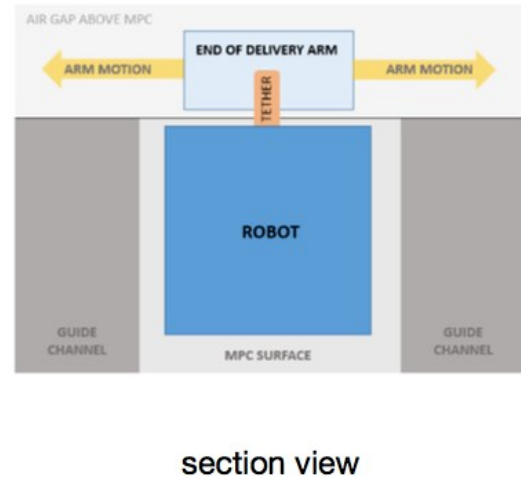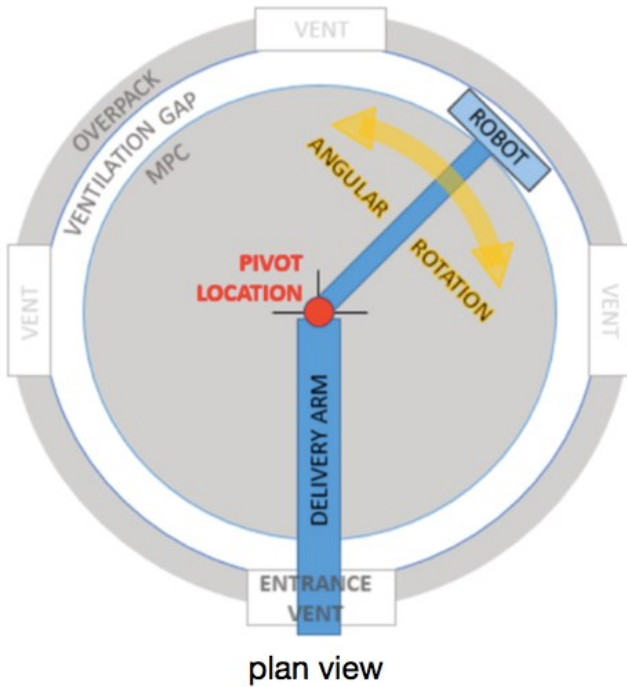
Figure 2.4.57. Diagram of initial delivery arm concept from McNelly, showing the arm insertion and pivoting to different ventilation channels
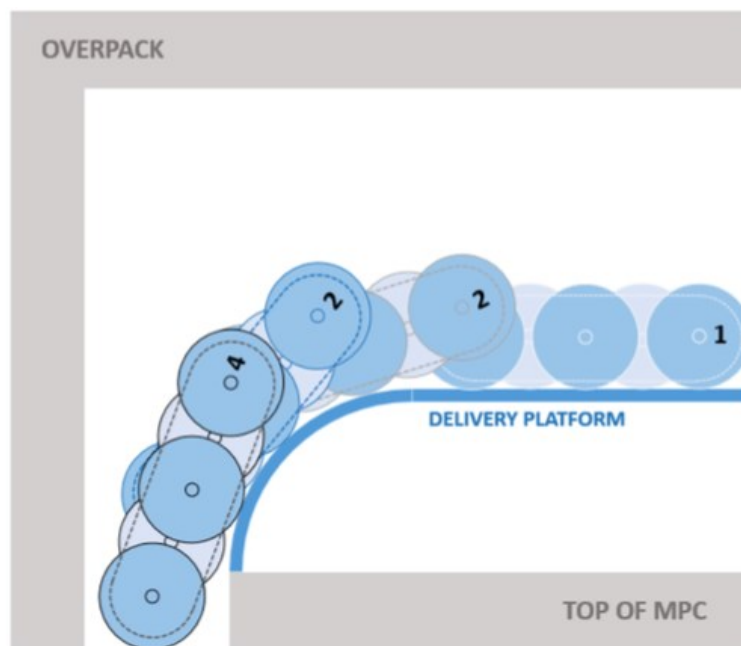
Figure 2.4.58. Diagram of initial delivery arm concept from McNelly, showing it shaped to allow gravity to assist in sensor car insertion into the ventilation channel

Initial prototypes were constructed with no pivoting mechanism, instead focusing on the shaped end of the delivery arm for gravity-assisted sensor robot insertion and extraction. The prototype

brought to the May 2016 McGuire Nuclear Site field test was built out of thin steel flashing and used a section of 4" diameter PVC pipe to create the smooth, radiused end needed for sensor car insertion and extraction.

2.4.6.4.2 First prototype of pivoting delivery arm

To direct the sensor robot into different ventilation channels, the next versions of the delivery arm were designed to include a cable-actuated pivot. The arm was constructed out of thin steel flashing for the flexibility required to enter the cask through the ventilation opening.

Figure 2.4.59. *The pivoting delivery arm prototype in two different positions*

The pivot axis was located 3' from the end of the delivery arm, at the center of the top of the MPC, and the arm pivoted 45 degrees in both directions (Figure 2.4.59), providing a 90 degree inspection range for a single vent inlet. Two 1/16" steel cables ran through cable housings attached to the delivery arm. One end of each cable was secured to a wooden disk bolted to the pivoting section of the arm, and the other end of each cable was secured to a second wooden disk, which was attached to the stationary section of the arm with a single bolt around which it can rotate. When the stationary arm disk was rotated, the cables pushed and pulled on the pivoting arm disk, and the rotational motion was transferred. While this prototype placed the controls at the ventilation opening in the overpack, the cables and housing can be extended to place the controls below the opening and out of a direct line of sight into the cask, reducing the operator's exposure to radiation. While making this prototype, the need to modify the end of the delivery arm to match the radius of the MPC was realized (Figure 2.4.60).
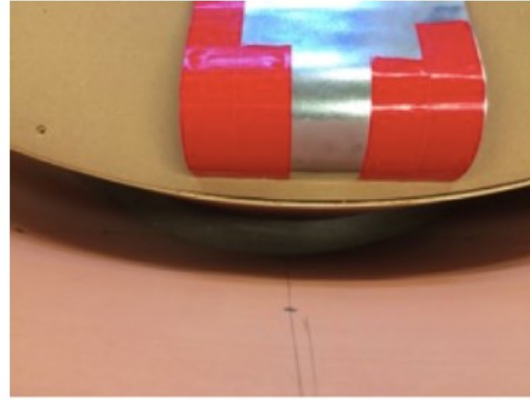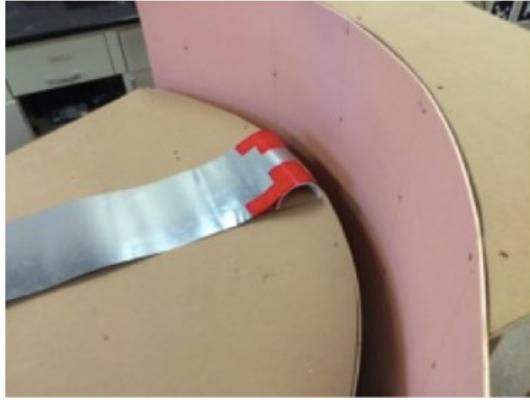
Figure 2.4.60. *Demonstrating the radius of the MPC compared to the end of the first pivoting delivery arm prototype*

2.4.6.4.3 Version 2 - Testing at Hatch Nuclear Plant

A new prototype of the delivery arm was completed for use at the Hatch Plant field test. The delivery arm had a rounded end constructed out of 3D printed plastic to accurately match the radius of the MPC while meeting the entry angle requirements for the sensor robot (Figure 2.4.61). This end shape was mounted to a aluminum plate with PEEK plastic sliders that prevent metal-to-metal contact when the arm is placed on top of the MPC. A sheet metal strip was then attached to the radiused end to create the surface for the sensor robot to travel on.
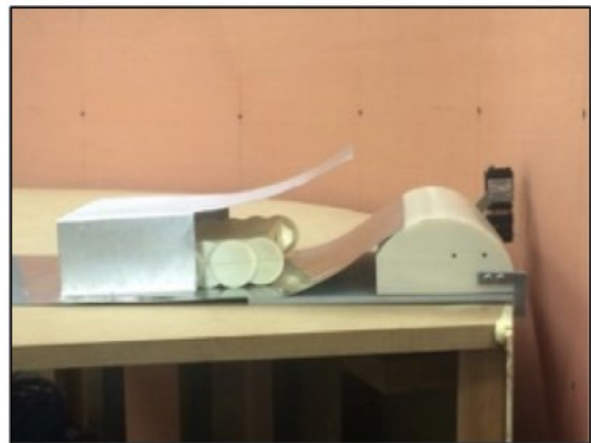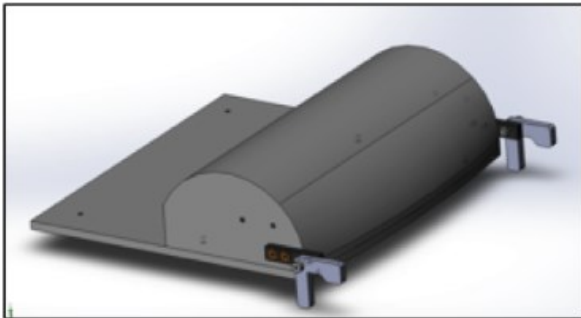
Figure 2.4.61. *3D printed delivery arm prototype*

A garage for the sensor robot, made out of sheet aluminum, was riveted to the arm to secure the cars in place on the arm during arm insertion and removal. A Point Grey BlackFly camera was mounted to the end of the delivery arm looking down the ventilation channel, allowing the operator to keep track of the position and progress of the sensor car while in the ventilation channel (Figure 2.4.62).

Figure 2.4.62. Early prototype of delivery arm garage and camera mount

2.4.6.4.4 Version 3 - Guiding and Capturing the Sensor Robot Cars

While testing the prototype delivery arm built for the May 10, 2016 Holtec visit, it was observed that a structure was needed to passively capture and guide the sensor robot in to place when retracting the robot from the ventilation channel. The radius end of the delivery arm went through multiple design iterations to have guides for the data tether, support cables, and robot wheels (Figure 2.4.63). Each prototype iteration was 3D printed out of PLA.
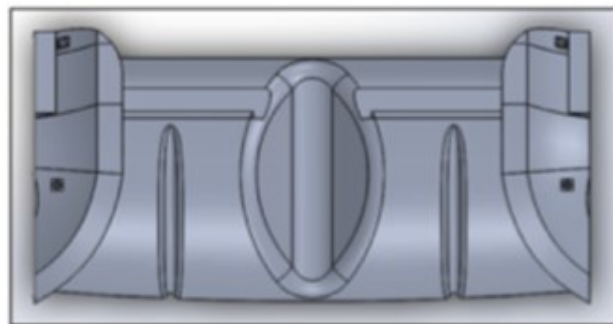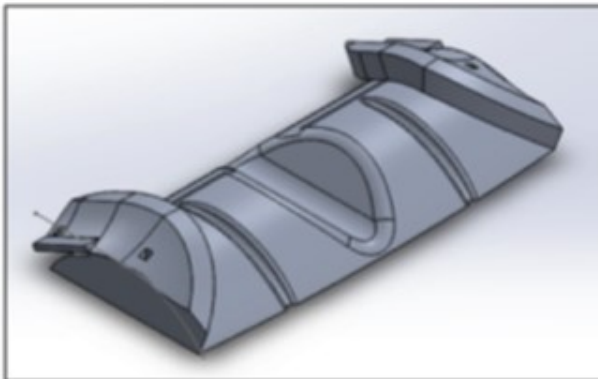
Figure 2.4.63. CAD visualization of delivery arm radius end from different angles, showing sensor car guides, support cable guides, and data tether guide

The arm end guide and garage interface were carefully designed to guide the sensor cars in and out of the ventilation channel with no wedging or jamming. The garage for the sensor cars was designed to be waterjet cut out of aluminum and bent into the desired shape, using the cut slots to guide the bends (Figure 2.4.64). The garage was built as one continuous piece along the delivery arm to prevent the sensor cars from getting jammed in the garage while the sensor cars were in motion. The height of the garage was reduced in order to prevent jamming that may occur while feeding the delivery arm through the vent, and to ensure that the sensor cars smoothly slide in and out of the garage. Narrow strips of flexible aluminum extending from the end of the garage to the radius end of the delivery arm were added to guide the sensor cars during their retraction. The smooth transition from the end of the garage to the radius end of the

delivery arm ensures that the sensor cars do not get caught or jammed during insertion or retraction, and allows for passive extraction if needed.

Figure 2.4.64. *3D printed delivery arm end guide structure installed on delivery arm, with sensor cars in garage.*

Figure 2.4.65. *Front and rear view of bent aluminum garage*

Figure 2.4.66. *Top view of bent aluminum garage*

With the addition of the full housing for the winch cables, the delivery arm garage needed a way to hold the cable housings in place. Two slotted housing stops made out of UHMW polyethylene were attached to the top of the garage (Figure 2.4.67). The slots allowed the cable to slide into the housing while still attached to the robot train.
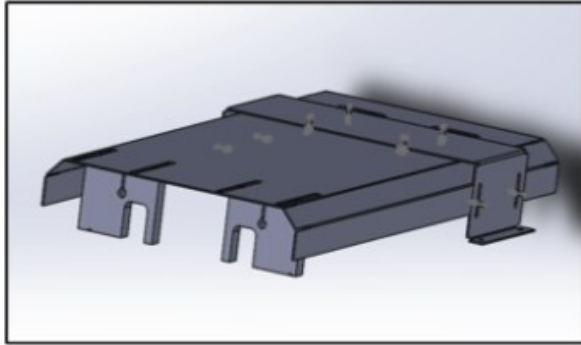
Figure 2.4.67. *CAD concept and built version of garage with cable housing stops*

While the garage design worked reliably during in lab testing, difficulties arose when testing the system with the LIBS team. After attaching all the necessary data tethers and winch support cables to the robot train, the robot train could not easily be set up inside the garage to prep for inspection. To simplify the installation and prep for inspection, the final garage design was modified to be a "clamshell" that hinges at the front, allowing the garage to pivot forward for placing the sensor train inside (Figure 2.4.68).
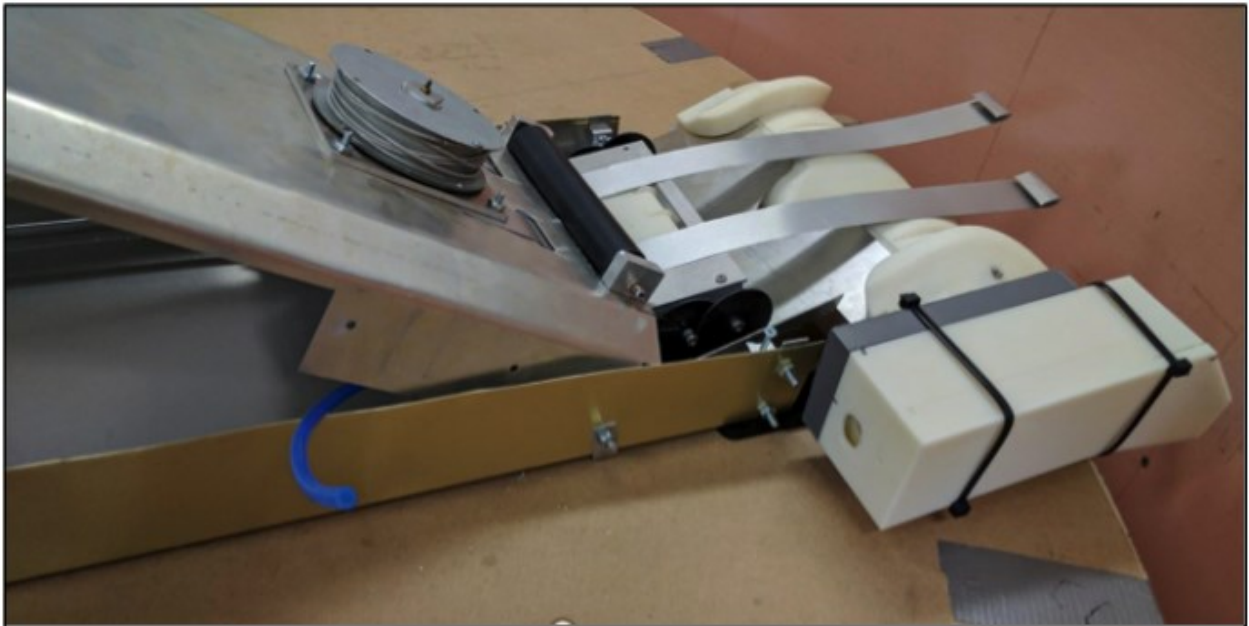
Figure 2.4.68. *Clamshell garage, hinged at front for placing robot train inside*

The cable stops were modified and attached to the base of the delivery arm, such that the entire robot train, when attached to the support cables and data tether could be placed into the garage,

with the clamshell closed over the top. This drastically simplified access to the robot and reduced prep time before an inspection, compared to previous designs.

2.4.6.4.5 Sensor Car Train Pushing Mechanism
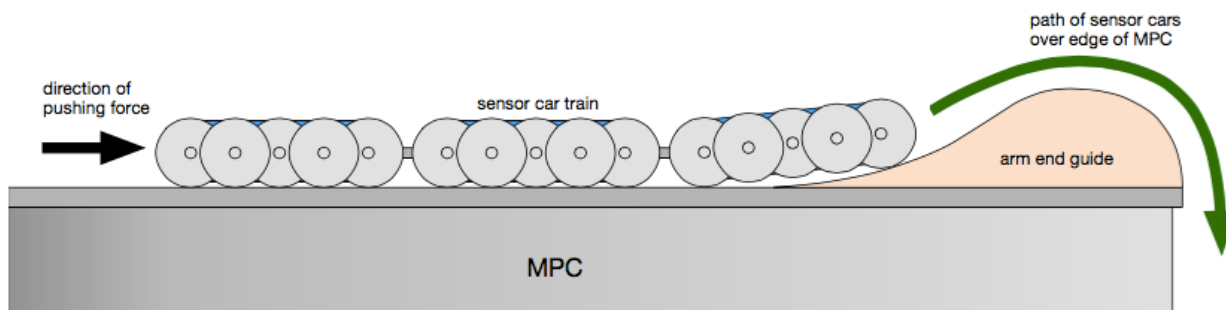
Figure 2.4.69. *Diagram showing sensor car train path of motion over the end guide of the delivery arm*

Because the car needed to be pushed out of the garage and over the raised end of the arm (Figure 2.4.69), a pushing mechanism using linear bearing blocks and rods was designed. Initially, the bearing blocks were rigidly mounted to the delivery arm behind the garage, and the 8mm bearing rods travelled through the bearing blocks to push the robot train. The end of the bearings rods were attached to a constant force spring to apply the pushing force. However, during testing, the moving bearing rods conflicted with the data tether and support cables when the arm pivoted. Also, since the arm would be inserted and removed from the ventilation opening while the robot train was fully retracted in the garage, the bearing blocks would be fully extended, sticking out of the back of the garage and could impact the arm's mobility. To solve this, the pushing mechanism was redesigned to have stationary, rigidly mounted bearing rods and moving bearing blocks (Figure 2.4.70).
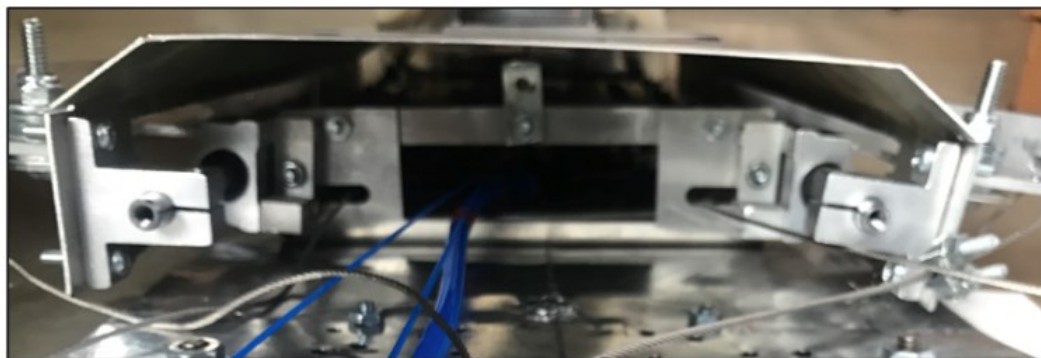
Figure 2.4.70. *Back view of the garage showing the bearing rod mounting*

The two bearing rods were mounted on either side of the garage, and the bearing blocks were connected together with an L-shaped piece of aluminum, which pushed against the back of the rearmost car in the robot train. This redesign meant that the constant force spring reel had to be relocated to the front of the garage on top, and required a change in direction for the spring reel

cable. After first trying a Teflon guide, which resulted in too much friction, an ABS roller was built to sit on top of the front edge of the garage (Figure 2.4.71).
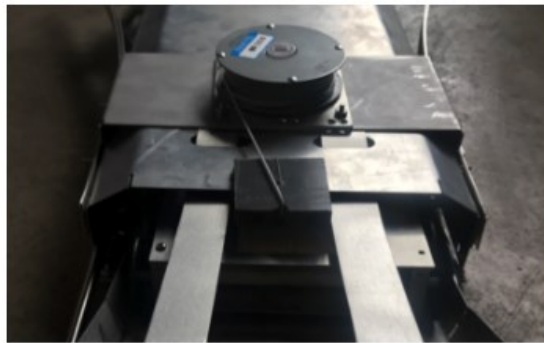
(a) teflon guide   (b) ABS roller

Figure 2.4.71. Two methods of changing direction of spring reel cable

While testing on the full height mock up, it was clear that although the spring reel was capable of pushing the robot train over the edge, it gave no feedback to the operator about the status of the robot. If the robot train was getting stuck or jammed, the operator should be alerted right away. Additionally, with the spring reel under constant tension while the robot was retracted into the garage, it made it difficult to set the robot train in the garage the when preparing for inspection. The spring reel placement also reduced the clearance when inserting and removing the arm from the vent opening. For the final iteration of the pushing mechanism, fabricated pulleys were mounted in line with each bearing rod, and the pulling cable runs back along the delivery arm in full housing (Figure 2.4.72). This removed the spring reel from the top of the garage, greatly simplifying the design, and allowed the operator to apply force to the pushing mechanism themselves as needed.

Figure 2.4.72. Pulley for pushing mechanism cable

2.4.6.5 Cameras and camera boxes

To shield the in-cask cameras from gamma radiation, a periscope-inspired prototype shielding box was designed taking advantage of the reflective properties of gamma radiation versus visible light. While visible light is reflected by mirrored surfaces, gamma radiation is not. Using two mirrors to direct visible light around a corner, the camera can capture images while the gamma ray's direct line-of-sight to the camera is blocked. The first camera box prototypes were 3D printed PLA and aluminum, and were used to determine dimensions and allowable field-of-view (Figure 2.4.73).

For the next iteration, the box was modified with sides that could be filled with lead shot for additional radiation shielding (Figure 2.4.74). Two camera boxes were designed to be mounted in different locations: one camera mounted to the inside of the vent anchor assemble to look inside the cask along the top of the MPC, and the second mounted on the end of the delivery looking down into the ventilation channel at the sensor cars.

Figure 2.4.73. *Aluminum and 3D printed camera box prototypes, showing the cam- era and two mirrors*
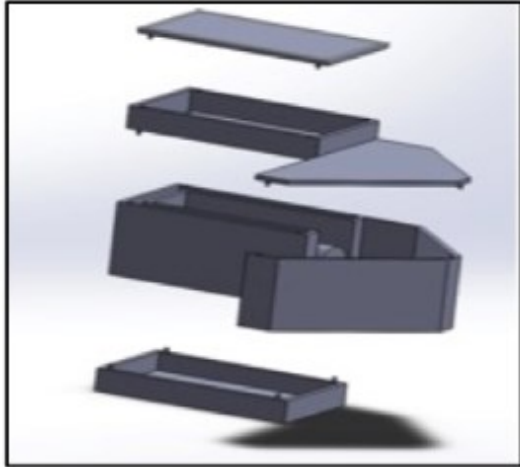
Figure 2.4.74. *Exploded diagram (left) and completed 3D printed camera box prototype filled with lead shot (right)*

2.4.6.6 Robot Sensor Train

2.4.6.6.1 Initial Concept

As described earlier, McNelly's wedging and jamming dimensional analysis set the largest maximum external dimensions of each individual sensor car. Adding wheels and rounding the corners to reduce friction decreases the usable space significantly in each car, but using multiple sensor cars increases the total usable sensor space. Using these dimensions McNelly created a concept design for a wheeled sensor car (Figure 2.4.75), and outlined the idea of the sensor cars being linked together in a train to carry the required sensors.
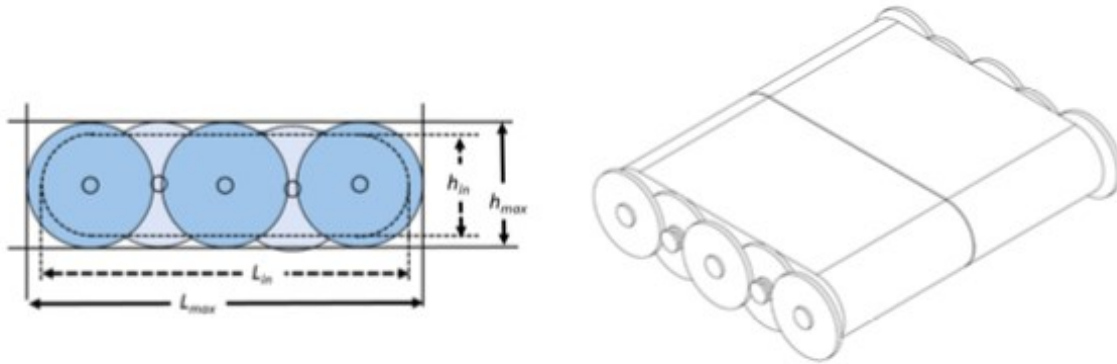
Figure 2.4.75. *Diagrams of wheeled sensor car concept, from McNelly*

Based on these initial concepts and dimensional constraints, a first wheeled prototype was designed, and 3D printed out of PLA plastic. The sensor car has 10 wheels total, with 5 on each side. The wheel-axle-bearing assembly was sandwiched in place between the two halves of the robot body, which was assembled together with countersunk screws. The screws threaded into helicoils on the top half of the robot body, which allowed for the pieces to be assembled and

disassembled multiple times, and created a strong mechanical connection between the two halves (Figure 2.4.76).

Cameras, lighting, and other equipment were mounted inside the robot body with adhesive putty. Figure 2.4.77 shows the prototype with two Point Grey Blackfly cameras for stereo vision and a LED to illuminate the interior of the cask.
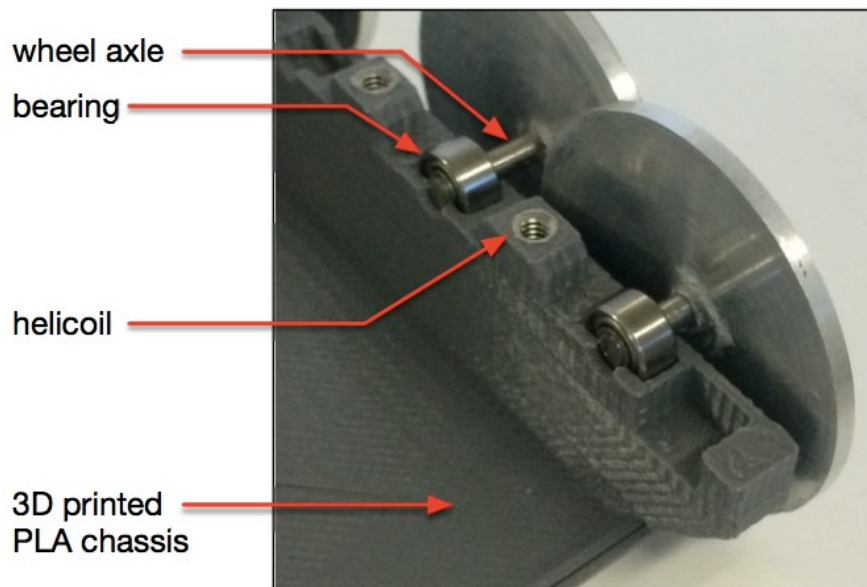
Figure 2.4.76. *3D printed sensor car prototype close-up, showing bearing seat and wheel-axle-bearing assembly*

Figure 2.4.77. *3D printed sensor car prototype, showing camera lenses, LED, and wheels*

2.4.6.6.2 Prototype Built for McGuire Test

Since the May 2016 McGuire Nuclear Plant test would be taking place in a real cask, it was extremely important to not damage the cask or MPC by leaving any parts behind inside the cask. To ensure the durability of the sensor cars, the design was modified to have no moving parts. The

shape of the wheels was included in the main chassis of the cars, and three cars were connected together into a train (Figure 2.4.78). Two Point Grey cameras and one LED were mounted in the front car, and a stainless steel air hose and two Ethernet cables ran out of the rear car back to the control center.
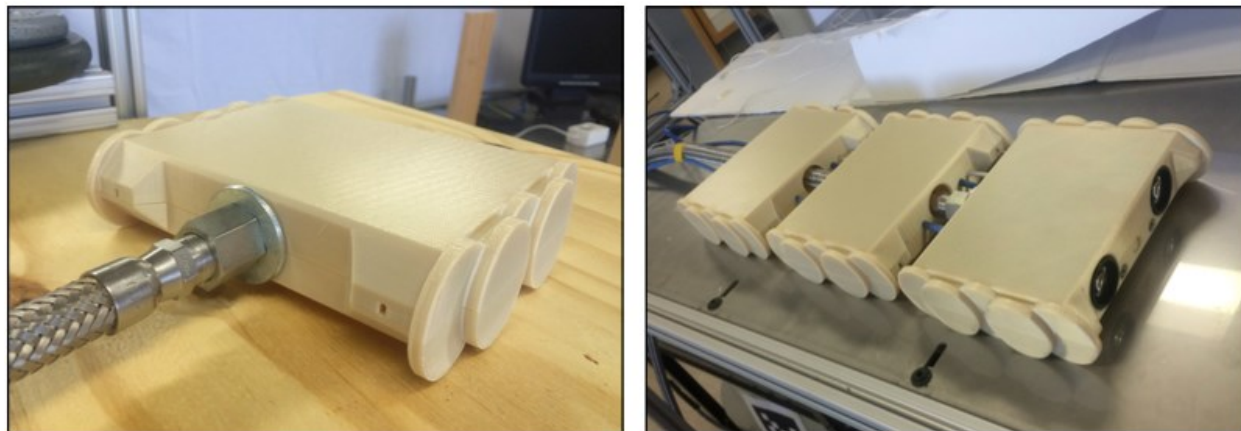
Figure 2.4.78. *The prototype sensor car train designed and built for testing at McGuire Nuclear Plant, showing air hose connection (left) and cameras in front car (right)*

2.4.6.6.3 Modular Aluminum Chassis

After testing the previously described 3D printed prototype at McGuire Nuclear Station, work began on a new modular, aluminum car chassis. In developing the 3D printed prototypes of the sensor robot cars, some limitations of 3D printed plastic were encountered when it comes to ease of assembly and structural integrity. Since plastic does not thread well, it was difficult to securely attach sensors to the chassis, and for attaching the cars together in a train. Additionally, the increased thickness that the plastic material required for strength reduced the available space inside the sensor car. Aluminum was chosen for the next prototype for its strength, light weight, and machinability.

The top, bottom, front, and back plates were waterjet cut out of 0.080" aluminum sheet, and each plate screwed into the larger side pieces made out of machined 3/8" aluminum stock. The wheel axles also screwed into the side pieces. This design allowed for different top, bottom, front, and back plates to be swapped in or out depending on changes to the interior sensors mounting or other needs. The first car had holes in the top plate for the stabilizing arms, and one hole in the bottom plate for the EMAT sensor. The second car was fully enclosed on the top and bottom. Both cars has holes in the front and rear plates for cables to run through. The wheels were cut out of PEEK to prevent metal-on-metal contact during the inspection, thus avoiding the possibility of scratching the MPC canister.
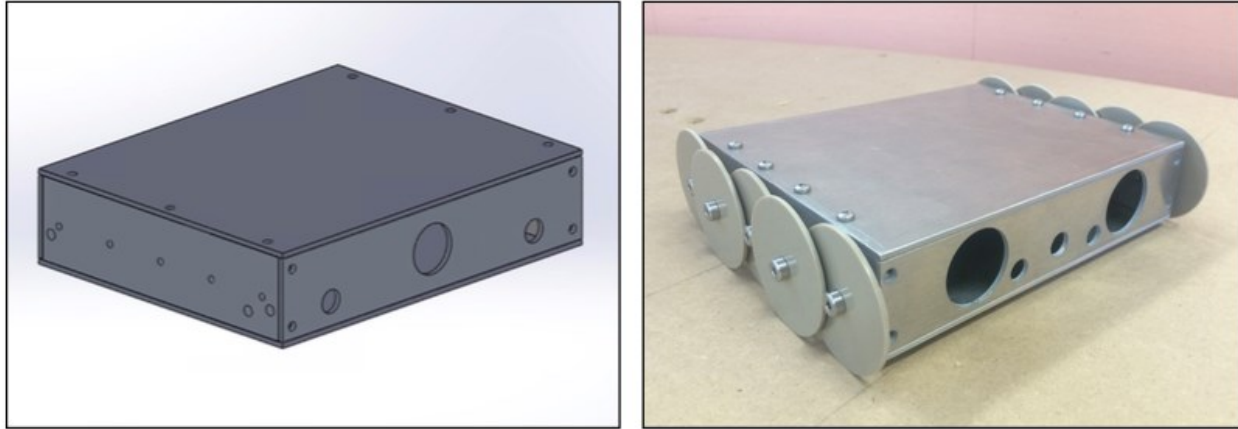
Figure 2.4.79. *The modular aluminum sensor car prototype, shown as a Solidworks assembly (left) and as-built with wheels (right)*

In preparation for the planned Hatch Nuclear Plant field test, an actuated 2-car train was constructed that was capable of taking EMAT sensor measurements on both the cask mock up and on a real cask. The first car contained a camera, two LEDs to illuminate the interior of the cask channel, the EMAT sensor actuation mechanism, and the stabilizing arms (Figure 2.4.80). The second car contained the wiring connectors for the EMAT sensor cables, the servo signal and power cables, the camera USB cable, and the lighting power cable. The cable bundle connecting the sensor robot to the control, power, and data acquisition systems was a full 50' long, corresponding to the length necessary for a real cask inspection.

Figure 2.4.80. *Bottom view of sensor car train showing camera, EMAT sensors, lighting, and cable bundle*

The camera in the prototype car was a miniature pinhole USB camera to simplify collecting visual data while the sensor robot takes measurements. During inspection, the EMAT sensor actuation mechanism pushed the sensors against the MPC, while the stabilizing arms held the sensor car against the MPC.

The 2-car train was set up on the metal cask mock up to test the EMAT sensor data collection process, and to test the accuracy of EMAT sensor measurements when taken from the actuated sensor robot, as seen in Figure 2.4.81.
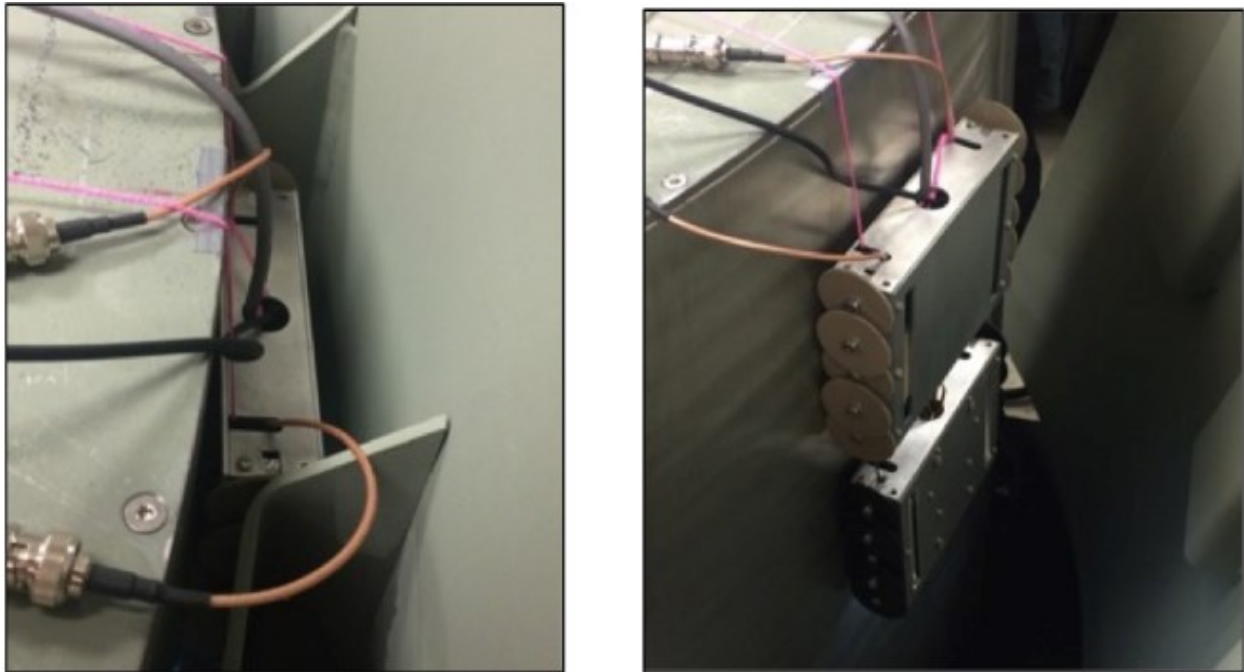
Figure 2.4.81. *The prototype sensor car train taking EMAT sensor measurements on the metal cask mockup*

2.4.6.7 Field Testing System Prototypes

2.4.6.7.1 Lessons Learned from Testing at McGuire Nuclear Station

The robotic inspection system was field tested in an empty NAC cask at McGuire Nuclear Station, North Carolina on May 18-19, 2016. The full robotic system was inserted into the top vent and staged on the MPC for a mock inspection. The cask lid was removed to allow access to the top of the MPC to provide a visual validation of the performance of the current robotic system. For use in analysis and testing, video was collected from both cameras (Figure 2.4.82) during two separate traversals down the channels.

The motor and winch spool encoders also operated as designed, giving the operators real-time information about the sensor robot's location within the vent shaft.

Figure 2.4.82. *Still from in-car video recording during cask inspection at McGuire*

The physical testing on a real-world cask showed that the design brought to McGuire was feasible for inspection, with further work to refine and simplify the system. One lesson learned during the field-testing was that the delivery system was cumbersome to install on the exterior of the cask. The entire system must be raised up to the top of the cask on a scissor lift (Figure 2.4.83).
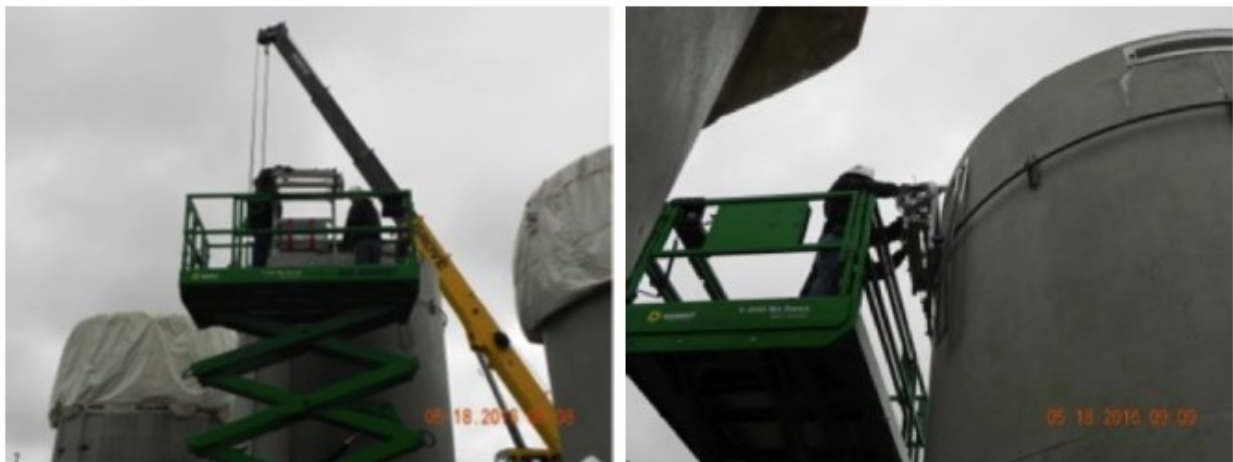
Figure 2.4.83. *The system being raised up and installed on the top of the cask at McGuire, showing the scissor lift required for access*

This lead to the decision to make the subsequent iterations of the delivery system smaller and lighter to simplify installation on the cask. Additionally, the hanging counterweights were considered a safety risk for the operators around the cask, and were removed in later prototypes. The bottom of the cask ventilation channel had moving water due to rain, making the visual laser range finding method less effective due to the reflection and refraction of the laser beams off the water.

As described earlier, the McGuire demonstration prototype did not have movable wheels to make it more durable and less prone to mechanical failure. The lip on the end of the delivery arm, which hangs over the edge of the MPC to secure the delivery arm during insertion and extraction of the sensor robot, needed to be refined to better hold the delivery arm in place. The insertion of the robot can be seen in Figure 2.4.84.
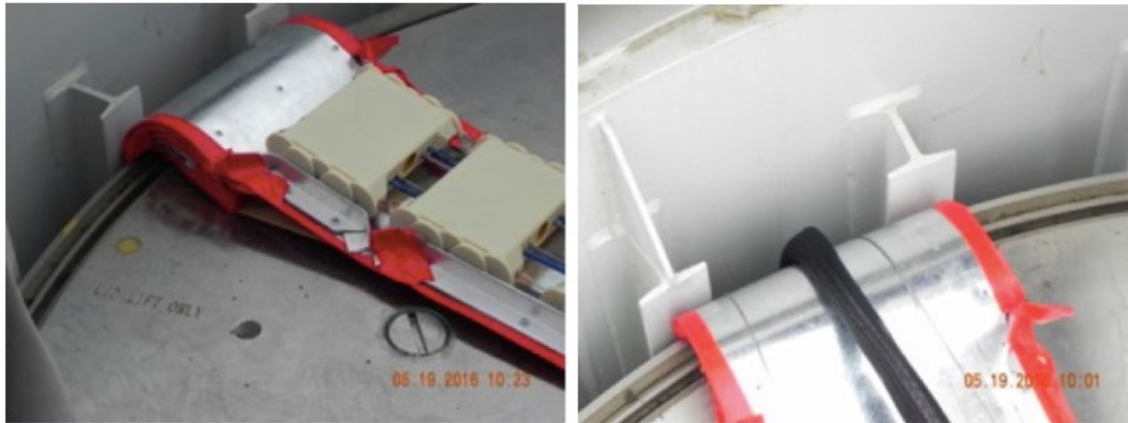
Figure 2.4.84. *The robot being inserted into the vent channel at McGuire*

It was also decided that a camera needed to be added to the end of the arm to allow the operator to observe the sensor robot during insertion and removal, providing more methods of visual feedback to the operator about the status of the robot within the cask. Weatherproofing the system also became a goal, since the operators and power supply sit outside during the inspection (Figure 2.4.85). This was made especially clear when it began to rain during the second day of the demonstration.
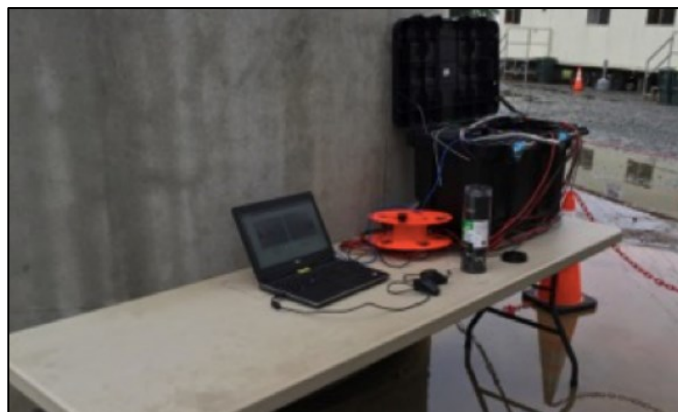
Figure 2.4.85. *The power supply box and laptop controlling the winch motor positioned at the base of the cask during inspection at McGuire*

2.4.6.7.2 Team visit and testing at Holtec

On May 10, 2017, the delivery team and the EMATS team visited Holtec Manufacturing to perform tests on real casks. The delivery group focused on two main tests, one using a completed

full-size MPC, and one using a cask lid featuring the ventilation opening. To test the capabilities of the winch and sensor cars, Holtec set up a completed MPC next to a tall scaffold to allow access to the lid of the MPC. The winch and power supply were set up on the scaffold, and the delivery arm and sensor cars were set up on the lid of the MPC, using plastic to protect the MPC lid from scratches (Figure 2.4.86).
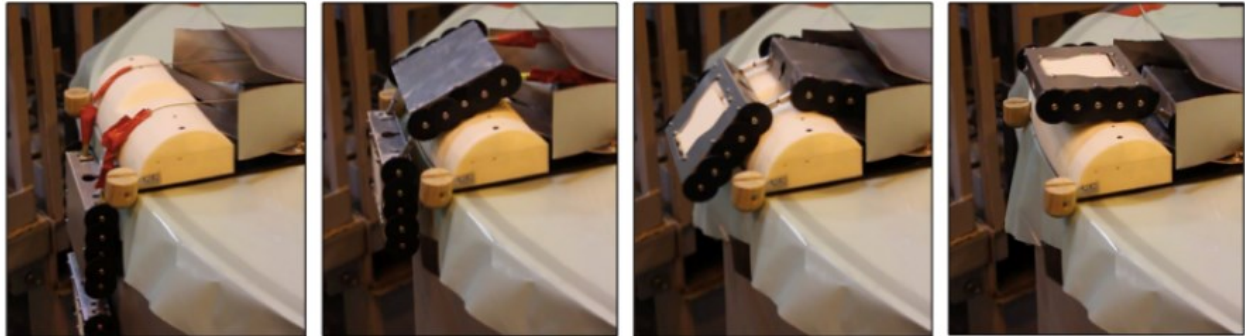
Figure 2.4.86. *Left to right – sensor cars retracting into the garage at Holtec*

Using the winch, the operator raised and lowered the sensor cars the full height of the MPC multiple times, checking the sensor car behavior during this process. The sensor cars tracked straight down the MPC, and stayed on the surface of the MPC, even without the use of stabilizing arms (Figure 2.4.87 and 88). It was observed that a method of adjusting the yaw of the sensor cars was needed to ensure the sensor cars were aligned for the best EMATS measurement.
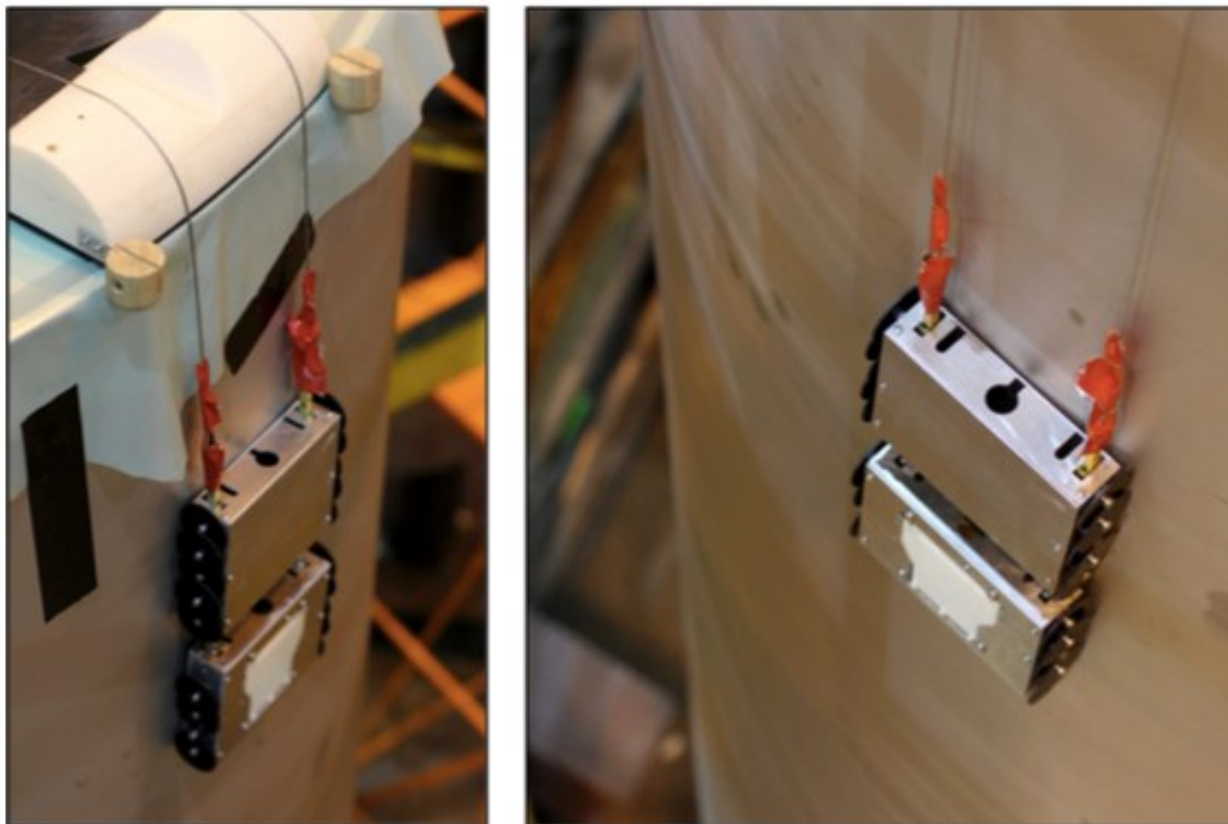
Figure 2.4.87. *Sensor cars traveling down the MPC at Holtec*

Holtec also set up a cask lid raised 3' off the ground to test delivery arm and vent anchor insertion. A metal plate was placed beneath the lid to simulate the MPC lid, and the cask lid was placed at multiple heights to represent different MPC heights. The delivery arm pivoting mechanism was tested to be capable of a full 120 degrees along the simulated MPC lid without the sensor cars inside. However, when objects were added into the delivery arm to simulate the weight of the sensor cars, the pivot would begin to jackknife. This behavior revealed that a mechanism would need to be added to the delivery arm to secure the pivot point in the center of the MPC and prevent jackknifing.

Figure 2.4.89. *Delivery arm and sensor cars on the MPC at Holtec*

2.4.6.8 MPC mock ups

2.4.6.8.1 In-lab MPC Mock-up

One of the main lessons learned during the McGuire field test was the need for a full-scale mock-up to accurately test the full inspection process from start to finish. A new mock-up of the HI-STORM 100S cask interior was fabricated that represents the section of the cask that the inspection system will interact with. This included one entry vent, a section of the top surface of the MPC, and the ventilation channel between the MPC and overpack walls that the robot will descend into. The top of the mock-up allowed for a 90 degree pivoting range of the delivery arm to be tested. The mock-up was 4" tall to allow for testing in the lab. The mock-up was first modeled in SolidWorks for visualization (Figure 2.4.90), with the dimensions taken directly from the HI-STORM 100S cask drawings provided by the manufacturer.
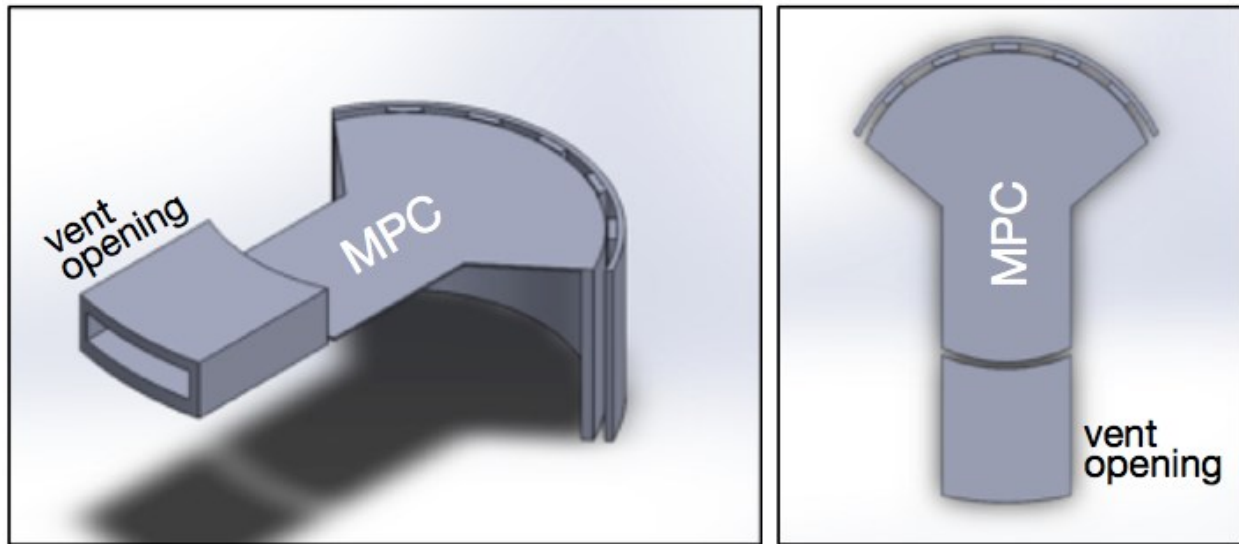
Figure 2.4.90. *Solidworks model of the lab cask mock-up*

The top surface representing the MPC was made of 3/4" MDF cut to the same 6' radius of the MPC. The interior surfaces of the vent openings were also 3/4" MDF. The curved surfaces representing the MPC and overpack walls were constructed of 1/4" plywood shaped around a structural plywood frame, as shown in Figure 2.4.91.

Figure 2.4.91. *Two different views of the constructed cask mock-up*

2.4.6.8.2 Full-height MPC mock-up

In preparation for the final demonstration in September 2017, a full-height mock-up of the MPC was constructed. The construction process and materials were similar to the desk level MPC mock-up built for in-lab testing. The entire mock-up is constructed out of 4 modules that could be stored separately and then stacked to full height when needed (Figure 2.4.92).

The top and bottom panels of each module were 1/2" MDF, and the vertical support risers and horizontal tie-ins were pressure-treated pine 2x4 boards. The MDF top and bottom panels were cut to match the MPC radius using a router pattern bit and a pattern laser-cut out of acrylic. After the top and bottom panels were attached together with the vertical risers, 1/4" flexible plywood was screwed into the risers to match the bend radius of the MDF top and bottom panels. Each module was stackable onto the others without tools using a series of holes and dowel rods in the top and bottom, respectively. The bottom module was sized to be interchangeable with the metal mock-up from the EMATS team, allowing the metal mock-up to be slotted in place to take EMATS or LIBS measurements using the full-height mock-up.
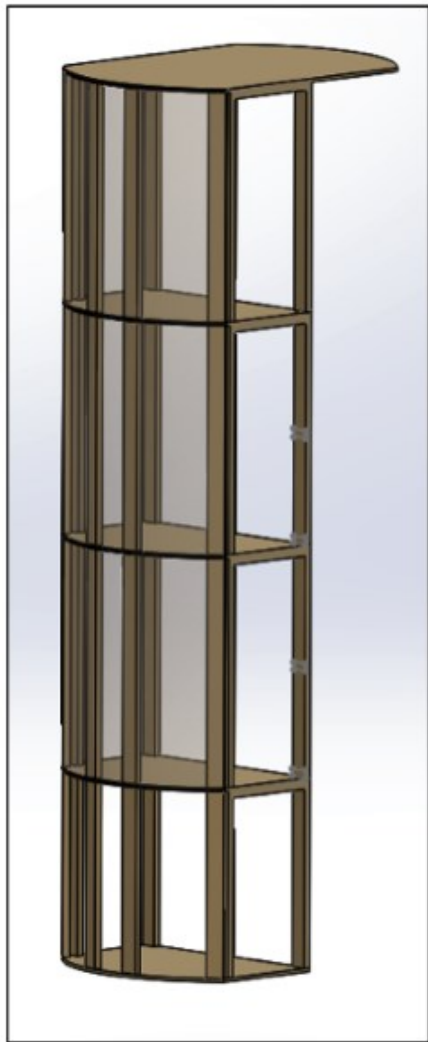
(a) CAD model   (b) assembled mock-up in location

Figure 2.4.92. Full sized MPC Mock-up

2.4.7 Final Build Documentation

2.4.7.1 Final Vent Anchor and Mount

The final vent anchor design has two main – one part that the operator inserts inside the ventilation opening and locks in place, and another part that was designed for attaching the winch assembly. The section of the vent mount that is inserted into the ventilation channel consists of two U-shaped rails, joined by a ABS plastic sheet. Each rail has both a vertical and horizontal four-bar linkage that acts as the locking mechanism (Figure 2.4.93).
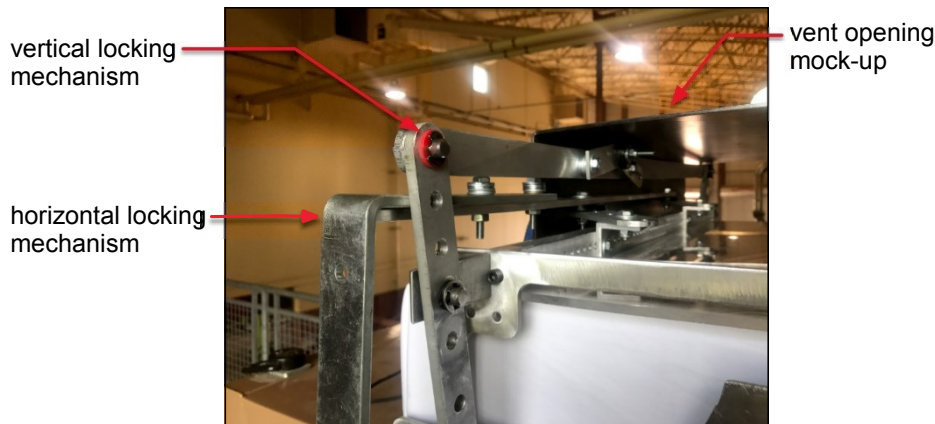
Figure 2.4.93. *View from outside cask, showing vertical and horizontal locking mechanisms*

Each linkage is opening or closed by rotating threaded rods with a handheld impact driver (Figure 2.4.94). The end of each rail has a hook and wheel assembly to allow for a smooth insertion into the ventilation channel, and to help lock the vent anchor in place (Figure 2.4.95). The ABS sheet joining the two rails provides a surface to slide the delivery arm across when inserting the arm inside the cask, and the end of the ABS sheet is beveled downward to aid in delivery arm extraction. All surfaces on the vent anchor contacting the cask have PEEK wheels or sliders to prevent damage.
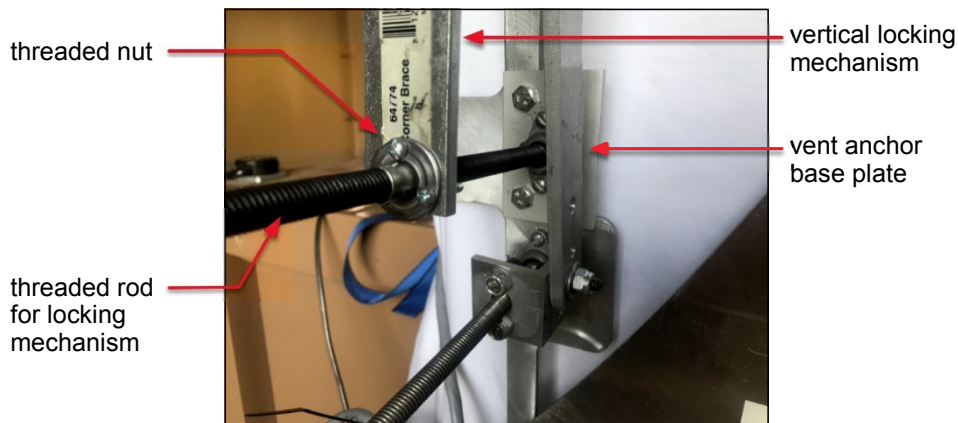
Figure 2.4.94. *Close up of thread rod and nut for tightening locking mechanism on vent anchor*

vent opening mock-up

vertical locking mechanism

end hook

delivery arm

Figure 2.4.95. *View of vent anchor inserted and locked into place from inside cask vent opening mock-up*

The winch assembly mounts to a hole in the middle of the vent anchor, and has toggle clamps that latch onto hooks at the bottom of the vent anchor base plate.

To allow the operator to see inside the cask during an inspection, a bright LED, typically used for architectural lighting, was installed on the end of the vent anchor mechanism that inserts into the cask. The LED is controlled from the power supply at the control center, allowing it to be turned on or o , and dimmed if needed. Since the LED runs of 36V, it has its own dedicated power cable made out of red-black zip cable. Anderson powerpole connectors panel mounted to the aluminum plate of the vent anchor give it quick and reliable connections. A single PGR BlackFly camera is also mounted to the end of the vent anchor mechanism, housed within a shielded camera box, as described in Section 6.5.1. The vent mount camera is focused and aligned to see the delivery arm as it is inserted into the cask, and to monitor the sensor robot train as it is inserted and extracted from the ventilation channel. The camera is powered over Ethernet (PoE) and the connected Ethernet cable plugs into a panel mount connector next to the power connector for the LED. The camera cable, LED power cable, and a ground cable are all bundled together in one cable sleeve to simplify connections between the vent anchor and power supply.

2.4.7.2 Final Winch
The final winch assembly components are shown in Figure 2.4.96. Coming from sensor cars, the the cables run through the sensor car yaw adjustment mechanism, through the cable tensioning arms, through the motor-controlled lead screw guide, and then onto the main winch spool.
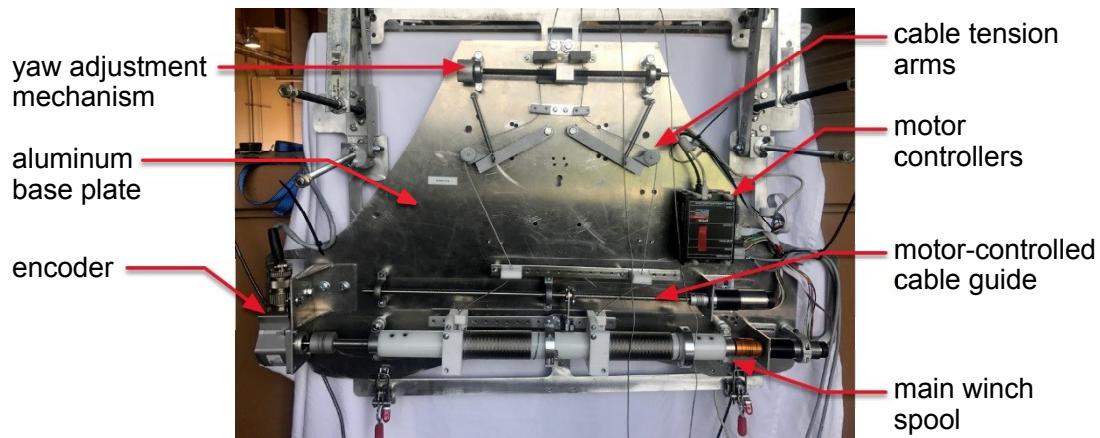
Figure 2.4.96. *Final winch assembly, showing all components*
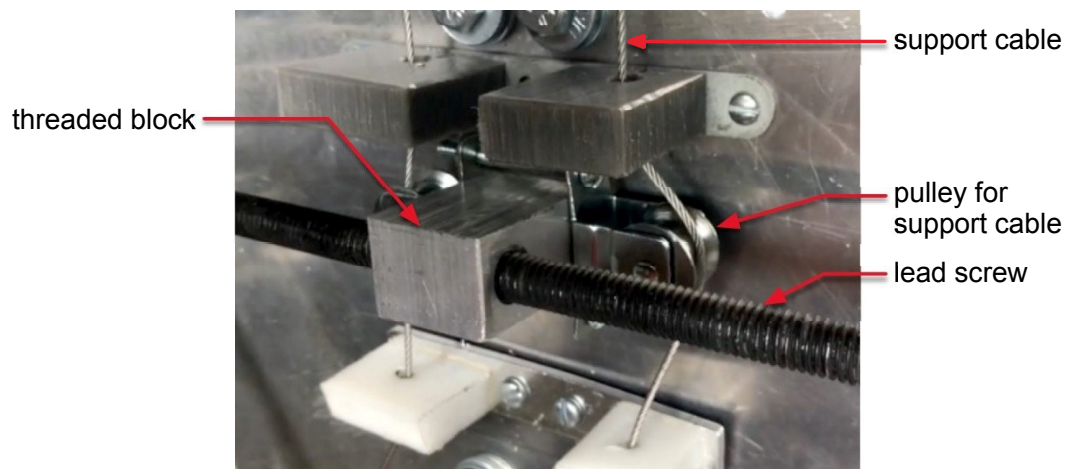
Figure 2.4.97. *Sensor car yaw adjustment mechanism*

The sensor car yaw adjustment mechanism consists of two plastic pulleys attached to a lead screw (Figure 2.4.97). One support cable runs on the left pulley, and the other runs over the right pulley. As the lead screw is turned by the operator, the two pulleys move left or right, increasing the length that one support cable needs to travel and raising up that side of the car. This allows the sensor cars, while deployed in the ventilation channel, to be adjusted to vertical alignment for the most accurate EMATS and measurements. The operator uses the image from the front-facing in-car camera to make yaw adjustments.
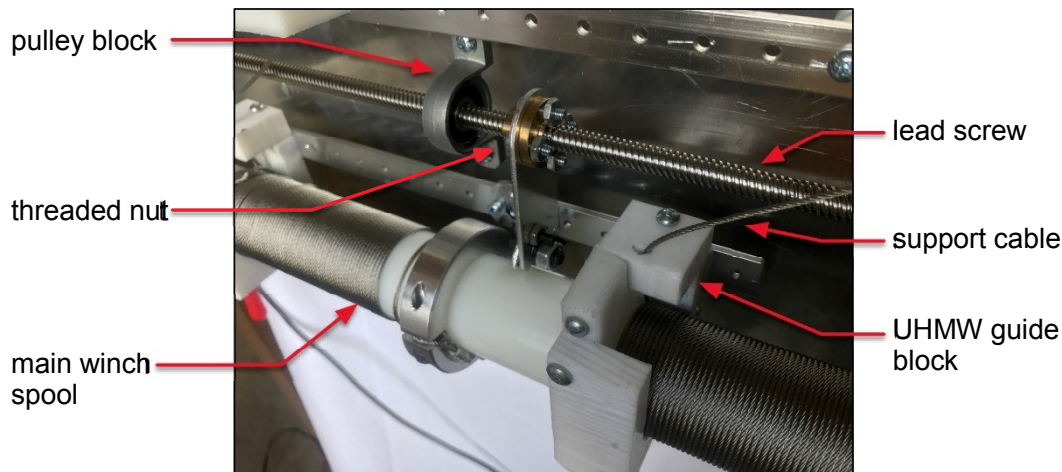
Figure 2.4.98. Motor-controlled support cable guide

The cable tensioning arms consist of two spring-loaded arms with plastic pulleys on each end. As the tension in a support cable increases, the respective tensioning arm rotates and stretches out the spring, equalizing the tension in the cable to a set amount. This also allows the operator to have a visual indication of the tension in the support cables, which is helpful to notice when the sensor car is jammed or stuck in the channel.

The motor-controlled cable guide (Figure 2.4.98) consists of UHMW polyethylene blocks with holes for the support cable to travel through. The two blocks are attached to a lead screw, which is supported by two bearing blocks and rotated by a brushless electric motor. The motor has an integral encoder, which when combined with the motor controller (Figure 2.4.99), allows fine positioning and velocity control by the control PC. The guide motor is programmed to follow the rotation of the main winch spool in order to neatly wrap the support cables around the main spool. The cable guide motor can also be manually adjusted by the operator in case of cable tangles or jams.
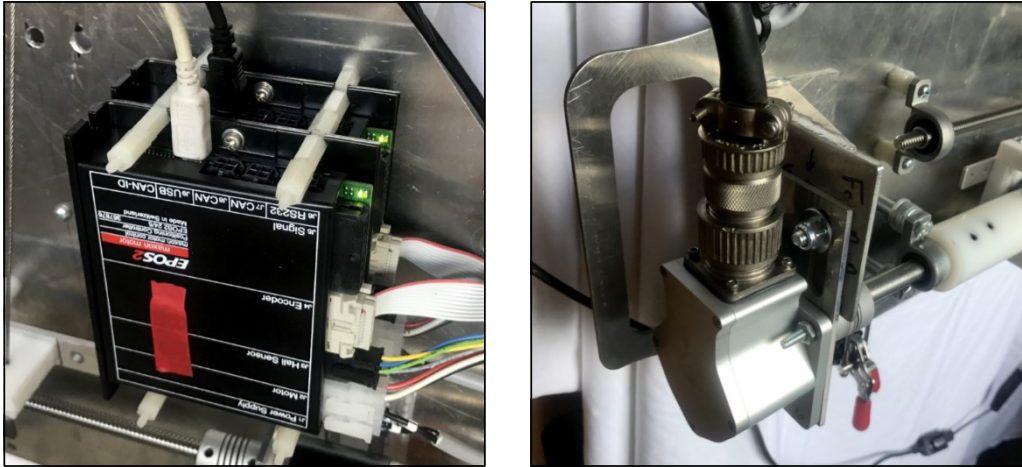
Figure 2.4.99. *Winch motor controllers mounted to winch baseplate (left) and main winch spool encoder mounted to spool shaft (right)*

The support cables finally reach the main winch spool, which they wrap around as controlled by the main winch motor. The ABS plastic spool is mounted to a steel axle, and directly driven by another brushless electric motor and motor controller. The opposite end of the spool axle is attached to an optical encoder to measure the winch spool rotational position (Figure 2.4.99). The speed and rotational direction of the winch spool is controlled from the control center PC by the operator.

All components are mounted to an aluminum plate with a hook and latch system for attachment to the vent anchor. The motor power cable, motor controller USB, and encoder data cable have connectors mounted to the winch plate for quick connections to the winch cable tether that connects to the control center.

2.4.7.3 Final Delivery Arm
The delivery arm had three functional requirements for the system – securely transporting the sensor car train into the cask onto the top of the MPC, positioning the sensor car train for insertion into each ventilation channel, and aiding the insertion and removal of the sensor car train into the ventilation channels. Each main feature fulfills one of these requirements.

2.4.7.3.1 Delivery Arm Garage
The delivery arm garage secures and holds the sensor cars during the delivery arm insertion into the cask. The final garage design consists of a bent aluminum structure shaped to hold the sensor car train securely, and prevent jamming during entry and exit. The garage structure is hinged at the front to allow the operator to open up the structure and place the robot train inside during setup for an inspection (Figure2.4.100).
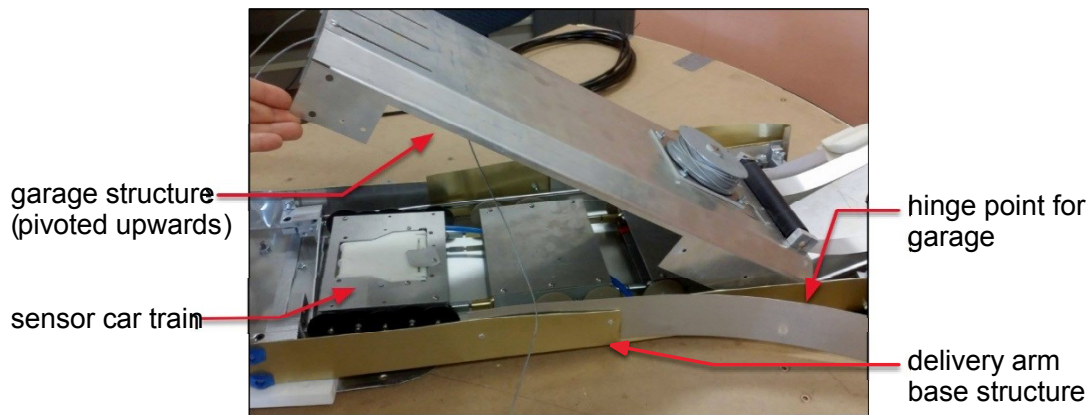
Figure 2.4.100. *Delivery arm garage for sensor car train, showing pivoting clamshell design*

Within the garage structure, there are two parallel linear bearing rods on either side of the path of the sensor car train. Two linear bearing blocks, connected by an aluminum plate, run along the rods and are attached to bowden cables that run back along the arm to outside the cask (Figure 2.4.101). The sensor car train is placed in front of the bearing assembly, which pushes on the back of the sensor car train. This allows the operator to push the cars out of the garage and over the curved end of the delivery arm for insertion into the ventilation channel.
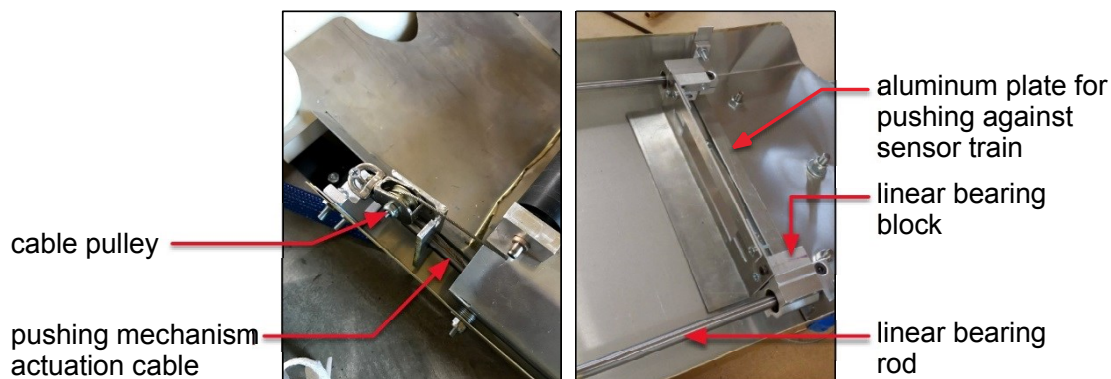
Figure 2.4.101. *Delivery arm pushing mechanism*

2.4.7.3.2 Delivery Arm Sensor Car Train Deployment

From the wedging and jamming analysis in McNelly [2], it was shown that the end of the delivery arm must be hump shaped to set the approach angle of the sensor cars into the ventilation channel. The final arm end guide is a complex shape 3D printed out of PEEK plastic, designed to catch and direct the sensor car during extraction (Figure 2.4.102). The part also has guides for the support cables and data tether. The end guide has a smooth connection to the garage, in order to prevent jamming or wedging inside the garage. The bottom of the delivery arm is covered with PEEK and UHMW polyethelene sliders to prevent damage to the MPC, and the end of the arm has two rounded PEEK hooks to latch onto the edge of the MPC.

One PGR blackFly camera is mounted to the side of the arm end guide, inside the periscope-inspired shielding box. The camera is positioned and focused to see to the cask channel guides,

and the live image from this camera is used by the operator to position the end of the delivery arm between the channel guides, allowing the robot train to inspect multiple ventilation channels.
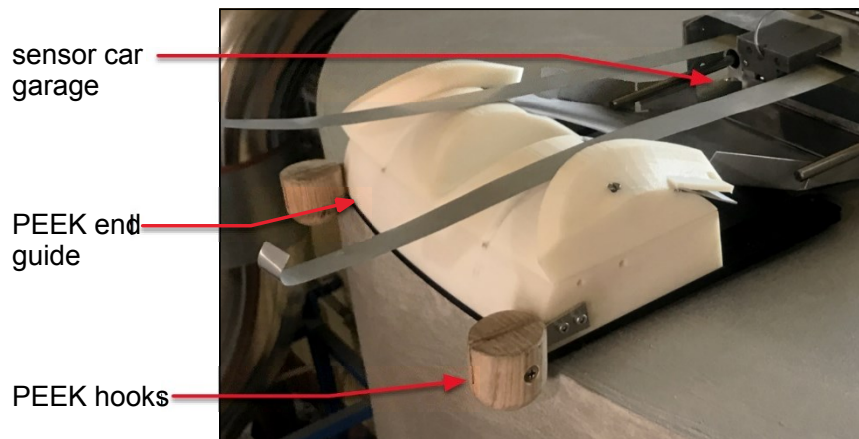
Figure 2.4.102. Delivery arm PEEK sensor car guide

2.4.7.3.3 Delivery arm pivot mechanism

To position the delivery arm at different ventilation channels, the operator can pivot the delivery arm 45 degrees in each direction after entering the cask. The final pivoting mechanism consists of a large, flat aluminum pulley wheel rigidly mounted to the moving half of the arm, with a rotating connection to the other, stationary half of the arm (Figure 2.4.103). The wheel has a channel milled in the edge sized to hold a thin steel bowden cable.

The cable loops around the wheel, clamps in the middle, and runs back to the exterior of the cask through compression-less housing. The operator uses a mechanism to pull on each cable, rotating the pulley wheel and pivoting the end of the delivery arm. To keep the pivot located in the center of the MPC lid, the operator extends two aluminum arms attached to the stationary half of the delivery arm that press up against the underside of the cask lid (Figure 2.4.104).
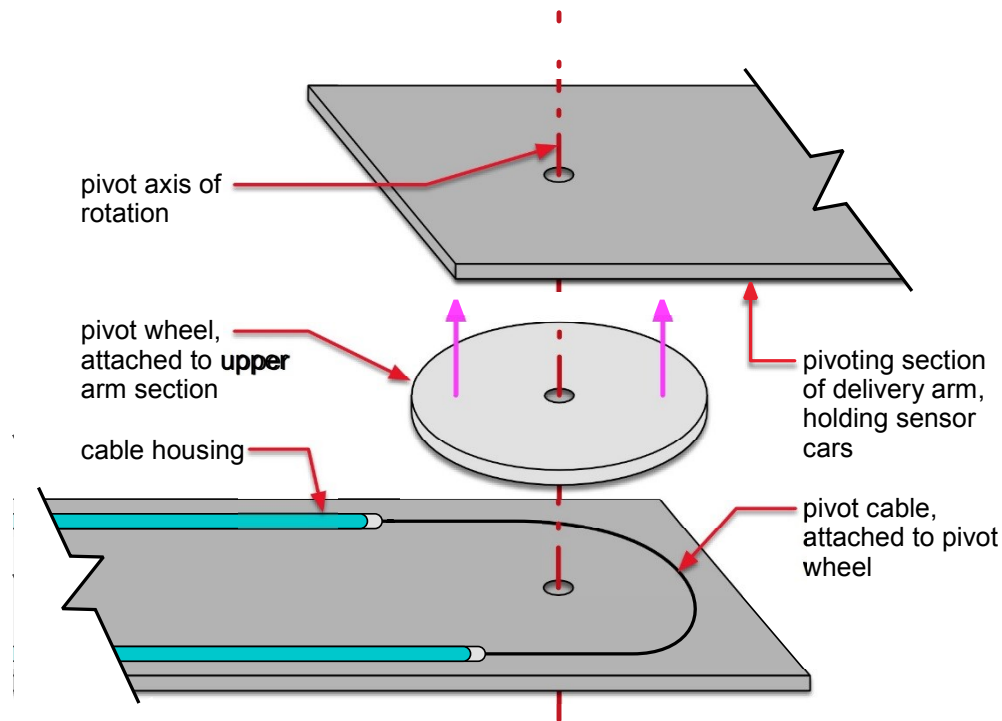
Figure 2.4.103. *Diagram of delivery arm pivot mechanism construction*
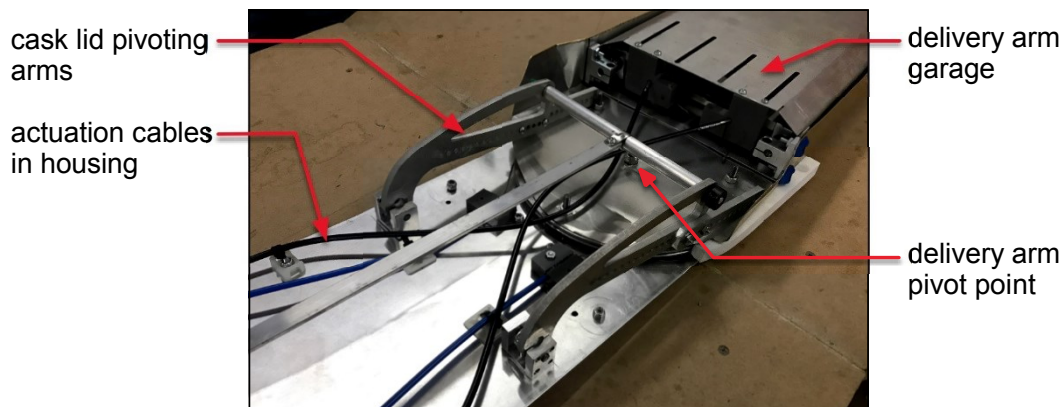
Figure 2.4.104. *Delivery arm pivot and arms to push against overpack lid*

2.4.7.4 Final Robot Sensor Train

After successful fabrication and testing of the pneumatic components, the final layout for the sensor car train for the Holtec and Penn State demonstrations was constructed (Figure 2.4.105). The first car contains the EMAT sensors and actuators, LED headlights, and front-facing camera. The second car contains the LIBS optics and actuator. The third and last car contains the Geiger counter, and the thermocouple sensor and actuator (Figure 2.4.106).
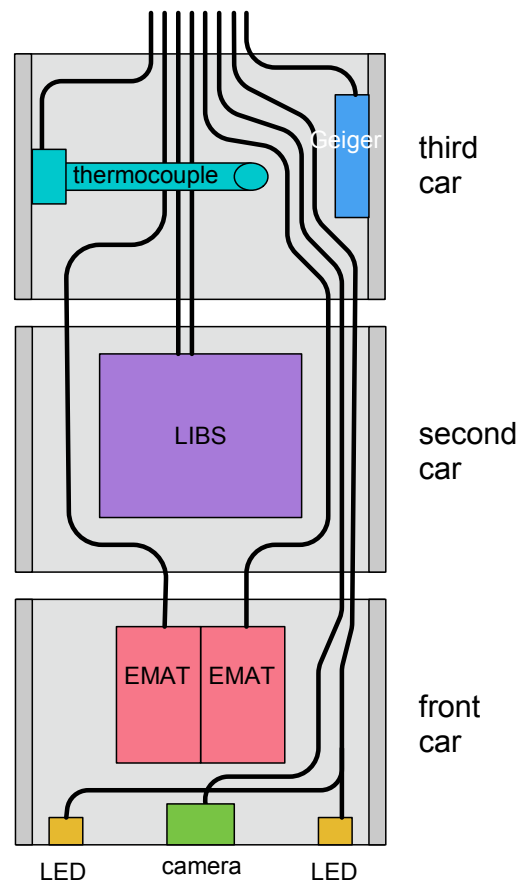
Figure 2.4.105. *Diagram of final sensor car layout, showing data and power cables – pneumatic actuators and air lines not shown*

The second and third cars contain pass-through data cables, power cables, and pneumatic lines for the cars in front. All data, power, and pneumatic lines are bundled together at the rear of the third car and housing in a plastic cable sleeve for the 50' length of the tether back to the control center.

Each car is constructed out of aluminum as previously described earlier. The top, bottom, front, and back plates are waterjet cut out of 0.080" aluminum sheet, and the larger side pieces are machined out of 3/8" aluminum stock. The axles for the 10 PEEK wheels, and the top, bottom, front, and back plates and screw into the side pieces. While the dimensions and overall design of each car was the same, individual cars have unique access and mounting holes to support the specific sensors carried in each car. The cars are linked together into an articulated train using pivoting rod ends screwed into the side panels of each car. Two steel support cables run from the back car, through housing mounted to the delivery arm, and back to the winch.
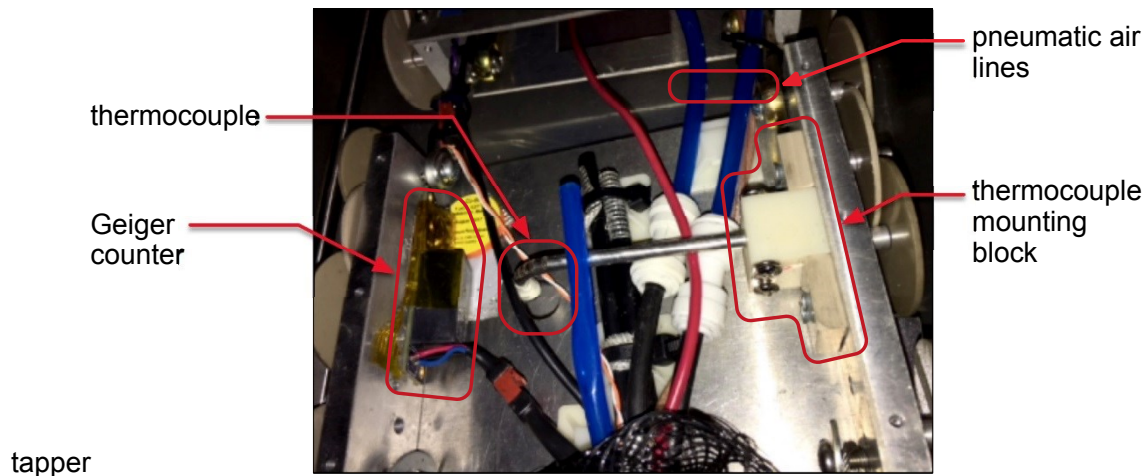
Figure 2.4.106. *Thermocouple and Geiger counter installed in third car.*

2.4.7.5 Final Control Center and System Power Supply

The final power supply is housed in a durable, waterproof, wheeled box for weather resistance and portability (Figure 2.4.107). From the mains plug, the first connection is into a 12V DC power supply. This feeds into a West Mountain Radio PWRgate battery back up system. The PWRgate automatically charges or draws from a 12V deep cycle battery, providing an uninterrupted power supply in case the connection to mains power is cut o . From the PWRgate, it connects to a voltage regulator display and into an emergency cut o switch before connecting into a 40A fusebox (Figure 2.4.108) to distribute power to all the features of the system.

Figure 2.4.107. *Interior of power supply box; deep cycle battery is below the tray on the left*

Figure 2.4.108. Fuse box for 12V power distribution

The fuse box distributes 12V power directly to the encoder DAC board, the connections for the winch motors cables, the 12V – 36V step up transformer for the vent anchor LED, the 12V – 49V step up transformer for the powered Ethernet network switch, and the 5V regulator for the beagle bone board. All connectors are Anderson powerpoles for ease of use and reliable connections.

To simplify the process of setting up the system, all cables running between the power supply to the winch and vent anchor are bundled and housed in two cable sleeves – one for the winch, and one for the vent anchor. The winch bundle has one 12V red-black zip cable, one Ethernet cable, one USB cable, one encoder data cable, and one ground cable. The vent anchor bundle has one 36V red-black zip cable (with yellow and black connectors to distinguish it from the others running at 12V), one Ethernet cable, and one ground cable.

Figure 2.4.109. Labeled panel mount connections for winch and vent anchor cable bundles

Both bundles are 50' long total. Where possible, the connections at the power supply are panel mounted and labeled for quick and easy setup (Figure 2.4.109). One USB cable and one Ethernet cable from the power supply box connect to the control computer. The network switch in the power supply box is also used to connect the LIBS and EMATS computers to a local network network. The Lab View and ROS network was set up by the system integration team to time sync

the delivery system, EMATS measurement, and LIBS measurements together (Figure 2.4.110).
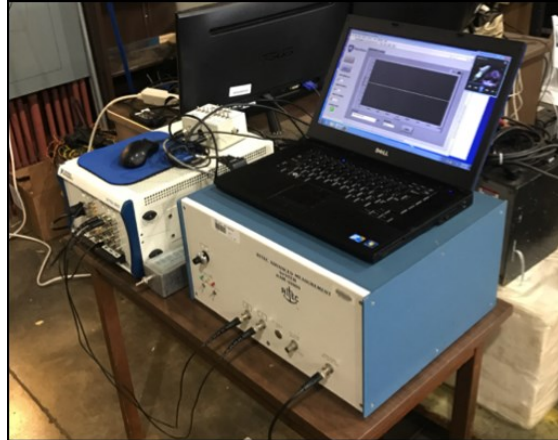
Figure 2.4.110. EMATS computer and equipment next to MPC mock up

2.4.8 Final Technology Demonstrations

2.4.8.1 Demonstration on MPC at Holtec

On September 6-8, 2017, the delivery team and EMAT sensor team visited Hotlec International in Turtle Creek, PA for final system testing on a completed MPC placed within an overpack. The cask was located on-site at Holtec's factory and placed within a pit sized such that the cask ventilation openings were accessible from the ground. The inspection system was set up, and the system inserted into the cask first with the overpack lid removed, and after confirming that everything worked properly, with the overpack lid in place (Figure 2.4.111). The sensor cars were maneuvered on top of the lid of the MPC, and traveled the full length up and down multiple ventilation channels (Figure 2.4.112). A series of videos captured the full inspection process, from system set up on the cask, sensor robot insertion into the cask, maneuvering down the ventilation channels, and extraction and removal from the cask. Operating the system with the overpack lid on was the closest simulation possible of a loaded cask inspection.
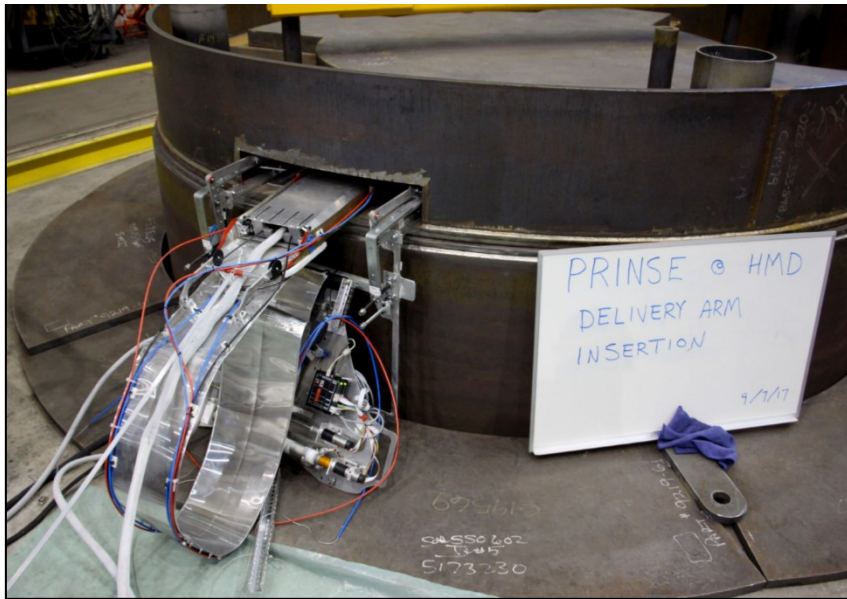
Figure 2.4.111. *View of vent anchor inserted and locked into place on cask at Holtec, with the lid on*

Both the thermocouple and EMAT sensors were operational and collecting data from the MPC while in the ventilation channel, with the overpack lid on. However, the EMAT sensor team encountered unexpected noise issues while at Holtec and was unable to collect meaningful data on the MPC in the overpack. The noise was later confirmed to be a grounding issue, and shared ground connections were added to all components after returning from Holtec.
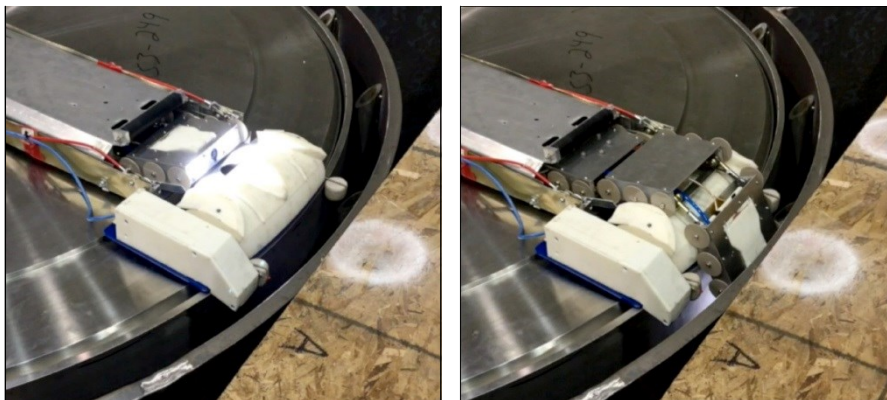
Figure 2.4.112. *View of delivery arm on top of MPC and the sensor robot entering the ventilation channel of the cask at Holtec, with the lid on*

2.4.8.2 Demonstration on Full-sized Mock-up at Penn State

On September 26, 2017, all teams involved in the project demonstrated the final technology to an audience of the advisory board and various industry representatives at Penn State facilities. Using the full-sized mock-up, the inspection system was used to show a live full inspection process, including gathering EMATS and LIBS measurements while on the MPC mock up. Before

the inspection on the mock-up each team gave brief presentations covering their work, including LIBS inspection, EMAT sensor crack inspection, temperature and radiation measurements, robot sensor car delivery and maneuvering, data systems, and concrete NDI.

The prototype system showed the ability to enter the cask through the ventilation opening, to maneuver within the cask on the top surface of the MPC in order to access multiple ventilation channels, and to enter and traverse the ventilation channel while collecting sensor data. Additionally, Laser Induced Breakdown Spectroscopy (LIBS) optics, Electromagnetic Active Transducers (EMATs), temperature measurement probe, and Geiger-Muller counter data was gathered from mock inspections on both a manufactured MPC from Holtec Manufacturing, and on a full-sized MPC mockup constructed as part of this thesis. During both final technology demonstrations, the system was controlled through a computer GUI and integrated measurements from all sensors through a local area network.

A more detailed description of the robotic delivery system is provided in the Master's theses of McNelly [2], Van Sant [9], and Bracken [10]. In particular, significant portions of Van Sant's thesis work are used in this description of the robot delivery system, with permission.
References

1. Lambert, J., S. Bakhtiari, I. Bodnar, C. Kot, and J. Pence (2012) "Extended in-situ and Real Time Monitoring Task 3: Long-Term Dry Cask Storage of Spent Nuclear Fuel," *US Nuclear Regulatory Commission*.

2. McNelly, B. P. (2015) "Design of a Nuclear Inspection Robot: Considering Dimensional, Force, Sensor Packaging, and Thermal Constraints," MS Thesis, Department of Mechanical and Nuclear Engineering, Penn State University.

3. Whitney, D. E. (1982) "Quasi-static assembly of compliantly supported rigid parts," *Journal of Dynamic Systems, Measurement, and Control*, **104**(1), pp. 65–77.

4. Lissenden, C., A. Motta, I. Jovanovic, S. Brennan, K. Reichard, J. Popovics, and T. Knight (2015) "NEUP 14-7356 Quarterly Report Y1Q3,"

5. Lissenden, C., A. Motta, I. Jovanovic, S. Brennan, K. Reichard, J. Popovics, and T. Knight (2016) "NEUP 14-7356 Quarterly Report Y2Q2,"

6. Lissenden, C., A. Motta, I. Jovanovic, S. Brennan, K. Reichard, J. Popovics, and T. Knight (2016) "NEUP 14-7356 Quarterly Report Y2Q4,"

7. Shah, M.A.A., K.S.M. Hahari, M.F.A. Jalal, A. Anuar (2015) "Development of a 1-inch boiler tube inspection robot," in IECON 2015- 41st Annual Conference of the IEEE Industrial Electronics Society, pp. 004340-004344.

8. "High Temperature Plastics | Regal Plastics" https://www.regal-plastics.com/plastic-sheeting/hightemperature-plastics/, accessed 10 March 2018.

9. Van Sant, I., 2018, "Design and fabrication of a nuclear dry cask inspection robot: integrating laser induced breakdown spectroscopy and electromagnetic active transducer

measurement methods," M.S. thesis in Mechanical Engineering, Penn State, University Park, PA.

10. Bracken, J., 2018, "The C+C DSM method: managing change propagation while prototyping a robotic inspection system for dry nuclear waste storage casks," M.S. thesis in Mechanical Engineering, Penn State, University Park, PA.

2.5 Modeling and Measurement of Environment

2.5.1 Radiation Dose Assessment

2.5.1.1 Cask Geometry

Detailed models of the cask geometry and materials were developed for use in Monte Carlo radiation transport simulations. Models were developed using information gathered from Holtec documents submitted to the NRC (most notably the Final Safety Analysis Report, FSAR) and available through the NRC documents library (Holtec, 2010). Specifically, models were developed for the MPC-24, MPC-32, and MPC-68 canisters (Priest, 2016). The HI-STORM 100s METCON was also modeled. The METCON (metal/concrete) is the cylindrical structure with inner and outer cylindrical steel shells with concrete in between to act as a shield and also as protection against a projectile. The METCON can be paired with any of the canisters. A cutaway of the METCON and MPC-32 canister is shown in Figure 2.5.1. A cross section and larger details are shown in Figures 2.5.2 and 2.5.3. The individual assemblies are modeled as homogenous regions over which the source particles are distributed.

2.5.1.2 Radiation Source

The radiation source strength and source energy spectra for both neutrons and photons were computed for different used fuel burnup/depletions and cooling times of 5, 15, 25 years. A five-year cooling period is seen as the approximate minimum time considered before placing used fuel in dry cask storage. A 25-year cooling time is more representative of older fuel that has been discharged in the longer past. A PWR source strength and spectrum was computed for 57.5 MWd/kg depletion. Similarly for BWR, this was done for a depletion of 25.4 MWd/kg. Two methods/computer codes from the SCALE6.1 code package, Origen-ARP and Origami, were used (Rearden, 2017). One notable difference between these approaches is the ability to create an axially varying profile in the fuel depletion and hence an axially varying neutron and gamma-ray source profile for use in transport calculations. A representative source gamma-ray source spectrum is shown in Figure 2.5.4 and compares the two different approaches with one obtain from the literature. All three compare well.

The transport calculations were accomplished using MCNP6.1 (LANL, 2014). Again, the individual used fuel assemblies were modeled as homogenous source regions. Dose conversion factors for personnel (LANL, 2014) were used to compute dose equivalent for in the vicinity of METCON vents where personnel might be found during an inspection. Figure 2.5.5 shows the locations of dose tallies near these vents. Dose conversion factors were computed in this effort to yield dose in rad-Si for electronic equipment positioned inside the METCON as would be the case for any inspection of the canister. Table 2.5.1 lists the tally locations for reporting gamma-ray doses.

The results for the HI-STORM 100S, MPC-32 with 25-year cooling time are shown in Table 2.5.2 and Figure 2.5.6 (dose from gamma-rays). The complete dose assessment including neutron dose and for other canister designs and other cooling times can be found in Priest (2016).

An additional study was conducted with the geometry modified to remove the gamma-ray vent shield to estimate the dose that might be expected during the inspection activities when the shield is removed. The photon dose rate for the MPC32 without the gamma-ray vent shields is shown in Table 2.5.3. The evaluated dose rates show that doses without gamma-ray shields are 3 to 4 times higher than with the shields.

2.5.1.3. Evaluation of a shielded car on MPC lid

The gamma-ray dose rate was evaluated on top of the lid and inside the vent to understand the dose expected for electronic equipment used during inspection. In this scenario, the car with electronics would enter through the METCON vent and sit on top of the lid while sending probes over the outer surface of the canister. Evaluations were made for the Hi-STORM 100S, MPC-32 with higher burnup fuel (57MWD/kg) with 25 years cooling. This modeling was done with the gamma-ray outlet vent shields removed to simulate the conditions during inspection.

The dose rate on top of the lid (Figure 2.5.6) is less than 10 rad-Si/hr (neutron dose on the lid is three orders of magnitude lower). However, just over the annulus space (still near the lid edge) the gamma-ray dose rate increases by an order of magnitude to nearly 80 rad-Si/hr. Downward along the surface of the canister wall the gamma-ray dose rate increases as high as 7000 rad-Si/hr. A shielded camera car was evaluated at the edge of the lid as shown in Figure 2.5.7. The shield material is lead at 0.5cm thick. With the lead shielding the gamma-ray dose rate is 1.16 rad-Si/hr. This dose rate is an average over the volume of the car taken as 8cm wide, 10cm long, 5cm high. There should be some variability inside the car and obviously closer to the edge would be higher.

The gamma-ray dose inside the outlet vent is 0.0359 rad-Si/hr. This compares with the personnel dose in the vent near the outlet of 0.014083 rem/hr (Table 2.5.2). The neutron dose for personnel was found to be approximately the same as this dose.

Table 2.5.1. Explanation of individual photon tallies considered within separate MCNP *cases.*

Tally Description	No.	Description
P: Si Dose, MPC Wall	F112	F2 surface tally on the MPC wall, modified with mass attenuation coefficients
P: Si Dose, MPC Wall, DF	F132	F2 surface tally on the MPC wall, modified with dose function
P: Flux, MPC Wall	F152	F2 surface tally on the MPC wall
P: Flux, METCON Wall	F162	F2 surface tally on the METCON wall
P: Dose, outlet vent	F195	F5 detector tally, 3cm in radius, located 5cm inside the vent mouth
P: Dose, inlet ven4t	F205	F5 detector tally, 3cm in radius, located 5cm inside the vent mouth
P: Dose, METCON Wall	F212	F2 surface tally on the METCON wall, modified with dose function
P: Dose, MPC Lid	F222	F2 surface tally on the MPC lid, modified with dose function
P: Flux, MPC Lid	F302	F2 surface tally on the MPC lid
P: Dose, left outlet	F405	F5 detector tally, 3cm in radius, 15cm left of vent mouth
P: Dose, right outlet	F415	F5 detector tally, 3cm in radius, 15cm right of vent mouth
P: Dose, bottom outlet	F425	F5 detector tally, 3cm in radius, 15cm below of vent mouth
P: Dose, left inlet	F435	F5 detector tally, 3cm in radius, 15cm left of vent mouth
P: Dose, right inlet	F445	F5 detector tally, 3cm in radius, 15cm right of vent mouth
P: Dose, above inlet	F455	F5 detector tally, 3cm in radius, 15cm above vent mouth
P: Dose, w/o Pb shield	F684	F4 volume tally, in annulus of canister
P: Dose, 4-side Pb shield	F694	F4 volume tally, with 4-side 5mm Pb sheets, in annulus of canister
P: Dose, 6-side Pb Shield	F704	F4 volume tally, with 6-side 5mm Pb sheets, in annulus of canister
P: Dose, METCON ext. 15cm	F815	F5 detector tally, 30cm in radius, 15cm outside of inlet vent
P: Dose, METCON ext. 45cm	F825	F5 detector tally, 30cm in radius, 45cm outside of inlet vent
P: Dose, METCON ext. 75cm	F835	F5 detector tally, 30cm in radius, 75cm outside of inlet vent
P: Dose, METCON ext. 105cm	F845	F5 detector tally, 30cm in radius, 105cm outside of inlet vent

Table 2.5.2. *The photon transport data for the HI-STORM 100S and MPC-32, populated with Westinghouse 17x17 assemblies enriched to 3.5%, with an ORIGAMI axial emission profile, a discharge burnup of 57.535 MWd/kg, and cooled for 25yr.*

Tally	Out	RE	Units
P: Si Dose, MPC Wall	3.4940E+03	0.0002	Rad(Si)/hr
P: Si Dose, MPC Wall, DF	3.9598E+03	0.0002	Rad(Si)/hr
P: Flux, MPC Wall	5.4987E+09	0.0002	photon/cm^2·sec
P: Flux, METCON Wall	6.8241E+03	0.0895	photon/cm^2·sec
P: Dose, outlet vent	1.4083E-02	0.2815	Rem/hr
P: Dose, inlet vent	1.2283E-02	0.4396	Rem/hr
P: Dose, METCON Wall	6.7790E-03	0.0920	Rem/hr
P: Dose, MPC Lid	1.3701E+00	0.0383	Rad(Si)/hr
P: Flux, MPC Lid	3.7116E+06	0.0406	photon/cm^2·sec
P: Dose, left outlet	8.5217E-05	0.4334	Rem/hr
P: Dose, right outlet	7.5090E-05	0.3364	Rem/hr
P: Dose, bottom outlet	1.6083E-03	0.9422	Rem/hr
P: Dose, left inlet	3.8947E-03	0.9333	Rem/hr
P: Dose, right inlet	5.6053E-04	0.5317	Rem/hr
P: Dose, above inlet	2.8357E-03	0.8307	Rem/hr
P: Dose, w/o Pb shield	3.8120E+03	0.0111	Rad(Si)/hr
P: Dose, 4-side Pb shield	1.7072E+03	0.0145	Rad(Si)/hr
P: Dose, 6-side Pb Shield	1.2543E+03	0.0168	Rad(Si)/hr
P: Dose, METCON ext. 15cm	1.5009E-02	0.6973	Rem/hr
P: Dose, METCON ext. 45cm	4.8478E-03	0.1504	Rem/hr
P: Dose, METCON ext. 75cm	3.6021E-03	0.1141	Rem/hr
P: Dose, METCON ext. 105cm	3.0167E-03	0.1000	Rem/hr

Table 2.5.3. *Dose rate (photon) at the inlet and outlet vents for the MPC32 with the gamma-ray vent shields removed and at 25-year cooling.*

	Dose Rate (rem/hr)	Relative Error
Outlet vent	0.0441	0.0622
Inlet vent	0.0407	0.1021
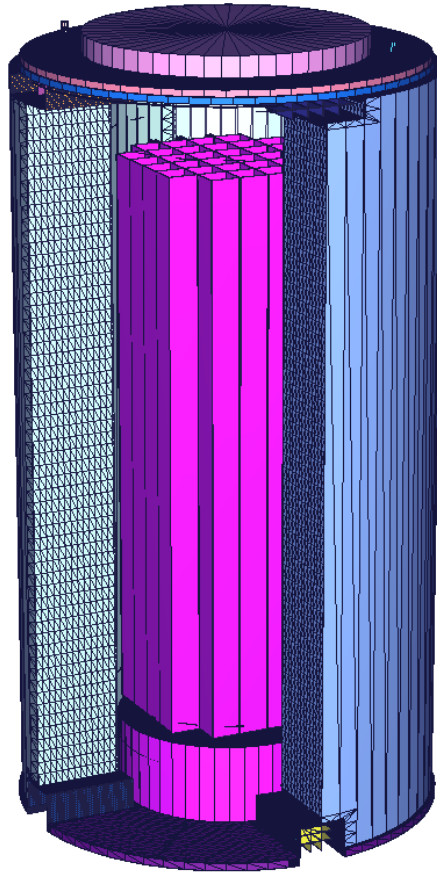
Figure 2.5.1. *MCNP rendering of quartered cutaway of the HI-STORM 100S and MPC-32 as designed in MCNP.*
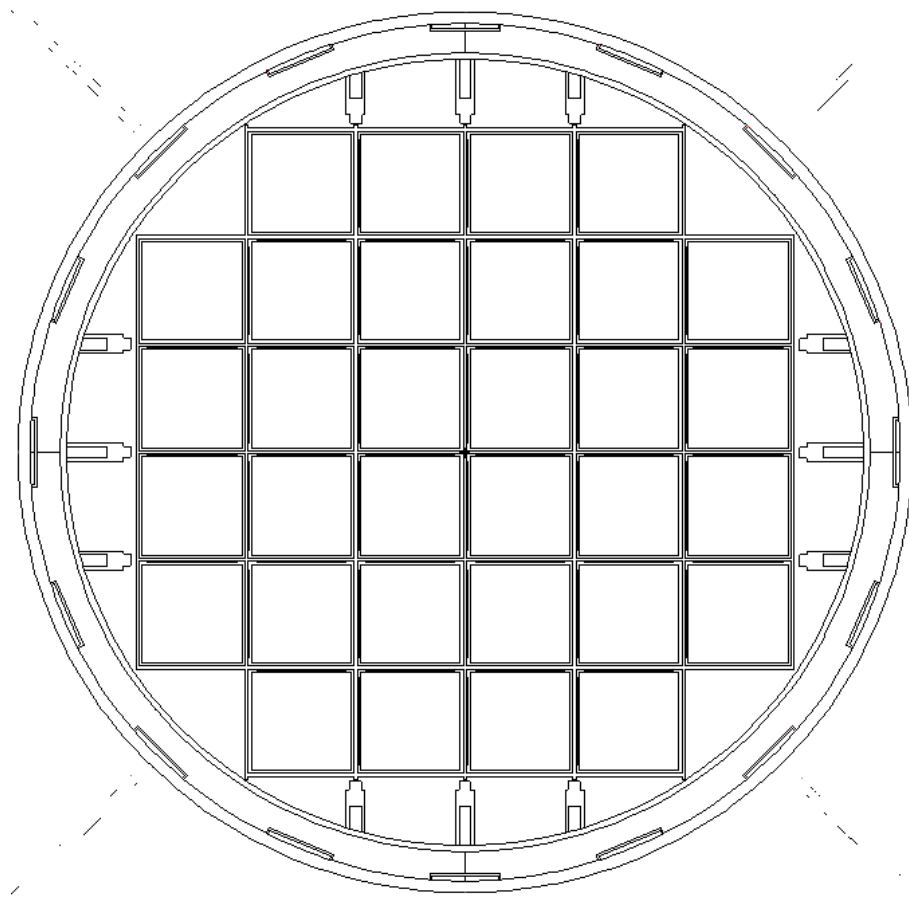
Figure 2.5.2. MCNP rendered cross section in the XY plane of the MPC-32 canister and the open annulus space.
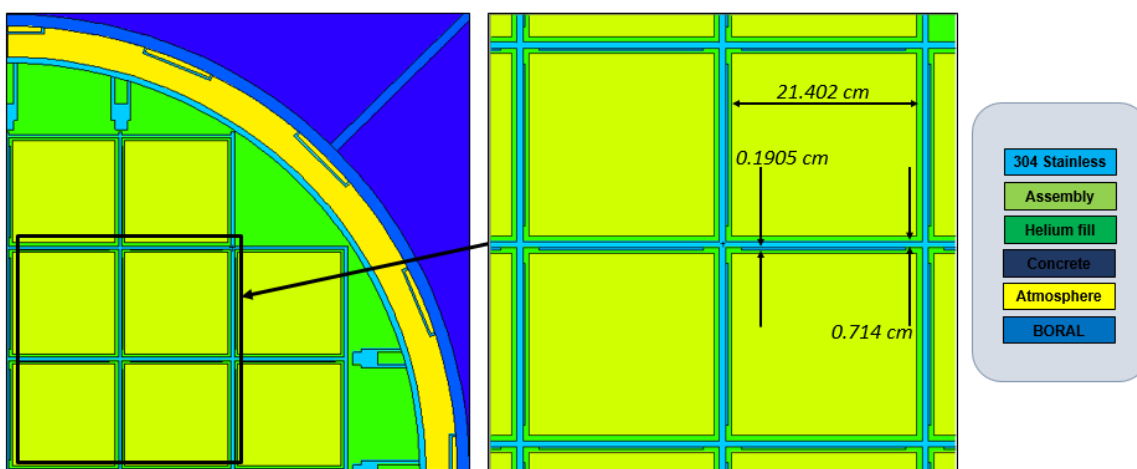
Figure 2.5.3. MCNP rendered detailed cross section in the XY plane of the MPC-32 basket.
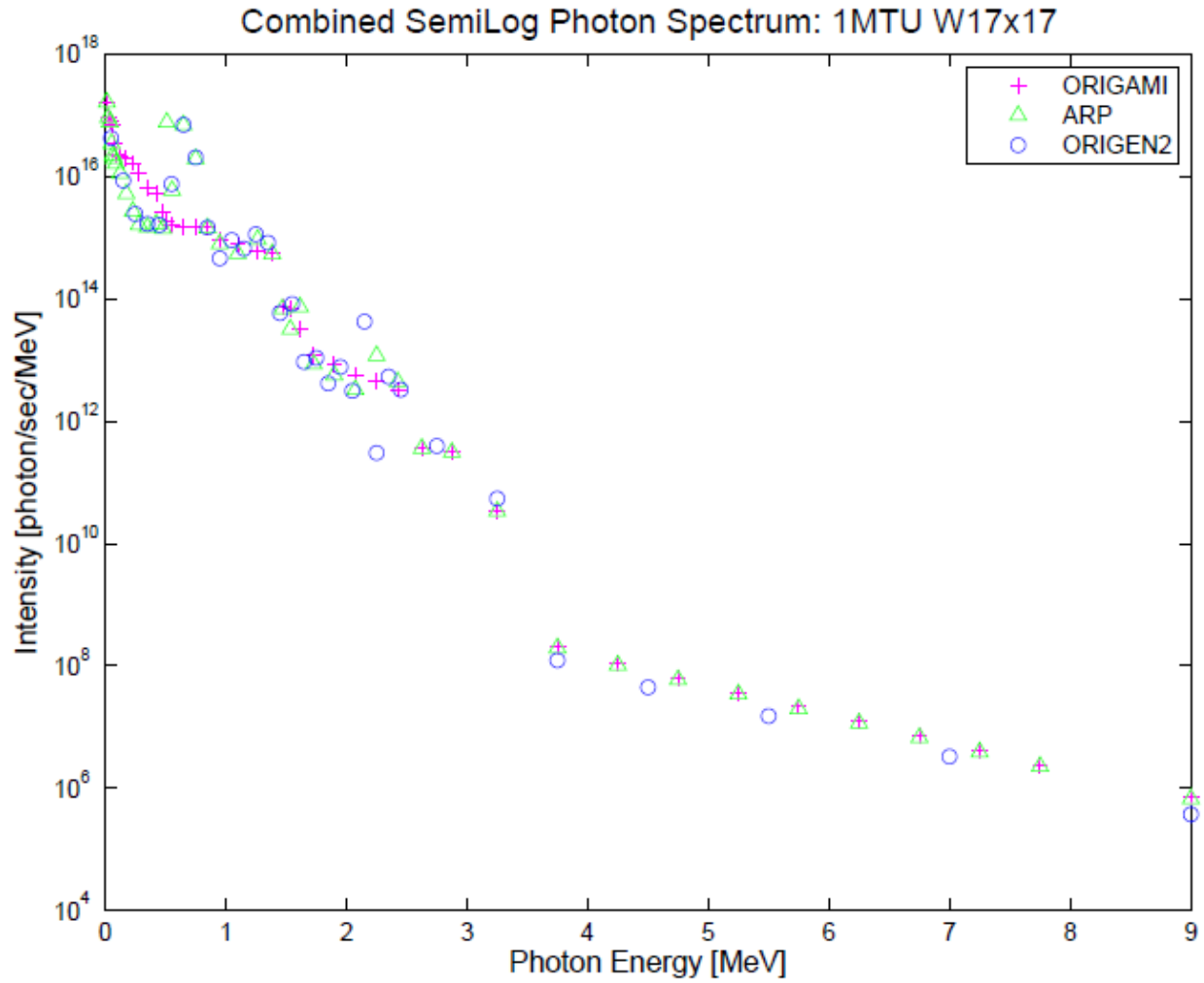
Figure 2.5.4. *The Semilog photon spectra for 1 MTU of W17x17 computed for ORIGAMI, ARP, and compared to literature Origen2 data from Cuta (2001).*
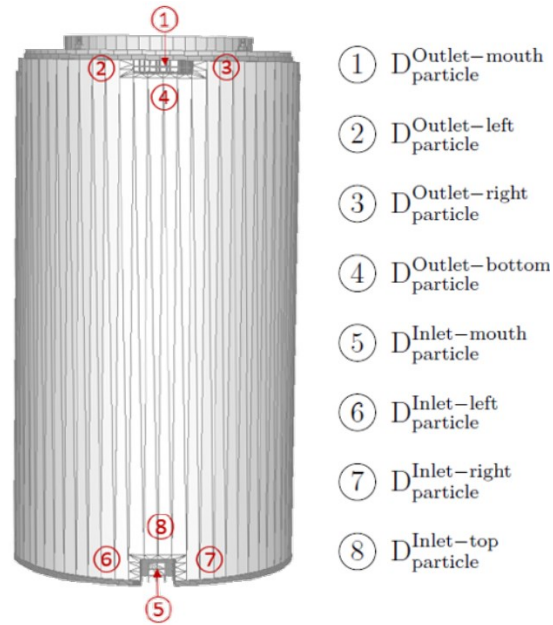
Figure 2.5.5. *Illustration of the locations of estimated dose rates for personnel during cask inspections.*
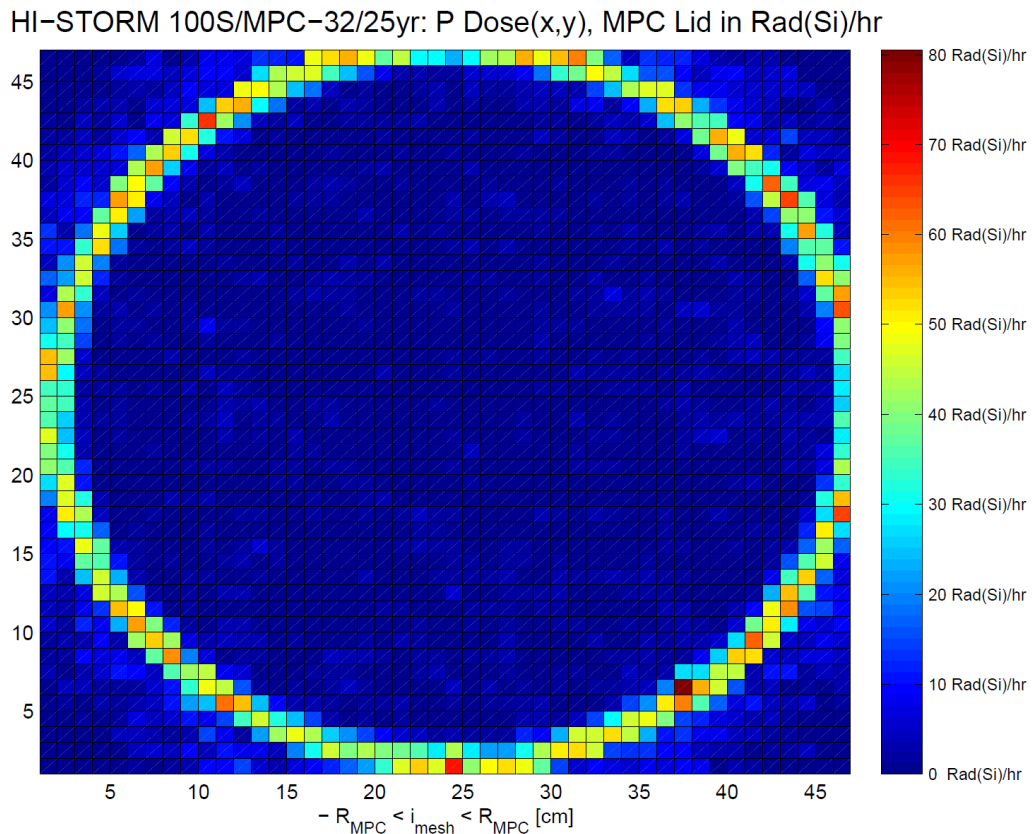
Figure 2.5.6. *Gamma-ray dose rate in rad-Si/h on the lid and over the annulus space. This is evaluated over a matrix of cells 4cm wide.*
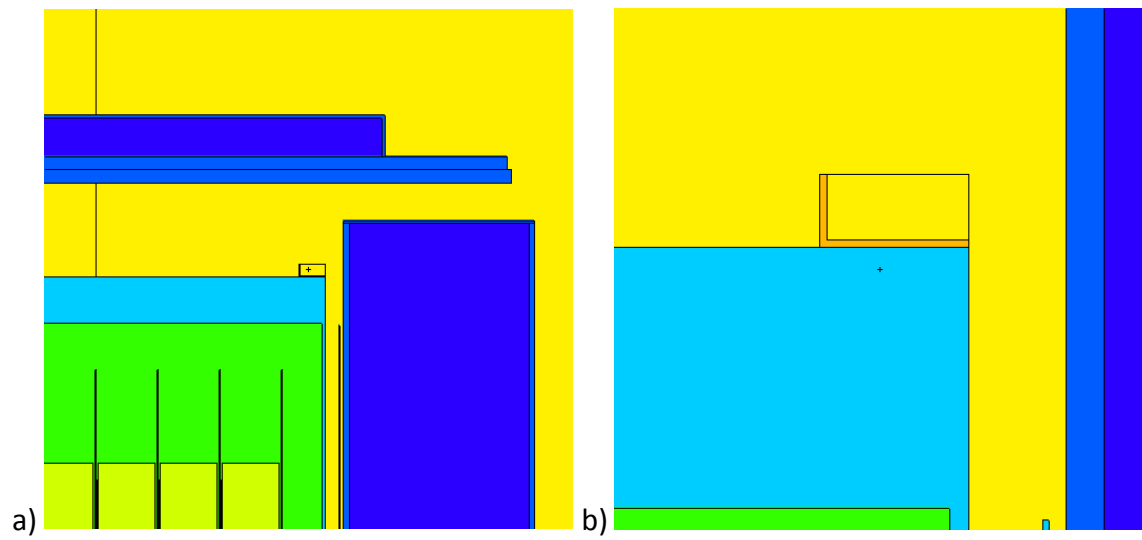
Figure 2.5.7. a) Illustration of the MCNP model for evaluation of dose (shown at a slice of y=3cm). The shielded camera car is shown at center, b) a close up of the camera car.

2.5.2 Thermal Assessment

Thermal analysis of the HI-STORM 100 cask used COBRA-SFS Cycle 4 (Michener, et al., 2015). A detailed COBRA-SFS model was obtained from PNNL/ORNL for use in these studies (see Figure 2.5.8) (Cuta, 2013). This model contains 32 fuel assemblies each containing 264 fuel rods each with fuel diameter of 0.309 inches and rod diameter of 0.36 inches. Each of the 32 fuel assemblies is modeled with a heat generation rate of 0.0015 MBTU/hr*ft^3 for a total decay heat load of 31.5 kW. The assembly height 178.3in and active fuel length of 144 inches. This model contains a detailed subchannel region modeling the length of the fuel assemblies (178.3 in). The base and lid are modeled as simple one-dimensional heat conduction. The model computes the rod temperatures and cask surface and overpack surface temperatures as well as the air annulus temperature. Of interest in this case is the cask wall surface, inner wall of the overpack, and air annulus temperatures since these will contact the robotic equipment used in inspections. The cask wall surface is always the hottest of these surfaces, so the maximum temperatures reported are for this surface. Conductive heat transfer is modeled in the solid components, and convective heat transfer is modeled in the gaps between. This model performs a steady-state analysis of the system at the user defined parameters for the materials involved, fuel heat generation, and ambient conditions.

An effort was undertaken to validate the model using limited available measured cask data from Waldrop (2016). Changes were made to the model to match the assembly loading and power profile of the measured casks as well as better approximate the ambient conditions during measurement. Results of this effort showed that COBRA-SFS tended to predict higher cask surface temperature by 10 to 50˚F which is conservative and was considered sufficient for this effort again given the limited available measured data with which to compare.

To support the proposed inspection efforts, the predicted cask temperatures were analyzed for varying used fuel burnup and cooling times. For this analysis, the decay heat load was varied over a range to simulate varying fuel conditions. For a given canister the discharge burnup of the fuel placed inside and its cooling time (time since discharge from the reactor) will determine to the greatest extent the decay heat load. The results are shown in Figure 2.5.9.

Next the fuel conditions were analyzed to determine how the decay heat load varies with fuel burnup and cooling time. This analysis was done using ORIGEN-ARP version 6.1 and selected fuel assembly type Westinghouse 17x17 OFA. A range of fuel discharge burnup was evaluated as shown in Table 2.5.4 with the given fuel (in reactor) power and cycle length. In all cases, three cycles were modeled with 30 day refueling between cycles. The specific power (MW/MTU) was varied to yield the final specific discharge burnup (MWD/MTU). The evaluation was done on a unit mass of 1 MTU. The result is shown in Figure 2.5.10 with a family of curves for different discharge burnup showing decay heat generated (kW/canister) over varying cooling time (years). As stated, the decay heat generated has been scaled to the mass of used fuel expected to be loaded in the canister.

The COBRA-SFS results were fit by equations to predict the maximum cask wall temperature as a function of decay heat. A family of curves were then generated to provide the maximum cask

wall temperature for varying used fuel discharge burnup and cooling time. Results are shown in Figure 2.5.11. The two functional requirements identified for this work of 250˚F and 350˚F are also shown on the figure as the horizontal black lines. Here it can be seen that the highest burnup fuel will not permit investigation before about 14 years at the 350˚F functional requirement and 50 years at the 250˚F requirement. Considering that used fuel would likely remain in the used fuel pool for a minimum of 5 years, the lower burnup fuel would not restrict investigations at any time.
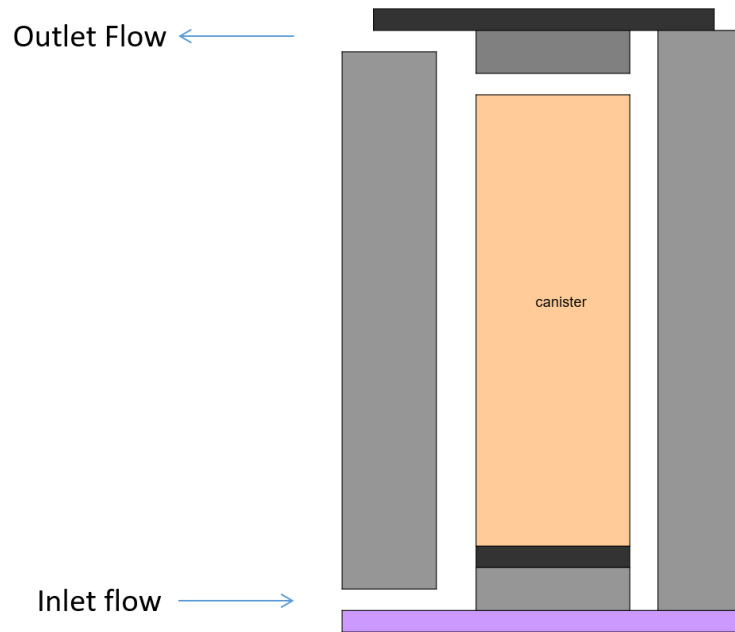
Figure 2.5.8. Illustration of the COBRA-SFS model (after Cuta, 2013).
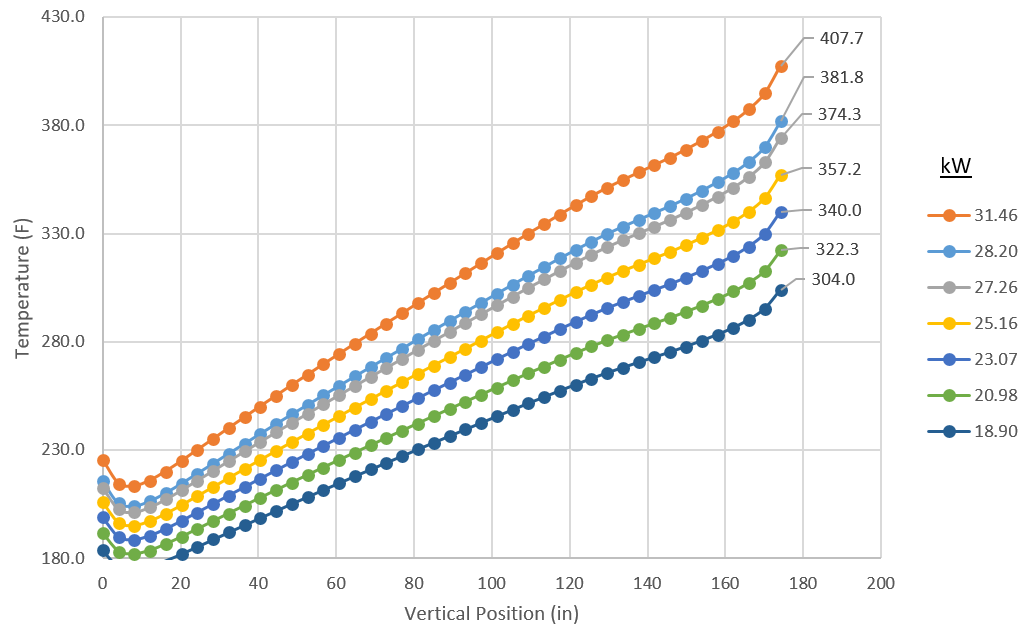
Figure 2.5.9. Maximum cask wall temperature (˚F) for various cask decay heat loads (kW).

Table 2.5.4. *Fuel depletion parameters of power and cycle length for evaluated discharge burnup.*

	Burnup (MWD/MTU)					
	70000	57790	50000	40000	30000	20000
Day/Cycle	Power (MW/MTU)					
522.6	64.44	53.20	46.03	36.82	27.62	18.41
504.8	53.18	43.90	37.98	30.39	22.79	15.19
521.8	18.17	15.00	12.98	10.38	7.79	5.19
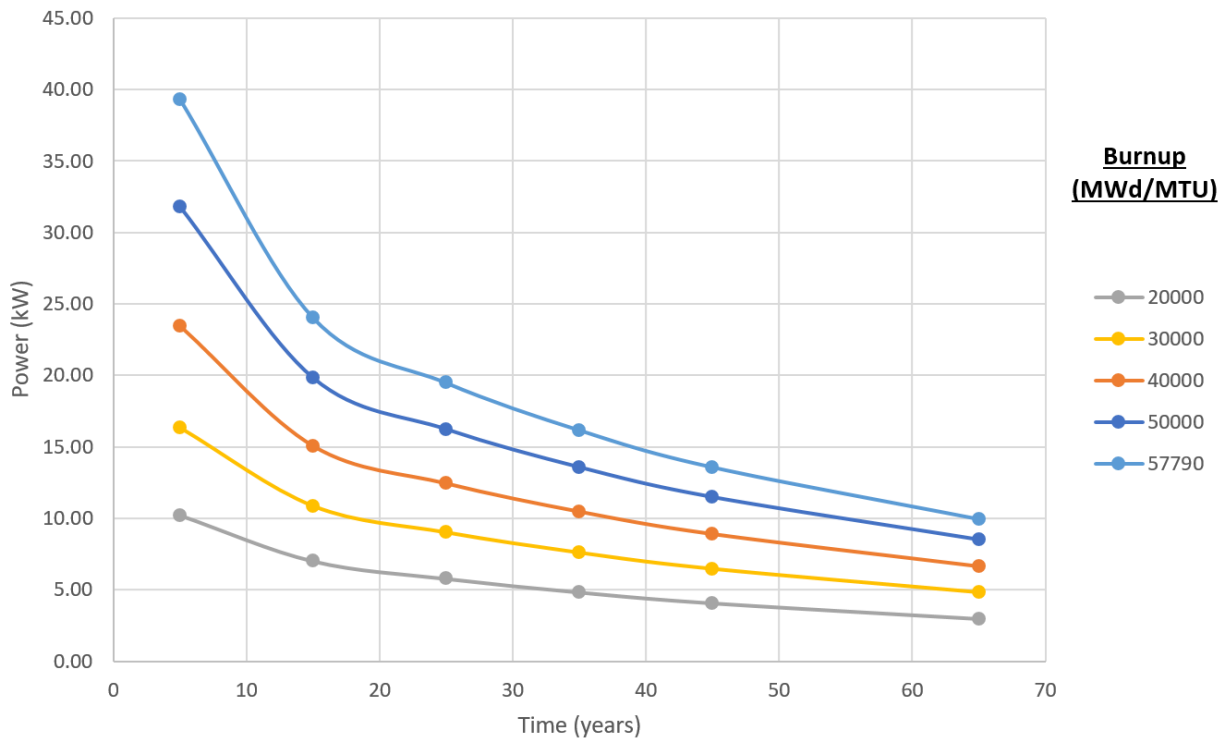
Figure 2.5.10. *Decay heat load for the canister for varying discharge burnup and cooling time. Note, loading with some of the heat loads shown are precluded based on licensed heat load limits for canisters.*
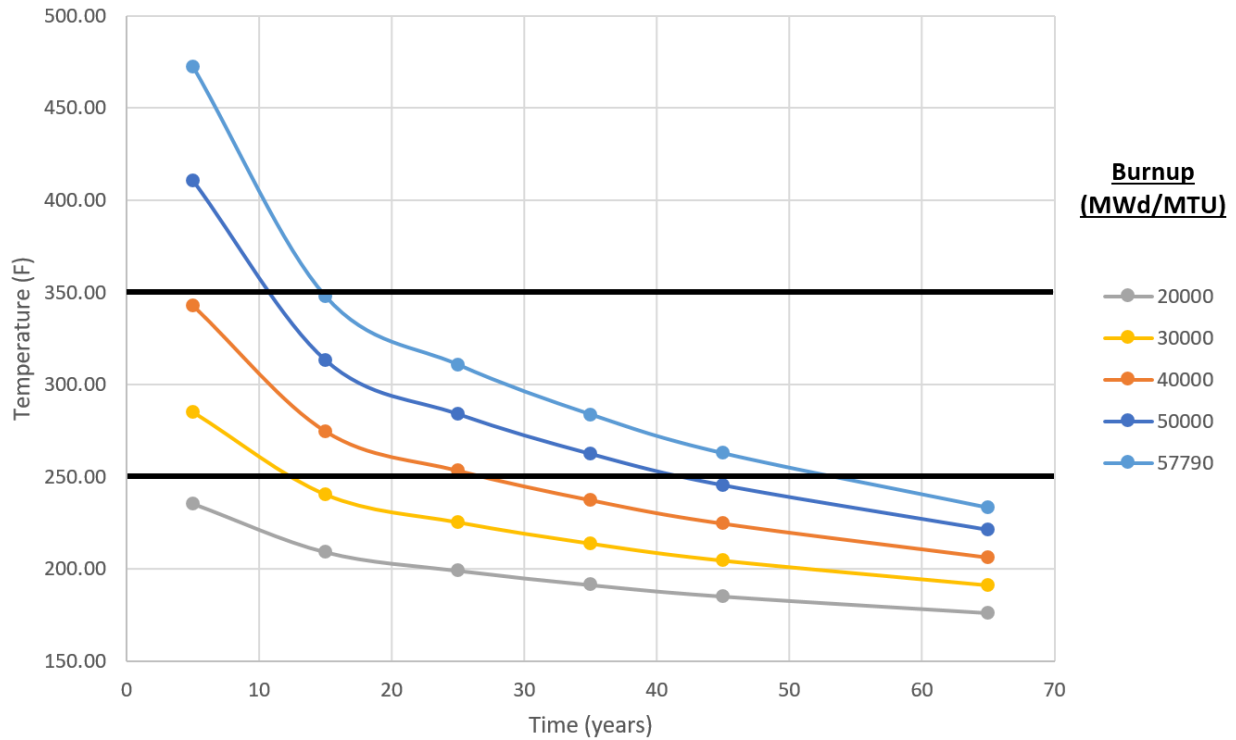
Figure 2.5.11. *Maximum cask wall temperature for varying discharge burnup and cooling time. The two functional requirements identified for this work are also marked as the two horizontal lines for 250˚F and 350˚F.*

2.5.3 Measurements

2.5.3.1 Geiger-Muller radiation sensor

The inspection system included a Geiger-Muller sensor for measuring radiation levels inside the space between the MPC and overpack. An initial design was assembled and tested by Brendan Sporer, an undergraduate intern advised by Professor Jovanovic. The Systems Engineering team developed a miniaturized circuit to provide high voltage power to the Geiger-Muller radiation sensing tube, and provide signal conditioning on the output pulses from the tube. The circuit board, with the Geiger sensor bulb and Pico 500V power supply, is shown in Figure 2.5.12 (left), along with the exempt radiation source (right) used to test the response of the sensor. The system was initially tested for a milestone report using the setup shown in Figure 2.5.13.

For the final demonstration at Penn State, the Geiger circuit board was integrated into Car 3 of the robot with a small, 1μCi exempt Co-60 source placed underneath it for testing. During the final demonstration, the data system displayed and recorded both total counts and counts/sec during robot deployment; the average count rate was about 1 count/sec.
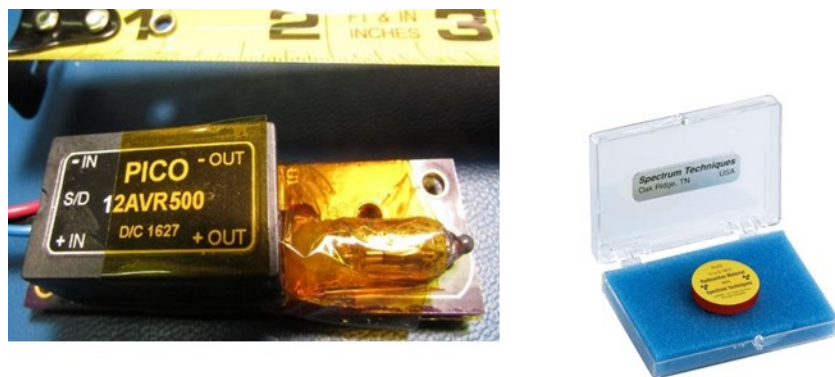
Figure 2.5.12. *Geiger counter circuit board (left) and exempt Co-60 source (right)*
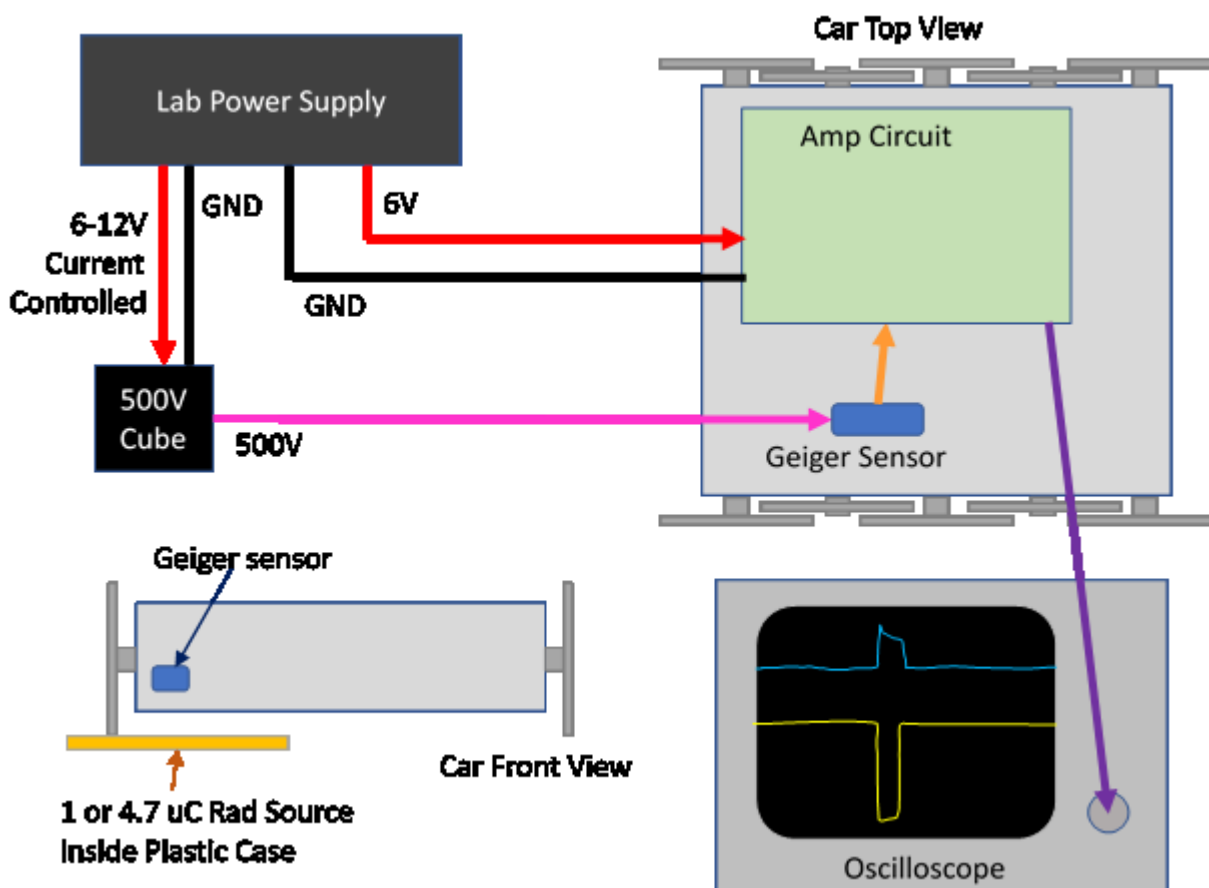
Figure 2.5.13. *Milestone test setup for Geiger sensor in Car.*

Circuit Radiation Sensitivity. The power supply and transistor amplifier used in the Geiger circuit are located in Car 3, and would experience the full radiation environment; the thermal environment will depend on the age of the spent fuel and the level of cooling provided by the compressed air system. Bipolar NPN transistors such as the 2N2222A used in this circuit are available in rad-hard versions from, for example, ST Microelectronics, with a radiation rating of

100 krad. Given the maximum radiation level in the canister from the University of South Carolina model of 10-12 krad/hour, this part might need to be replaced after an 8-hour shift in a particularly high-radiation canister. The 500V power supply from Pico includes integrated circuits and would probably not last long in a radiation environment. In the prototype this power supply was placed on the circuit board with the Geiger sensor and analog amplifier in order to minimize the lead length and potential exposure of high voltages to the project personnel, particularly students. For a system operated by trained nuclear power professionals, the decision might be made to place the high-voltage supply outside the canister and run the power in through the tether cable. A 4.7 megaohm resistor is used in series between the power supply and the sensor; placing the resistor at the power supply then inserting a 50 foot or longer lead between this resistor and the sensor would limit the current in the cable to a safe level, but might affect the performance of the system.

2.5.3.2 Temperature sensor

Current management of spent nuclear fuel relies heavily on thermal modeling to assess the temperature of the fuel. Complex heat diffusion finite element analyses of the fuel, cladding, basket, canister, and overpack are conducted and need to be verified by temperature measurements due to uncertainties in the model inputs. Additionally, it is important to know the temperature distribution inside the cask for stress corrosion cracking models that address salt deliquescence and for managing the operations of the robotic inspection system. Temperature measurements at a limited number of points on the outer surface of the canister were made during inspections at Hope Creek and Diablo Canyon that were organized by EPRI. However, the measurement device had a larger thermal mass and required a long time (tens of minutes) to acquire a stable measurement. The temperature sensor design addresses all of these issues, and while the design evolved significantly from concept to prototype, only the prototype (see Figure 2.5.14) is described herein.

The temperature sensor is located in the 3rd (trailing) car of the train along with the Geiger-Muller radiation sensor. The sensor itself is a Type K thermocouple with beaded wire (Extech TP870). The thermocouple wire is threaded through a 316 stainless steel sheath (3/16" outer diameter with 0.035" wall thickness). A 90-degree bend is formed in the sheath with the help of Dremel cuts. A 304 stainless steel foil (0.005" thick) is cut and hemispherical tip formed by pressing a ball bearing into the foil. The foil was then cut to fit over the 3/16" diameter of the end of the sheath. Temperature resistant epoxy was used to affix the thermocouple bead inside the hemispherical tip and then the tip was joined to the sheath after threading the thermocouple wire through the sheath. A connection block was 3D printed (ABS plastic was used as a surrogate for temperature and radiation resistant ultem 9085). The connection block has terminals for the thermocouple wire in the sheath and that goes to the temperature readout circuit, a 3/16" hole for the sheath, and is mounted inside the car by a spring-loaded pin connection. The robotics team designed a pneumatic actuation system that pushes the sheath out through a hole in the bottom of the car to make a measurement. This extension is resisted by the spring-loaded connection, which in the event of a pneumatic system failure retracts the measurement tip back into the car.

The hemispherical tip of the temperature sensor that contacts the outer surface of the canister to make the measurement is small, and thus the required pneumatic force to provide good contact is also quite small. The tip is made from 316 stainless steel in order to not scratch the canister surface while making measurements. However, the tip is not intended to be in contact with the canister while the cars are moving. The small size of the contact zone also results in a short time for the thermocouple to acquire a stabilized reading (tens of seconds). It is important to note that thermocouple readings from mechanical contact are less than fused contact by a spot weld. However, it is straightforward to determine the linear calibration factor to correct for this as shown in Figure 2.5.15.
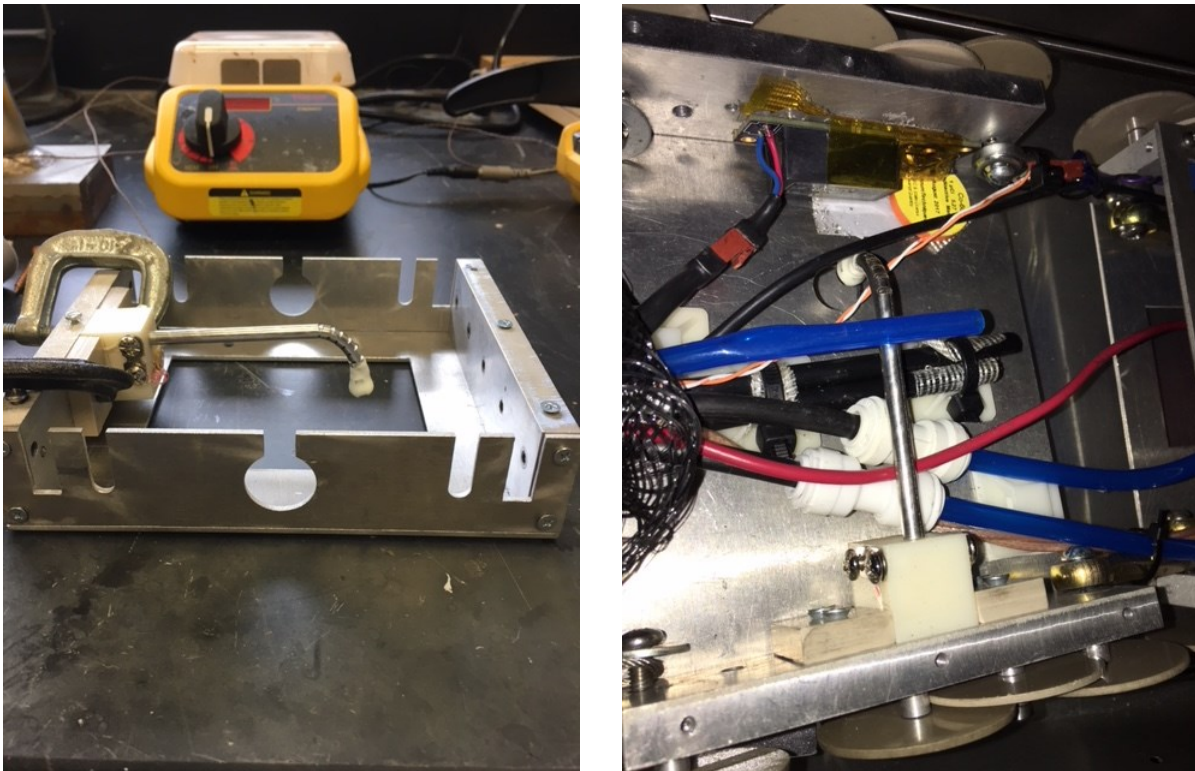
Figure 2.5.14. Temperature sensor mounted in car chassis before and after other components are mounted.
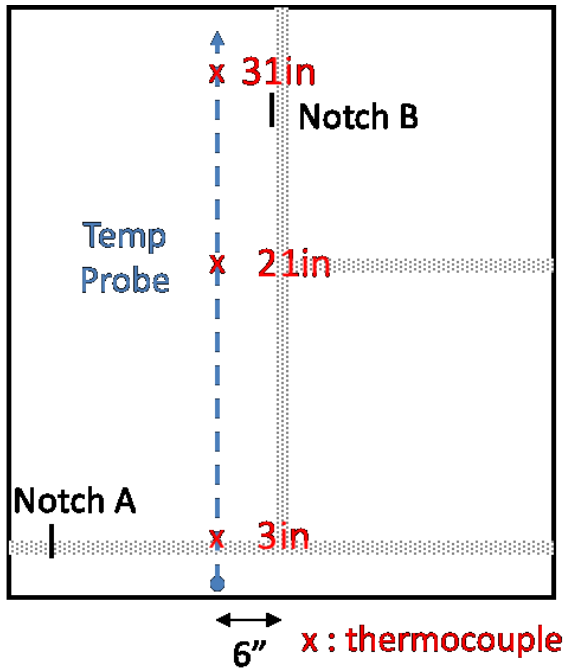
Thermocouple	70F	250F	300F	350F
At 3 in	70.2	99.3	112.3	133.4
At 21 in	70.6	249.6	300.1	350
At 31 in	70.4	236.3	289.1	324.7
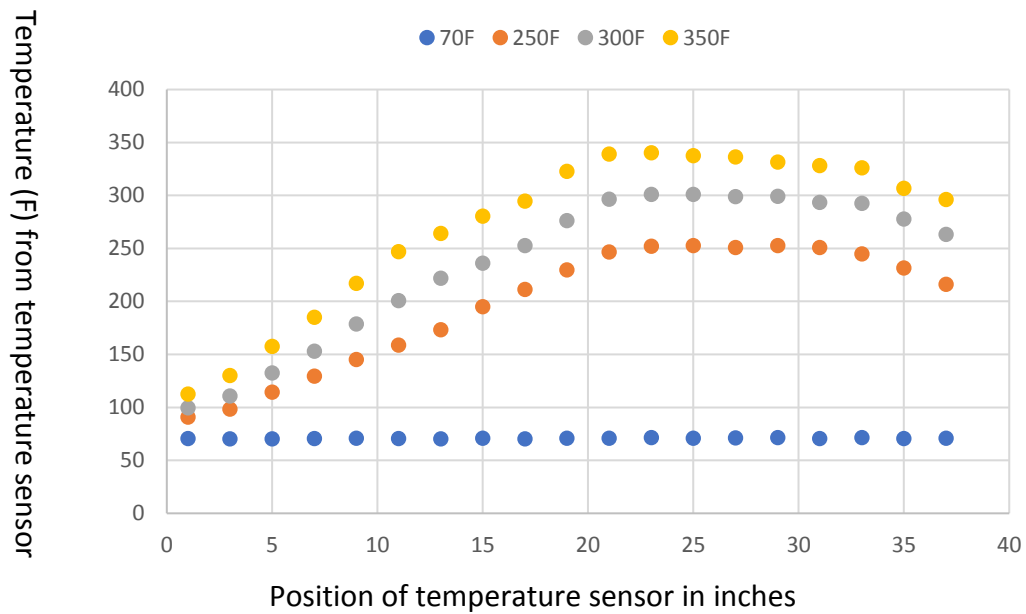
Figure 2.5.14. Test of temperature sensor on MPC mockup. Readings are taken after 10 s and corrected using the calibration, $T = 1.7733T_p - 54.207$.

2.5.4 References

Cuta, J. M., U.P. Jenquin, M.A. McKinnon. *Evaluation of Effect of Fuel Assembly Loading Patterns on Thermal and Shielding Performance of a Spent Fuel Storage/Transportation Cask*. Tech. rep. Pacific Northwest National Laboratory, 2001.

Cuta, J. M., H. E. Adkins, Preliminary Thermal Modeling of Hi-Storm 100s-218 Version B Storage Modules At Hope Creek Nuclear Power Station ISFSI, FCRD-UFD-2013-000297PNNL-22552 Rev.1, August 30, 2013

Holtec Center. "Holtec International Final Safety Analysis Report for the HISTORM 100 Cask System", in NRC Agencywide Documents Access and Management System (ADAMS), 2010

Los Alamos National Laboratory, MCNP6 Users Manual - Code Version 6.1.1beta, LA-CP-14-00745, June 2014)

Michener, T. E., J.M. Cuta, D.R. Rector, and H.E. Adkins Jr, COBRA-SFS: A Thermal-Hydraulic Analysis Code For Spent Fuel Storage And Transportation Casks, PNNL, October 2015

Priest, C.R., Dosimetry, Activation, and Robotic Instrumentation Damage Modeling of the Holtec HI-STORM 100 Spent Nuclear Fuel System, Thesis, University of South Carolina, 2016

Rearden, B.T. and M.A. Jessee, Eds., SCALE Code System, ORNL/TM-2005/39, Version 6.2.2, Oak Ridge National Laboratory, Oak Ridge, Tennessee. Available from Radiation Safety Information Computational Center as CCC-834, 2017

Waldrop, K., Diablo Canyon Stainless Steel Dry Storage Canister Inspection, ERPI, 2016

2.6 Systems Engineering

Summary. The Systems Engineering group performed a variety of tasks to support design, construction, and testing of the prototype robotic inspection system in concert with the other teams:

1. Worked with the other teams to define the system architecture and capture it with system architecture diagrams (Section 2.6.1)

2. Developed, assembled, and tested the overall System Control and Data Interface, including the LabVIEW-based Inter-System Messaging protocol and the Vent Interface System hardware and software (Section 2.6.2);

3. Led the radiation and thermal testing of a number of components (2.6.3);

4. Designed, built, and tested the Geiger-Mueller radiation measurement system (2.5.2.1);

5. Defined cabling requirements, surveyed the market for available cables, and worked with two custom cable manufacturers to obtain quotes for custom cables meeting the thermal, radiation, and other environmental specifications (2.6.4);

6. Assisted LIBS, EMAT, and Delivery system teams during system integration and demonstration (2.6.5).

2.6.1 Physical Architecture Development and Capture

The systems engineering group took on the integration task of creating system architecture diagrams that capture the physical layout of subsystems and how they interconnect with one another. These diagrams include cable bundles, computers, instruments, power and support systems, as well as space allocations in the robot train. The systems engineering group coordinated with subsystem representatives to compile the necessary information, identify potential conflicts, and coordinate needs such that each subsystem could integrate smoothly.

2.6.1.1 Integrated Single Tether versus Parallel Tethers

The delivery system inserts the robotic inspection train into the cask, and the cable bundle containing the retrieval cables, electrical power, sensor measurement signals, cooling air hose and LIBS fiber comes out the back. The insertion arm includes two Ethernet cameras for the purpose of observing and recording the vent insertion process from the ground. The winch frame contains further cabling associated with the winch motor controls, which must be brought to the ground as well. The team designed an integrated approach to system cabling which incorporated a BeagleBone-based embedded computer and Ethernet hub mounted on the Vent Interface. The robot train tether would terminate at the Winch frame, where the electrical signals from the train would connect to the BeagleBone. Special interconnects would be required for LIBS fiber and EMAT coaxial cables. From this point, a single bundle would drop to the ground systems. This design reduces the amount of cabling between the vent and ground control equipment, and is shown in Figure 2.6.1.

In the demonstration prototype, the robot train, vent interface, and winch system each had its own cable tether, which terminated at their respective ground systems. This was done primarily

to allow for parallel development of subsystems. The resulting architecture is shown in Figure 2.6.2.
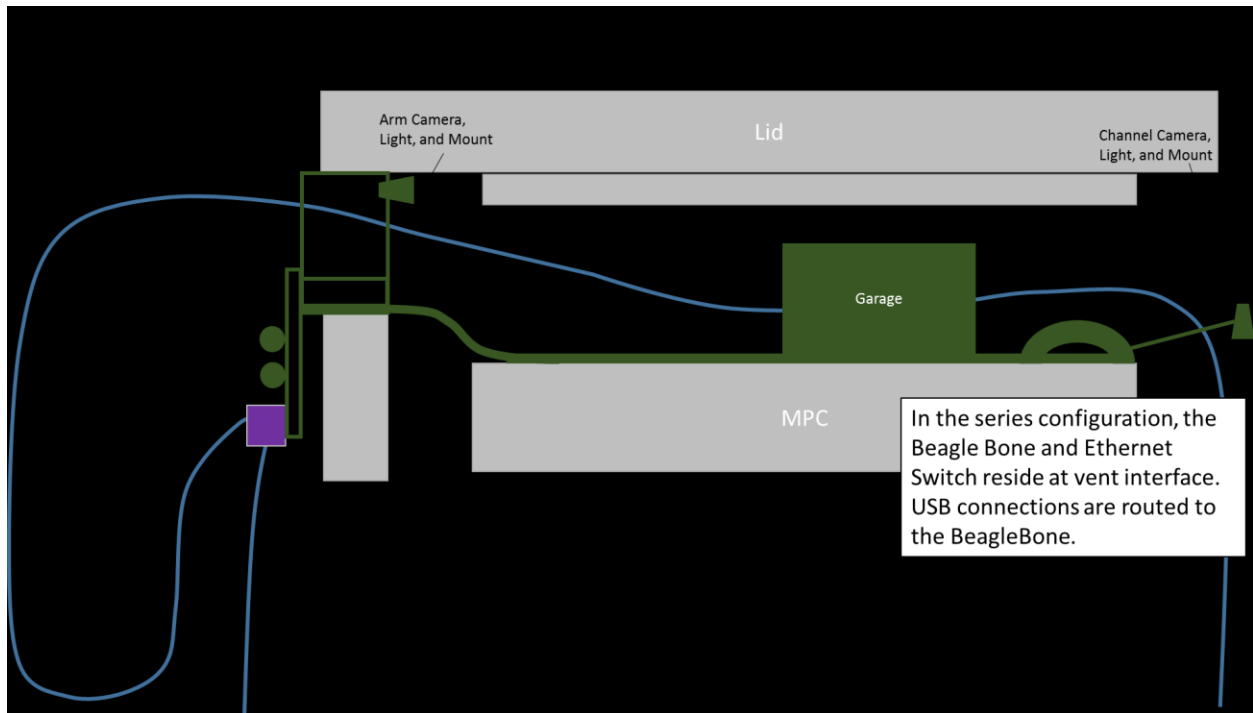
Figure 2.6.1. Series Tether Configuration (integrated approach)
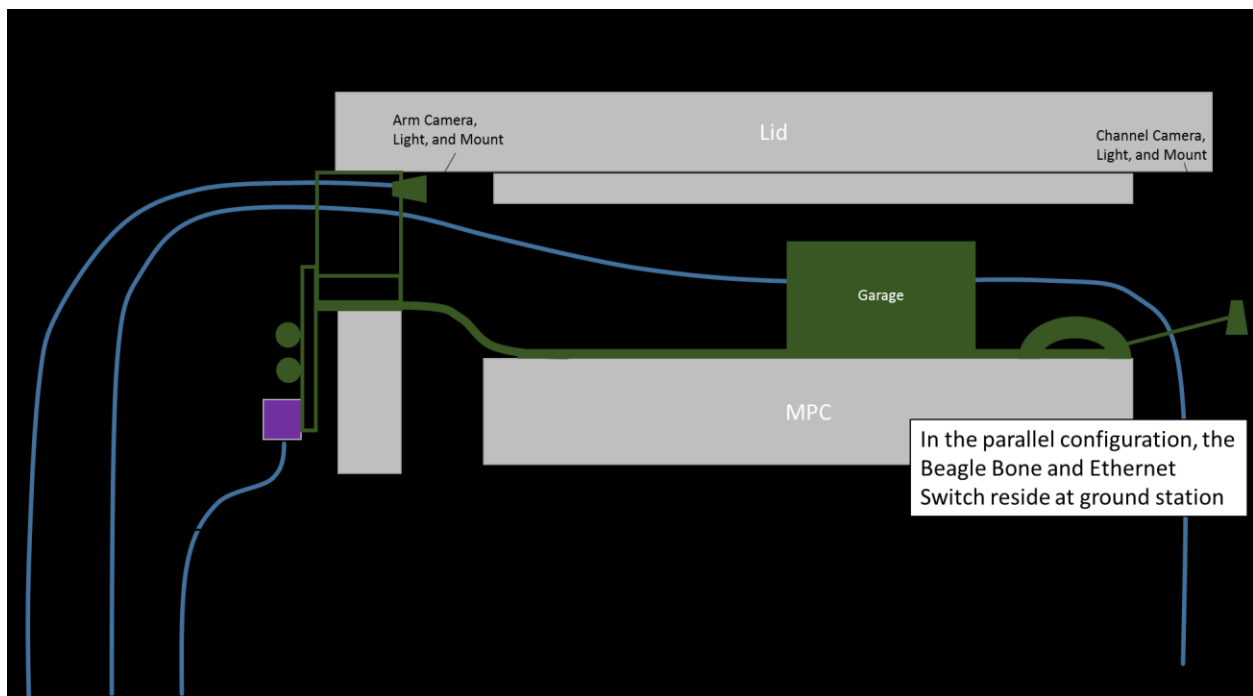
Figure 2.6.2. Parallel tether configuration as actually demonstrated

Additional details of how the train connects with the ground-based systems are shown in Figure 2.6.3. Figure 2.6.4 is a more detailed diagram of the sensor train, showing the contents of each car as well as the wires and tubes which pass between cars and form the tether from the back of the train to the rest of the system. The LIBS and EMAT sensors both require specialized cabling between the transmit/receive elements in the robot train and the transmission source/detector instrumentation on the ground.

Figure 2.6.3. *Canister Inspection System Diagram showing data system and sensor locations*
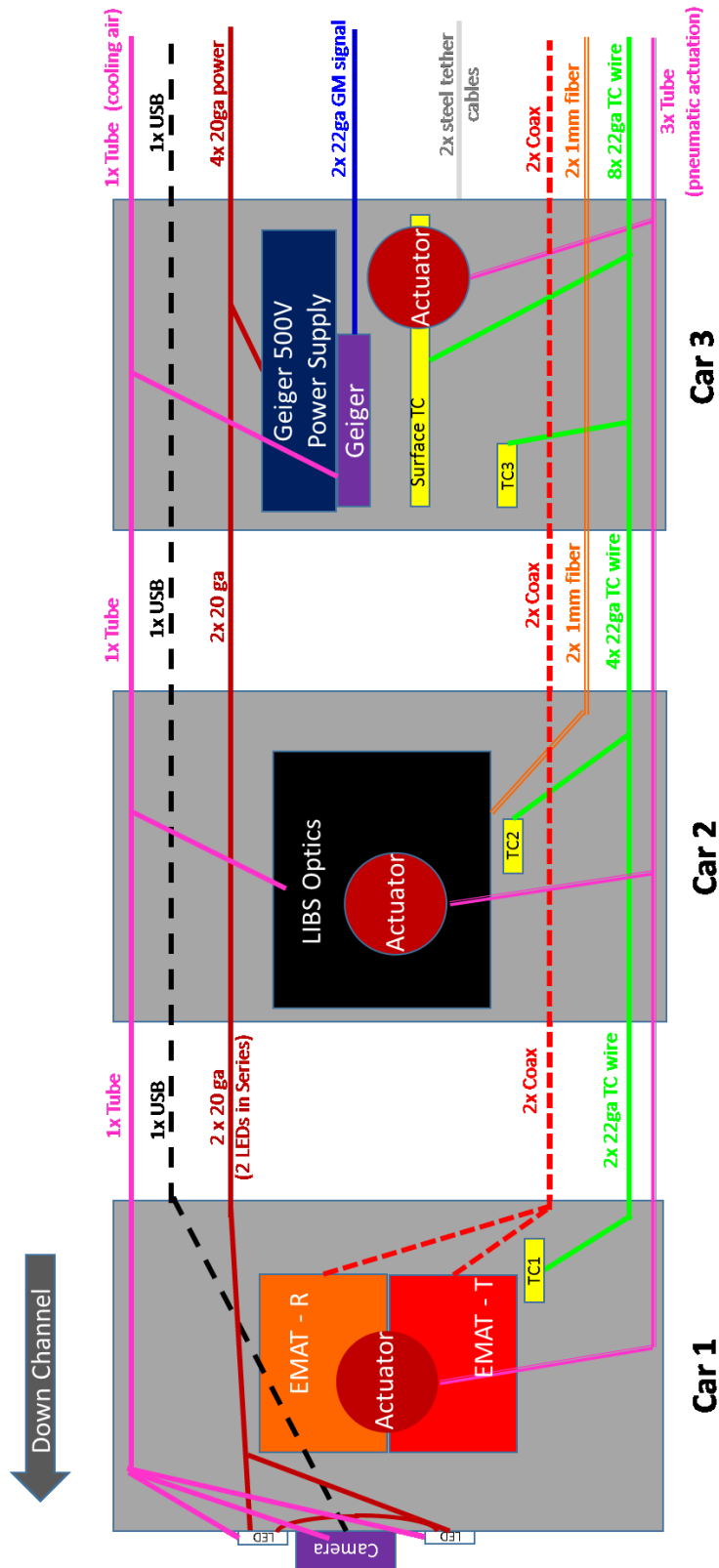
Figure 2.6.4. *Diagram of Sensor Train showing contents of each car, and cable tethers between cars and to external system*

Multi-sensor inspection and robotic systems for dry storage casks 217

2.6.2 System Control and Data Interface

Systems Engineering team was responsible for communication and synchronization between the robot deployment mechanism and the sensor systems. Knowledge of the robot's position at a given time is critical for the sensor systems to synchronize inspection measurements with position in the canister.

2.6.2.1 Inter-System Messaging Protocol

The Systems Engineering group identified the need for a communication protocol between subsystems. Synchronizing time, position, and status information between the LIBS, EMAT, and Robot Control subsystem and their respective computers is necessary to accurately maintain data from each inspection and allow correlation of data from inspections conducted at different times. To meet this need, systems engineering developed a communication protocol and software interface definitions. The communication protocol is fundamentally a set of User Datagram Protocol (UDP) messages, however, as both the LIBS and EMAT subsystems are controlled by LabVIEW, some pre-packaged LabVIEW functions were written. A generic subsystem is able to include the LabVIEW blocks in their code and communicate status with the robot controller

The protocol exposes robot position and movement information, a heartbeat signal, and provides Network Time Protocol (NTP) synchronized time among all subsystem computers. It also provides a method for each subsystem computer and operator to acknowledge receipt of time and position information, and to declare when the subsystem-customizable status messages. The details of this protocol are summarized below:

- The robot controller sends out a timestamped heartbeat message at a rate of 1 Hz, including a ready/not-ready bit indicating if the controller detects a healthy network AND the operator has indicated 'system ready' – to be used as a user-controlled safety interlock.
- The position measurement system sends out timestamped position and motion messages at a minimum rate of 1 Hz. Additional updates are sent for each robot incremental displacement based on the output of the encoder mounted on the delivery arm, and whenever motion starts/stops.
- Each subsystem on the network checks the timestamp of the incoming messages for arrival within the past second, to establish whether or not the message is to be considered 'good'. Following receipt of a heartbeat message, the subsystem issues a timestamped response message providing its status to the robot controller.
- The robot controller monitors response messages as well as for loss of communications. The subsystem status, and other information are reported to the operator.
- Status and response as reported by the subsystems are recorded along with the rest of the robotic system's data logs for position, velocity, camera streams, temperatures, Geiger activity, etc.

Four LabView Virtual Instruments (VI) were provided for inclusion in the control software for each subsystem:
1. A Main VI to be inserted in the top level of the subgroup LabVIEW application;

2. A Status VI to read the system status as reported by the master computer; and
3. A Response VI which the subsystem software can use to relay the status of their system.
4. A Get Synchronized Time VI to obtain a synchronized timestamp for data acquisition purposes
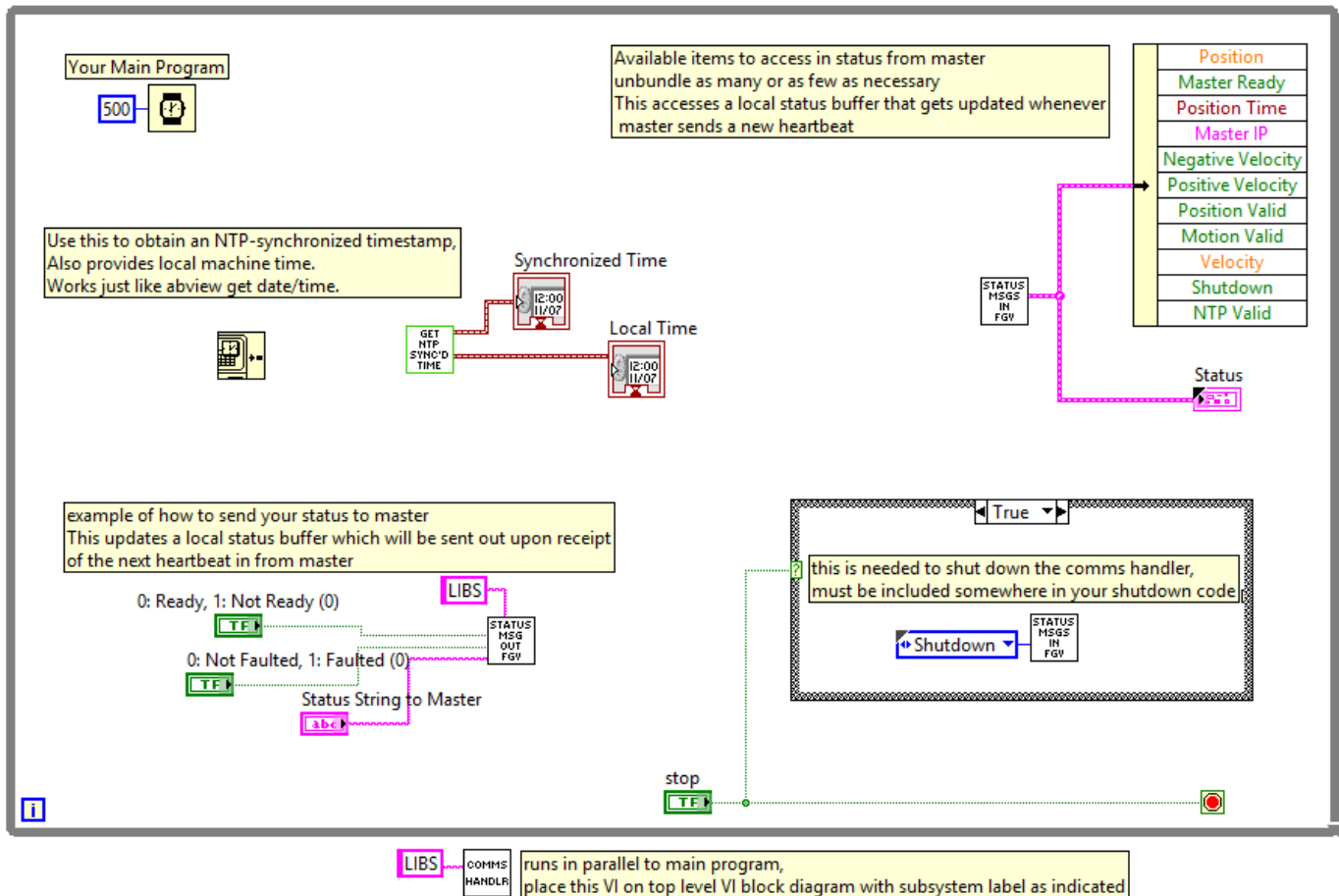
Figure 2.6.5. *Network communications infrastructure example.*

2.6.2.2 System Controller (BeagleBone)

With the integrated tether design goal as stated above, an embedded computer solution was required to serve as an interface for the Geiger counter, thermocouple measurement, and motor control functions. The embedded computer acquires and digitizes the sensor outputs, and converts discrete motor control messages into analog pulse-width-modulated signals. A commercial-off-the-shelf embedded computer made by BeagleBone (BeagleBoneBlack) was chosen as the development platform, as it met the processing and communication requirements and is an open hardware design. A custom mating thermocouple interface and IO breakout board was designed to allow for the control of R/C servos, digitize up to 8 thermocouple channels, measure the Geiger pulse signal, and also interface to a quadrature rotary position encoder. The interface board was designed and build by the PSU team. The BeagleBoneBlack and custom interface board are shown in Figure 2.6.6.

Software was developed in the form of C, C++, Python, and bash scripts to automate the acquisition of thermocouple and Geiger pulse measurements and transmit the information to the control laptop. The R/C servo functionality was developed but ultimately not used. The quadrature encoder hardware interface was not tested and used; instead, this function was accomplished with an existing encoder interface for the demonstration system already used by the delivery arm team in their developmental testing.

The thermocouple measurements and Geiger counter pulses are broadcast by the BeagleBone on to the ROS network. These measurements, along with the robot train position and velocity information, camera streams, and subsystem status/response messages, are displayed in a GUI on the robot control computer. The robot control computer also initiates a data recorder based on the Robotic Operating System (ROS); everything on the ROS network can be recorded for data recordkeeping purposes. The Control GUI can be seen in Figure 2.6.7.
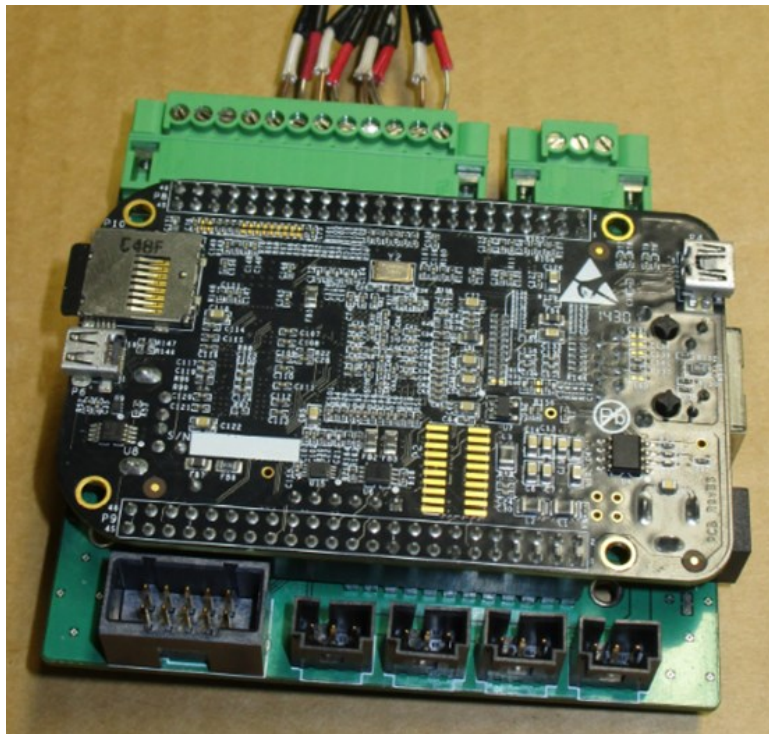
Figure 2.6.6. *Photo of BeagleBone Embedded Linux Computer and ARL custom interface board. Clockwise from top: 8x Thermocouple inputs, Geiger sensor input, Ethernet jack, power jack, 4x RC servo headers, quadrature encoder header, SD card containing operating system and software.*
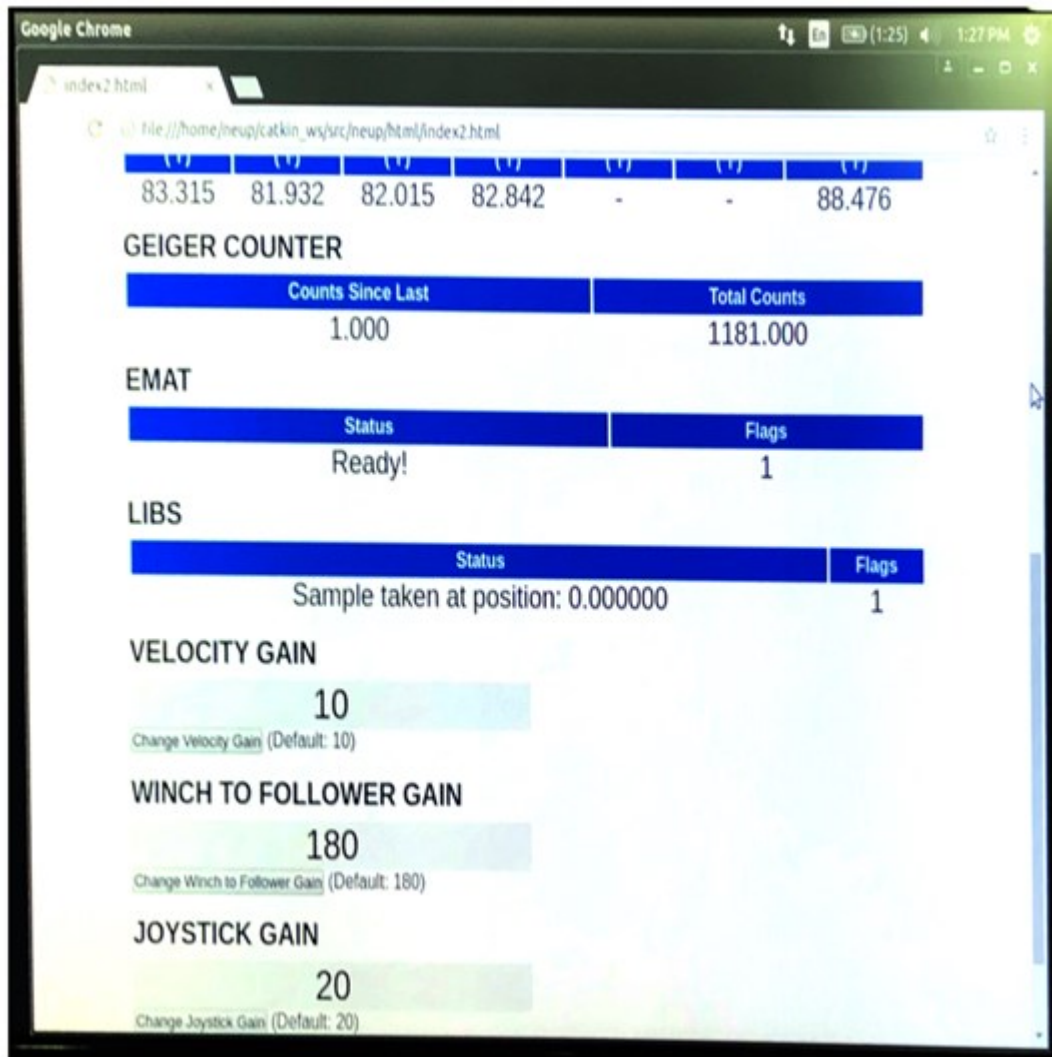
Figure 2.6.7. *Robot control GUI showing thermocouple measurements, Geiger counter activity from Co-60 source, and subsystem status reporting*

2.6.3 Environmental Testing

2.6.3.1 Imaging System Environmental Testing

Systems Engineering and the Robotics Team worked together to choose candidate cameras, lenses, and LEDs to be used for the arm and vent imaging systems; these components were then tested for heat tolerance in a thermal chamber at the Applied Research Laboratory and for gamma radiation tolerance in the Gammacell at the Penn State Radiation Science and Engineering Center. The cameras chosen were a Point Grey Blackfly Ethernet camera and a Ximea xiQ USB camera, each approximately a 1 inch cube. The cameras were used with lenses made by Tamron and Edmond respectively; each lens is approximately 1 inch in diameter and 1.5 inches long. Systems Engineering chose the Lumex Titanbright white light LEDs and drivers, and connected two of these LEDs in series with a Maxim LED driver board to provide lighting for the robot camera. In order to exercise and monitor the cameras, lenses, and LEDs, they were all

tested and operated together during environmental testing, and image frames from the cameras were pulled out of the chambers during testing for live monitoring and recording. The LED driver board will probably be located outside of the canister so it was not tested for thermal or radiation tolerance.

Table 2.6.1 is a summary of the camera, lens, and LED environmental testing results. The cameras survived the thermal testing, but failed the radiation tests. Details of the testing are described below. The cameras failed during radiation testing, but the design did not include any radiation shielding, which would improve their operating time. Also, the radiation testing was conducted at what the team believed were worst-case radiation levels.

Table 2.6.1. *Summary of Results from Image System Environmental Testing*

Camera, Lens, and LED Environmental Test Summary						
Cameras				Co-60 gamma rays		
Manf./Name	**Part Number (S/N)**	**Sensor**	**Thermal Test Results**	**Radiation Test Results**	**Total Dose (krad)**	**Canister Time (hr) @ 10 krad/hr**
Point Grey Blackfly	BFLY-PGE-13E4C-CS S/N 15204887	e2v 1.3 Mpix CMOS EV76C560	passed 8hr @ 113F/45C	failed after 115 sec (~2 min)	11.8	1.2
Ximea xiQ	MQ013CG-E2 S/N 22505551	e2v 1.3 Mpix CMOS EV76C560	passed 8hr @ 131F/55C	failed after 230 sec (~4 min)	23.6	2.4
Lenses						
Manufacturer	**Part Number**	**Description**	**Thermal Test Results**	**Radiation Test Results**		
Tamron	M118FM12	1/1.8 12mm F/1.4-16 Aspheric Fixed-Focal + Iris	passed 8hr @113F/45C & 1 hr @131F/55C	passed 115 sec (~2 min)	11.8	1.2
Edmond	85-349	16mm, f/1.8, Fixed Focus, no Iris	passed 8 hr @ 131F/55C	passed 230 sec (~4 min)	23.6	2.4
LED						
Manf./Name	**Part Number**	**Description**	**Thermal Test Results**	**Radiation Test Results**		
Lumex Titanbrite	SML-LX1610UWC/A	Hi Brightness cool white LED, leaded TO252-3	passed 8hr @ 113F/45C & 8 hr @ 131F/55C	passed 345 sec (~6 min)	35.5	3.5

Imaging System Gamma Radiation Testing. Figure 2.6.8 shows two views of the imaging system with a color target and resolution target, mounted in a fixture and ready for insertion into the Gammacell. On the left is the Ximea camera with Edmond lens, and on the right is the Point Grey Blackfly camera with the Tamron Lens mounted to it.
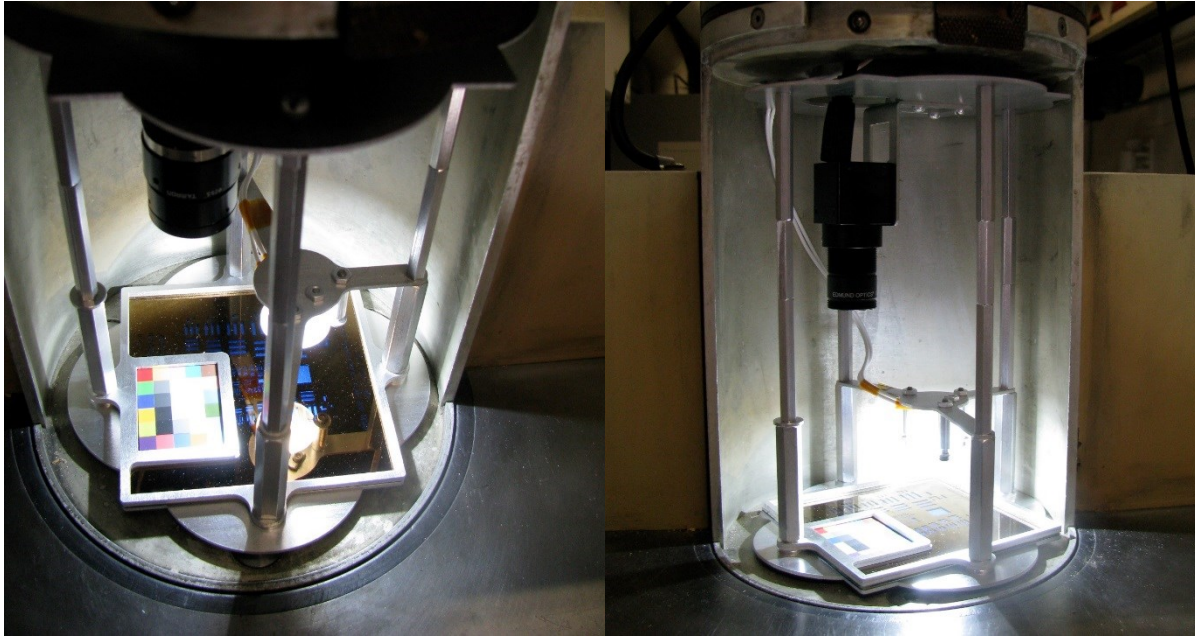
***Figure 2.6.8**. Photos of Image System installed in test fixture for gamma ray testing.*

Figure 2.6.9 shows two images captured from the Blackfly camera/Tamron lens; on the left is an image taken before insertion into the Gammacell, and on the right is an image taken while the camera system is running inside the Gammacell. This is one of the last images from the camera before it failed. In both cameras the main visual effect of the gamma rays was a "snow" effect during irradiation until the camera suddenly stopped sending images.
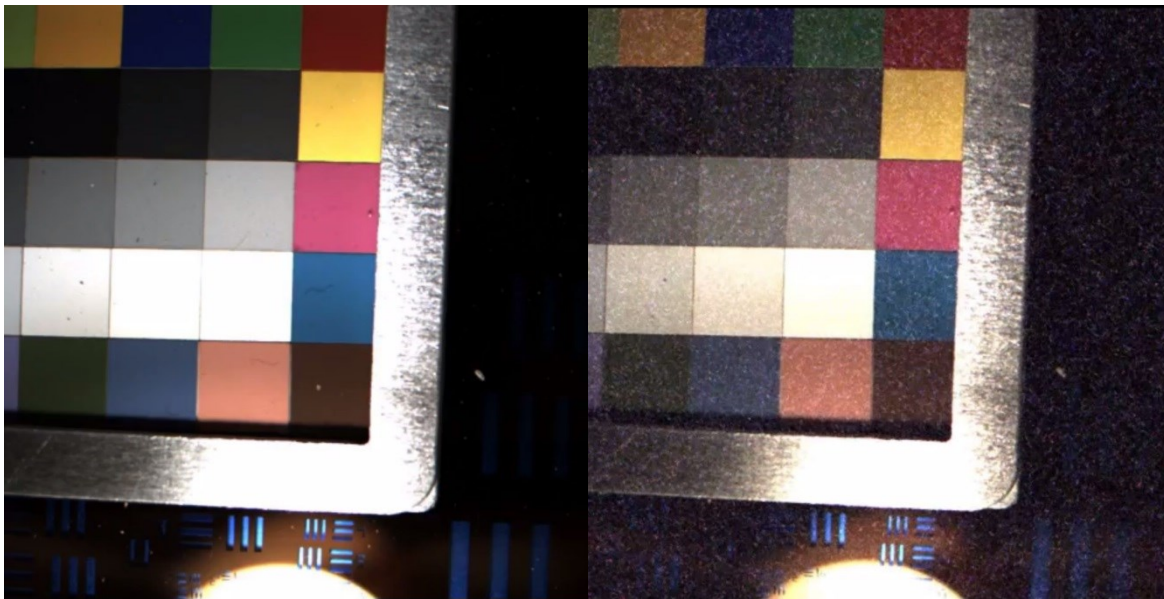
***Figure 2.6.9**. Frames from the Imaging system before insertion into the gamma chamber (left) and while operating in the gamma chamber (right).*

Imaging System Thermal Testing. The cameras, lenses, and LEDs were tested in the thermal chamber using the same fixture shown for the radiation testing. The Blackfly-Tamron combination was tested for eight hours at the Blackfly specified maximum temperature of 113F/45C, the Ximea-Edmond combination was tested for eight hours at the Ximea specified maximum temperature of 131F/55C, and the Ximea-Tamron combination was tested for one hour at the Ximea specified maximum temperature of 131F/55C. The LED survived the combined tests. None of the components showed any apparent degradation due to thermal testing either during or after the test. These temperatures are well below the maximum temperatures expected inside the canister vent so a cooling system similar to the air tube system prototyped for this project will be needed.

2.6.3.2 Chassis Thermal Testing

The prototype car chassis was designed by the Robotics Team and consists of aluminum frame parts, stainless steel fasteners, and wheels made of the high temperature/radiation resistant plastic PEEK (Polyether ether ketone); it is designed to survive the full specified maximum canister vent temperature of 350F/177C and to have very little sensitivity to gamma radiation. For this reason, it was tested to higher temperatures than the other parts and was not tested for gamma radiation sensitivity.

Systems Engineering tested the robot car chassis and wheels by placing the prototype on an aluminum plate in the ARL thermal chamber, then placing a five pound weight on the car and checking that the car rolled freely in this position. The oven door was closed and the temperature was ramped up to 350F over the course of 1 hour and held at this temperature for 20 minutes. After this period the door was opened and the robot was tested and was found to roll as well as at room temperature. The rolling test was designed to show that the robot cars could be retrieved from an actual canister after exposure to high temperatures for a time representative of a cask inspection. Figure 2.6.10 is a photo of the test setup.

Figure 2.6.10. Robot chassis with wheels in ARL thermal chamber for thermal testing

2.6.3.3 Coolant Hose Thermal Testing

The System Engineering and Robotics groups together conducted a thermal test on the cooling hose, a corrugated stainless steel inner hose with a 3/8" inner diameter protected by a stainless steel outer braid. The hose was tested using the ARL Thermal Test Chamber, an air flow meter and control valve purchased for the testing, a data acquisition system set up for the testing, and facility-supplied compressed air. A 50' section of hose was placed inside the thermal chamber, and the chamber was set to heat to 175C. Compressed air was introduced to the hose outside the temperature chamber and the exit temperature of the air at the other end of the hose was measured.

We observed that the cooling air flow through the hose presents enough of a loss to the thermal chamber that its heater was unable to keep up with the desired set point of 175C. Over the course of the test, we saw a consistent delta of 25-30C drop from oven temperature to outlet air temperature. This is unacceptable cooling performance, and it is largely believed to be caused by the internally corrugated nature of the hose creating significant pressure drop due to turbulent flow. Alternative hose materials are being investigated, with platinum-cured silicone currently being a top candidate. This type of hose is rated for 350F/177C, gamma resistant, is internally smooth to allow for better flow, and does not have the comparably high thermal conductivity of a steel hose.

Temperature data from the thermal test are presented in Figure 2.6.11. Here it is seen that the temperature chamber is reaching a steady state of approximately 140C with the flow rate measured at 6.5 CFM. The flow rate is reduced to 1 CFM to allow the chamber to get up to temperature, and the flow rate is returned. The 25-30C delta between environmental chamber and cooling air exit from the hose is seen.

It is worth noting that the full 50' of hose, less inlet and outlet hose stubs, was inserted into the temperature chamber for this test. This is a worst-case situation as the full exterior surface of the hose is subjected to the high ambient temperature. Pictures of the experimental setup can be seen in Figure 2.6.12.
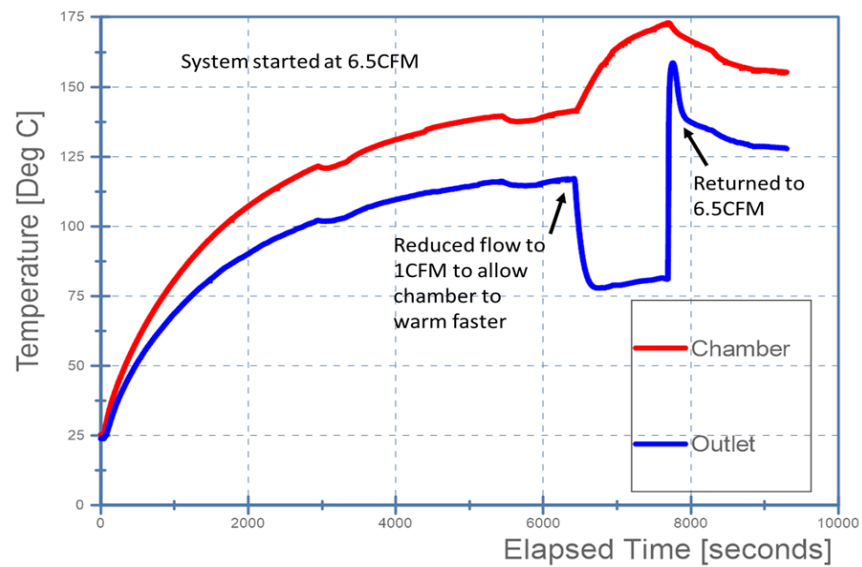
Figure 2.6.11. Temperature measurements during cooling hose thermal tests
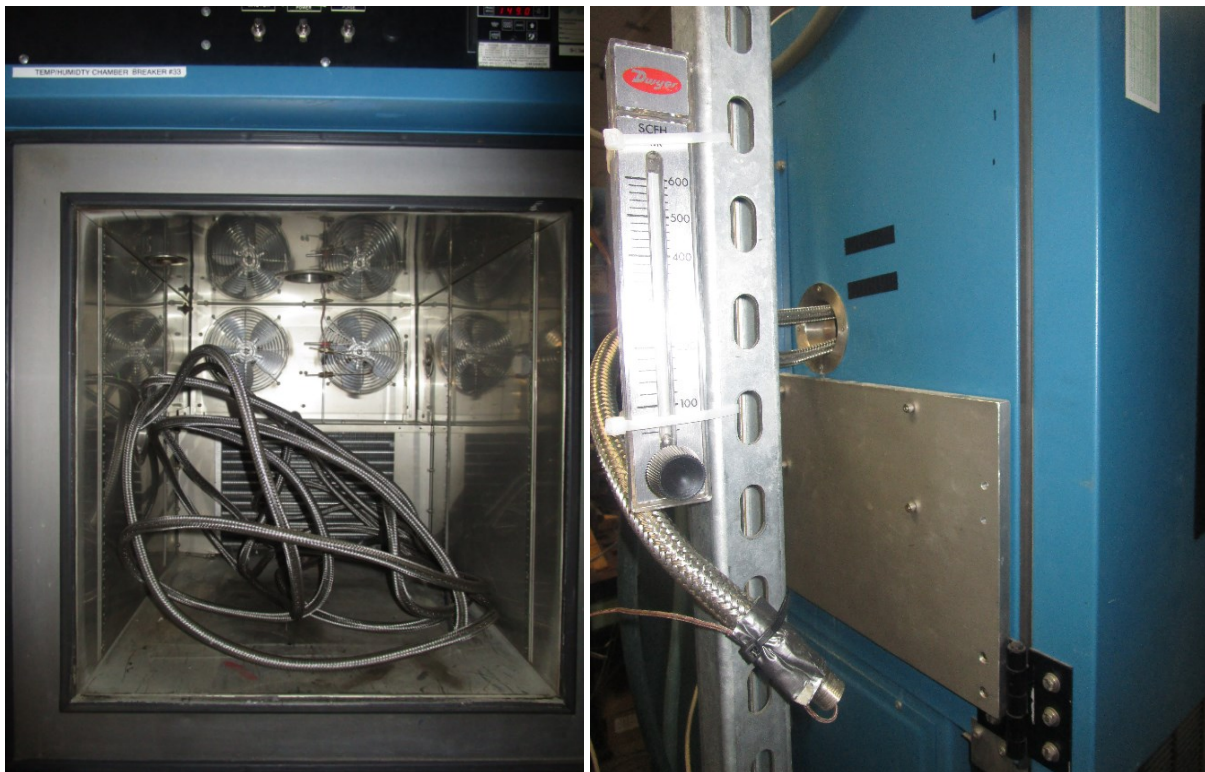
Summary. The prototype chassis and wheels can survive the full 350F/177C maximum expected temperature of the canister, and should survive the radiation from many trips into the canister. The corrugated metal air hose does not have sufficient insulation and does not move enough air, probably due to turbulence from the corrugations; it will probably be replaced by a silicone hose for the in-canister design. The unshielded cameras tested would last only an hour or two in a canister with a radiation dose rate of 10 krad/hr. A model produced by the University of South Carolina showed that 2 cm of lead on five sides of the car (leaving the front open for the lens) would only increase this by a factor of 2 or 3 and with a significant penalty in weight and loss of room in the car. Shielding just the cameras poses similar space and weight challenges. Other cameras are likely to have the same issue due to the nature of silicon imagers and integrated circuits, so if a camera is used on the robot, it will need to be considered expendable. The team also tested optical fiber bundles as an alternative to active cameras. These are routinely used in remote inspection systems. The optical fiber bundles (boroscopes), however, typically have a very shallow field of view; thus, they are good for close-up inspection, but not suitable for guiding the insertion of the robot into the canister.

2.6.4 In-Canister Cable Selection

Systems Engineering also performed a market survey to determine the availability of suitable electrical cables to be used inside the canister. The combination of high temperature (250F minimum, 350F preferred), gamma radiation resistance of at least 1 Megarad (MRad), and halogen-free cable, makes nearly all commercial cables unsuitable. We investigated two cable types which will need to run inside the canister: high-voltage power and signal cables for the EMAT sensors and Ethernet communication cables.

The EMAT group usually uses coaxial cable but sometimes uses twisted shielded pairs of wires; the peak voltage of their pulses can vary. Based on consultation with the EMAT group the minimum peak operating voltage we used for the study is 550V. We found one commercial manufacturer, Axon, which makes a suitable twisted shielded pair cable. Axon makes the halogen-free POLIAX™ cable X2419TSTX2, twisted shielded pair, tin-plated copper, which is rated for use up to 130C/266F and has a peak operating voltage of 846V, and is rated for gamma radiation up to 300 MRad. The minimum order is 820 feet, which would cost $1960 and would provide enough cable for several inspection systems. We did not find any manufacturer that was able to produce high temperature, rad resistant, halogen-free coax cable. Since we did not need to demonstrate the system in a high temperature, high radiation environment, we used standard commercial-grade cables for our testing and system demonstration.

We found no commercial Ethernet cable that even approaches meeting the combination of thermal, radiation, and halogen-free requirements. As a result, we contacted several manufacturers to discuss custom cables. New England Wire offered to produce a custom cable meeting the Ethernet specs (but not certified); this cable would meet our performance and temperature requirements, but because the insulator would be ETFE, it would not be halogen-free. Engineers at the company stated that ETFE can withstand up to 1 MRad gamma radiation in some tests, but the presence of heat and oxygen in combination with gamma radiation causes accelerated deterioration.   The minimum order of this custom high-temperature Ethernet cable would be 1000 feet, at a cost of $8651. Once again, since we did not need to demonstrate the system in a high temperature, high radiation environment, we used standard commercial-grade cables for our testing and system demonstration.

2.6.5 System Integration

In addition to the work outlined in the previous section, the systems engineering team provided assistance during integration efforts between the LIBS, EMAT, and delivery subsystems. This included assistance with LabVIEW software development, ROS Robot control software development, EMAT sensor noise sensitivity mitigation via a system grounding investigation, coordinating mechanical and electrical interfaces across subsystems, and mechanical and electrical assembly.

Systems Engineering compiled a Master Equipment List (MEL) which lists the components of each subsystem down to the box level, and the mass and power draw of each. The components are grouped into four systems, with the Electrical/Computer Ground Support further divided into three subsystems:

1. Mechanical/Thermal Ground Support (brown)
2. Electrical/Computer Ground Support (violet)
    a. EMAT System Ground Support
    b. LIBS System Ground Support
    c. Robot Control & Data Interface Ground Support
3. Vent Interface System and Insertion Arm (green)
4. Robot Sensor Train and Tether Cable (blue)

The **Mechanical/Thermal Ground Support** consists of only one component, the Air Compressor; this component has the highest single power draw, but it runs only occasionally when the accumulator pressure drops below a preset value, and given a sufficiently long air hose it can be set up some distance from the rest of the ground support equipment and plugged into a power outlet which is supplied by a different circuit.

The **Electrical/Computer Ground Support** system consists of three subsystems developed by different groups. The EMAT group has the capability to assemble their equipment into several different configurations; the ground support system listed is the most complex and has the highest capability among these options. The LIBS group developed a portable version of their laboratory system for the demonstration at Penn State; the system listed here is the next step in

portability, a proposed field deployment system. The Robot Control and Data Interface ground support listed is the as-built system.

Vent Interface System and Insertion Arm – the components listed here represent the as-built system which would be installed into the mouth of the vent. Power for this portion of the system is supplied remotely by the Power Conversion Box in the Robot Control and Data Interface System and so is included on that line of the MEL.

The **Robot Sensor Train and Tether Cable** listed here is the as-build system used in the demonstration. Electrical power for this system is also provided by the Power Conversion Box and so is included in this line, and the LIBS optical system inside Car 2 is passive, focusing laser pulses generated by the Ground Support system. The mass of this system and the Vent Interface System and Insertion Arm are totaled to calculate the mass of the Total Elevated System.

MASTER EQUIPMENT LIST - NEUP IRP PRINSE System

Ground Support: Mechanical/Thermal

Subsystem/Component	Total Mass, lb	Total Mass, kg	Total Power, W	Description (Vendor, Part #, etc.)
Air pump/compressor	95.92	43.50	**1800**	Only runs occasionally, can be remoted
Total	**95.92**	**43.50**	**1800**	

Ground Support: EMAT System, RAM-5000 version

Subsystem/Component	Total Mass, lb	Total Mass, kg	Total Power, W	Description (Vendor, Part #, etc.)
High Power Pulser	38.78	17.59		RITEC RAM-5000
Digitizer	23.01	10.44		National Instruments PXIe-1062Q chassis
Workstation	29.43	13.35		Dell T3600
Workstation Monitor	12.76	5.79		Dell
Uninteruptible Power Supply	41.20	18.68		APC Smart UPS-1000
Laptop	6.59	2.99		Dell Latitude E6510
Matching Network, Transmit	1.43	0.65		RITEC TEM-128
Matching Network, Receive	0.90	0.41		RITEC REMP-128
Band-Pass Filter, 100 KHz-500 KHz	1.53	0.69		Kiwa Electronics
Preamplifier	1.61	0.73		Olympus 5660B
Total, EMAT Ground Support	**157.24**	**71.31**	**435.00**	

Ground Support: LIBS System, proposed field deployment

Subsystem/Component	Total Mass, lb	Total Mass, kg	Total Power, W	Description (Vendor, Part #, etc.)
Nd:YAG Laser	55.00	25.00	**1200**	Quantel Evergreen 70
Spectrometer	45.00	20.00	10.00	HORIBA Jobin Yvon
ICCD Camera	3.50	1.60	60.00	Andor DH334T-18F-03
Laptop	9.00	4.10	100.00	
Optical Breadboard	43.00	19.50	0.00	Thorlabs
LIBS optics, on cart and in vehicle	5.00	2.20	0.00	Thorlabs / Edmund Optics
Total, LIBS Ground Support	**160.50**	**72.40**	**1370**	

Ground System: Robot Control & Data Interface, as built

Subsystem/Component	Total Mass, lb	Total Mass, kg	Total Power, W	Description (Vendor, Part #, etc.)
Power conversion box w/ battery	82.47	37.40	7.31	Custom
Laptop	4.41	2.00	280.80	
Total, Robot Control & Data Interface	**86.88**	**39.40**	**288.11**	
GROUND SYSTEM Without Air Compressor	**405**	**183**	**2093**	
GROUND SYSTEM With Air Compressor	**501**	**227**	**3893**	
	lbs	**kg**	**W**	

Vent Interface System and Insertion Arm, as built

Subsystem/Component	Total Mass, lb	Total Mass, kg	Total Power, W	Description (Vendor, Part #, etc.)
Winch and Insertion Arm	35.50	16.10		Custom
Vent Mount	22.71	10.30		Custom
Winch Motor Power and Comms	7.72	3.50		Custom
Vent Power and Comms	7.06	3.20		Custom
Total, Vent Interface and Insertion Arm	**72.99**	**33.10**	**0.00**	

Robot Sensor Train and Tether Cable, as built

Subsystem/Component	Total Mass, lb	Total Mass, kg	Total Power, W	Description (Vendor, Part #, etc.)
Car 1: EMATs, Camera, LEDs				
Car 2: LIBS Optics				
Car 3: Geiger, Surface Thermocouple				
Total, Cars 1, 2, and 3	4.19	1.90		
Tether Cable	8.16	3.70		
Total, Robot Sensor Train and Tether	**12.35**	**5.60**	**0.00**	
TOTAL ELEVATED SYSTEM	**85**	**39**	**0**	
	lbs	**kg**	**W**	

System Totals

	lbs	kg	W
TOTAL ELEVATED SYSTEM	85	39	0[1]
GROUND SYSTEM Without Air Compressor[2]	405	183	2093
GROUND SYSTEM With Air Compressor	501	227	3893
TOTAL SYSTEM Without Air Compressor[2]	490	222	2093
TOTAL SYSTEM	586	265	3893
	lbs	**kg**	**W**

2.7 Technology Integration and Demonstration

Technology integration was fostered by a series of meetings that brought together different project participants on a quarterly basis, i.e.: full-team meeting, advisory board meeting, sensor group meeting, and delivery group meeting. Of course, individual teams met on a much more frequent basis. Being connected to the EPRI-organized Extended Storage Collaboration Program (ESCP) greatly helped our team to understand the problem, see what other groups were doing to try to solve it, and have several opportunities to make site visits and participate in demonstrations. The project timeline at the end of this section identifies all of our activities throughout the course of the project. Before the timeline, we summarize the two-part final technology demonstration

2.7.1 Final Demonstration – Part I

In our original proposal the Holtec Manufacturing Division (HMD) in Pittsburgh was identified as the location of our final technology demonstration, which was facilitated by having Holtec on our advisory board. We worked with Holtec throughout the course of the project to arrange the demonstration at HMD. While our original idea was to invite an audience to watch the demonstation live, that turned out to be impractical due to the safety requirements associated with HMD being a large-scale manufacturing plant.

Holtec placed an MPC-32 canister into a HI-STORM 100S Version B 218 model overpack. The lid was placed on the MPC and finally the HI-STORM lid was lifted into place. There is only a very small step down (~1") from the outlet vent to the MPC lid. The cask assembly was then placed in a pit to make the outlet vents accessible without scaffolding or harnesses. No gamma shields or bird screens were installed in the outlet vents. This overpack has short guide tubes at the top in lieu of full-length guide channels in many fielded casks. Thus, the sensor train must maintain a vertical path down and back up on its own. The MPC has two full-height axial welds and no mid-height circumferential weld. The MPC has basket supports but no basket. The MPC sits on a 3" thick baseplate inside the overpack. The PRINSE system contacts the stainless steel MPC through halogen-free PEEK wheels and bearings, although in this prototype the bearings are UHMW.

The members of the Penn State team that went to HMD are: Cliff Lissenden, Sean Brennan, Karl Reichard, Bobby Leary, Ian Van Sant, Jen Bracken, and Hwanjeong Cho. The LIBS and concrete inspection systems were not part of the HMD test program.

September 5
- Clean up the Test Track facility where we had been practicing on our mockup.
- Packed up the PRINSE (proactive robotic inspection of nuclear storage enclosure) system.
- Traveled to HMD.
- Safety training, unpacked, and setup PRINSE system (see Fig. 2.7.1).
- Tested insertion of PRINSE system.
- Identified problems: (1) delivery arm got stuck on MPC lid, (2) sensor train would not drop down from hump at end of delivery arm in annulus between MPC and overpack, and (3) significant electrical noise in received EMAT signals.

Figure 2.7.1. *Cask in pit – vent bracket installed in one outlet vent and command station setup on left side.*

September 6

- Dwight Clayton (ORNL), a member of our advisory board, joined us as an observer.
- Re-arranged our PRINSE setup to allow HMD access to a nearby work area.
- Requested that HMD remove the overpack lid (with a crane) to allow us to see inside and resolve problems. See Figs. 2.7.2-2.7.4.
- Found that the delivery arm was catching on the groove for the closure weld ring because the ring was not in place. Requested that HMD put the two semi-circular weld rings in place. This solved problem (1).
- Found that sensor car 3 equipped with temperature probe and mini GM tube was restraining sensor car 1 from descending into the annulus. The problem was solved by adding weights to car 1.
- Demonstrated the robotic delivery system and sent the sensor train all the way to the bottom between four different sets of guide tubes as would be done in an inspection. See Fig. 2.7.5. The travel speeds down and back up were approximately 0.5 and 1 in/s respectively. The final trip down and back up took only 10 minutes.
- Demonstrated that the bumper installed on sensor car 3 keeps the sensor train from getting stuck on the bottom of the guide tubes.

- Investigated the source of electrical noise in the EMAT receiver. Too much noise was coming from the winch motors to collect any useful data. A-scan and B-scan data were collected with the winch motors off, but even these data were corrupted by noise.

Figure 2.7.2. Delivery arm in place on MPC lid (no closure weld ring).
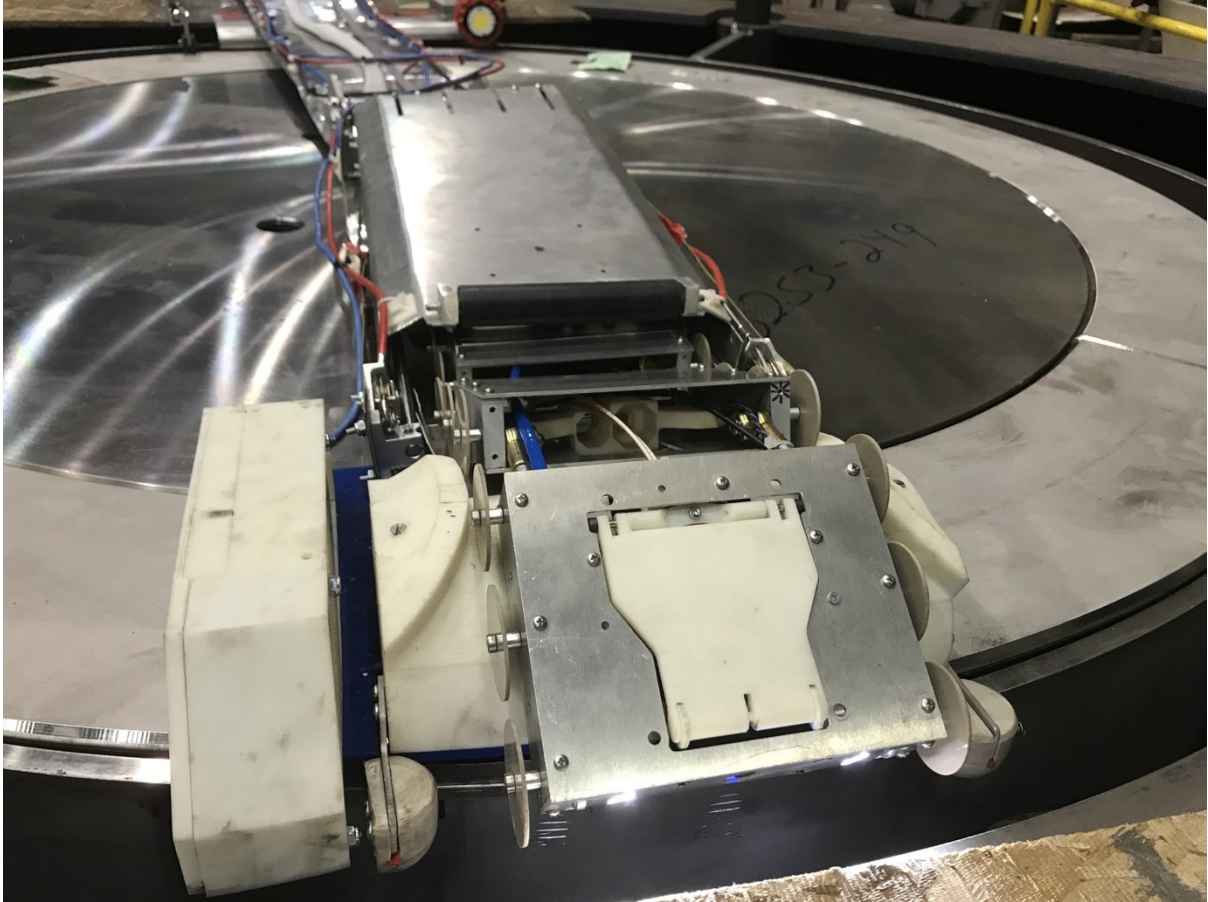
Figure 2.7.3. *Sensor car 1 going over the edge and into the annulus. The box on the left side of the hump contains a camera to look down into the annulus. The camera itself is shielded and positioned to be in a location having lower gamma radiation than the annulus. Sensor car 2 is going up the hump, while sensor car 3 is still inside the garage.*

Figure 2.7.4. Sensor car 1 pulling car 2 over the hump.
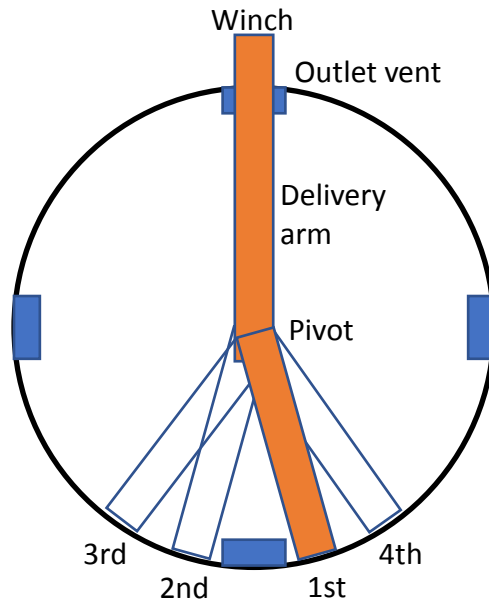
Figure 2.7.5. *Sensor train deployed into four different guide tube gaps.*

September 7

The final day (see Figs. 7-11) was devoted to filming video clips of the PRINSE system after the overpack lid was put back in place. These clips were edited for showing the audience in Part II of the demonstration. The video clips show:

- Setup of Tests
- HI-STORM Lid Off
- Vent Bracket Installation
- Connect Winch and Insert Arm
- Delivery Arm On MPC
- Pivot Delivery Arm
- Over the Edge
- Full Maneuvers
- Delivery Arm Removal
- Vent Bracket Removal

Figure 2.7.6. *Vent mount installed in outlet vent.*
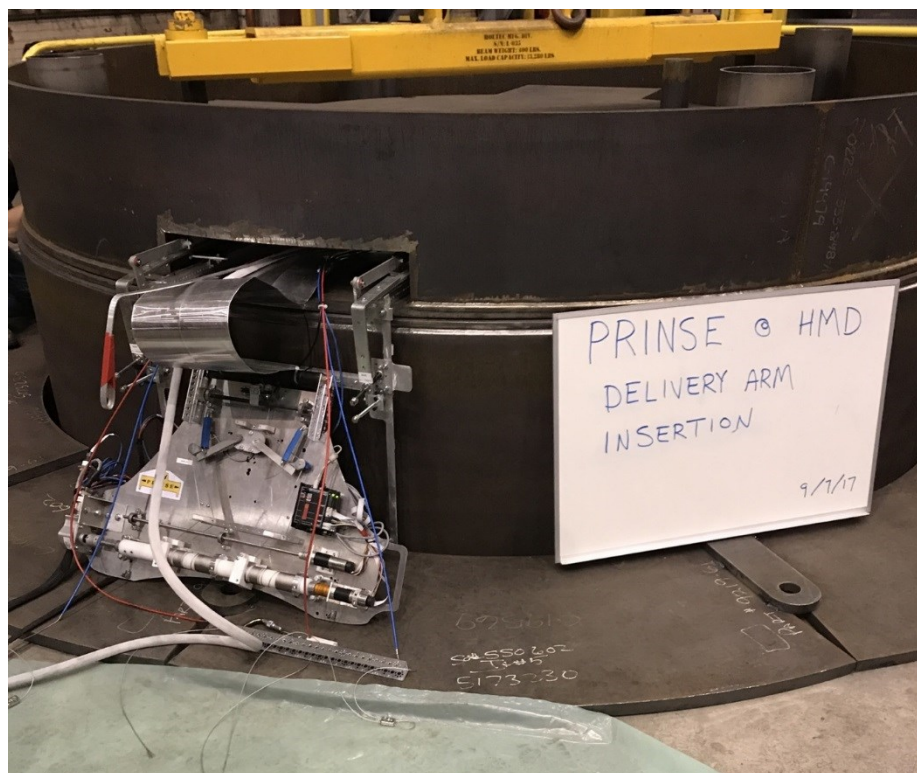
Figure 2.7.7. *Winch connected to vent mount after inserting delivery arm into the outlet vent.*

Figure 2.7.8. Delivery arm deployed on MPC with overpack lid in place.
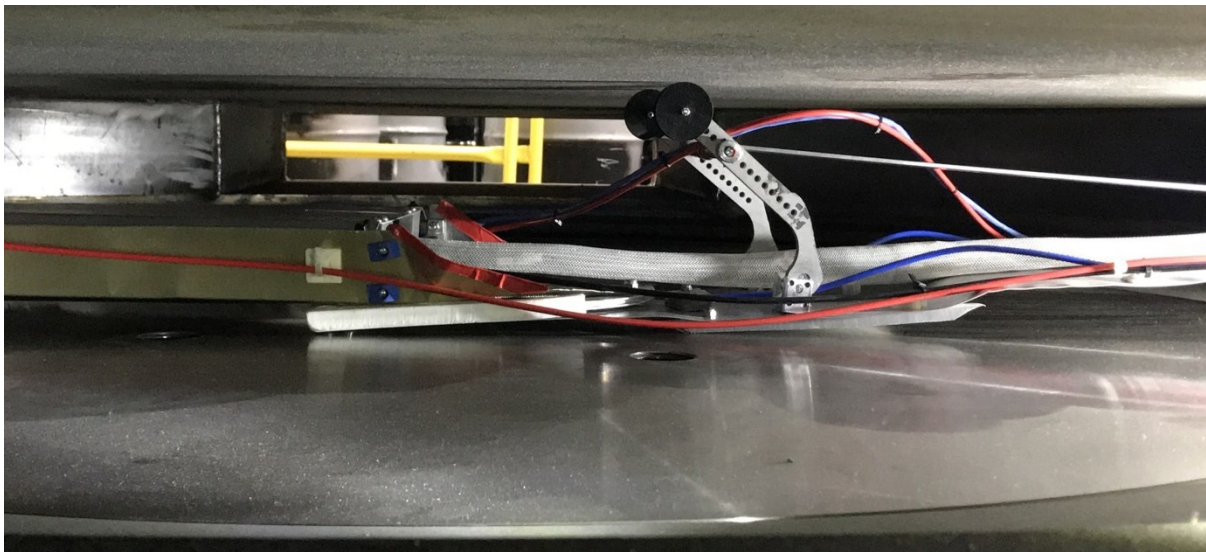
Figure 2.7.9. Support for pivot point on bottom of overpack lid to enable easier motion of end of delivery arm that deploys sensor train into the annulus.

Figure 2.7.10. *PRINSE system team at HMD.*

2.7.2 Final Demonstration – Part II

The robotic inspection systems developed by Penn State, Michigan, Illinois, and South Carolina under a DOE NEUP Integrated Research Project were demonstrated at Penn State on September 26. In the past three years, the robotic inspection systems went from embryonic ideas, through research of unique sensing systems and robotic delivery methods suited to the dry cask storage environment, into system engineering and integration, and finally to prototype fabrication, development, and field testing.

There were 47 people in attendance at the final technology demonstration, representing the project team, the advisory board, DOE labs, the NRC, utilities, vendors, and technology developers. The project team gave presentations that described the functionality of the systems and previewed the live demonstration. Videos showed installation and maneuverability trials of the PRINSE (Proactive Robotic Inspection of Nuclear Storage Enclosures) system in a HI-STORM 100S Version B cask at the Holtec Manufacturing Division.

The dry storage casks have two components: a welded stainless steel canister that confines the spent fuel and a thick concrete-steel overpack structure that encloses the canister. A live demonstration of the system was conducted on a full-height cask mockup, which included a stainless steel section representative of an actual canister shell segment. This demonstration showed: LIBS (laser induced breakdown spectroscopy) for detection of chlorine on the canister surface, EMATs (electromagnetic acoustic transducers) for detection of stress corrosion cracks, a

thermocouple probe to measure the canister surface temperature, a miniature Geiger Mueller tube for measurements of gamma radiation dose. The sensors were delivered via a robotic support system through an outlet vent using a vent-mounted delivery arm. The robotic maneuvers included staging the delivery arm atop the canister lid, and deployment of the sensor train over the edge of the lid in order to travel to the bottom of the canister, and then recovery of the robot back into the delivery arm system atop the canister mock-up.

The objective of the robotic inspections is to provide a means to assess the structural integrity of the dry storage casks in order to recertify independent spent fuel storage installations (ISFSIs) to meet the demands of extended dry storage. Robotic inspection is necessary due to the elevated temperature, radiation dose, and constrained geometry inside the protective overpack. Chlorine deposited on the canister surface could induce stress corrosion cracking of the canister and thus its detection and quantification are important as is the detection of possible cracks. Our LIBS system has detected chlorine levels as low as 10 mg/m^2 on stainless steel using a double pulse laser while remotely delivering the pulses and acquiring data through 25 m of optical fiber. While the audience did not get to see the LIBS system detect chlorine at the time of demonstration, the system was used successfully in the hours just prior to the demonstration. We believe that an additional step to qualify the performance of anti-reflection coatings on the remote optics deployed in the robotic car will resolve the concerns with robustness and reliability of LIBS delivery. The EMAT-based crack detection system is designed to inspect 100% of the canister fabrication welds even though 50% of the weld lines are inaccessible. This is possible because the EMAT system sends shear-horizontal guided waves that propagate circumferentially around the canister creating reflections from cracks, which are detected by the EMAT receiver. Two artificially created crack-like defects just 21% through-wall thickness and 20 mm long located in the welds were observed in the live images during the demonstration. Finally, the deterioration of exterior overpack concrete surfaces is also investigated by our inspection systems. A remote scanning system for exposed concrete surfaces that uses fully air-coupled piezoelectric transducers demonstrated the characterization of microcracks and cracks hidden below the concrete surface, which can provide an early indication of needed maintenance actions.

The presentations and videos are available on a file sharing site. Please Contact Cliff Lissenden (Lissenden@psu.edu) for more information.

2.7.3 Project Timeline

2014

September 29-October 1, Charlotte, NC: Introduce IRP to the community at the Dry Canister
Storage System Nondestructive Evaluation Inspection Workshop sponsored by EPRI
(Lissenden)

December 5, Pittsburgh, PA: Tour the Holtec Manufacturing Division (6 team members)

2015

February 16-17, University Park, PA: Initial Advisory Board meeting (all)

March 15-19, Phoenix, AZ: Present research at Waste Management Conference (Beck)

April 3, Salem, NJ: Visit Hope Creek ISFSI (4 team members)

April 20: Submit technical functions and requirements for the project along with alternatives
analysis

April 24: proposed functions and requirements to the Advisory Board

May 4, Orlando, FL: proposed functions and requirements at the EPRI-sponsored Extended
Storage Collaborative Program meeting (Lissenden)

May 22, University Park, PA: four Toshiba-Westinghouse undergraduate fellows started their
10-week summer program (Melody Strayer, Ishak Johnson, Keith Sponsler, Elias Yishak)

June 9-11, Las Vegas: give technical progress briefing at the DOE Used Fuel Disposition meeting
(Lissenden)

June 30: Darrell Dunn from the Renewals and Materials Branch of the Division of Spent Fuel
Management of the U.S. NRC presented at our full team meeting

July 20: submitted Milestone 6 report on model calibration (Knight)

July 20: re-submitted revised functions and requirements document

September 2-4, Phoenix, AZ: Observe EPRI-organized field demo at Palo Verdi (Leary)

October 20: submitted Milestone 7 report on radiation measurement (Jovanovic)

October 20: determined the maximum size of a robotic sensor car (Brennan team)

November 3, Idaho Falls, ID: project briefing at Fuel Cycle Technologies meeting (Lissenden)

December 1-3, Charlotte, NC: project briefing at the EPRI-sponsored Extended Storage
Collaboration Program meeting (Lissenden)

2016

January 20: submitted Milestone 2 report on sensor selection (Lissenden)

March 21-24, Las Vegas, NV: presented concrete NDI progress at SPIE Smart Materials/NDE
conference (Song)

April 20: submitted Milestone 1 report on fiber delivery of LIBS (Jovanovic)

May 9, University Park, PA: host a visit from NWTRB (Lissenden and Motta)

May 13, University Park, PA: host an Advisory Board meeting on LIBS, EMATS, robotics, and
show the laboratory mock-up

May 17-19, Charlotte, NC: evaluated prototype components of robotic system on NAC cask at
McGuire ISFSI (4 team members)

June 7-9, Las Vegas, NV: presented an IRP update at the DOE Used Fuel Disposition meeting
(Lissenden)

June 14, Charlotte, NC: participated in meeting to discuss seeding flaws in PNNL canister mockup (Lissenden)

July 17-21, Vancouver, CA: presented three peer-reviewed papers at the ASME Pressure Vessels and Piping Conference (Lissenden and McNelly)

July 20: submitted Milestone 5 report on robotic delivery (Brennan)

July 20: submitted Milestone 4 report on concrete NDI (Popovics)

October 20: submitted Milestone 9 on sensors and delivery (all)

October 20: submitted Milestone 8 on the data collection system (Reichard)

October 23-28, Philadelphia, PA: presented concrete NDI progress at the American Concrete Institute (ACI) 2016 Fall Convention (Song)

November 6-10, Las Vegas, NV: presented IRP update at the American Nuclear Society Winter Meeting (Lissenden and Xiao)

November 28-December 2, Honolulu, HI: presented research on noncontact EMATs at Acoustical Society of America conference (Lissenden)

2017

January 2-4, Baxley, GA: visit to Hatch nuclear power plant site to observe used fuel canister inspection (Popovics and Song)

January 20, Ann Arbor, MI: created a double pulse laser setup for LIBS (Jovanovic)

February 8, Pittsburgh, PA: visit Holtec Manufacturing Division to plan final technology demonstration (4 team members)

May 1, Savannah, GA: presented IRP update at EPRI-sponsored Extended Storage Collaboration Program meeting (Lissenden)

May 10, Pittsburgh, PA: robotics and canister NDI teams visited Holtec Manufacturing Division to conduct preliminary tests (6 team members)

May 23-25, Las Vegas, NV: presented IRP update at DOE Spent Fuel and Waste Science and Technology meeting (Lissenden)

June 2, Pittsburgh, PA: canister NDI teams visited Holtec Manufacturing Division to conduct additional tests (Lissenden and Cho)

June 12, San Francisco, CA: presented IRP update at ANS meeting (Motta)

July 13-14 Gaithersburg, MD: concrete NDI team visited NIST facility to conduct tests on ASR concrete samples (Popovics and Song)

July 16-20, Waikaloa, HI: gave two presentations on IRP at the ASME Pressure Vessels and Piping Conference (Cho)

July 16-20, Provo, UT: gave two presentations on IRP at the Review of Progress in Quantitative Nondestructive Evaluation (Lissenden and Popovics)

July 25-27, State College, PA: tested integration of LIBS and robotics systems at Test Track facility (LIBS and robotics teams)

September 5-7, Pittsburgh, PA: Final Technology Demonstration – Part I at HMD (robotics and canister NDI teams)

September 6-9, Washington, DC: presented scanning concrete NDI system at IEEE International Ultrasonics Symposium (Song)

September 12-14, Palo Alto, CA: presented characterization of distributed cracks in concrete research at the International Workshop on Structural Health Monitoring (Song)

September 26, State College, PA: Final Technology Demonstration – Part II at Test Track (all)

September 27-28 Gaithersburg, MD: concrete NDI team visited NIST facility to conduct follow up tests on ASR concrete samples (Popovics and Song)

October 3-4, State College, PA: presented robotic inspection system to the International Center for Actuators and Transducers (Lissenden)

October 20: submitted Milestone 3 report on canister NDI (Lissenden)

October 20: submitted Milestone 10 report on the final technology demonstration (all)

2018

March 19-20 Gaithersburg, MD: concrete NDI team visited NIST facility to conduct follow up tests on ASR concrete samples (Popovics and Song)

3. ACCOMPLISHMENTS

Over the course of the project, we have met the ten milestones that we initially laid out:

M1. Demonstrate that photonic bandgap fiber delivery of LIBS/RS based compositional analysis can detect salt residue on a stainless steel plate. Report Date: Y2Q2 (3/30/16).

M2. Make selection between EMAT and MST for canister NDI. Report Date: Y2Q1 (12/30/15).

M3. Benchmark EMAT/MST sensors with respect to bulk wave ultrasonics and eddy current methods. Report Date: Y3Q4 (9/30/17).

M4. Validate data analysis schemes to characterize concrete degradation, given air-coupled sensor data. Report Date: Y2Q3 (6/30/16).

M5. Demonstrate the guided wand robotic system mobility and positional tracking in lab mockups of dry storage systems. Report Date: Y2Q3 (6/30/16).

M6. Calibrate radiation transport and thermal modeling with accepted standards. Report Date: Y1Q3 (6/30/15).

M7. Demonstrate fiber-based dosimeter capability. Report Date: Y1Q4 (9/30/15).

M8. Verify that the data collection system stores data in an efficient useful manner. Report Date: Y2Q4 (9/30/16).

M9. Demonstrate sensor delivery and data acquisition with the guided wand robotic system. Report Date: Y2Q4 (9/30/16).

M10. Demonstrate the multisensory robotic system within dry storage mockups provided by our industrial partners. Report Date: Y3Q4 (9/30/17).

In summary, we have developed, built, and demonstrated the proactive robotic inspection of nuclear storage enclosures (PRINSE) system for vertical axis dry storage casks. The double pulse laser-induced breakdown spectroscopy (LIBS) system takes advantage of an optical fiber to deliver intense light to the canister surface that enables surface composition characterization in-situ in real time. Chlorine concentrations as low as 10 mg/m^2 were detected on stainless steel. Additionally, a simpler laser setup was created to detect sodium as a surrogate for chlorine and sodium was detectable when the chlorine concentration was as low as 0.5 mg/m^2. The electromagnetic acoustic transducers (EMATs) enable detection of stress corrosion cracks. The EMATs generate shear-horizontal waves that propagate around the canister and are reflected by cracks enabling 100% of the canister weld lines to be inspected. The EMAT-based crack detection system was tested at the Pacific Northwest National Laboratory on a canister containing blind defects and was shown to detect the crack sizes it was designed to detect. In addition, a miniature

Geiger-Muller radiation sensor was constructed, as was a thermocouple-based canister surface temperature probe.

The novel marsupial robotic system was designed specifically for the HI-STORM family of spent nuclear fuel storage casks. The command center and winch outside the cask control the delivery arm and train of cars that traverse the outside of the canister from the cask ventilation system. The sensors are housed in the cargo bays of three cars that comprise the train, which is lowered to the bottom of the canister by the winch. Encoders on the winch enable the sensors to be delivered to a prescribed location, e.g., for re-inspection of a problem area. The PRINSE system is designed for an elevated temperature and gamma radiation environment, although not all components of the prototype are made from the final materials. The PRINSE system was tested on a full canister that was placed inside a HI-STORM cask at the Holtec Manufacturing Division. It was also demonstrated on a full-height mockup at Penn State to a live audience.

Two different approaches for nondestructive inspection of horizontal and vertical axis types of concrete overpack systems are developed. A fully contactless air-coupled scanning ultrasonic test platform and a frequency-wavenumber domain data analysis method are used for horizontal concrete overpack systems. Analysis, numerical simulation and experimental results demonstrate that distributed cracks in concrete can be detected and cracked regions localized within a scanned region of concrete. In a separate effort, a semi-coupled test platform and a guided wave attenuation-based data analysis method are used for vertical overpack systems. Analysis, numerical simulation and experimental results show that the bonding conditions of steel-concrete interfaces can be quantitatively characterized using the guided wave signal analysis scheme.

PART III. FUTURE DIRECTIONS

While the project team met all milestones and exceeded our own expectations in some areas (e.g., sensitivity of LIBS to chlorides), there is still room for significant further development. Our goal was to build a working prototype, which was accomplished. However, there is a still much effort to transform the working prototype into a reliable product for commercial use. One task is the definition of key geometric tolerances for commonly-used casks to ensure the suitability of the PRINSE system to the full range of vertical-axis casks throughout the country. Another task is to develop data registration methods specific to cask inspection that allow year-to-year comparisons. These data could be used to assist the spent nuclear fuel community in the definition of recertification procedures for independent spent fuel storage installations.

Future work for the LIBS subsystem should include future optimization on chlorine concentration resolution with a larger concentration window. The final optics design works as fully intended, though iterative system integration should address the need for strain relief on the optic fibers. Finally, a means of easily keeping the final optics clear of plasma debris should be implemented.

The crack detection capabilities of the EMAT-based subsystem would be improved by mounting EMATs that send and receive shear-horizontal ultrasonic waves in the axial direction to complement the current circumferential waves system. Sending waves in the axial direction would improve detection reliability, improve robot position localization based on end-wall echoes from the top of the canister, and identify any robot mis-orientation angles. It could potentially be accomplished by using separate orthogonal coils on the same magnet array to minimize space. The EMAT coil design could also be optimized for specific send and receive functions. Likewise, the use of the wrap-around wave signals to complement the short-range weld-line data would provide another means of redundancy and increase reliability.

The data collection speed of the contactless concrete NDI system can be further improved by integrating the current ultrasonic scanning system to a mobile robotic platform and incorporating a compressed sensing technology. Compressed sensing is a convex optimization-based mathematical process to reconstruct a full data sets from a sparsely and randomly sampled data sets within the domain of interest. Although the multi-channel MEMS sensor array enables data collection of large data sets, it still takes nontrivial time duration to collect ultrasonic wavefield signal sets across a large inspection area. A compressed sensing approach based on convex optimization would enable a significant decrease in the data acquisition time by reducing the total number of spatial sampling points. Furthermore, the mobile robotic platform would make it easier to move the scanning system one local inspection region to another.

The robotic delivery subsystem improvements include tether management, using temperature and radiation resistant cables, cooling the cameras and radiation sensor, and shielding the cameras in the car. In order to stay within budget and allow for quick design changes, many parts and components of the system were 3D printed out of PLA plastic. However, the design allows these parts to be printed out of PEEK or ULTEM for radiation and heat resistance, allowing easy replacement of these components. Due to budget constraints, the data cables, power cables, and

pneumatic lines running inside the tether to the sensor cars were not radiation or temperature resistant. For loaded cask inspection, these would need to be replaced by suitably rated components, which may require special manufacturing and long lead times. General small parts reliability, such as safety wiring bolts and screws, would also be required.

The prototype PRINSE system has separate control systems for robot maneuvering, LIBS system measurements, and EMAT measurements in order to allow maximum flexibility during development of these systems. However, for commercial use it is preferred to have the entire PRINSE system controlled by a single computer. Thus, three control systems would be integrated into one. Moreover, the modular design of PRINSE enables complementary sensing systems such as eddy current arrays and a hygrometer to be added.

All of the above future directions are related to the PRINSE system being used for in-service nondestructive inspection. The potential exists that stress corrosion cracks are identified, which would require decision-making regarding whether the canister needs to be replaced, repaired, the degradation mitigated, or that the cracks not yet severe enough to warrant action. Such decision-making requires full characterization of the extent of cracking (length and depth). One significant future direction is to extend the crack detection capabilities of the PRINSE system to crack characterization capabilities. The PRINSE system is the only technology capable of in-service inspection of 100% of the canister weld lines for stress corrosion cracking. The novelty of the PRINSE system is that it uses ultrasonic shear-horizontal waves to inspect behind guide channels that obstruct direct access to the canister surface. If the system can be extended from crack detection to crack characterization, then it serves as enabling technology for in-service repair and mitigation. Without full in-service inspection capabilities, in-service repair and mitigation methods are moot. With full in-service inspection capabilities, the PRINSE system could be further extended to perform mitigation by laser welding or cold spray methods.

PART IV. LIST OF PUBLICATIONS

4.1. Patents

The team presented numerous progress reports to the advisory board, the EPRI ESCP community, the DOE, ANS, and the NWTRB throughout the course of the project (as listed in the Project Timeline). Because we disclosed our intellectual property in these updates we have not filed any patent applications.

4.2. Journals

1. S. Choi, H. Cho, C.J. Lissenden, 2018, "Nondestructive inspection of spent nuclear fuel storage canisters using shear horizontal guided waves," *Nuclear Engineering Technology*, Vol. 50, pp. 890-898.

2. S. Choi, H. Cho, M. Lindsey, C.J. Lissenden, 2018, "Electromagnetic acoustic transducers for robotic nondestructive inspection in harsh environments," *Sensors* Vol. 18, 193.

3. D.G. Fobar, X. Xiao, M. Burger, S. Le Berre, A.T. Motta, I. Jovanovic, "Robotic delivery of laser-induced breakdown spectroscopy for sensitive chlorine measurement in dry cask storage systems," submitted for publication.

4. X. Xiao, S. Le Berre, D.G. Fobar, M. Burger, P.J. Skrodzki, K.C. Hartig, A.T. Motta, I. Jovanovic, 2018, "Measurement of chlorine concentration on steel surfaces via fiber-optic laser-induced breakdown spectroscopy in double-pulse configuration," *Spectrochimica Acta Part B: Atomic Spectroscopy*, Vol. 141, pp. 44-52.

5. S. Choi, H. Cho, M. Lindsey, C.J. Lissenden, 2018, "Electromagnetic acoustic transducers for robotic nondestructive inspection in harsh environments," *Sensors* Vol. 18, 193.

6. X. Xiao, S. Le Berre, K. Hartig, A. Motta, I. Jovanovic, 2017, "Surrogate measurement of chlorine concentration of steel surfaces by alkali element detection via laser-based breakdown spectroscopy," *Spectrochimica Acta Part B: Atomic Spectroscopy*, Vol. 130, pp. 67-74.

7. C.J. Lissenden, S. Choi, H. Cho, I. Jovanovic, A. Motta, K. Hartig, X. Xiao, S. Le Berre, S. Brennan, K. Reichard, R. Leary, B. McNelly, 2017, "Toward robotic inspection of dry storage casks for spent nuclear fuel," *ASME J. Pressure Vessel Technology*, Vol. 139, 031602.

8. S. Choi, H. Cho, C.J. Lissenden, 2017, "Selection of shear horizontal wave transducers for robotic nondestructive inspection in harsh environments," *Sensors*, Vol. 17, 5.

9. S. Ham, H. Song, M.L. Oelze, J.S. Popovics, 2017, "A contactless ultrasonic surface wave approach to characterize distributed cracking damage in concrete," *Ultrasonics*, Vol. 75, pp. 46-57.

10. H. Song, J.S. Popovics, 2017, "Characterization of steel-concrete interface bonding conditions using attenuation characteristics of guided waves," *Cement and Concrete Composites*, Vol. 83, pp. 111-124.

Proceedings

11.   J. Bracken, S. Brennan, I. Van Sant, C. Lissenden, K. Reichard, "Nuclear storage cask inspection robotics as a case study in system design challenges," In: Proceedings of the ASME 2018 International Mechanical Engineering Congress and Exhibition, IMECE2018-88374.

12.   J. Bracken, S. Brennan, C. Lissenden, T. Simpson, I. Van Sant, K. Reichard, M. Ng, "Change propagation during prototyping: a case study of a robotic inspection system for dry nuclear waste storage casks," In: Proceedings of the ASME 2018 International Design Engineering Technical Conferences & Computers and Information in Engineering Conference, DETC2018-86283.

13.   C.J. Lissenden, I. Jovanovic, A.T. Motta, X. Xiao, S. Le Berre, D. Fobar, H. Cho, S. Choi, 2018, "Remote detection of stress corrosion cracking: surface composition and crack detection," In: *Review of Progress in Quantitative Nondestructive Evaluation*, Vol. 37, D.E. Chimenti, L.J. Bond, Eds., American Institute of Physics Proc. 1949, 110003.

14.   H. Cho, S. Choi, M.S. Lindsey, C.J. Lissenden, 2017, "Electromagnetic acoustic transducer (EMAT) development for nondestructive inspection of spent nuclear fuel storage canisters," In: *Proceedings of the ASME 2017 Pressure Vessels & Piping Conference*, ASME International, PVP2017-65926.

15.   H. Song, J. Park, J.S. Popovics, 2017, "Development of an automated contactless ultrasonic scanning measurement system for wavefield imaging of concrete elements," Ultrasonics Symposium (IUS), 2017 IEEE International, Washington D.C.

16.   H. Song, J.S. Popovics, 2017, "Characterization of distributed cracks in concrete using randomly scattered wavefield extraction," Structural Health Monitoring 2017, F.K. Chang and F. Kopsaftopoulos, Eds.

17.   C.J. Lissenden, A.T. Motta, S. Brennan, K. Reichard, I. Jovanovic, T. Knight, J. Popovics, 2016, "Development of robotic multisensory inspection system for used nuclear fuel canisters," *Transactions of the American Nuclear Society,* Vol. 115, pp. 201-204.

18.   X. Xiao, S. Le Berre, K. Hartig, A. Motta, I. Jovanovic, 2016, "Quantitative Determination of Chlorine Concentration by Measurement of Sodium Deposited on Steel Via Laser-Induced Breakdown Spectroscopy," *Transactions of the American Nuclear Society,* Vol. 115, pp. 205-207.

19.   S. Choi, H. Cho, M.S. Lindsey, C.J. Lissenden, 2016, "Surface crack detection in welded stainless steel canisters using shear horizontal waves," *Proceedings of the ASME 2016 Pressure Vessels & Piping Conference*, ASME International, Paper PVP2016-63311.

20.   C.J. Lissenden, S. Choi, H. Cho, A. Motta, I. Jovanovic, K. Hartig, X. Xiao, S. Le Berre, S. Brennan, K. Reichard, R. Leary, B. McNelly, 2016, "Robotic inspection of dry storage casks for spent nuclear fuel," *Proceedings of the ASME 2016 Pressure Vessels & Piping Conference*, ASME International, Paper PVP2016-63312.

21.   H. Song, J. Popovics, 2016, "Hidden disbond detection in spent nuclear fuel storage systems using air-coupled ultrasonics," SPIE Proceedings Volume 9803, 980331.

Prepared a section (4.15) in EPRI Report 3002010617 entitled, "Extended Storage Collaboration Program (ESCP): Nondestructive Evaluation Subcommittee – Industry Progress Report" dated October 2017.

4.3. Theses

1. Ian Van Sant, 2018, "Design and fabrication of a nuclear dry cask inspection robot: integrating laser induced breakdown spectroscopy and electromagnetic active transducer measurement methods," M.S. thesis in Mechanical Engineering, Penn State, University Park, PA.
2. Jennifer Brackens, 2018, "The C+C DSM method: managing change propagation while prototyping a robotic inspection system for dry nuclear waste storage casks," M.S. thesis in Mechanical Engineering, Penn State, University Park, PA.
3. Noah Shandelman, B.S. honors thesis in Mechanical Engineering, May 2017.
4. Samuel Le Berre, Remote detection of corrosive environment integrated in a multi-sensor robot for dry storage safety assessment, M.S. in Nuclear Engineering, May 2017.
5. Xuan Xiao, Sensitive quantification of chlorine on steel surfaces via fiber-optic laser-induced breakdown spectroscopy, M.S. in Nuclear Engineering, May 2017.
6. C.R. Priest, Dosimetry, Activation, and Robotic Instrumentation Damage Modeling of the Holtec HI-STORM 100 Spent Nuclear Fuel System, M.S. Thesis, University of South Carolina, 2016.
7. Jacob Beck, A combined approach to localization for a nuclear cask inspection robot, B.S. honors thesis in Mechanical Engineering, May 2016.
8. Brendan McNelly, Design of a nuclear inspection robot: considering dimensional, force, sensor packaging, and thermal constraints, M.S. in Mechanical Engineering, December 2015.

4.4. Presentations

1.   C.J. Lissenden, "Robotic inspection of stainless steel vessels with SH waves from EMATs," *NDE Conference and Exhibition on Non-Destructive Evaluation 2017*, Chennai, India, 14-16 December, 2017, (Invited).

2.   C.J. Lissenden, "DOE NEUP IRP: PRINSE proactive robotic inspection of nuclear storage enclosures," *EPRI Extended Storage Collaboration Program*, Charlotte, North Carolina, 14-16 November, 2017.

3.   C.J. Lissenden, "Robotic Multisensor System for Inspection of Dry Storage Casks for Used Nuclear Fuel," *International Center for Actuators and Transducers*, State College, Pennsylvania, 3-4 October, 2017, (Invited).

4.   H. Song, J. Park, J.S. Popovics, 2017, "Contactless ultrasonic wavefield imaging of concrete elements using an automated scanning MEMS ultrasonic sensor array," Ultrasonics Symposium (IUS), 2017 IEEE International, Washington D.C.

5. C.J. Lissenden, I. Jovanovic, A. Motta, X. Xiao, S. Le Berre, D. Fobar, H. Cho, S. Choi, "Remote detection of stress corrosion cracking: surface composition and crack detection," *Review of Progress in Quantitative Nondestructive Evaluation*, Provo, Utah, July 16-20, 2017.

6. C.J. Lissenden, S. Choi, H. Cho, I. Jovanovic, A. Motta, X. Xiao, S. Le Berre, S. Brennan, K. Reichard, I. Van Sant, M. Zugger, "Robotic inspection system for spent nuclear fuel canisters," *ASME Pressure Vessels and Piping Conference*, Waikoloa, Hawaii, July 16-20, 2017.

7. H. Cho, S. Choi, M. Lindsey, C.J. Lissenden, "Electromagnetic acoustic transducer (EMAT) development for nondestructive inspection of spent nuclear fuel canisters," *ASME Pressure Vessels and Piping Conference*, Waikoloa, Hawaii, July 16-20, 2017.

8. A.T. Motta, "Multisensor inspection and robotic systems for dry cask storage," *American Nuclear Society Conference Symposium on Advanced Instrumentation and Monitoring Methods for Dry Storage of Spent Nuclear Fuel*, San Francisco, California, June 12, 2017.

9. C.J. Lissenden, "Approaching multisensory inspection and robotic systems for dry cask storage," *Department of Energy Spent Fuel and Waste Science and Technology Working Group Meeting*, Las Vegas, Nevada, May 23-25, 2017.

10. C.J. Lissenden, "Multisensory inspection and robotic systems for dry cask storage," *EPRI Extended Storage Collaboration Program Meeting*, Savannah, Georgia, May 1, 2017.

11. K.M. Reichard, C.J. Lissenden, "Systems and Structures Health Management Technical Group Update," *Center for Acoustics and Vibration Annual Workshop*, State College, Pennsylvania, April 25-26, 2017.

12. C.J. Lissenden, "Electromagnetic acoustic transducers for nondestructive inspection of dry storage canisters for used nuclear fuel," *IEEE Richland Section Meeting*, Pacific Northwest National Laboratory, Richland, Washington, February 1, 2017. (invited)

13. H. Cho, S. Choi, M. Lindsey, C.J. Lissenden, "Electromagnetic acoustic transducers for nondestructive inspection of dry storage canisters for used nuclear fuel," *5th Joint meeting of the Acoustical Society of America and the Acoustical Society of Japan*, Honolulu, Hawaii, November 28-December 2, 2016.

14. C.J. Lissenden, A.T. Motta, S. Brennan, K. Reichard, I. Jovanovic, T. Knight, J. Popovics, "Development of robotic multisensory inspection system for used nuclear fuel canisters," *American Nuclear Society Winter Meeting*, Las Vegas, Nevada, November 6-10, 2016.

15. X. Xiao, S. Le Berre, K. Hartig, A. Motta, I. Jovanovic, "Quantitative Determination of Chlorine Concentration by Measurement of Sodium Deposited on Steel Via Laser-Induced Breakdown Spectroscopy," *American Nuclear Society Winter Meeting*, Las Vegas, Nevada, November 6-10, 2016.

16. C.J. Lissenden, S. Choi, H. Cho, A. Motta, I. Jovanovic, K. Hartig, X. Xiao, S. Le Berre, S. Brennan, K. Reichard, R. Leary, B. McNelly, "Robotic inspection of dry storage casks for spent nuclear fuel," *ASME Pressure Vessels and Piping Conference*, Vancouver, Canada, July 17-21, 2016.

17. S. Choi, H. Cho, M.S. Lindsey, C.J. Lissenden, 2016, "Surface crack detection in welded stainless steel canisters using shear horizontal waves," *ASME Pressure Vessels and Piping Conference*, Vancouver, Canada, July 17-21, 2016.

18. C.J. Lissenden, "Multi-Sensor Inspection and Robotic Systems for Dry Storage Casks an Integrated Research Project," *Used Fuel Disposition Campaign Working Group Meeting*, Las Vegas, Nevada, June 7-9, 2016. (invited)

19. H. Song, J. Popovics, "Hidden disbond detection in spent nuclear fuel storage systems using air-coupled ultrasonics," SPIE Smart Structures and Materials + NDE and Health Monitoring, Las Vegas, Nevada, March 21-24, 2016.

20. C.J. Lissenden, "Multi-Sensor Inspection and Robotic Systems for Dry Storage Casks," *Extended Storage Collaboration Program Meeting*, Electric Power Research Institute, Charlotte, North Carolina, December 1-3, 2015. (invited)

21. C.J. Lissenden, "Multi-Sensor Inspection and Robotic Systems for Dry Storage Casks: an integrated research project sponsored by NEUP," *Department of Energy Fuel Cycle Technologies Annual Meeting*, Idaho National Lab, Idaho Falls, Idaho, November 3-5, 2015. (invited)

22. C.J. Lissenden, "IRP: Multi-Sensor Inspection and Robotic Systems for Dry Storage Casks," *Used Fuel Disposition Campaign Working Group Meeting*, Las Vegas, Nevada, June 9-11, 2015. (invited)

23. K.M. Reichard, C.J. Lissenden, "Systems and Structures Health Management Technical Group Update," *Center for Acoustics and Vibration Annual Workshop*, State College, Pennsylvania, May 5-6, 2015.

24. C.J. Lissenden, "Multi-sensor inspection and robotic systems for dry storage casks: functions and requirements," *Extended Storage Collaboration Program Meeting*, Orlando, Florida, May 4, 2015. (invited)

25. J. Beck, C.J. Lissenden, "Magnetostrictive transducers for nondestructive inspection of used fuel canisters in dry storage," *Waste Management Conference*, Phoenix, Arizona, March 15-19, 2015.

26. C.J. Lissenden, "Multi-Sensor Inspection and Robotic Systems for Dry Storage Casks," *Extended Storage Collaboration Program Meeting*, Electric Power Research Institute, Charlotte, North Carolina, December 1-3, 2015. (invited)

27. C.J. Lissenden, "Multi-Sensor Inspection and Robotic Systems for Dry Storage Casks: an integrated research project sponsored by NEUP," *Department of Energy Fuel Cycle Technologies Annual Meeting*, Idaho National Lab, Idaho Falls, Idaho, November 3-5, 2015. (invited)

28. C.J. Lissenden, "Multi-sensor inspection and robotic systems for dry storage casks," *EPRI 2014 Dry Canister Storage System NDE Inspection Workshop*, Charlotte, North Carolina, September 29-October 1, 2014. (invited)

29. C.J. Lissenden, "Multi-sensor inspection and robotic systems for dry storage casks," *Penn State Nuclear Engineering Seminar Series*, September 18, 2014. (invited)

Multi-Sensor Inspection and Robotic Systems for Dry Storage Casks

U.S. DEPARTMENT OF
ENERGY
Nuclear Energy

OVERVIEW

Purpose: Develop sensors, monitoring methodologies, and a delivery system to ensure safe dry storage of used nuclear fuel. A robotic device and new sensing systems are proposed to monitor for conditions conducive to stress corrosion cracking and inspect for cracks within dry storage casks. The multi-sensor inspection robotic system will be designed to access the canister surface through the ventilation system of the overpack.

Objectives: The robotic system will enable a broad range of measurements to be made through a common, multi-sensor interface for characterization and inspection methods, including: surface sampling via laser induced breakdown spectroscopy (LIBS) delivered by optical fiber, nondestructive inspection using linear and nonlinear ultrasonics, ultrasonic surface waves for the concrete overpack, and environmental sensing – temperature, relative humidity, ionizing radiation.

IMPACT

Logical Path:

Sensor Development

Overpack NDI · Canister NDI · Surface Composition

Robotic System

Model/Measure Environment

Data

Technology Integration and Demonstration

Outcomes: Robotic system traverses the dry storage cask ventilation system with sensors to measure temperature, radiation, surface composition, and damage. LIBS and EMAT sensors to characterize surface composition (chlorides) and cracking (especially stress corrosion cracks). System was demonstrated on Holtec HI-STORM 100S cask.

DETAILS

Principal Investigator: Cliff Lissenden
Institution: Penn State
Collaborators: UIUC, USC, UM, ORNL, PNNL, EPRI, Holtec
Duration: 36 months
Total Funding Level: $3,000,000
TPOC: Steve Marschman
Federal Manager: JC de la Garza
Workscope: IRP-FC-1

PICSNE Workpackage #:
NU-14-PA-PSU_-0401-01
Project 14-7356
DE-NE0008266

RESULTS

Results and Accomplishments: The Proactive Robotic Inspection of Nuclear Storage Enclosures (PRINSE) system prototype was built and tested on mockups and a production HI-STORM 100S Version B cask. The LIBS system integrated into the PRINSE system detected a chlorine concentration of 10 mg/m² on stainless steel. The crack detection system based on shear-horizontal ultrasonic waves was blind-tested on a mockup at PNNL. Over the course of the project we gave 28 presentations at meetings and conferences, published 10 journal articles and 11 proceedings papers, completed 6 Master of Science theses and 2 undergraduate honors theses.

PART VI. OTHER RELEVANT INFORMATION

<u>Faculty (7)</u>: Cliff Lissenden, Arthur Motta, Sean Brennan, Karl Reichard, Igor Jovanovic, John Popovics, Travis Knight

<u>ARL Staff (2)</u>: Mike Zugger, Ryan Weichel

<u>Post-docs (1)</u>: Sungho Choi

<u>Grad students (16)</u>:
Penn State: Hwanjeong Cho, ESM; Lu Chen, NE; Kyle Hartig, NE; Xiao Xuan, NE; Samuel Le Berre, NE; Bobby Leary, ME; Brendan McNelly, ME; Ian Van Sant, ME; Jen Bracken, ME
University of Michigan: Dave Fobar, NE; Milos Burger, NE; Patrick Skrodzki, NE
University of South Carolina: Kyle Singer, NE; Charles Priest, NE; Thomas Martin, NE
University of Illinois Urbana Champagne: Homin Song, CE

<u>Undergraduates (17)</u>:
Penn State: Ishak Johnson, NE; Brendan Sporer, NE; Jacob Beck, ME; Chad Lani, ME, Yewon Hwang, ME; Chris Velez, ME; Mike Gehrsitz, ME; John Ominski, ME; Matt Ng, ME; Franz Card, ME; Noah Shandelman, ME
Cedarville: Melody Strayer, ME; Valerie Martin, ME
North Carolina State University: William Murray, NE
Missouri University of Science and Technology, Keith Sponsler,
University of South Carolina, Kyle Singer, ME; Nathaniel Cooper, ME
University of Maryland, Elias Yishak, ME

Appendix A

A.1 CAD Images of Total Assembly
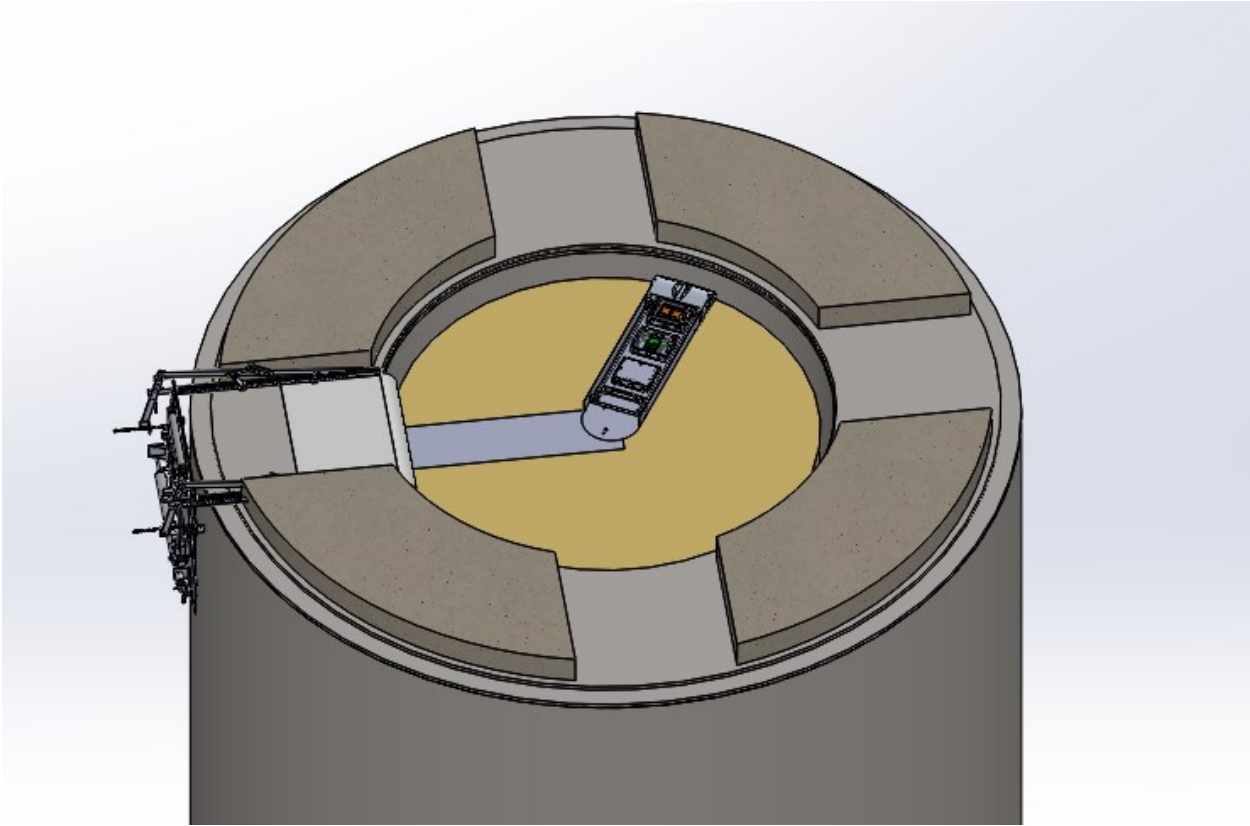
Figure A.1. *The robotic inspection system CAD model of the cask, sensor cars, insertion arm, vent mount, and winch. Note the cask lid components have been hidden so the whole robot system is visible. The insertion arm is shown in a bent position.*
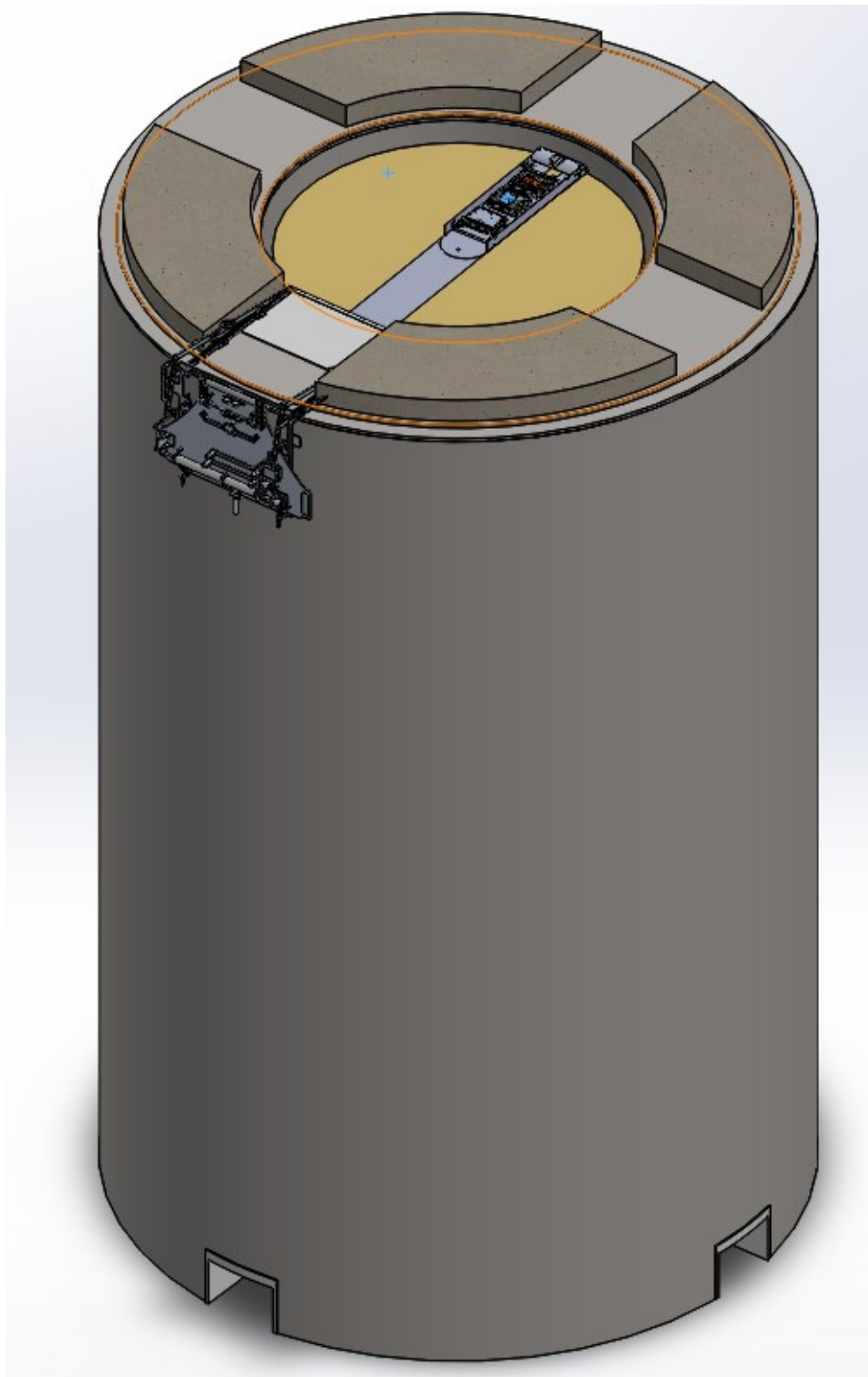
Figure A.2. *The robotic inspection system CAD model of the cask, sensor cars, insertion arm, vent mount, and winch, with the lower portion of the overpack visible. The insertion arm is deployed in the straight position atop the canister, within the overpack.*
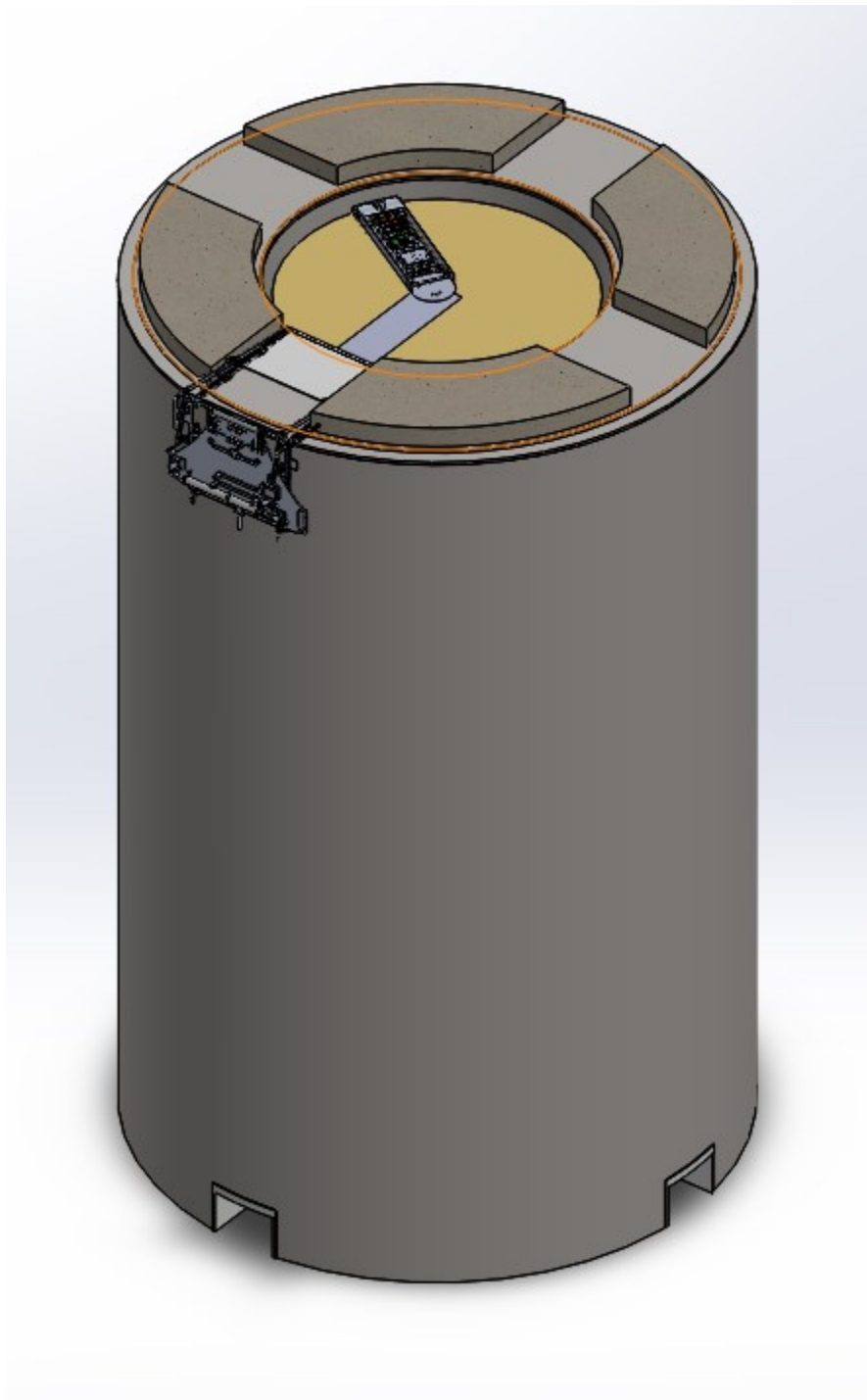
Figure A.3. *The robotic inspection system CAD model, as in the previous figure, except the insertion arm is deployed in a bent position.*
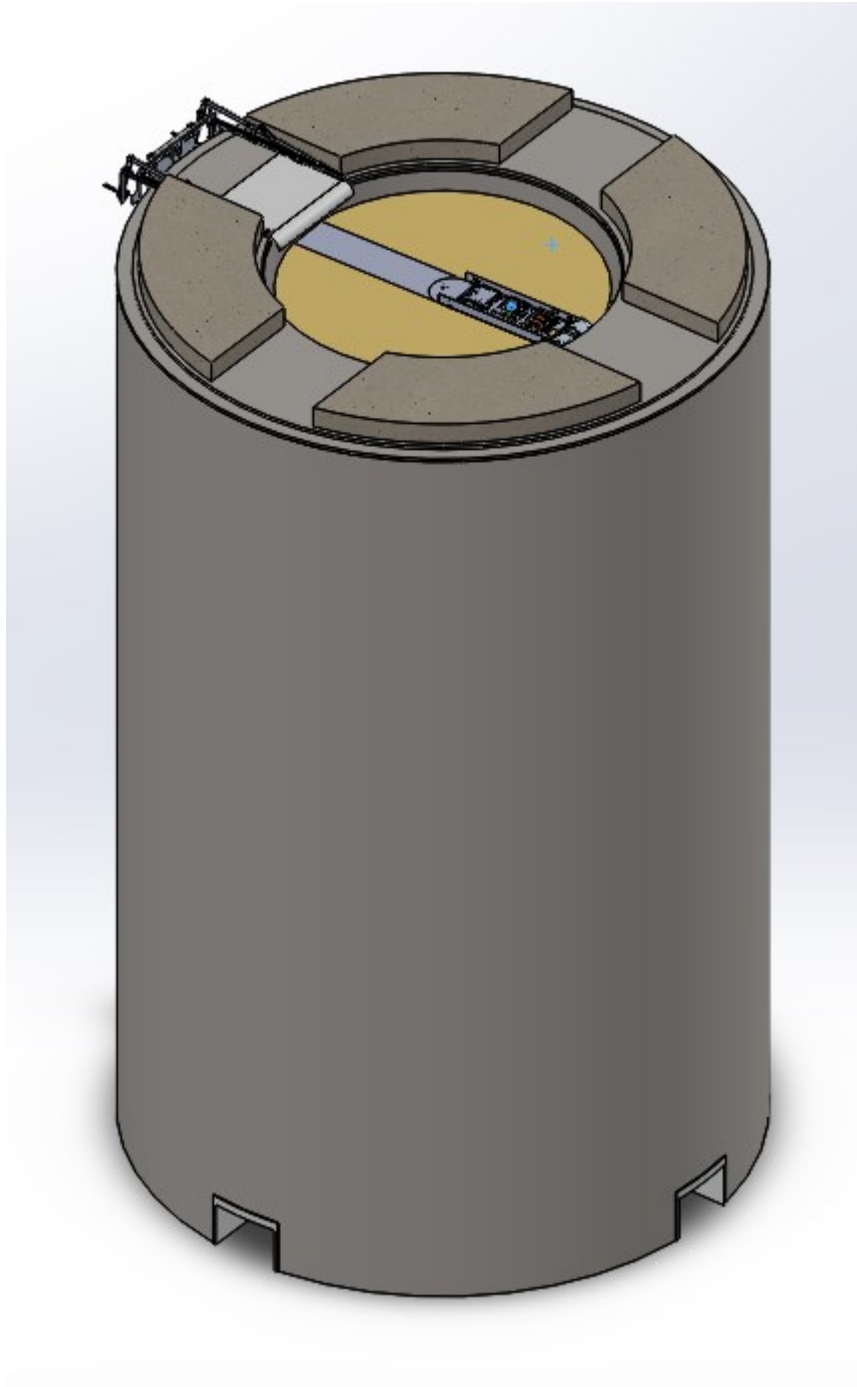
Figure A.4. *The robotic inspection system CAD model of the cask, as in the previous two figures, except the insertion arm is deployed in the straight position, and the system is turned so the internal edge of the vent mount system is visible.*
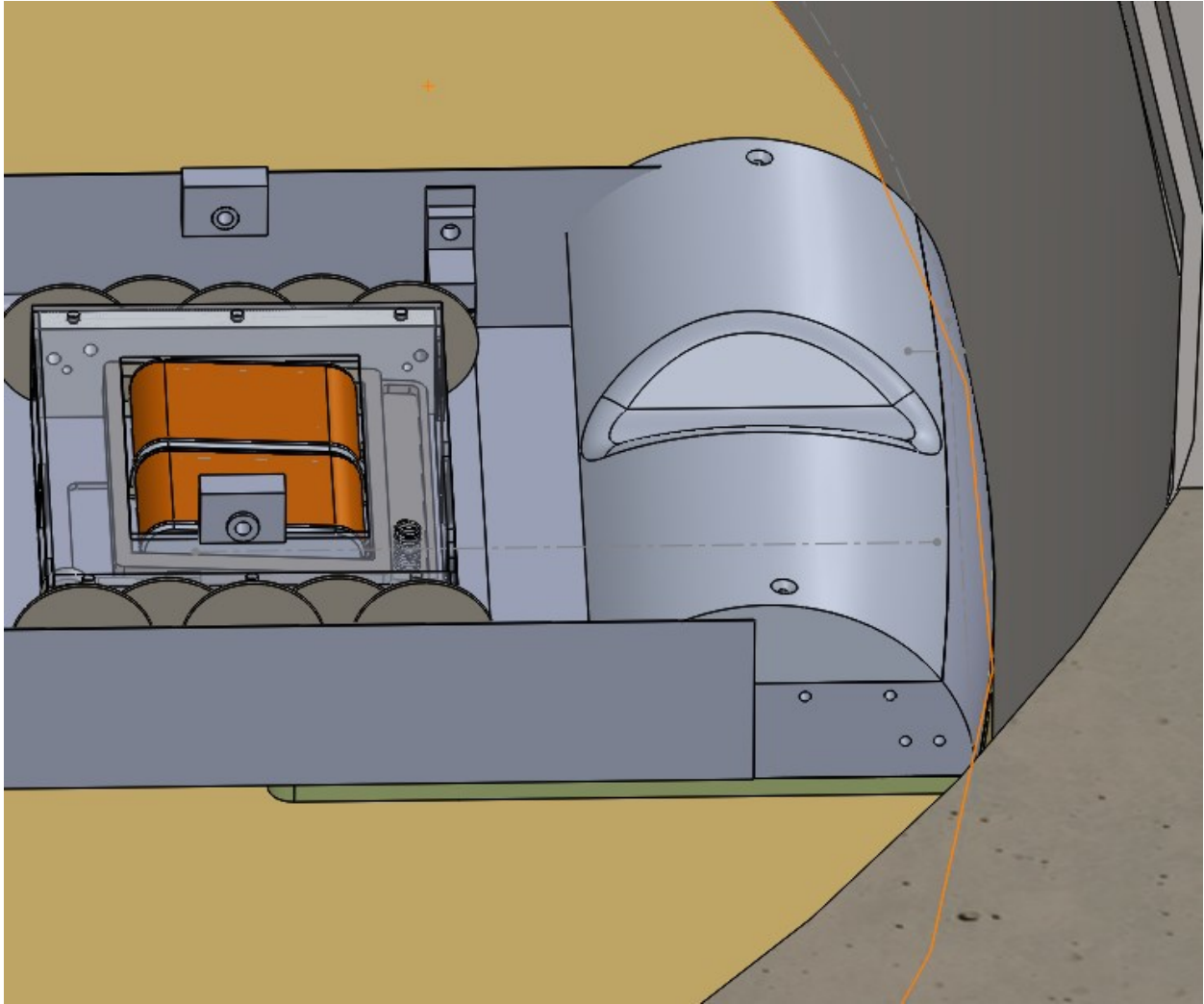
Figure A.5. *The robotic inspection system CAD model is shown here with a close-up view of the sensor cars and insertion arm. The hump on the end of the arm is used to prevent wedging and jamming.*

A.2 CAD Images of the Sensor Car Train
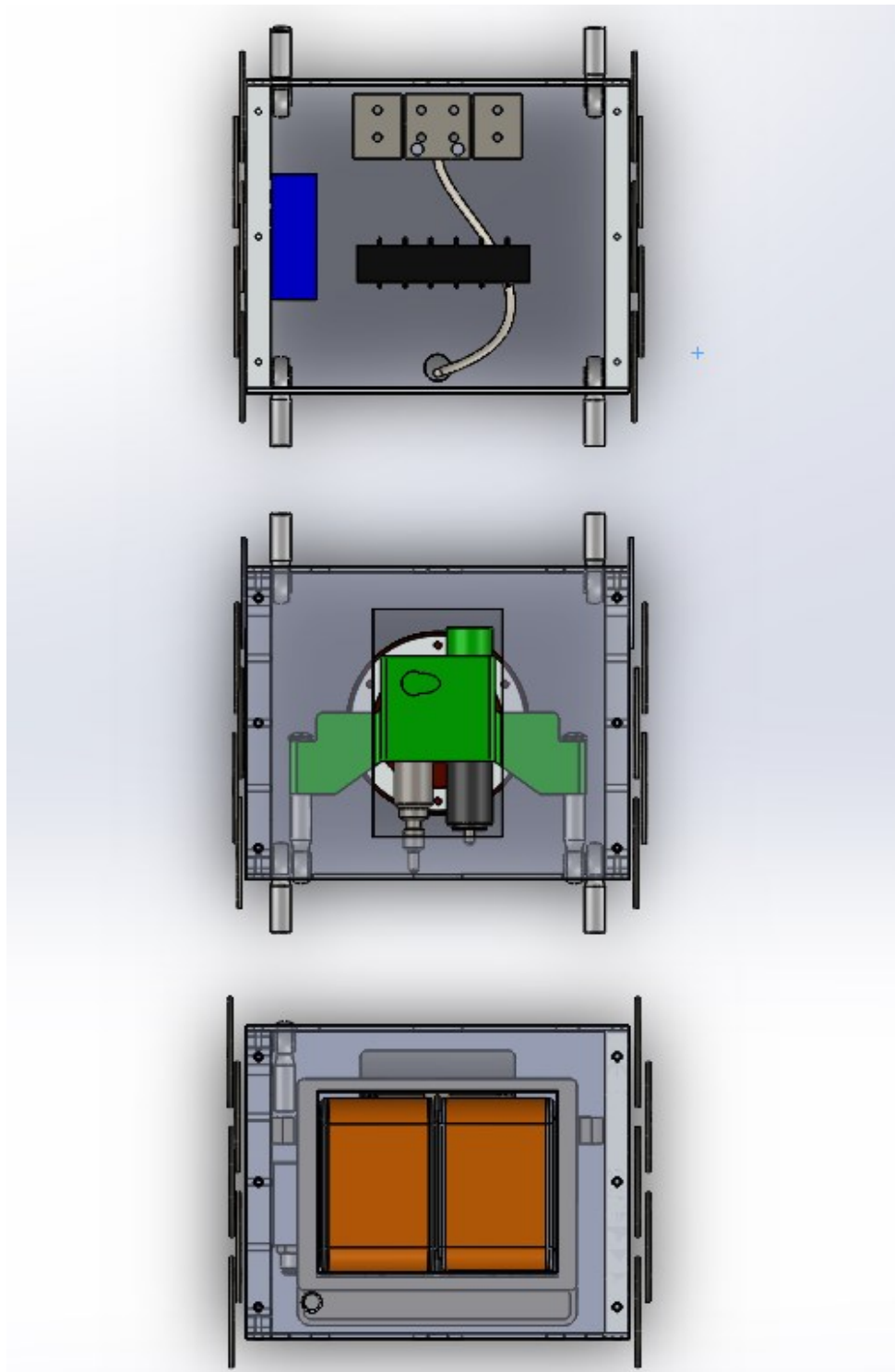
Figure A.6. *The sensor car train CAD model top view.*
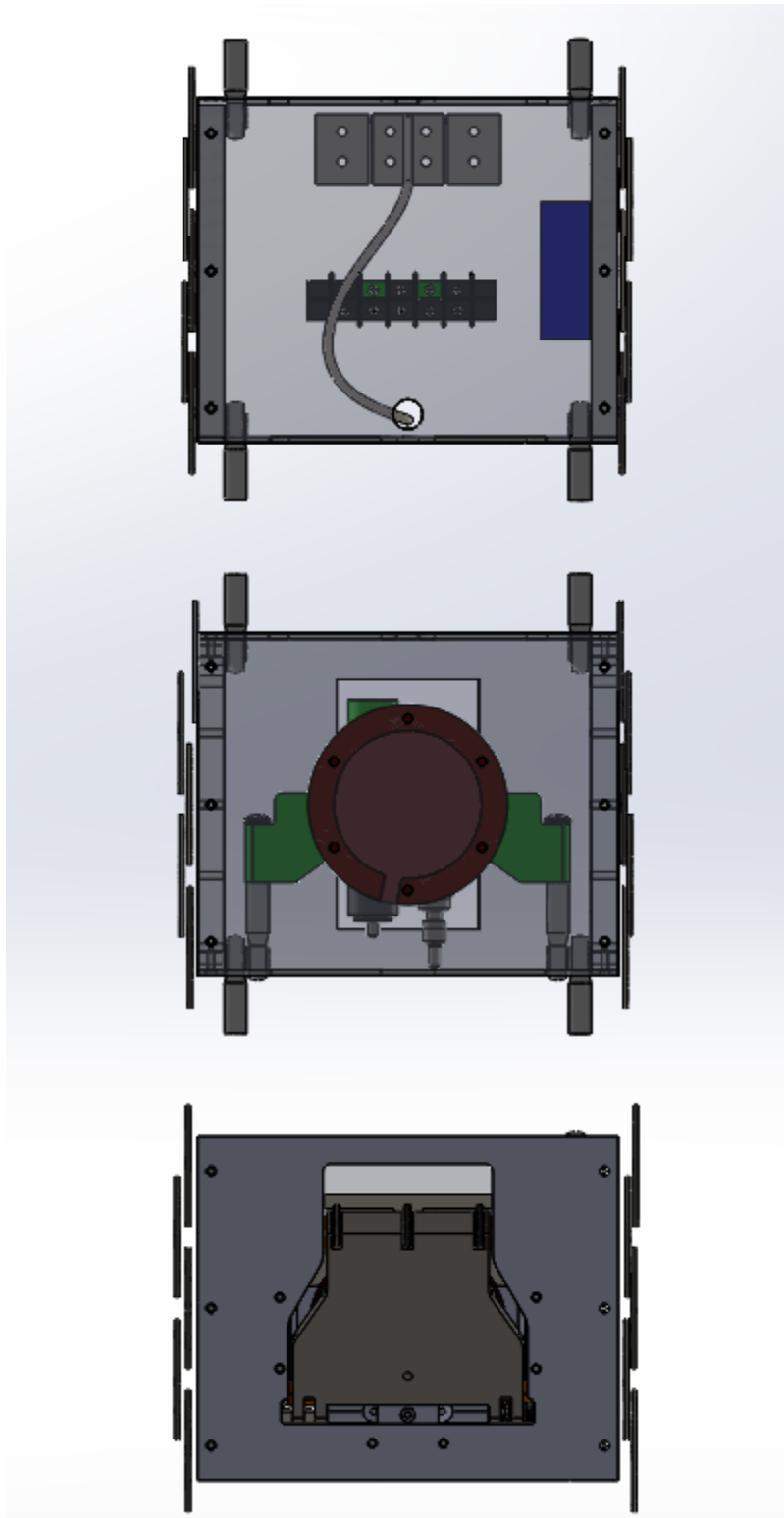
Figure A.7. *The sensor car train CAD model bottom view.*
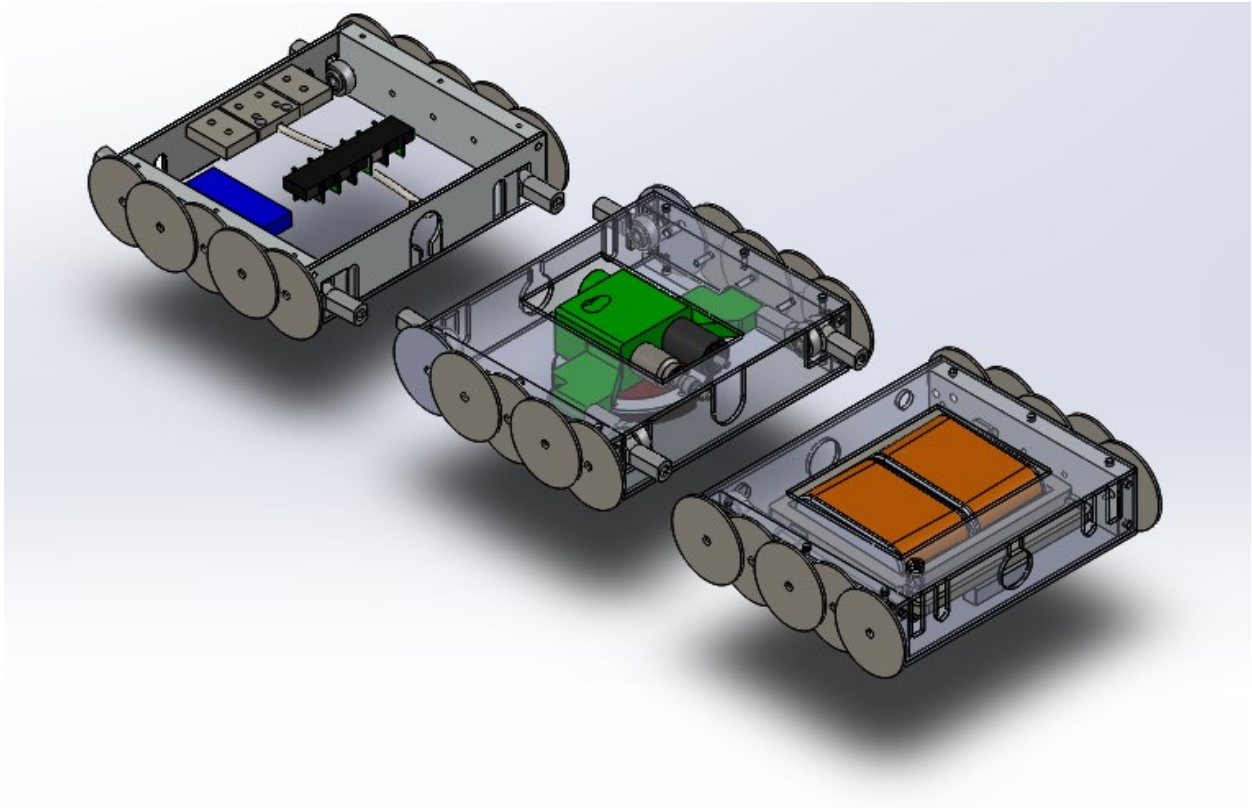
Figure A.8. *The sensor car train CAD isometric view.*
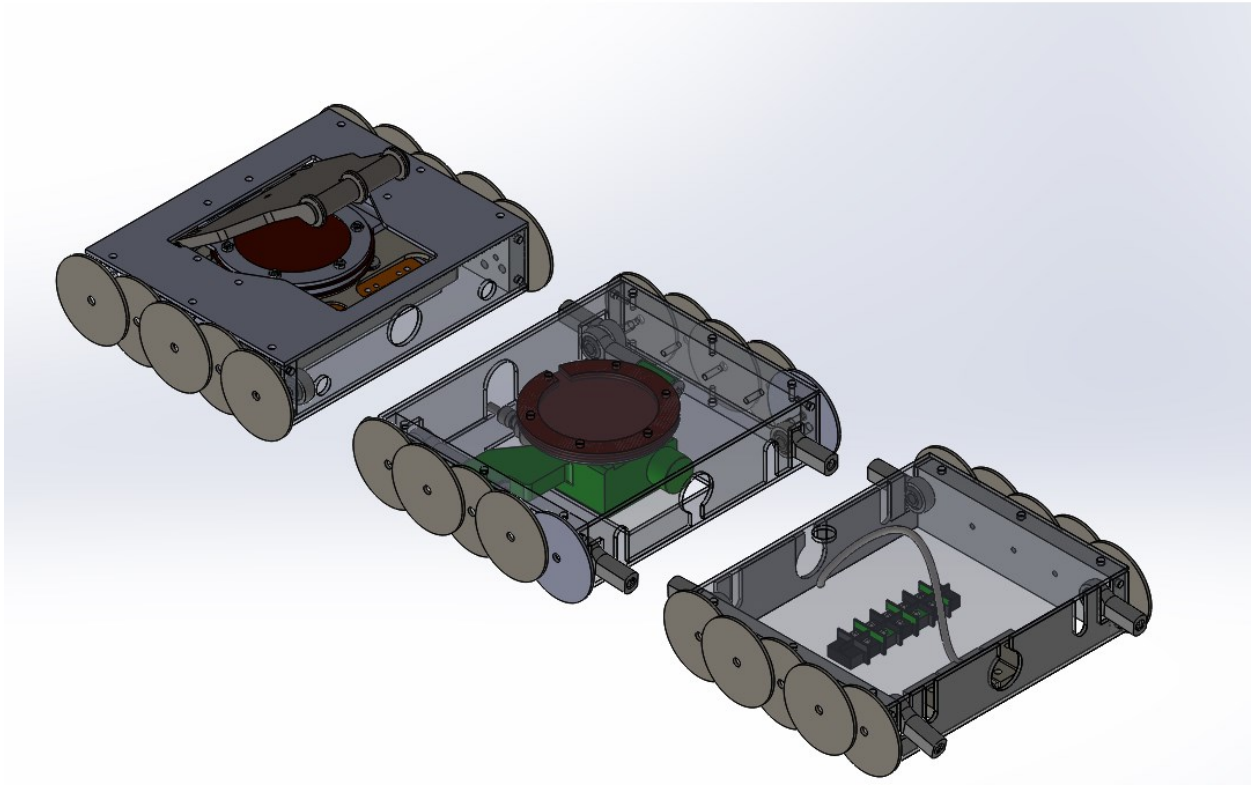
Figure A.9. *The sensor car train CAD model bottom isometric view.*

A.3 CAD Images of the Cask
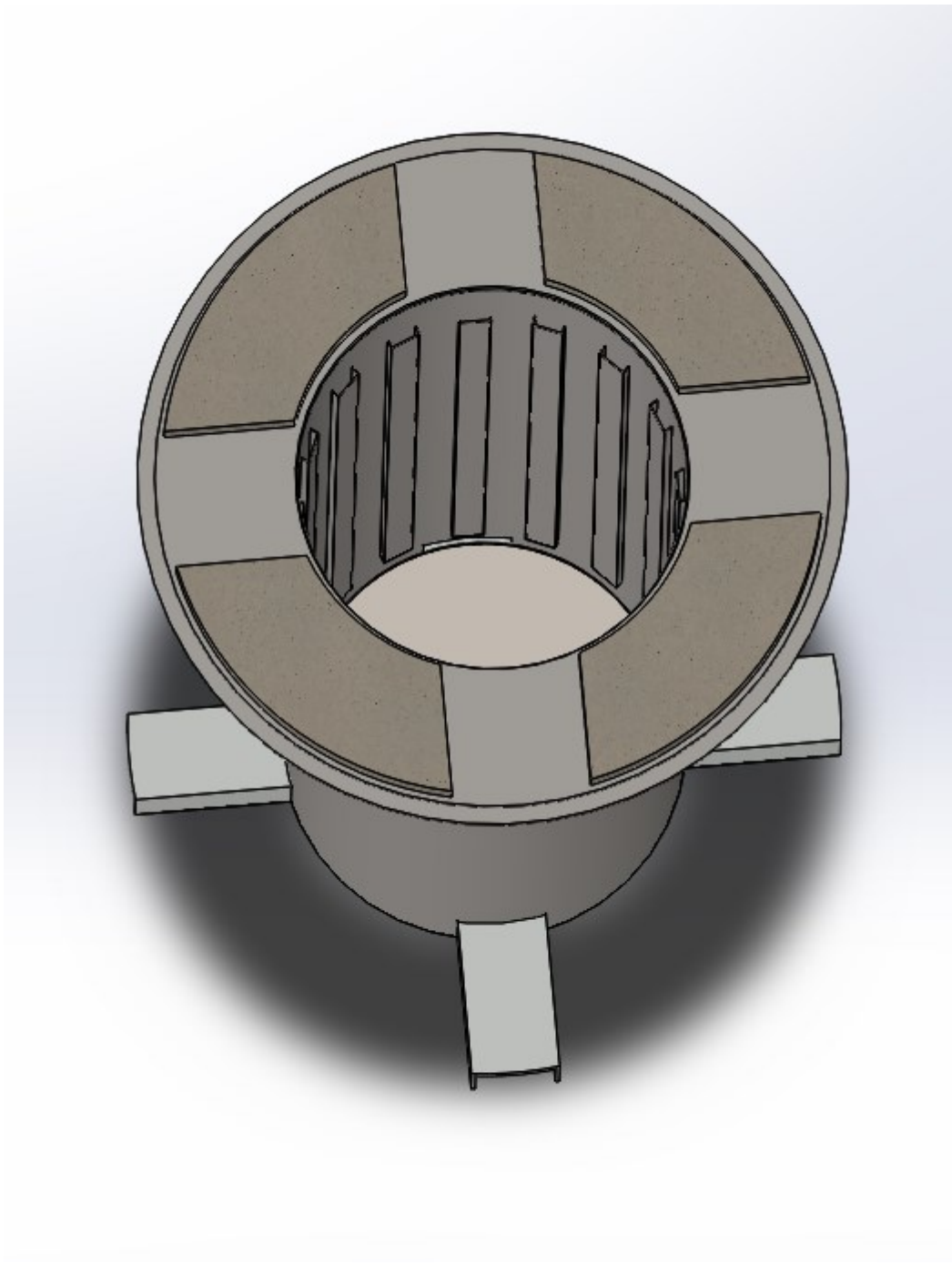
Figure A.10. *The interior components of the cask, including the vents and guide channels, with the exterior concrete portion hidden.*
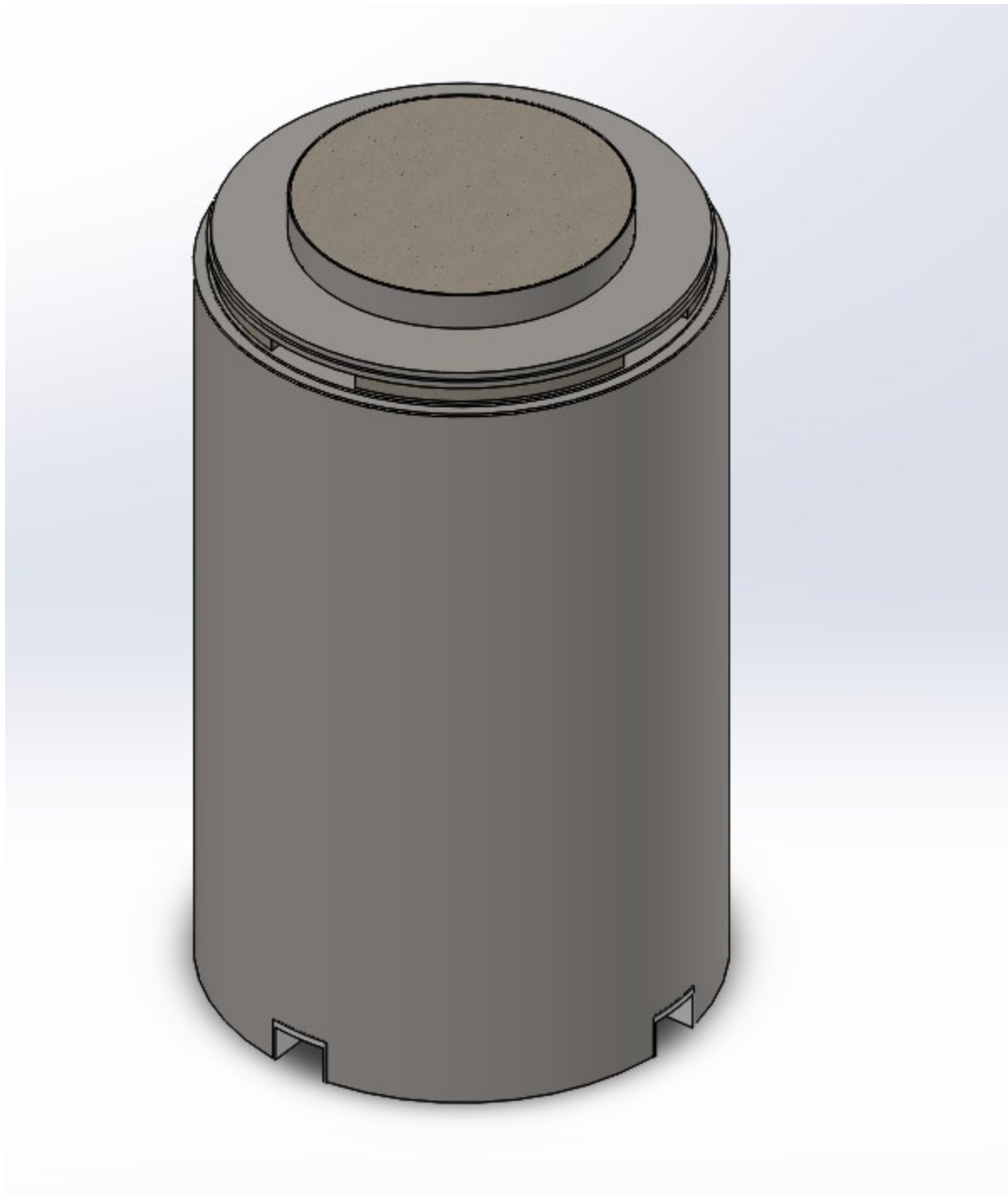
Figure A.11. *The entire CAD model of the cask.*
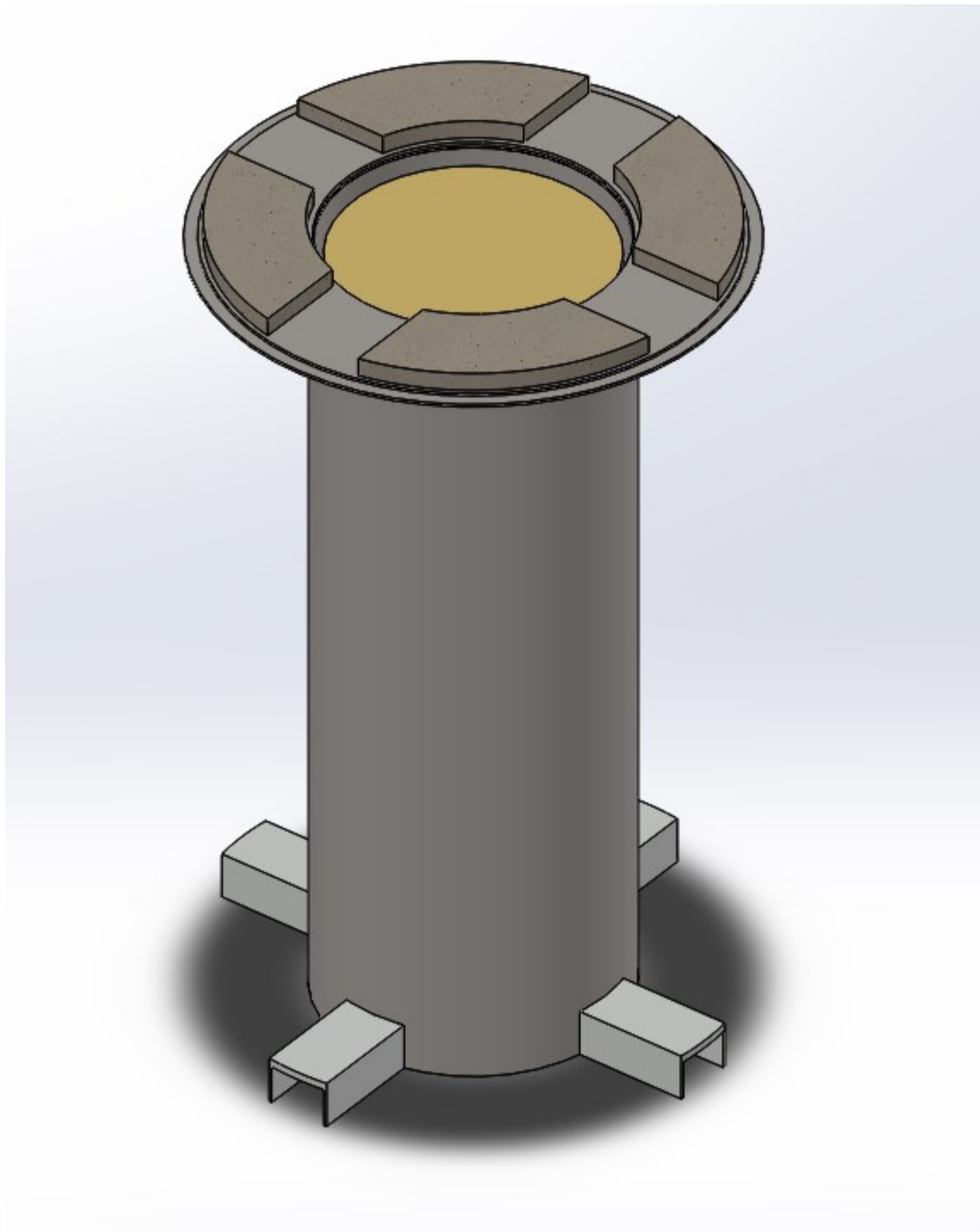
Figure A.12. *The internal CAD model of the cask with the internal lid visible.*
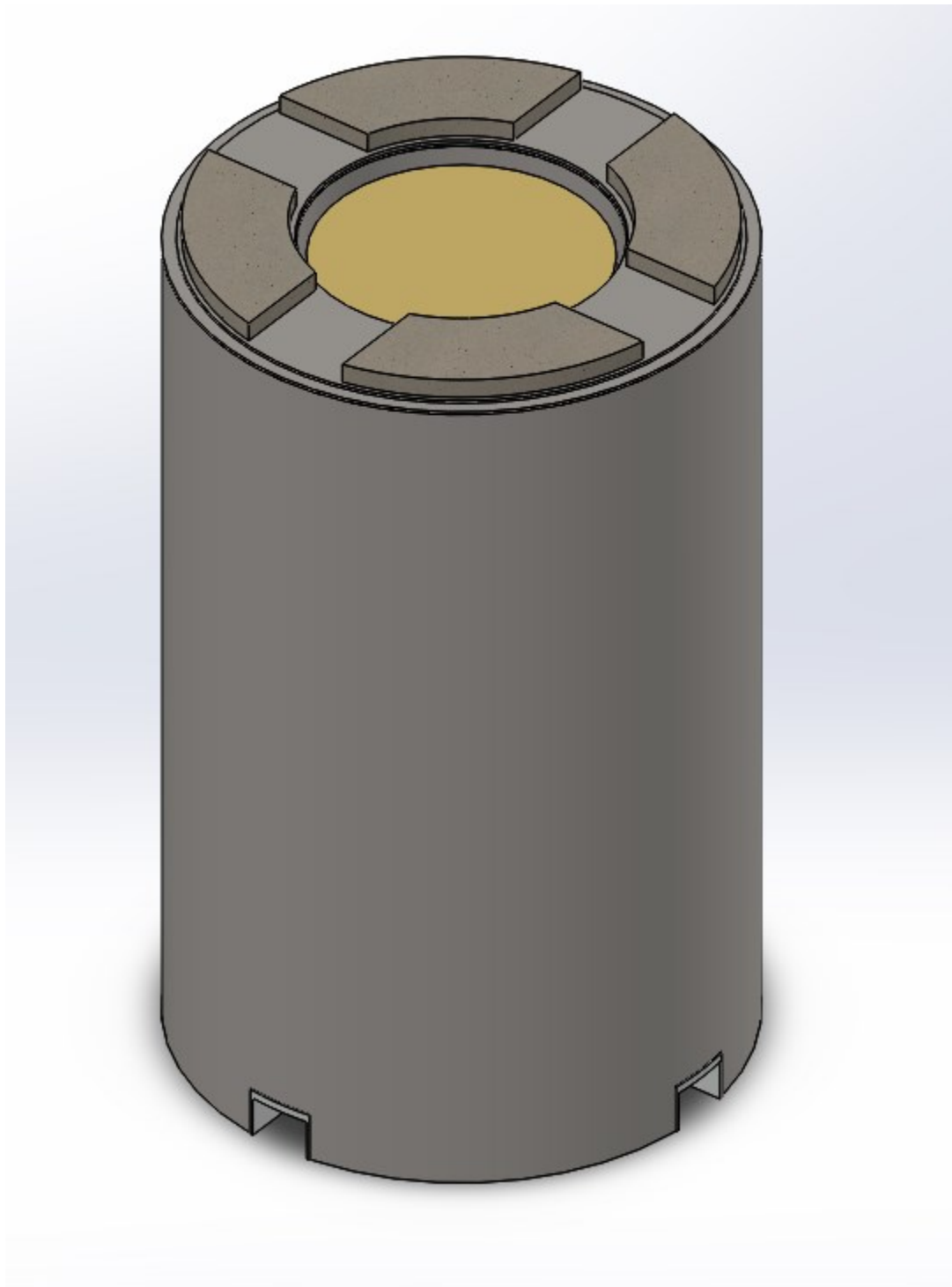
Figure A.13. *The entire CAD model of the cask, with the lid removed.*

A.4 CAD Images of the Vent Mount
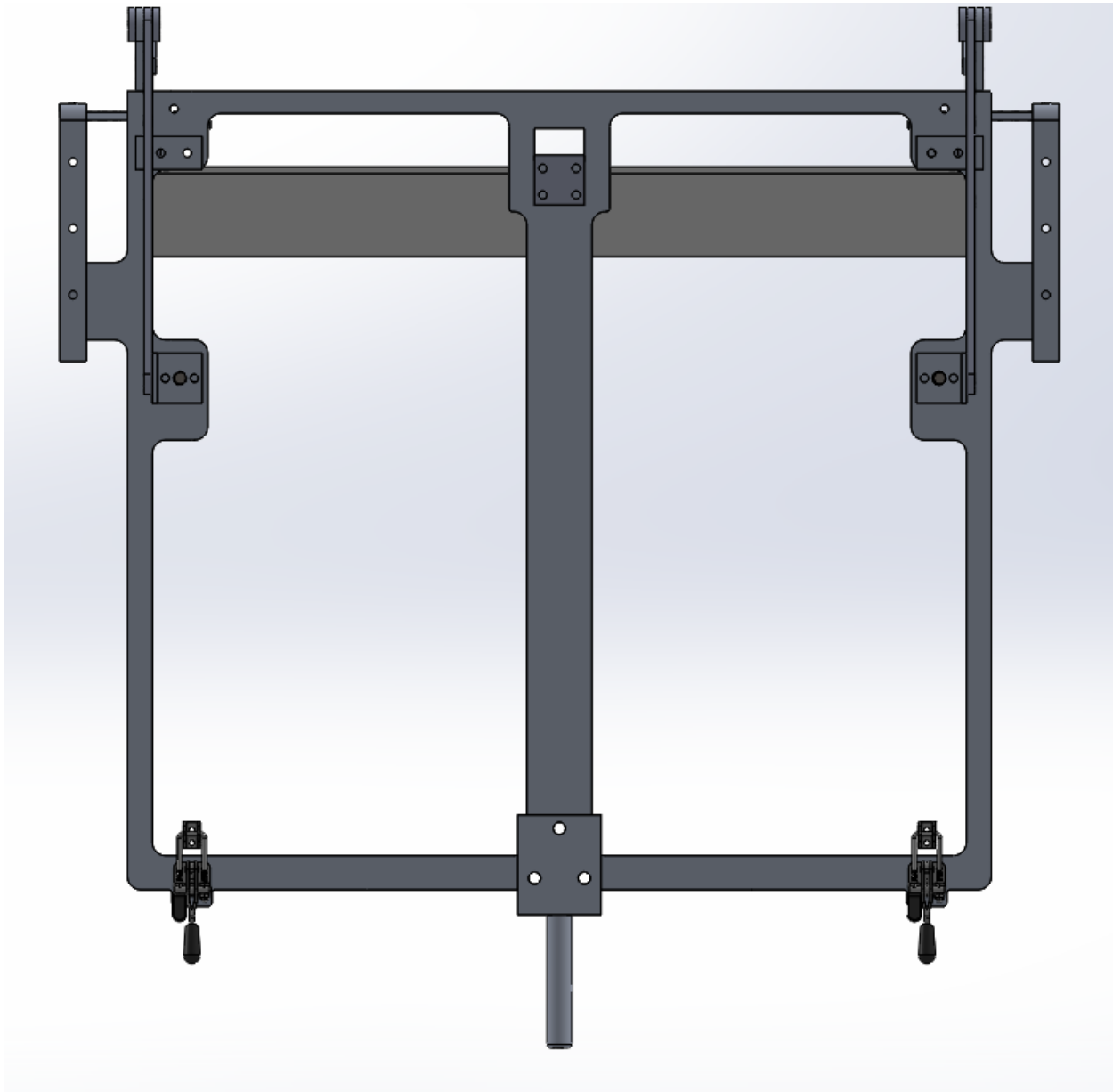
Figure A.14. *The vent mount frame, side view.*
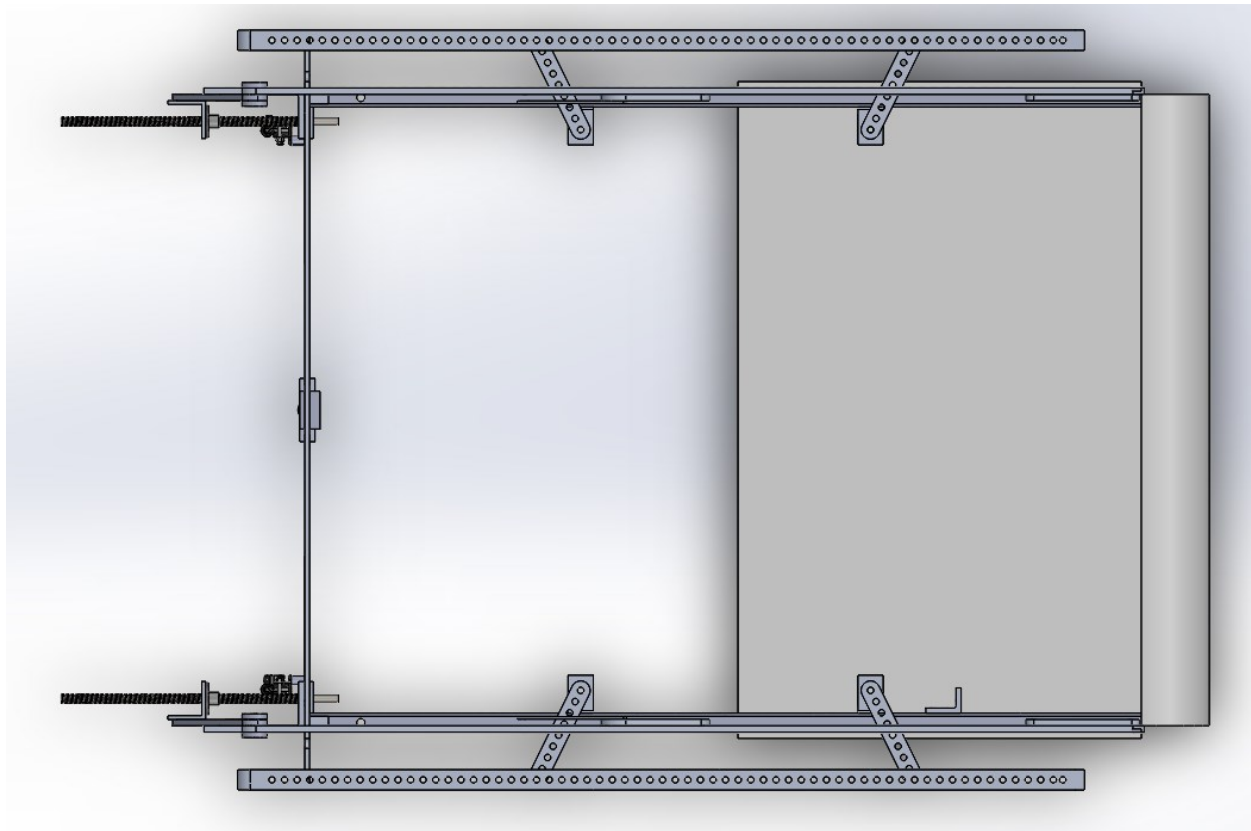
Figure A.15. *The top view of the vent mount CAD model.*
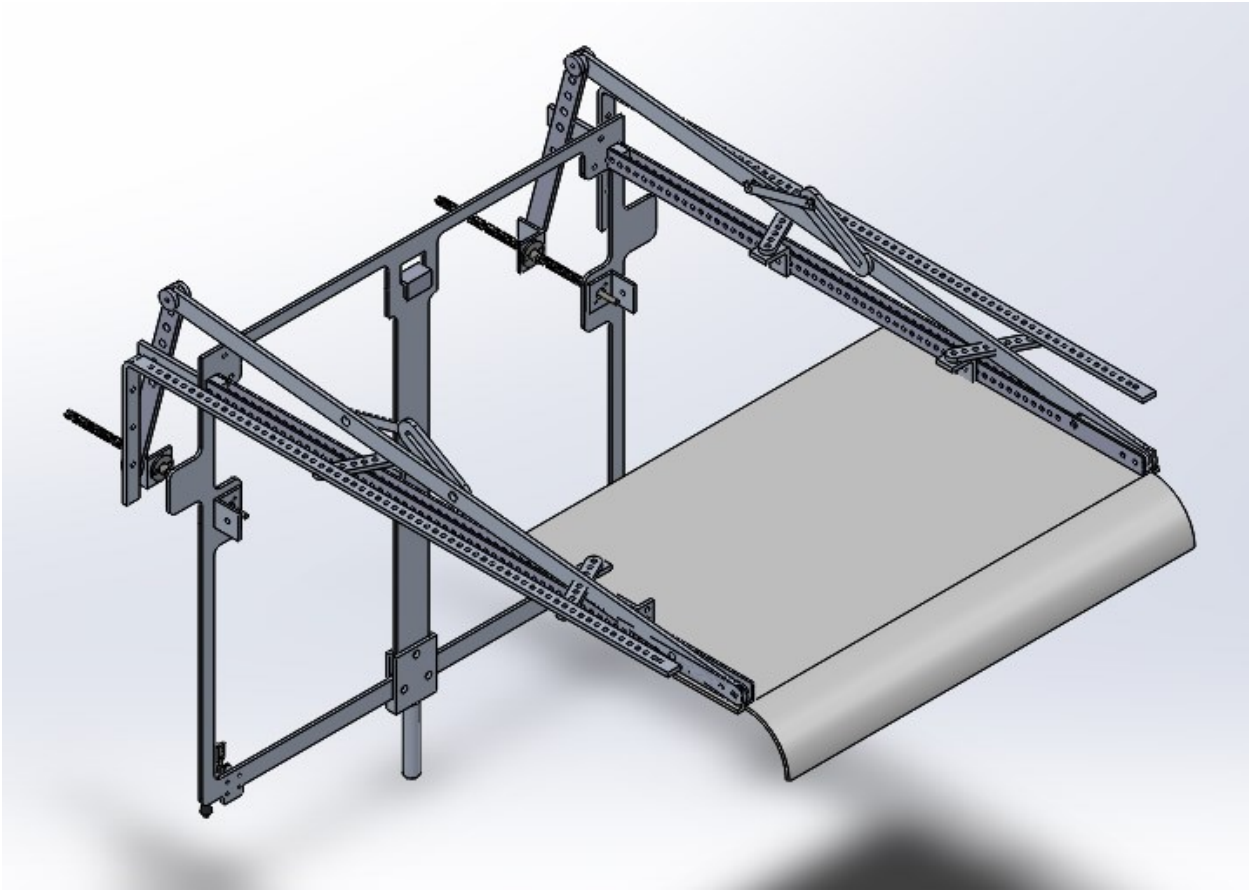
Figure A.16. *Isometric view of the vent mount CAD model.*

A.5 CAD Images of the Insertion Arm
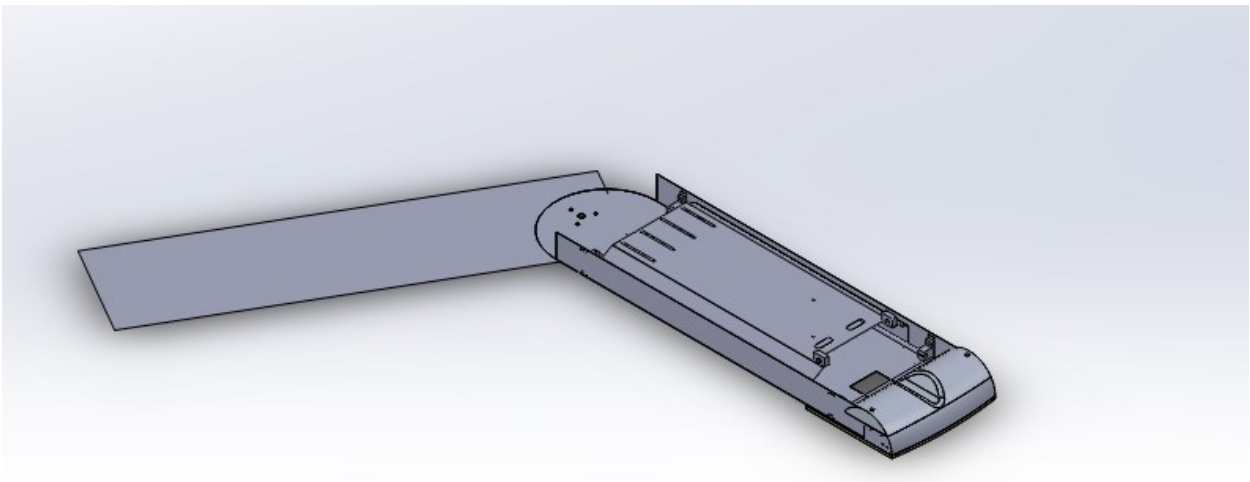
Figure A.17. *Isometric view of the insertion arm.*
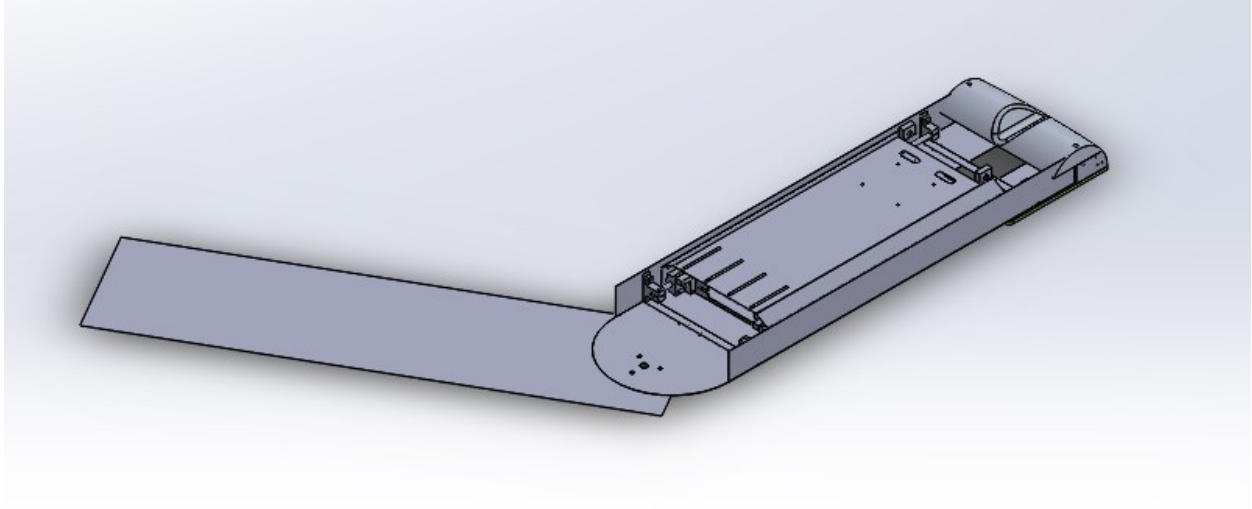
Figure A.17. *Alternative isometric view of the insertion arm.*
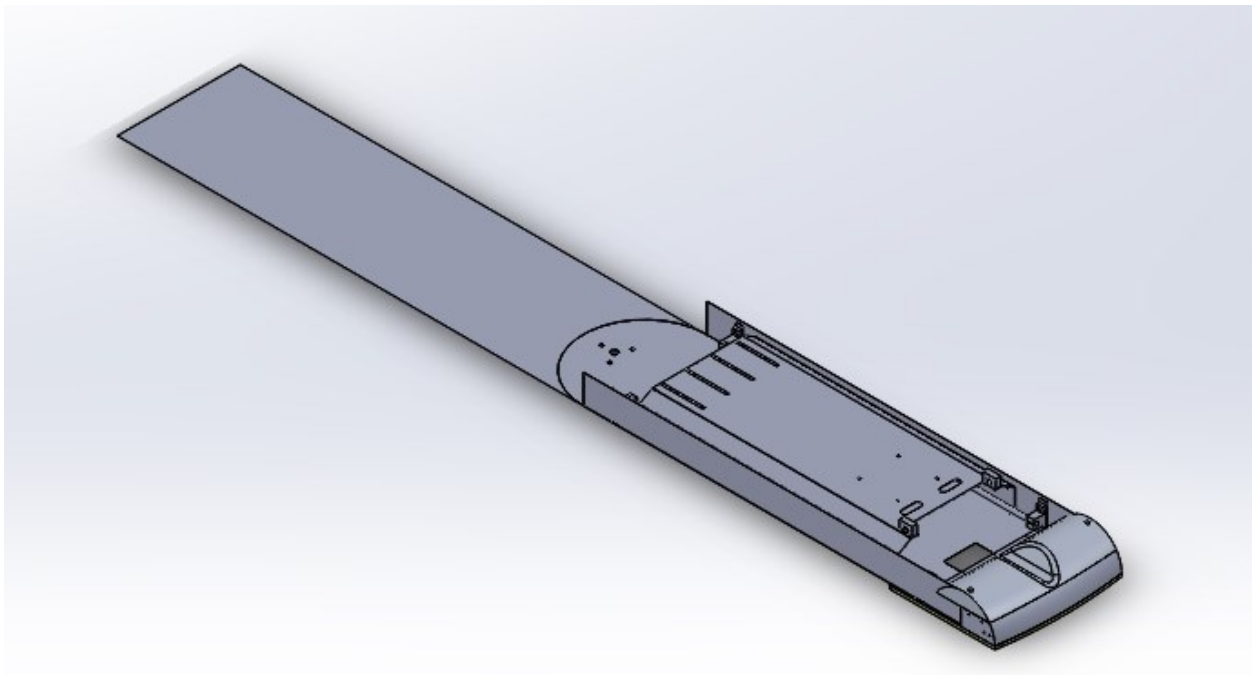
Figure A.18. *Isometric view of the insertion arm in the straight position.*

A.6 CAD Images of Winch and Winch Mounting Plate
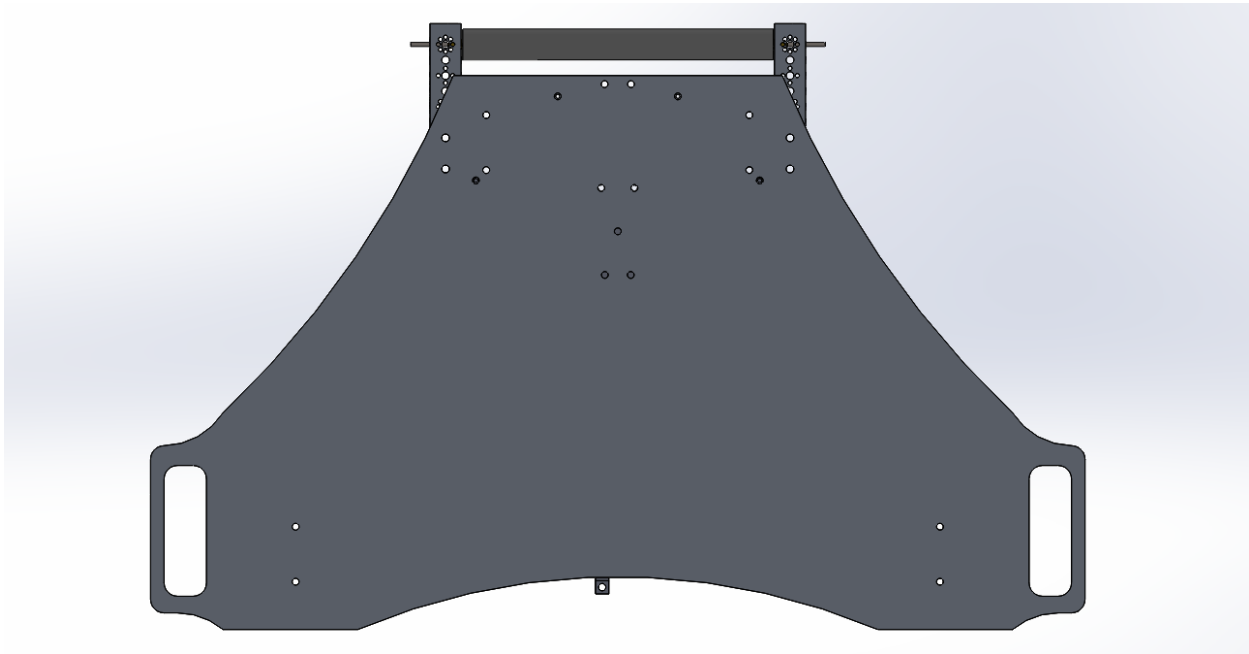
Figure A.19. *Back view of the winch plate CAD model.*
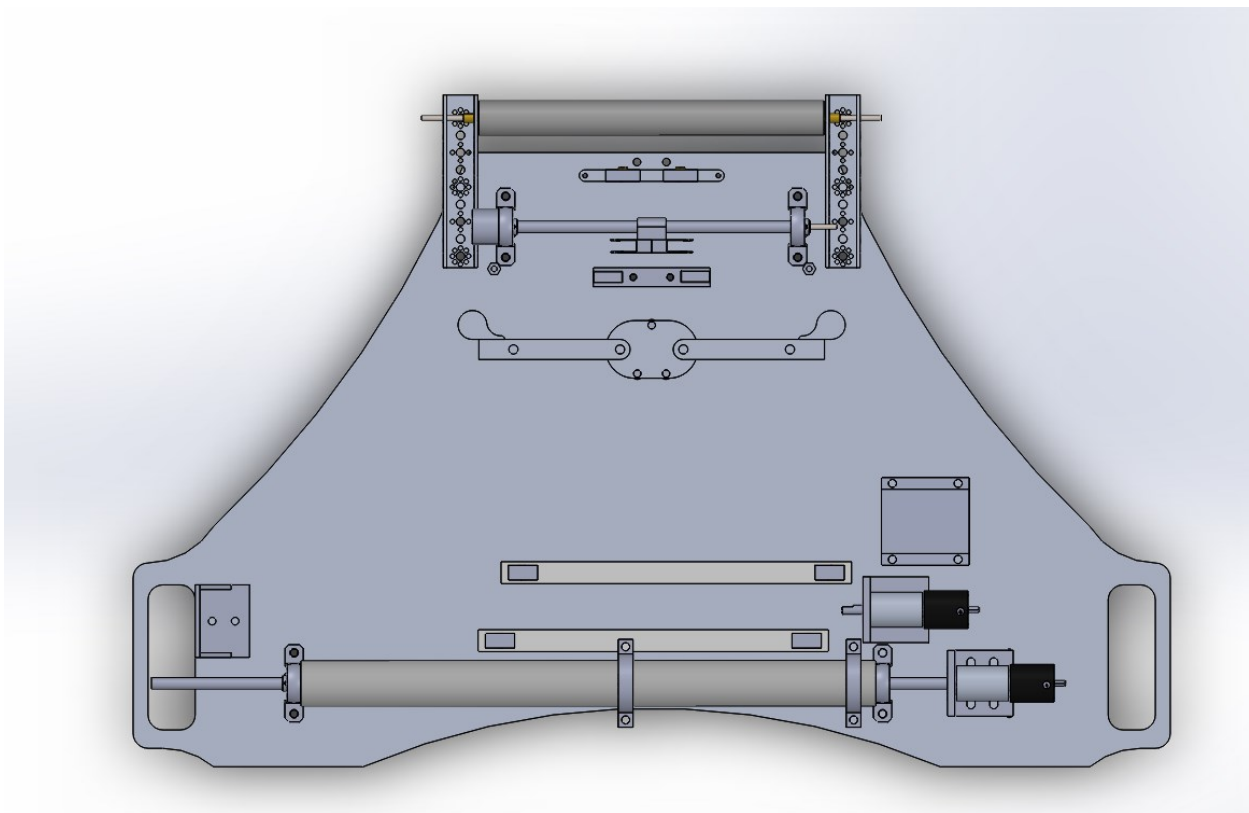
Figure A.20. *Front view of the winch plate CAD model, with winch and accoutrements.*
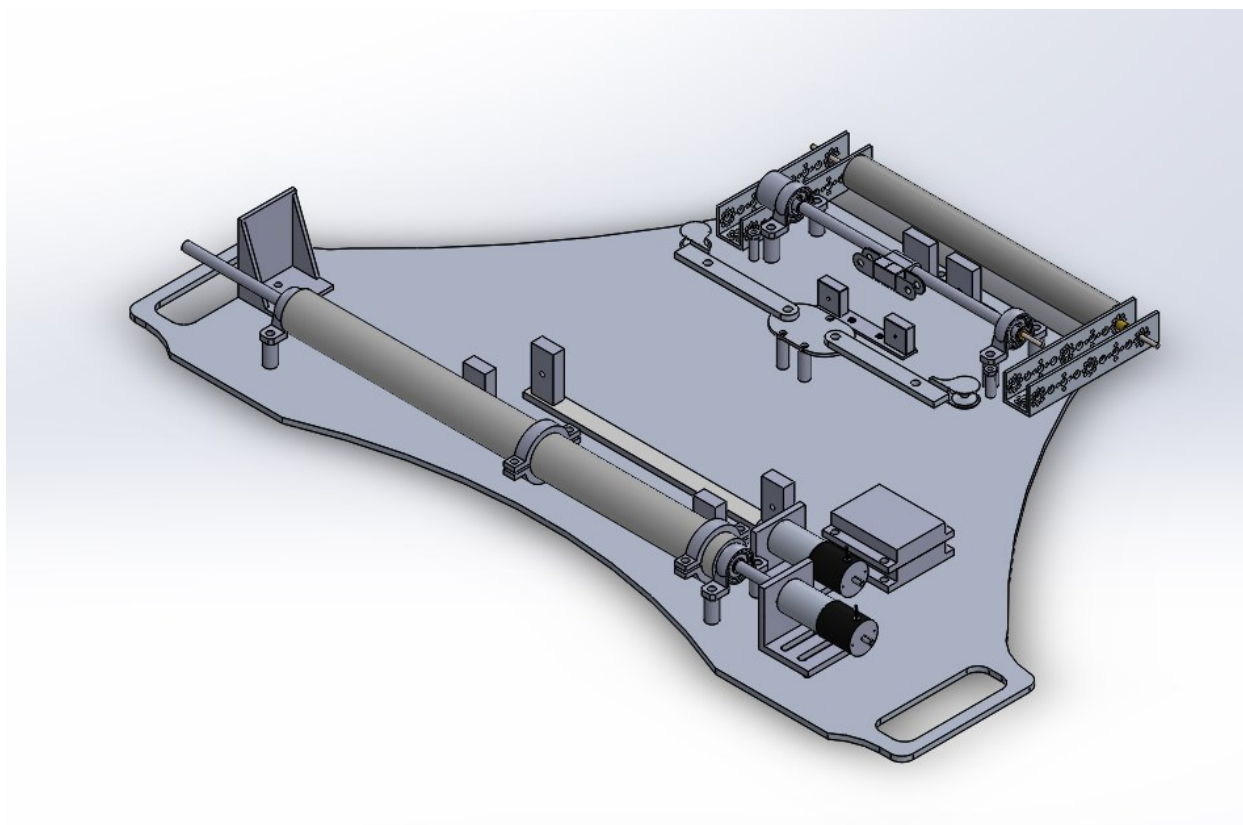
**Figure A.21.** *Isometric view of the winch mounting plate CAD model, with winch and accoutrements.*
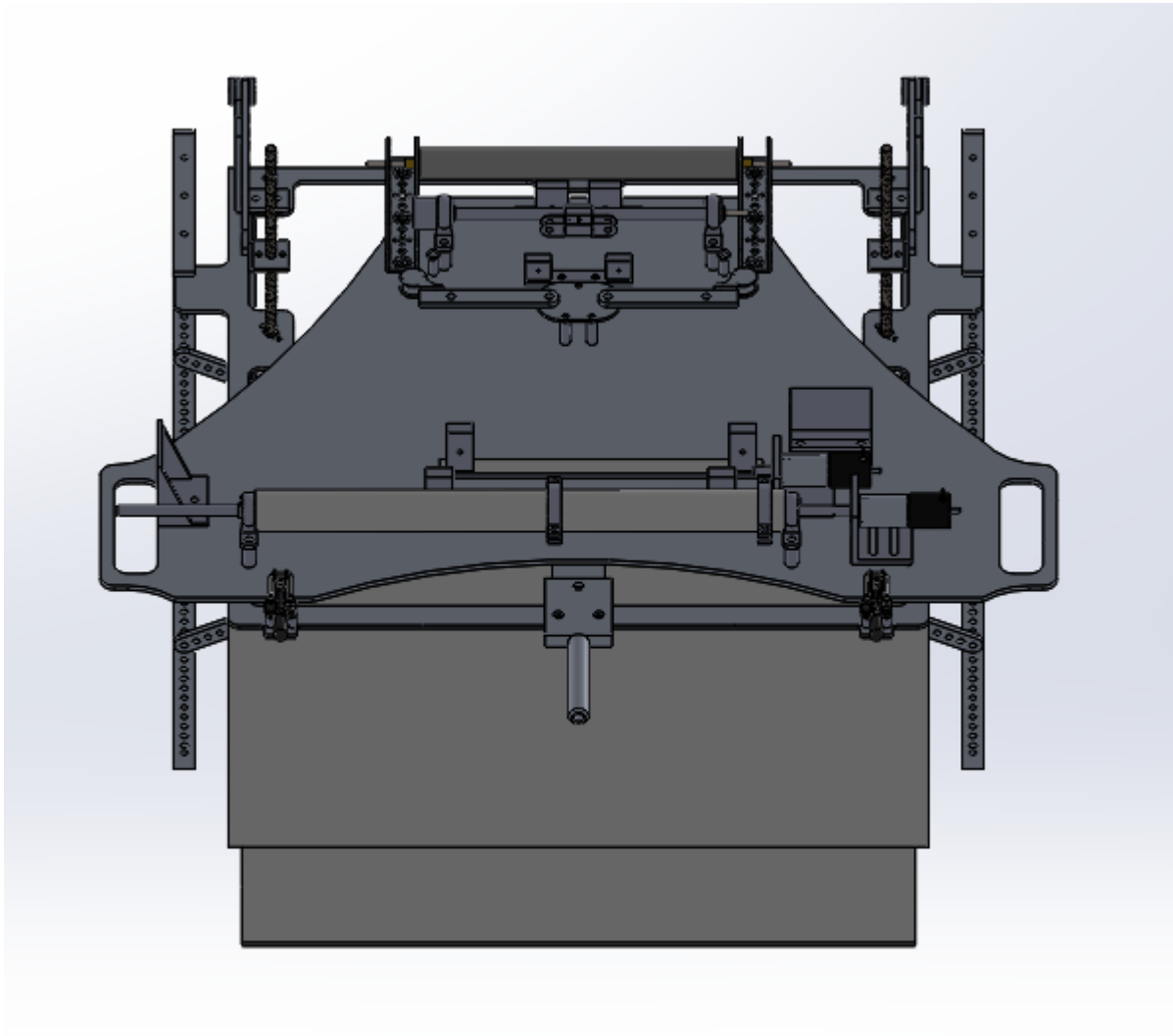
Figure A.22. *Front view of the winch assembly attached to the vent mount assembly.*
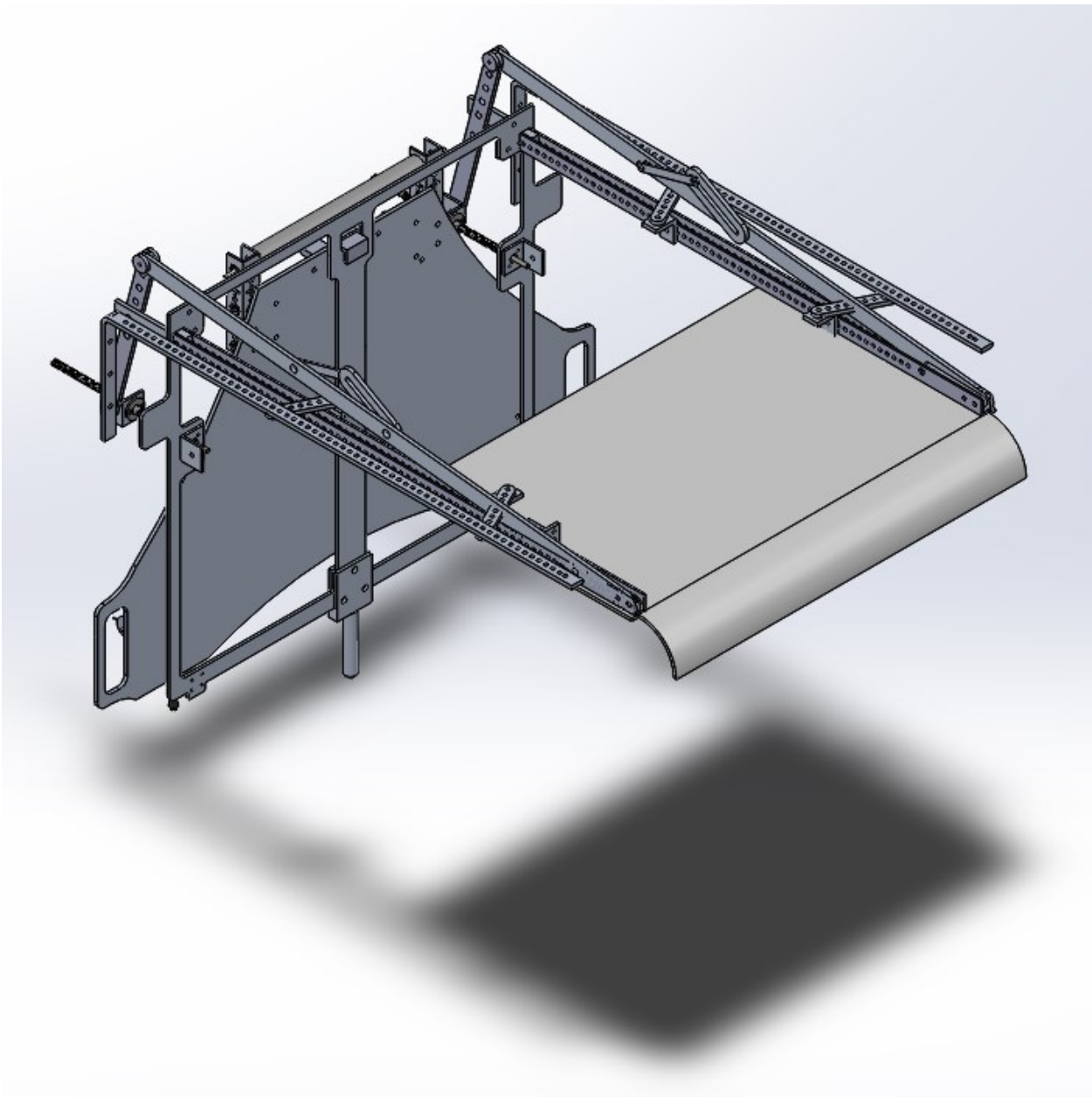
Figure A.23. *Isometric rear view of the winch assembly attached to the vent mount assembly.*
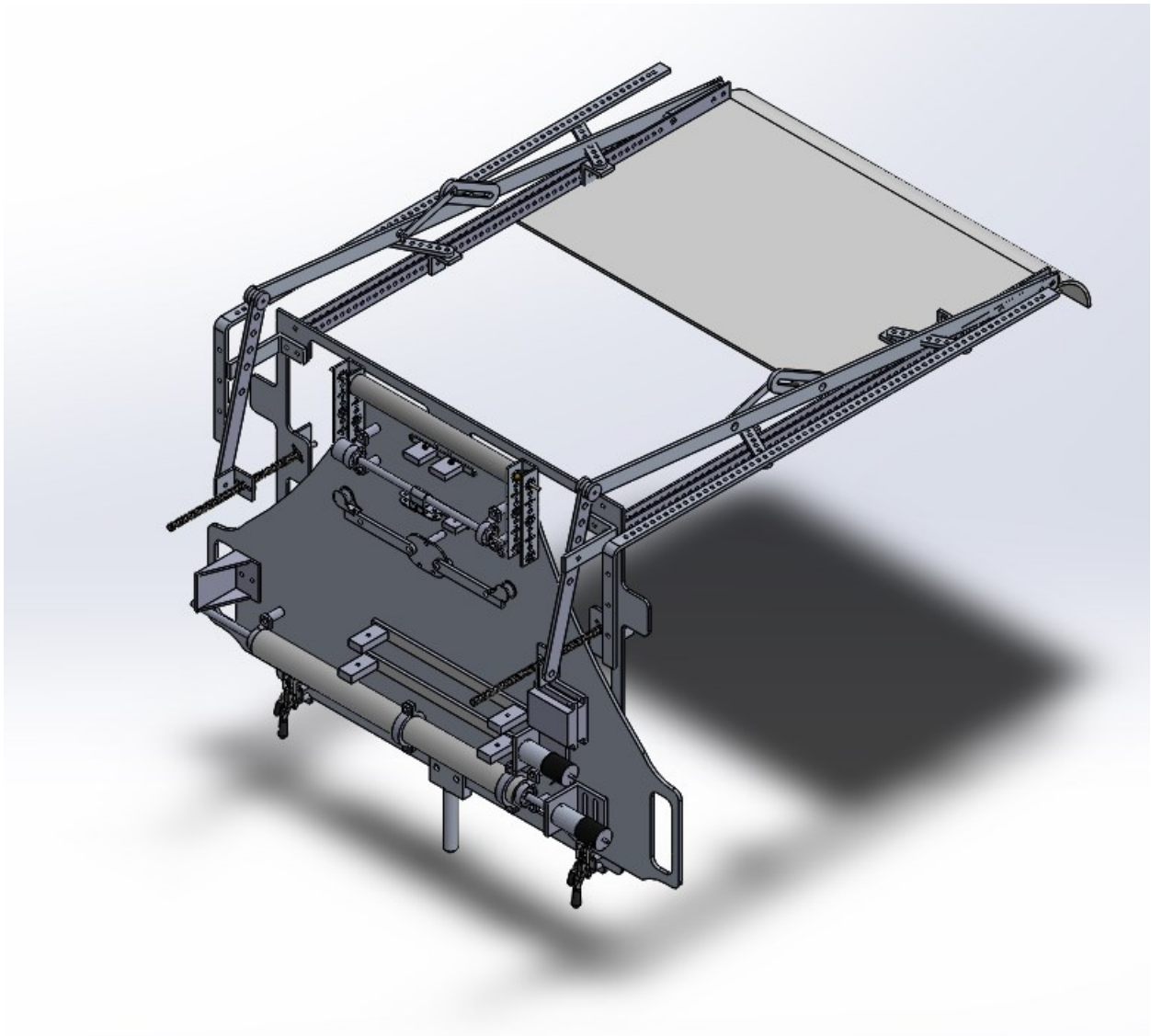
Figure A.24. *Isometric front view of the winch assembly attached to the vent mount assembly.*
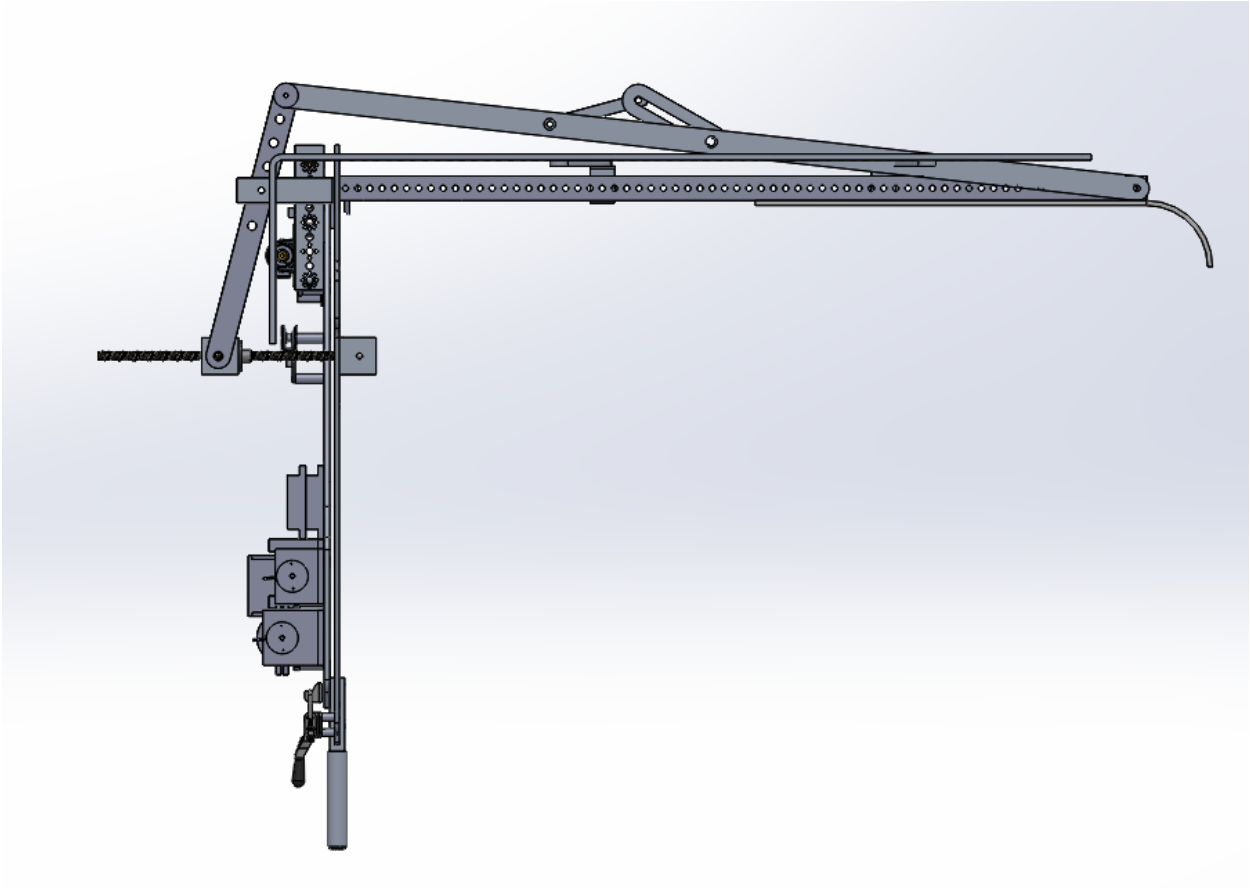
Figure A.25. *Side view of the winch assembly attached to the vent mount assembly.*
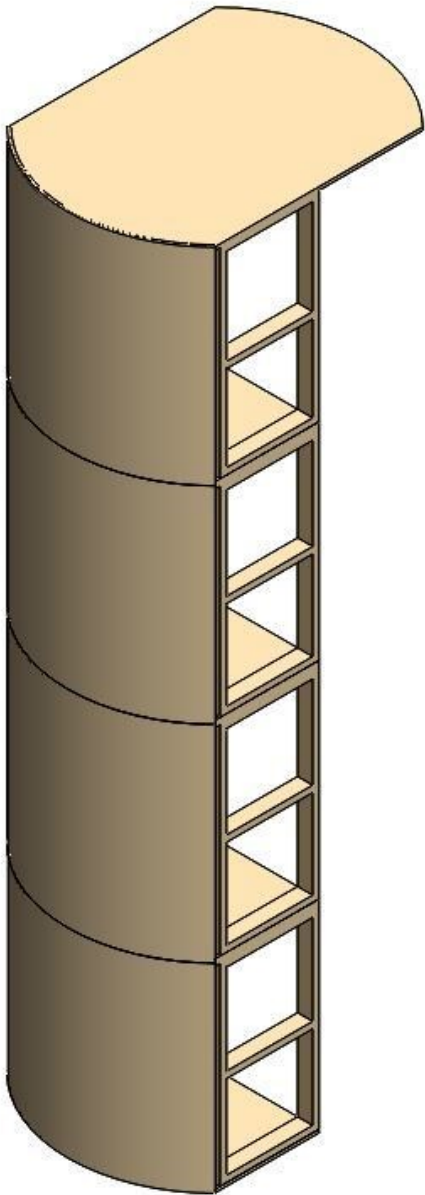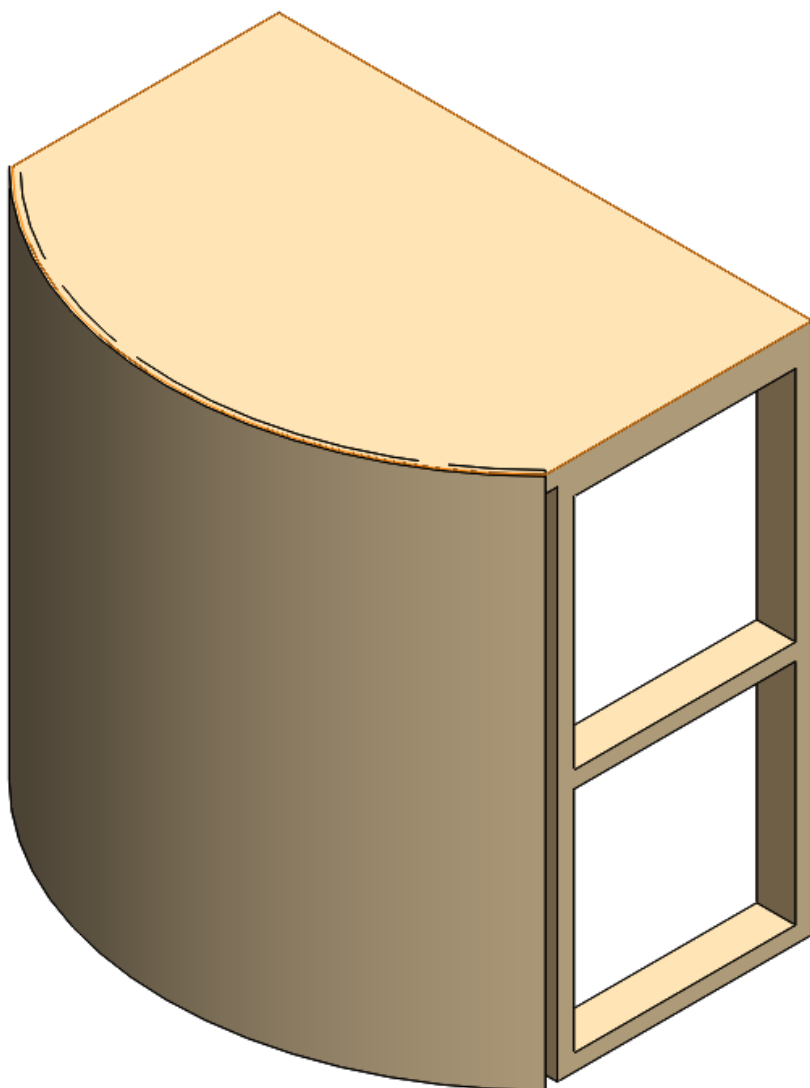
A.8 CAD Image of Camera Shield
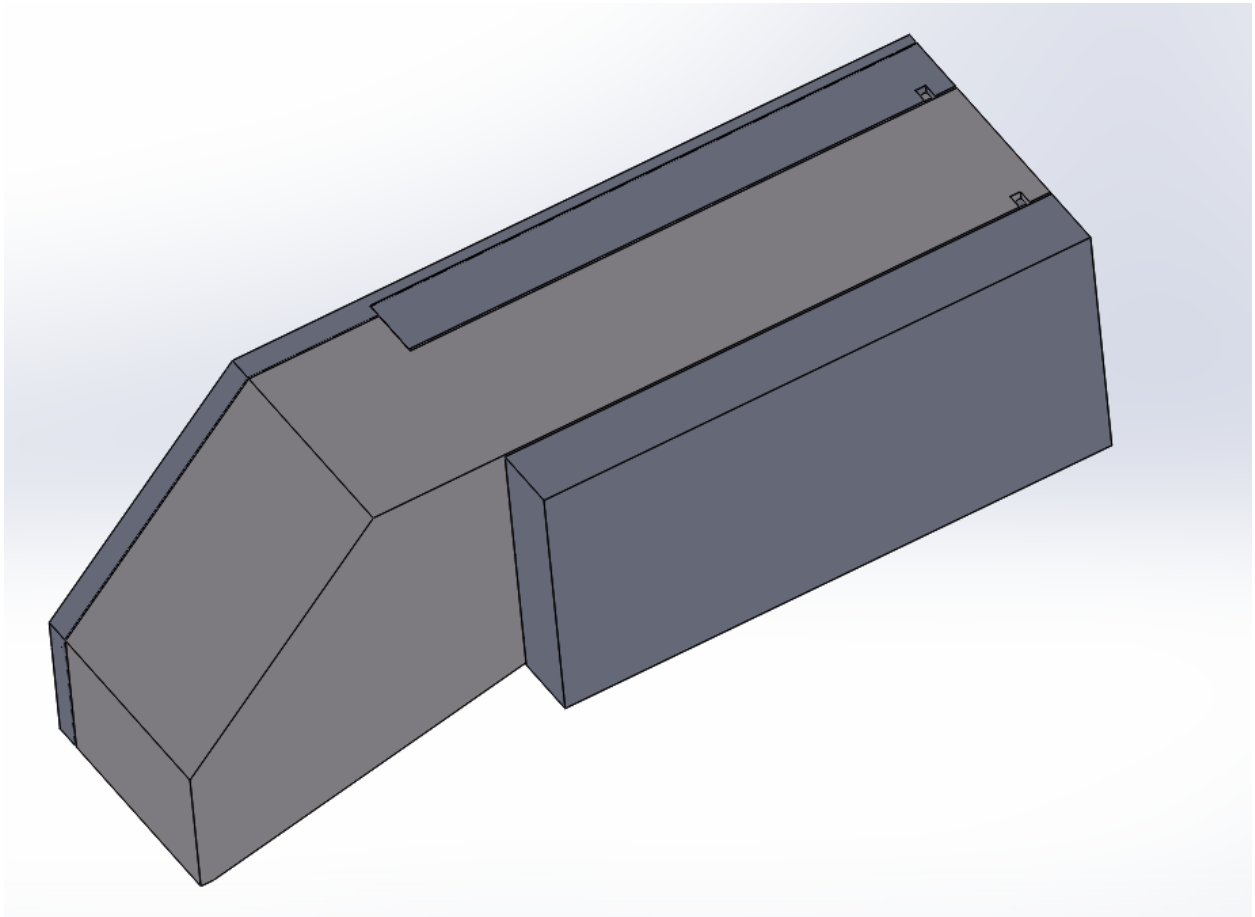
Figure A.26. *Isometric view of camera shield, also known as the "camera box."*
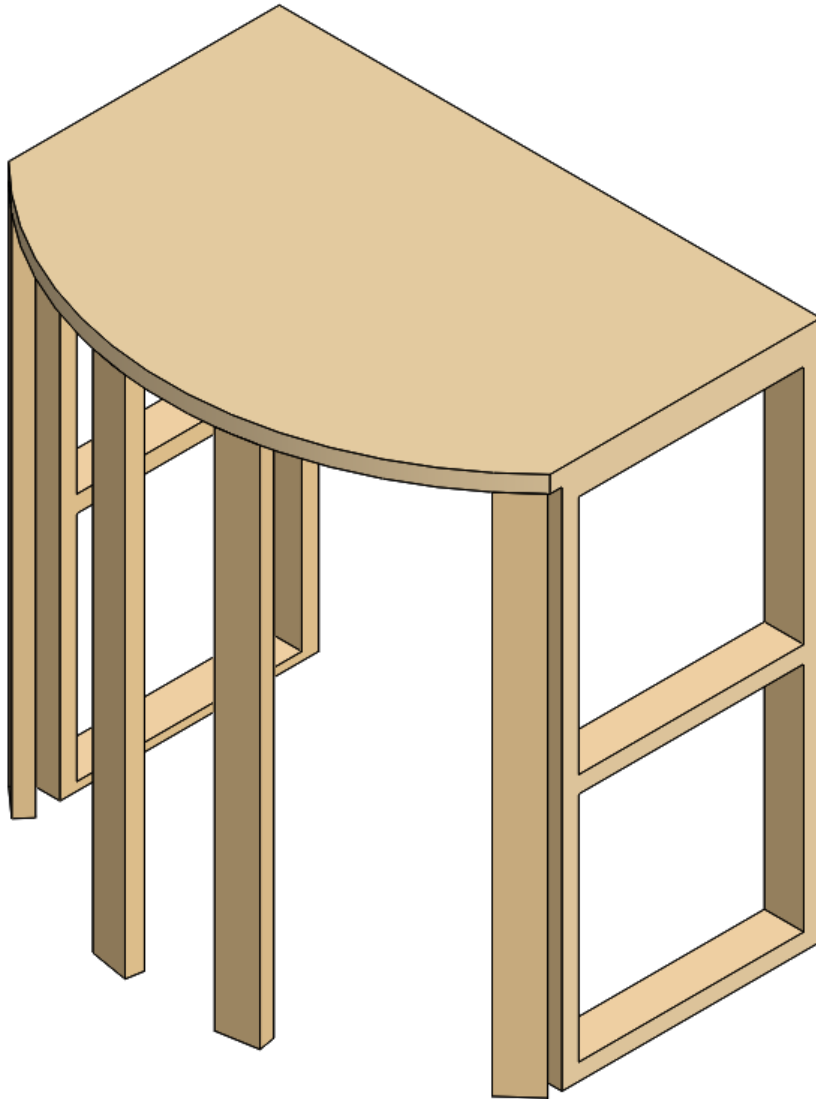
Figure A.27. *Isometric view of canister mock-up, fully assembled.*

Figure A.28. *Isometric view of canister mock-up segment.*

Figure A.29. *Isometric view of canister mock-up segment frame. Note that the middle two posts can be removed in order to replace the front section with a stainless steel segment for performing test inspections with the sensors.*